

UNIVERSITY OF EDINBURGH

DOCTORAL THESIS

---

# Preview-Based Control Methods for Ocean Wave Disturbance Mitigation for Underwater Robots

---

*Author:*

Kyle Liam WALKER

*Supervisor:*

Dr. Francesco  
GIORGIO-SERCHI

*A thesis submitted in partial fulfillment of the requirements  
for the degree of Doctor of Philosophy*

*in the*

Soft Systems Group  
School of Engineering

October 10, 2023



*For my parents and grandparents, my biggest fans...*



# Declaration of Authorship

I, Kyle Liam WALKER, declare that this thesis titled, "Preview-Based Control Methods for Ocean Wave Disturbance Mitigation for Underwater Robots" and the work presented in it are my own. I confirm that:

- This work was done wholly or mainly while in candidature for a research degree at this University.
- Where any part of this thesis has previously been submitted for a degree or any other qualification at this University or any other institution, this has been clearly stated.
- Where I have consulted the published work of others, this is always clearly attributed.
- Where I have quoted from the work of others, the source is always given. With the exception of such quotations, this thesis is entirely my own work.
- I have acknowledged all main sources of help.
- Where the thesis is based on work done by myself jointly with others, I have made clear exactly what was done by others and what I have contributed myself.

Signed:

---

Date:

---



*“You should do your PhD using the Kyle Walker method; try anything, go anywhere and have a laugh while doing it.”*

Adam A. Stokes, Robosoft 2022.



UNIVERSITY OF EDINBURGH

## *Abstract*

Institute for Integrated Micro and Nano Systems

School of Engineering

Doctor of Philosophy

### **Preview-Based Control Methods for Ocean Wave Disturbance Mitigation for Underwater Robots**

by Kyle Liam WALKER

A major factor in the drive to reduce the costs associated with offshore energy generation has been the development and adoption of robotic systems, which offer cost-efficient and safer alternatives in comparison to traditional human-operated maintenance procedures. With respect to renewable energy devices, challenges arise when attempting to deploy robotic technologies owing to the energetic environments in which devices are located, where large magnitude ocean waves are common-place. Here, shallow operational depth magnifies the complexity and associated risks of inspection and maintenance tasks, meaning traditional feedback control often lacks in performance and fails to guarantee safe operation; this has been a major limiting factor in technology uptake thus far. By investigating a solution to this control problem, the adoption of robotics by the sector will be accelerated, indirectly contributing to reducing operational costs and improving the uptake of clean ocean energy technologies.

In this thesis, the challenges highlighted above are investigated in relation to both rigid and soft robotic systems, aiming to devise a control methodology which can successfully minimize wave-induced disturbances. To do so, firstly a computationally inexpensive and generalised model to estimate the wave disturbances experienced by an underwater vehicle is developed and validated experimentally. Upon verification of this low-order model, an analytical reformulation is performed to establish scaling laws for positional error during feedback-controlled station keeping under wave disturbances. These scaling laws provide a first assessment tool in defining the level of control performance required and define a clear threshold of operative conditions beyond which feedback control becomes unreliable.

This motivates the need for more advanced control strategies. The proposed solution in this thesis is postulated on the inclusion of short-term horizon disturbances within the calculation of future control actions. An ocean wave predictor is implemented based on Deterministic Sea Wave Predictions (DSWP), a technique originally intended for renewable energy harvesters which operate at fixed-points. Here, the accuracy and applicability of DSWP is experimentally verified for short-time horizon conditions, which can be exploited for vehicle control applications. The ocean wave predictor is then implemented in two main control methods: one exploits the disturbance preview knowledge as a purely feed-forward control action, whilst the other embeds this knowledge within a Nonlinear Model Predictive Controller (NMPC) to optimise over a time horizon. A sensitivity analysis is performed with regards to robustness to noise and performance of both control methods, exploring the applicability with regards to real time operations. Lastly, a similar approach is adopted for control of a soft underwater manipulator, which could potentially be mounted on a station keeping vehicle. This explores the use of NMPC for controlling the position of the end-effector in the presence of wave disturbances. This final piece of analysis examines the applicability of the approach in relation to a system with highly nonlinear dynamics, where the body is anticipated to be influenced even further than the rigid-body case.

Upon presentation of the above work, this thesis introduces a solution for exploiting the predictive nature of wave-induced disturbances on submerged bodies to mitigate the experienced loads; in doing so, the effectiveness of this new approach is proven to vastly increase the operational range of existing robots, with minimal external infrastructure modifications required. This realistic solution presents a high potential opportunity to increase the level of automation currently deployed within the offshore sector, facilitating the ability to operate in hazardous scenarios safely and effectively.

## Acknowledgements

At the start of my Ph.D I was told by numerous people "*A Ph.D never turns out how you expect*" - a truer statement has never been spoken. However, even with the numerous setbacks, stress filled days and a global pandemic, I am extremely glad I chose to undertake one and to have met the people I have during the ride.

Firstly and most importantly, I would like to thank my supervisor (and good friend) Dr. Francesco Giorgio-Serchi, whom without I don't think I would have made it to the end. I had heard some stories of non-existent supervision when I started in 2019, but my experience couldn't have been further from this. Throughout the whole process his unwavering support and eagerness to find solutions to problems has been invaluable, enduring my miniature breakdowns and pushing me through them. Likewise, his encouragement to pursue any opportunity I came across has given me some memories and experiences I will never forget and for that I cannot express how grateful I am.

Likewise, I'd like to express my appreciation to Dr. Cosimo Della Santina and Dr. Kenjiro Tadakuma, who along with Dr. Giorgio-Serchi were kind enough to support my ventures and host me as part of their group during separate research stays. The experiences and knowledge imparted during these stays has guided parts of this thesis and hopefully fuels future exciting work, so thank you to both for facilitating this. I would also like to thank Prof. Adam A. Stokes, Prof. Aristides Kiprakis and Dr. David Forehand for their co-supervision and valuable insights when called upon throughout the last few years.

Similarly, I am appreciative of Dr. Brian Sellar and Dr. Gabriele Ferri for taking the time to review this thesis and offer their constructive comments and suggestions. I am also thankful to all of my lab mates and friends in Edinburgh, Delft and Sendai over the years who were always kind and helpful, particularly those during my visits abroad who made me feel extremely welcome. Special thanks also goes to Dr. Laura-Beth Jordan for sharing the stress of some last ditch experiments.

In terms of financial support, I gratefully acknowledge the support from UK Research and Innovation, The Scottish Funding Council, The Japan Society for the Promotion of Science and The Institution of Engineering and Technology for facilitating this work.

Finally I want to thank my family, particularly my parents; I would not be where I am or the person I am today without their continuous encouragement and support to pursue whatever I wanted to do.



# Contents

<b>Declaration of Authorship</b>	<b>v</b>
<b>Abstract</b>	<b>ix</b>
<b>Acknowledgements</b>	<b>xi</b>
<b>List of Figures</b>	<b>xx</b>
<b>List of Tables</b>	<b>xxii</b>
<b>List of Abbreviations</b>	<b>xxiv</b>
<b>1 Introduction</b>	<b>1</b>
1.1 Motivation . . . . .	4
1.2 Research Objectives . . . . .	5
1.3 Thesis Contributions . . . . .	6
1.4 Structure Outline . . . . .	7
<b>2 Literature Review</b>	<b>9</b>
2.1 Dynamic Control of Underwater Robots . . . . .	9
2.1.1 Classical Control for Underwater Vehicles . . . . .	9
2.1.2 Modern Control for Underwater Vehicles . . . . .	11
2.1.3 Sensing for Control of Underwater Vehicles . . . . .	18
2.1.4 Control of Soft Manipulators . . . . .	21
2.1.5 Challenges in Underwater Robot Control . . . . .	24
2.2 Ocean Wave Forecasting . . . . .	25
<b>3 Preliminaries</b>	<b>31</b>
3.1 Modelling the Ocean Environment . . . . .	31
3.1.1 Spectral Analysis . . . . .	31
3.1.2 Surface Wave Temporal Modelling . . . . .	33
3.2 Modelling of Underwater Vehicles . . . . .	39
3.2.1 Kinematics . . . . .	39
3.2.2 Rigid-Body Dynamics . . . . .	42
3.2.3 External Forces and Moments . . . . .	43
3.2.4 Nonlinear Dynamic Model for BlueROV2 Control . . . . .	46

3.3	Modelling of Soft Manipulators . . . . .	48
3.3.1	Kinematics . . . . .	49
3.3.2	General Parameter Derivation . . . . .	50
3.3.3	Soft Robot Model for Control . . . . .	53
<b>4</b>	<b>Parametric Analysis of Wave-Vehicle Interactions for Station Keeping Control</b>	<b>55</b>
4.1	Introduction . . . . .	55
4.2	Disturbance Estimation . . . . .	56
4.2.1	ROV Wave Disturbance Model . . . . .	56
4.2.2	Key Assumptions . . . . .	58
4.3	Experimental Study . . . . .	59
4.3.1	Methodology . . . . .	60
4.3.2	Instrumentation and Setup . . . . .	62
4.3.3	Model Validation . . . . .	65
4.3.4	Concluding Remarks . . . . .	71
4.4	Simulation Study: Feedback Controlled Station Keeping . . . . .	72
4.4.1	Parameter Identification . . . . .	72
4.4.2	Scenario Configuration . . . . .	74
4.4.3	Simulation Results . . . . .	76
4.4.4	Concluding Remarks . . . . .	78
4.5	Generalised Analytical Modelling . . . . .	78
4.5.1	Analytical Model Derivation . . . . .	79
4.5.2	Analytical Model Comparison . . . . .	82
4.6	Conclusions . . . . .	83
<b>5</b>	<b>Nonlinear Model Predictive Dynamic Positioning Exploiting Wave Disturbance Preview</b>	<b>87</b>
5.1	Introduction . . . . .	87
5.2	Deterministic Sea Wave Prediction . . . . .	88
5.2.1	Principles of Deterministic Sea Wave Prediction . . . . .	88
5.2.2	Estimation of Prediction Region . . . . .	89
5.2.3	Key Assumptions . . . . .	94
5.2.4	Disturbance Prediction Algorithm . . . . .	94
5.3	Wave Prediction Experimental Study . . . . .	95
5.3.1	Methodology and Setup . . . . .	96
5.3.2	Prediction Validation . . . . .	96
5.3.3	Concluding Remarks . . . . .	102
5.4	Model Predictive Control . . . . .	103
5.4.1	Linear Model Predictive Control . . . . .	104
5.4.2	Nonlinear Model Predictive Control . . . . .	106

5.5	Integrated System Simulation Study . . . . .	108
5.5.1	Simulation Configuration . . . . .	108
5.5.2	State Estimation . . . . .	114
5.5.3	Simulation Results . . . . .	116
5.5.4	Concluding Remarks . . . . .	126
5.6	Conclusions . . . . .	126
<b>6</b>	<b>Predictive Disturbance Rejection for Soft Underwater Manipulators</b>	<b>129</b>
6.1	Introduction . . . . .	129
6.2	Control Methodologies . . . . .	130
6.2.1	Model-Based Kinematic Control . . . . .	130
6.2.2	Nonlinear Model Predictive Control . . . . .	132
6.3	Soft Robot Wave Disturbance Model . . . . .	134
6.3.1	Hydrodynamic Parameter Specification . . . . .	136
6.4	Simulation Study . . . . .	136
6.4.1	Simulation Configuration . . . . .	138
6.4.2	Simulation Results . . . . .	140
6.5	Conclusions . . . . .	147
<b>7</b>	<b>Conclusions</b>	<b>149</b>
7.1	Summary . . . . .	149
7.2	Future Research Directions . . . . .	152
7.2.1	Nonlinear Model Predictive Dynamic Positioning Exploiting Wave Disturbance Preview . . . . .	152
7.2.2	Predictive Disturbance Rejection for Soft Underwater Manipulators . . . . .	154
7.2.3	Combined Vehicle-Soft Manipulator Control . . . . .	156
7.3	Implementation in the Field . . . . .	156
<b>A</b>	<b>Publications</b>	<b>159</b>
A.1	Published . . . . .	159
A.2	Under Review . . . . .	160
<b>B</b>	<b>Reference MATLAB Scripts</b>	<b>161</b>
B.1	WAMIT Symmetrising Script . . . . .	161



# List of Figures

1.1	Industry trends of ROV and AUV usage within the Oil and Gas sector.	2
1.2	(a) Significant height data sample and (b) operational boundary for an ROV.	3
1.3	The evolution of robotic manipulators over time.	4
2.1	PILIM adaptive controller block diagram.	11
2.2	Block diagram of a control architecture incorporating wave predictions and load estimations.	12
2.3	Example of the performance improvement potential of an MPC structure with embedded wave-induced disturbance considerations.	13
2.4	An example of an integrated path planning and MPC-based tracking control scheme.	15
2.5	Using deep reinforcement learning for vehicle path planning under constant ocean currents of 1m/s.	17
2.6	Example of different types of acoustic navigation configurations.	19
2.7	Example of controlling the configuration of a soft robot.	22
2.8	Variations of jamming techniques developed to control the stiffness capabilities of a wire-driven manipulator mechanism.	23
2.9	Visual representation of long-term and short-term wave forecasts and how they differ.	26
2.10	Basic principle of fixed-point DSWP.	28
2.11	Example of using a wave-rider LIDAR system for the purposes of DSWP.	29
3.1	Discretized wave spectrum	32
3.2	Polychromatic wave representation as a set of monochromatic waves.	34
3.3	Example of wave evolution elevations for a planar case.	35
3.4	Vector representation of the fluid particle velocities beneath the surface wave elevation.	36
3.5	Example of wave elevations for a multi-directional case.	39
3.6	Earth-fixed and body-fixed co-ordinate frames for a rigid body.	40
3.7	Thruster layout of the BlueROV2 Heavy.	48
3.8	Schematic representation of the PCC geometry for a two segment robot.	50

4.1	Particle velocities and resultant forces acting on the vehicle in both the local and global co-ordinate frame. . . . .	57
4.2	The FloWave Ocean Research Facility. . . . .	59
4.3	The ROV suspended in the purpose-built frame with the tank floor raised. . . . .	60
4.4	Numbering scheme adopted for the load cells. . . . .	60
4.5	The submerged ROV within the frame. . . . .	61
4.6	JONSWAP cases tested in the experimental study in Chapter 4 . . . . .	62
4.7	Positions of the underwater cameras associated with the motion capturing system in FloWave. . . . .	63
4.8	Load cell force vector components. . . . .	64
4.9	Comparison results for case R02 during wave-induced loads experiments. . . . .	66
4.10	Comparison results for case JS01 during wave-induced loads experiment. . . . .	67
4.11	Comparison results for case JS02 during wave-induced loads experiment. . . . .	67
4.12	Comparison results for case JS03 during wave-induced loads experiment. . . . .	68
4.13	Distribution of the experimentally collected data compared to the simulated data. . . . .	69
4.14	Normalised error relative to significant wave height for all cases. . . . .	70
4.15	Simplified BlueROV2 Heavy model. . . . .	73
4.16	Location of the wave buoy selected for analysis. . . . .	74
4.17	Temporal and spectral representation of test cases. . . . .	75
4.18	Recorded data and associated mean values from the Moray Firth WaveNet Site. . . . .	76
4.19	Vehicle maximum displacement from the desired station keeping position when subject to different waves. . . . .	77
4.20	Analytical model results for the surge. . . . .	83
4.21	Analytical model results for the heave. . . . .	84
5.1	DSWP generalised operation flowchart. . . . .	89
5.2	DSWP concept with respect to ROV control, where the measuring device is located at point $x_m$ and the wave prediction is performed at point $x_p$ . . . . .	90
5.3	Space-time diagram for the fixed-point method. . . . .	91
5.4	Bounded wave frequency spectrum . . . . .	92
5.5	Space-time diagram for the fixed-time method. . . . .	93
5.6	Experimental procedure for collecting the results during the DSWP experiments. . . . .	97
5.7	Comparison of the predicted wave against the recorded wave gauge data for case T1 . . . . .	98
5.8	Comparison of the predicted wave against the recorded wave gauge data for case T2 . . . . .	100

5.9	Comparison of the predicted wave against the recorded wave gauge data for case T3 . . . . .	101
5.10	Model Predictive Control concept . . . . .	104
5.11	The proposed framework for predictive disturbance mitigation . . . . .	109
5.12	Block diagram of the feed-forward disturbance mitigation technique. .	111
5.13	Block diagram of the feedback Cascaded Position-Velocity PID Controller. . . . .	112
5.14	Multiple shooting method schematic. . . . .	113
5.15	Block diagram representation of the Extended Kalman Filter (EKF). .	114
5.16	Temporal segment of the station keeping simulation. . . . .	115
5.17	Error results for each test case during the NMPC station keeping simulation study. . . . .	116
5.18	Violin plot for each test case during the NMPC station keeping simulation study. . . . .	117
5.19	Example of the effect of spectral noise on a tested wave. . . . .	118
5.20	Error results when considering spectral noise during the NMPC station keeping simulation study. . . . .	119
5.21	Temporal segment of the trajectory tracking mission. . . . .	121
5.22	Trajectory tracking spatial comparison for case W2. . . . .	122
5.23	Trajectory tracking spatial comparison for case W1. . . . .	123
5.24	Trajectory tracking spatial comparison for case W3. . . . .	124
5.25	RMSE and maximum error for the trajectory tracking mission; inclusive of noisy cases. . . . .	125
5.26	Power consumption during the trajectory tracking mission. . . . .	126
6.1	Block diagram for the soft robot feed forward with PD control strategy. .	131
6.2	Block diagram of the NMPC for soft robot end-effector control. . . . .	132
6.3	Visual representation of the fluid force integration across the soft robot body. . . . .	135
6.4	Tested wave spectra for the soft robot control analysis . . . . .	138
6.5	Set-point regulation of six separate points. . . . .	139
6.6	Temporal evolution of the (a) wave train and the resulting (b) segment tip positions, (c) actuation torques and (d) wave loading torques for the soft manipulator controlled with MPC. . . . .	140
6.7	RMSE error of the end-effector position when controlled with the MPC strategy. . . . .	141
6.8	Variation in error between the MPC strategy and the baseline feedforward + PD strategy for the soft manipulator. . . . .	142
6.9	End-effector positional error and joint angle evolution's for the trajectory tracking task of a star path. . . . .	143

6.10 Spatial representation of the end-effector trajectory tracking task for a star path. . . . .	144
6.11 Set-point regulation validation of the control with varying actuation capability for the soft manipulator. . . . .	145
6.12 RMSE of the soft manipulator end-effector in the presence of a mid-section actuation failure, in comparison to a fully actuated soft robot. .	146

# List of Tables

3.1	SNAME notation, commonly used for marine vehicles. . . . .	40
4.1	Experimental parameters for the test cases considered in Chapter 4. .	61
4.2	Locations of the mounting points (MP) relative to the centre of the vehicle body during the wave-induced loading experimental trials. . . .	64
4.3	Longitudinal locations of the wave gauges with respect to the centre of the tank and ROV in the global co-ordinate frame. . . . .	65
4.4	Correlation coefficients between the estimated forces and the experimental data. . . . .	69
4.5	Control parameters for the ROV during the station keeping mission. .	76
5.1	Longitudinal location of the wave gauges (measurement points) relative to the centre of the tank (0m). . . . .	96
5.2	Case specifications and references for the DSWP experimental trials. .	96
5.3	Effect of different thresholding methods on key parameters for each wave case. . . . .	101
5.4	Effect of varying distance between measurement and prediction points on key parameters for each wave case. . . . .	103
5.5	Parameters for each wave case considered in Chapter 5. . . . .	109
5.6	BlueROV2 Heavy dimensions and hydrodynamic parameters. . . . .	110
5.7	Parameters for the different ROV control strategies, both MPC and PD related. . . . .	110
5.8	Power consumed during tests when considering spectral noise. . . . .	120
6.1	Soft manipulator geometric and hydrodynamic parameters for each identical segment. . . . .	137
6.2	Control parameters for the soft robot. . . . .	137
6.3	Parameters for each wave case considered throughout Chapter 6. . . .	138
7.1	Summary of load estimation accuracy recorded during the analysis undertaken in Chapter 4. . . . .	150
7.2	Summary of achievable DSWP accuracy during the analysis undertaken in Chapter 5. . . . .	150
7.3	Summary of RMSE errors recorded during the analysis undertaken in Chapter 5. . . . .	151

7.4 Summary of RMSE errors recorded during the end-effector regulation analysis undertaken in Chapter 6 . . . . .	152
---	-----

# List of Abbreviations

<b>ROV</b>	Remotely Operated Vehicle
<b>AUV</b>	Autonomous Underwater Vehicle
<b>O&amp;M</b>	Operation & Maintenance
<b>MPC</b>	Model Predictive Control
<b>RAO</b>	Response Amplitude Operator
<b>DSWP</b>	Deterministic Sea Wave Prediction
<b>NMPC</b>	Nonlinear Model Predictive Control
<b>DoF</b>	Degree of Freedom
<b>EKF</b>	Extended Kalman Filter
<b>PID</b>	Proportional Integral Derivative
<b>SMC</b>	Sliding Mode Control
<b>PILIM</b>	Proportional Integral LIMited
<b>LQR</b>	Linear Quadratic Regulator
<b>MIMO</b>	Multiple Input Multiple Output
<b>NDT</b>	Non Destructive Testing
<b>WEC</b>	Wave Energy Converter
<b>MOPC</b>	Multi-Objective (Model) Predictive Control
<b>RMPC</b>	Robust Model Predictive Control
<b>RNMPC</b>	Robust Nonlinear Model Predictive Control
<b>Ex-MPC</b>	Explicit Model Predictive Control
<b>AI</b>	Artificial Intelligence
<b>RL</b>	Reinforcement Learning
<b>NN</b>	Neural Network
<b>IMU</b>	Inertial Measurement Unit
<b>RNN</b>	Recurrent Neural Network
<b>GPS</b>	Global Positioning System
<b>ROMS</b>	Regional Ocean Modelling System
<b>LIDAR</b>	Light Detection And Ranging
<b>AR</b>	Autoregressive Model
<b>GP</b>	Genetic Programming
<b>MT</b>	Model Tree
<b>ANN</b>	Artificial Neural Network
<b>PM</b>	Pierson Moskowitz
<b>LWT</b>	Linear Wave Theory

<b>CoG</b>	Centre of Gravity
<b>CoB</b>	Centre of Buoyancy
<b>PCC</b>	Piecewise Constant Curvature
<b>LC</b>	Load Cell
<b>WG</b>	Wave Gauge
<b>MoCap</b>	Motion Capturing System
<b>SWL</b>	Still Water Line
<b>MP</b>	Mounting Point
<b>FP</b>	Frame Marker Point
<b>PD</b>	Proportional Derivative
<b>Cefas</b>	Centre for Environmental Fisheries and Aquaculture Science
<b>RMSE</b>	Root Mean Square Error
<b>KC</b>	Keulegan Carpenter
<b>LMPC</b>	Linear Model Predictive Control
<b>ODE</b>	Ordinary Differential Equation
<b>C-PD</b>	Cascaded Proportional Derivative
<b>FF</b>	Feed Forward
<b>GPS</b>	Global Positioning System
<b>DVL</b>	Doppler Velocity Log
<b>KF</b>	Kalman Filter
<b>UKF</b>	Unscented Kalman Filter
<b>SNR</b>	Signal-to-Noise Ratio
<b>PR</b>	Probabilistic Roadmap
<b>RRT</b>	Rapidly Exploring Random Tree
<b>APF</b>	Artificial Potential Field
<b>DDQN</b>	Double Deep Q Network
<b>SDDQN</b>	Smooth Double Deep Q Network

## Chapter 1

# Introduction

Robotic systems are anticipated to play a large role in what is dubbed the *Fourth Industrial Revolution* [1, 2], but the vast majority of current solutions are still largely confined to extremely controlled environments where safety requirements are less stringent. Only recently have robots been conceived as mobile systems deployed in the real world in the shape of legged robots [3], aerial vehicles [4] and marine vehicles [5, 6] (amongst others) for assisting with inspection and maintenance tasks. Particularly in a marine environment, robotic vehicles have offered the potential to improve the safety of a number of operations [7], whilst simultaneously driving down the overall costs associated with energy generation and the requirement for systematic and routine maintenance during a plant’s lifetime [8]. This is supported heavily by the statistics displayed in Fig. 1.1 [9], showing a positive trend over time of increased Remotely Operated Vehicle (ROV) usage and Autonomous Underwater Vehicle (AUV) demand, paired with greater investment into technology development; this surpassed \$100 million in 2016 and has continued to rise since. Although these vehicles have been deployed and utilised for decades within the offshore oil and gas sector [10], the transition into other areas of offshore operations has yet to fully emerge.

Deploying autonomous systems to perform Operation and Maintenance (O&M) tasks has the potential to reduce workforce costs by up to 50% [11]. Offshore wind turbines, for example, are anticipated to have O&M costs ranging from 20 – 25% of total energy costs; in contrast to their onshore counterparts, this is 10% higher than the anticipated range of 10 – 15% [12]. This is mainly attributed to their remote and harsh operational environments, coupled with restricted weather windows for safe and effective O&M [13]. However, several problems exist when adopting autonomous systems, mainly stemming from the robot undertaking tasks independent of an operator [14]; this ultimately raises questions over system safety during deployment for interventive maintenance. Alternatively, a more realistic and attainable solution is the introduction of hybrid vehicles, which can operate fully autonomously in particular scenarios but are piloted in others [15, 16]. This breed of vehicle has the benefits of added safety measures, allowing pilot intervention at necessary intervals when safety is questioned [17]. Such mode of operation can facilitate, for instance, the vehicle being piloted to a particular location near a structure and subsequently maintain

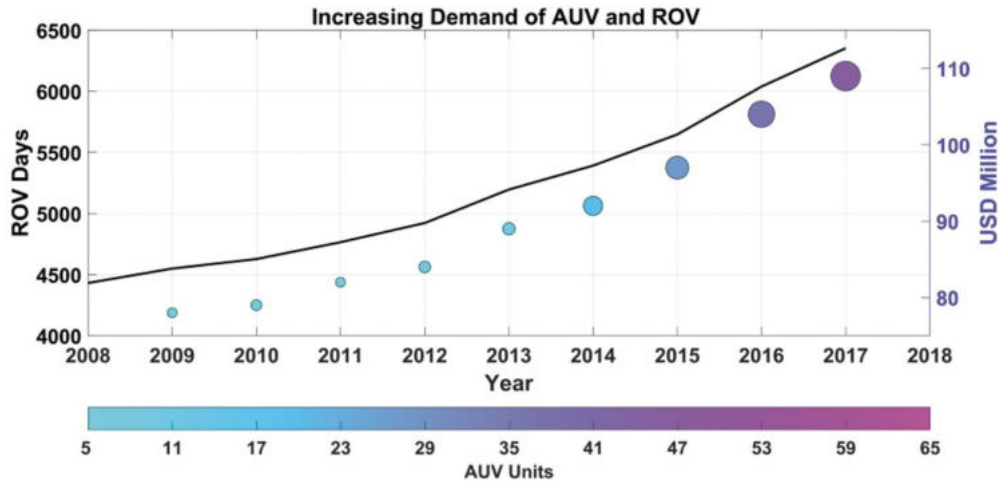


FIGURE 1.1: Industry trends of ROV and AUV usage within the Oil and Gas sector, where the size and color of the dots are relative to the number of AUV units (demand). The right axis refers to the investment in USD, showing a positive trend over time analogous to the number of ROV usage days (left axis) [9].

this position autonomously, thus allowing the pilot to focus solely on inspecting the structure or perform other peripheral contact maintenance procedures.

Particularly within the context of offshore marine renewable devices this becomes advantageous, as routinely deploying vehicles becomes restricted owing to the turbulent nature of the operational environment. As noted in [8], a major technological limitation preventing deployment is that "*in shallower waters, strong hover capabilities are necessary for close visual inspection and manipulation tasks, but current ROV capabilities do not perform well in the currents experienced at these water depths*". Although this refers specifically to currents, an analogous observation can be made for wave disturbances given that fundamentally they both result in fluid velocity and acceleration vector fields; the difference is that waves display cyclical behaviour. These disturbances can have a significant influence over the vehicle dynamic behaviour which can be detrimental to the safety of the operation, limiting the range of conditions in which vehicle can be deployed [18]. These encountered scenarios require a much higher degree of autonomy, reliability and robustness on the robot side, with the control complexity increasing accordingly; this complexity increases further when considering the nature of these environmental disturbances, which are often above the vehicle operational threshold in significant wave height or more commonly spectral peak period [9] (Fig. 1.2). An analogous observation can be made for intervention tasks, where the risk is exacerbated by the use of a manipulator to operate valves, inspect welds or perform other contact tasks. Indeed, in these scenarios the limitation extends from the control to include the structure of the manipulator itself - disturbances can be of significant magnitude and unexpected torques to the floating base can potentially lead to collisions [19], damaging the rigid joints and links which form the manipulator. As above, this presents the question of how these disturbances can

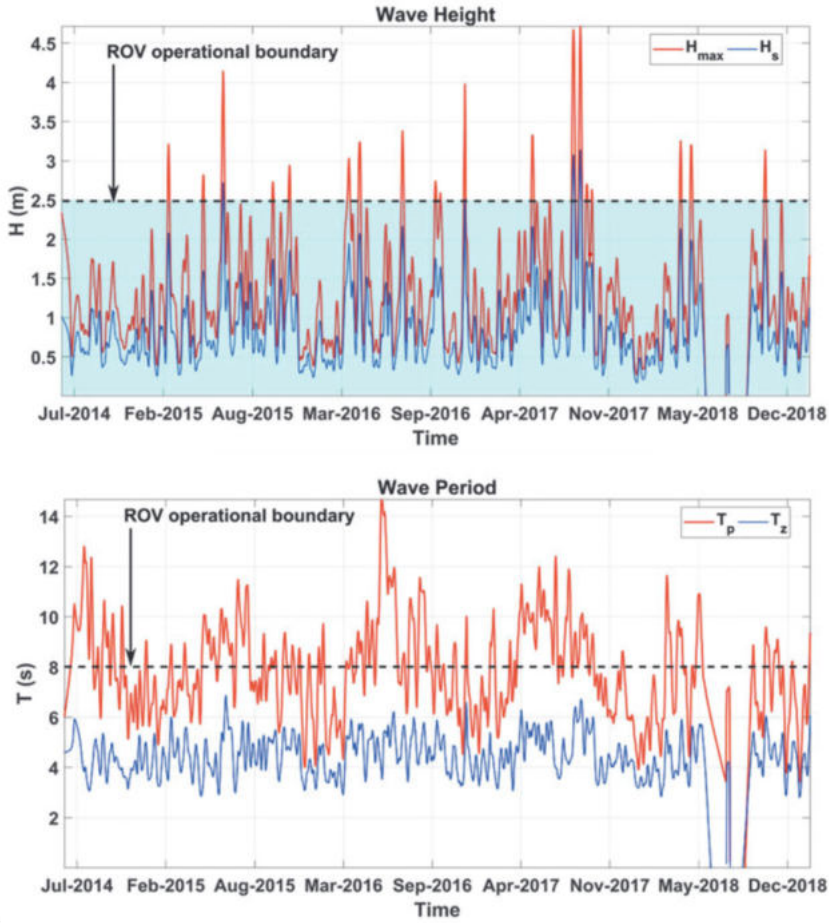


FIGURE 1.2: (a) Time series sample set of data for (a) sea state wave height parameters and (b) sea state period parameters showing the operational boundary for an ROV [9] where deployment would not even be considered by the operator.

be minimised and how the robustness of these systems in general can be improved to help facilitate a larger uptake in the marine renewable sector.

Throughout this thesis, the consideration and mitigation of wave-induced disturbances encountered by underwater robots is investigated, exploring the use of predictive control methods for both state control of an underwater vehicle and posture regulation of a conceptual soft robotic manipulator, the latter having the potential to be mounted on the floating base. This chapter provides an initial introduction to the motivation behind the work, discussing the relevance and importance of the topic before detailing a set of specific research objectives. Next, the specific contributions are listed, before finally giving an overview of the thesis structure and chapter organisation.

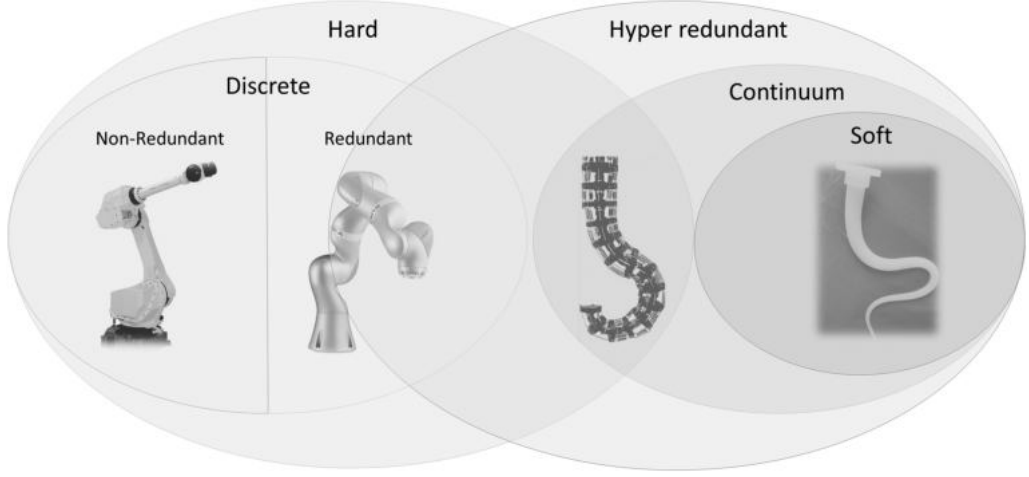


FIGURE 1.3: The evolution of robotic manipulators over time from left to right, with the state-of-the-art fully continuum representation on the far right capable of continuous bending [20].

## 1.1 Motivation

To broaden the range in which marine vehicles can be deployed and exploited to great effect, control strategies are required which can handle dynamic, nonlinear and large-magnitude disturbances to the system and minimise the risk of causing damage to the vehicle or plant (if operating nearby a device or structure). With the recent advance of computing power, predictive control schemes are gaining significant recognition for increasingly challenging applications, with a large portion of these focusing on dynamic robot control. In particular, Model Predictive Control (MPC) is one avenue which offers the potential to solve a multitude of problems associated with conventional methods and offer better performance [21, 22], mainly due to the capacity for handling constraints in the optimisation phase along with explicit consideration of nonlinear system dynamics [23].

Similarly, the structural robustness and control of intervention tools must be improved alongside vehicle control if the uptake of robotic systems is to continue increasing. These two elements form the basis of the majority of operations in the marine sector, where reliability is of the upmost importance for both navigation and manipulation. An interesting area which can be extremely applicable for achieving high reliability and robustness is the use of soft robotic concepts, such as those that are fundamental to continuum manipulators [20, 24] (like those shown in Fig. 1.3). Typically, current underwater manipulator designs are similar to the non-redundant example given in Fig. 1.3. Soft manipulators have surprisingly seen little transition into industry despite the superior flexibility offered by their hyper-redundant nature, especially within the offshore industry where the adoption of soft robotic technologies is virtually absent. The compliant nature of these soft structures and ability to handle disturbances without incurring significant damage is highly advantageous [9]; when coupled with a sufficient control scheme, soft robotics could offer highly effective

solutions in these particularly hazardous oceanic environments.

Focusing on the effect of environmental loading, the explicit inclusion of modelled disturbances as preview information within the control strategy is often overlooked. In a marine setting, the robot is often disturbed by environmental forces such as those induced by ocean waves; given that ocean waves have a large degree of associated predictability, formulating a preview of these forces in an anticipatory manner can potentially improve control performance [25]. If effective, the operational conditions of the robot will be greatly expanded, improving the ability to perform tasks where operation at close-proximity to submerged structures is required. Approaches thus far tend to formulate statistic based-disturbance models, for example evaluating Response Amplitude Operators (RAOs) [26], rather than forming an explicit discrete temporal prediction of the future system disturbance and incorporating this within the plant model; when disturbances are large and dynamic (as common in shallower waters), this current approach may fail to sufficiently capture the induced vehicle response required for effective mitigation.

These major factors form the key motivation behind this thesis, which aims to investigate the use of explicitly modelled temporal wave disturbance estimations within a general control framework to actively mitigate state perturbations. The strategy in question is intended to be applicable to various systems; this thesis aims to demonstrate this by applying the framework for control of both an underwater vehicle and an underwater soft robotic manipulator. When considered together, these form two key elements which can facilitate a greater uptake of robotics in the marine renewable sector, providing a solution to broaden the operational environments of current unmanned systems. Ultimately, the overarching benefit is the reduction of associated maintenance and inspection costs, assisting in improving the cost viability of energy generation from marine energy devices [11].

## 1.2 Research Objectives

As alluded to previously, there are still limitations with respect to the environments underwater vehicles are capable of safely operating within, specifically with respect to intervention tasks where the vehicle is situated in close proximity to subsea structures. This increases susceptibility to damage inflicted to either the structure or the vehicle, motivating the demand for improved techniques for wave disturbance mitigation. With respect to this, the fundamental objective of this thesis is to investigate the use of predictive control methods for wave disturbance rejection in underwater robotic systems, more specifically related to vehicle dynamic control and manipulator control. Expanding this into a set of defined objectives, this thesis aims to achieve the following:

1. Develop a low-order and computationally efficient method for estimating wave-induced disturbances on a submerged body. The aim of this objective is to

reduce the necessary computation for the control scheme, but also to generalise load estimations and provide a basis for the formulation of scaling laws for estimating key control related performance parameters.

2. Exploit wave disturbance predictions by developing a predictive control architecture for dynamic vehicle station keeping, explicitly considering disturbances as an additional direct input to the controller. This will encapsulate a wave forecasting algorithm coupled with MPC, drawing comparisons to alternative well-established control methods within the field.
3. Apply an analogous methodology to underwater soft robotic manipulators, with the aim of developing a controllable manipulator with a higher degree of robustness to environmental interactions than current rigid-link manipulators.

The common goal of all of the defined objectives relates to how the performance of the system control can be increased in underwater robotics when the plant is subjected to predictable disturbances.

### 1.3 Thesis Contributions

The major contributions in this thesis are as follows:

1. A detailed experimental validation of a piece-wise integration model for wave-induced load estimations (Chapter 4) [27, 28, 29, 30], coupled with an experimental validation of Deterministic Sea Wave Predictions (DSWP) over short distances for short time-horizon predictive control (Chapter 5). These constitute the predictive element of the overall proposed framework.
2. A generalised analytical model for estimating key station keeping performance metrics using only statistical wave parameters and lumped vehicle characteristics, offering a basis for performance scaling laws related to station-keeping vehicles in waves (Chapter 4).
3. A complete end-to-end framework for predictive disturbance rejection of wave-induced loads on an actively controlled underwater vehicle (Chapter 5). DSWP is used to obtain an estimate of wave disturbances ahead of time and a Nonlinear Model Predictive Controller (NMPC) generates the optimised control actions to maintain a stationary position (or follow a trajectory).
4. An NMPC framework for end-effector control of a multi-segment soft manipulator, enabling posture regulation and trajectory tracking via active rejection of unsteady wave disturbances (Chapter 6).

A related but minor contribution is a feed-forward control scheme for disturbance rejection [31], presented in Chapter 5, exploiting the same wave disturbance predictor model. This predictor provides model-based adjustments to feedback generated

control actions for mitigating vehicle displacement, representing an effective and computationally less burdening solution to a fully-fledged NMPC. As far as the author is aware, these have not been covered in the literature and constitute entirely novel contributions to the field of marine robotics.

## 1.4 Structure Outline

The remainder of this thesis is structured as follows: Chapter 2 presents a review of the literature in the field of dynamic control of underwater vehicles and soft manipulators, along with wave forecasting methods. Chapter 3 covers preliminary knowledge required for the following sections, namely the modelling of the ocean environment, underwater vehicles and soft robots. Subsequently, the novelties within this thesis are covered in Chapters 4-6.

Chapter 4 presents a proposed low-order wave-induced disturbance model, coupled with an experimental study performed to validate the model, whilst also introducing a proposed framework for generalising the behaviour of underwater vehicles using only well-known statistical parameters. Chapter 5 describes the proposed prediction and control framework for active wave disturbance rejection relating to an underwater vehicle covering the complete proposed framework for improving station keeping and trajectory tracking performance. This exploits DSWP and the wave disturbance model presented in Chapter 4 to provide preview information of estimated disturbances to the vehicle state ahead of time. An experimental study on DSWP over short distances is presented, which extends the experimental findings in Chapter 4 to prove the validity of the approach within the context of vehicle control. This predictive stage is then coupled with a NMPC to maintain the vehicle position in 3 Degrees of Freedom (DOF) in simulation, using an Extended Kalman Filter (EKF) to estimate the vehicle state throughout the operation. Chapter 6 investigates applying this same methodology to a soft robotic manipulator, also using a NMPC structure for maintaining the end-effector position under disturbances and in the presence of actuation failure, also in simulation.

Lastly, Chapter 7 provides concluding remarks summarising the findings of this thesis and suggests necessary directions of future work.



## Chapter 2

# Literature Review

### 2.1 Dynamic Control of Underwater Robots

The focus of this section is on reviewing state-of-the-art dynamic control methodologies being developed for deployment on underwater robots, specifically underwater vehicles and underwater soft robots. With regards to the former, a particular focus is placed on architectures designed for the purpose of performing vehicle *station keeping* - the act of remaining as stationary as possible under the influence of external disturbances. In the context of this thesis, *station keeping* specifically refers to minimising both positional and attitude displacements relative to a defined reference state. The reviewed control strategies have been conveniently grouped into what are commonly referred to as Classical Control strategies and Modern Control strategies in Section 2.1.1 and 2.1.2 respectively. For control of underwater soft robots, the review is not limited to applications underwater but general state-of-the-art control and is discussed in Section 2.1.4 . Finally, Section 2.1.5 presents a reflection on this component of the literature review, identifying the areas which the research objectives of this thesis are intended to contribute.

#### 2.1.1 Classical Control for Underwater Vehicles

In this review, classical control refers to the generation of control inputs relative to external impulses or cues through some form of feedback process. The controller is provided with information of the *reference* goal and typically exploits sensor measurements to determine an understanding of the system state, subsequently generating control actions to achieve the prescribed goal state. Classical control is generally the approach currently adopted within industry, usually offering a simpler reliable solution where operating environments are devoid of major disturbances and the plant behaviour has linear or close to linear dynamics. However, the increased need to deploy highly dynamic robots has led to more complex control strategies being required [8, 4]. This section of this review will therefore discuss approaches to classical control for underwater vehicles which have shown potential, but also highlight why more robust and higher performance control techniques are required.

One of the most recognised and widely used forms of classical control is Proportional-Integral-Derivative (PID) control [32]. The controller form can vary from operating as a stand-alone controller to a smaller component of a larger complex control hierarchy. State feedback is utilised with reference to a desired condition and the error is tracked, with the controller generating a control action relative to the objective of driving the system to the desired condition. Each term (Proportional, Integral, Derivative) has an associated gain which affects the response; each gain can also be fine tuned for improved controller performance, either using classical heuristic methods such as Ziegler-Nichols [32] or by other means such as using algorithms to *self-tune* the controller [33, 34, 35]. PID control for underwater vehicles has been extensively investigated [36, 37, 38, 39], but applicability is largely dependent on the scenario and ocean conditions. Often, a standard PID controller alone is not suitable when the operating environment is highly dynamic, for instance when surface waves propagate through the water column causing frequent and significant state perturbations [40]. In these situations, the corrective nature of PID control has a detrimental effect on set-point tracking performance [30, 21]; under wave-induced disturbances, this will ultimately drive the vehicle into a continuous *back-and-forth* motion as the control attempts to achieve the desired state configuration whilst being constantly displaced. Different methods have been developed to adapt and improve traditional PID control, combining the basic principle with advanced concepts to improve robustness, reliability and overall performance. For example, neural networks have been introduced for self-tuning purposes [41], but performance is not always consistent and can lead to erratic behaviour in some instances. Other concepts have introduced disturbance observers [42] or estimators to control certain degrees of freedom, still employing a PID control law to generate the control action but accounting for estimations in the process. However, given that the controller is still postulated based on a reactive response, the performance is fundamentally limited by the timescale of the disturbance relative to that of the actuators, thus can potentially lead to large deviations.

Alternatively, Sliding Mode Control (SMC) has been proposed for the control of underwater vehicles [43, 44, 45, 46], handling disturbances by treating them as uncertainty within the system [47, 48, 49] and compensating for the error by switching between the different modes. This offers an advantage over PID control, particularly in nonlinear system control [50, 51], but exposes the system to the well-documented problem of "*chattering*", which can cause undesirable oscillations in the control signal and lead to accelerated wear of the propeller motors. Attempts to remedy the chattering issue in SMC are numerous [52, 53], but the drawback is the additional complexity and tools required to reduce this effect and complete mitigation is not a guarantee. Similarly, varying forms of adaptive control have been proposed [54, 55, 56, 57, 58, 59] to account for unknown disturbances, for example the adaptive Proportional Integral Limited (PILIM) structure shown in Fig. 2.1 [56]. However, these works rarely consider significant magnitude disturbances and the approaches mentioned thus far do

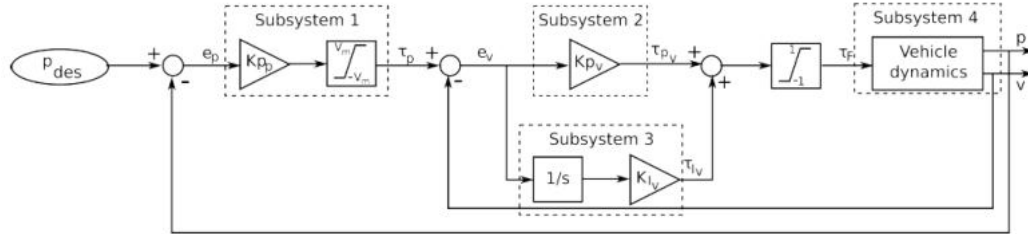


FIGURE 2.1: The PILIM adaptive controller adopted in [56] for deployment on an AUV.

not consider the often stringent constraints which are inherent within the plant models. If these constraints are violated, this can lead to unwanted behaviour, degrade control performance and in some cases result in instability [60].

Analysing the above mentioned methods generally highlights some common shortcomings; classical control methods cannot explicitly deal with constraints to perform an optimised control action, which can lead to poor performance both when regulating the vehicle state or tracking some trajectory. Similarly, there is no procedure for solving the control problem when explicitly considering external disturbances, whether this be in the form of environmental disturbances or simply measurement noise. Techniques exist to mitigate these, but due to the lack of an optimisation stage the performance of the control can vary from case to case. On the contrary, *modern control* offers an alternative to classical methods which possess the potential to tackle a large majority of these issues.

### 2.1.2 Modern Control for Underwater Vehicles

In contrast to the above mentioned approaches which purely exploit some form of feedback to respond to cues, there is also the possibility of performing control actions based on dynamic models of the system - this requires the system to have a degree of prior knowledge of plants internal (and in some cases external) dynamics. This is what is implied by the term *modern control* in this review; these control methods can be more computationally burdening but are also often less susceptible to disturbances, a major advantage for dynamic control problems.

One proposed method is the use of a Linear-Quadratic-Regulator (LQR), which offers improved performance over standard PID control due to being a form of optimal control. LQR control concerns a linear system or linearised system model and an associated quadratic cost function, through which an optimal solution can be calculated which minimises the cost function over a time horizon [61]; an optimal set of feedback gains is evaluated for the controller operation. LQRs have been proposed for tasks such as trajectory tracking [62, 63, 64] and state regulation [65] of underwater vehicles and have shown potential, but the deployment of an LQR requires linearisation of the nonlinear system dynamics, in some cases leading to poor performance on the control side [66]. It is possible to achieve better performance by employing techniques such as

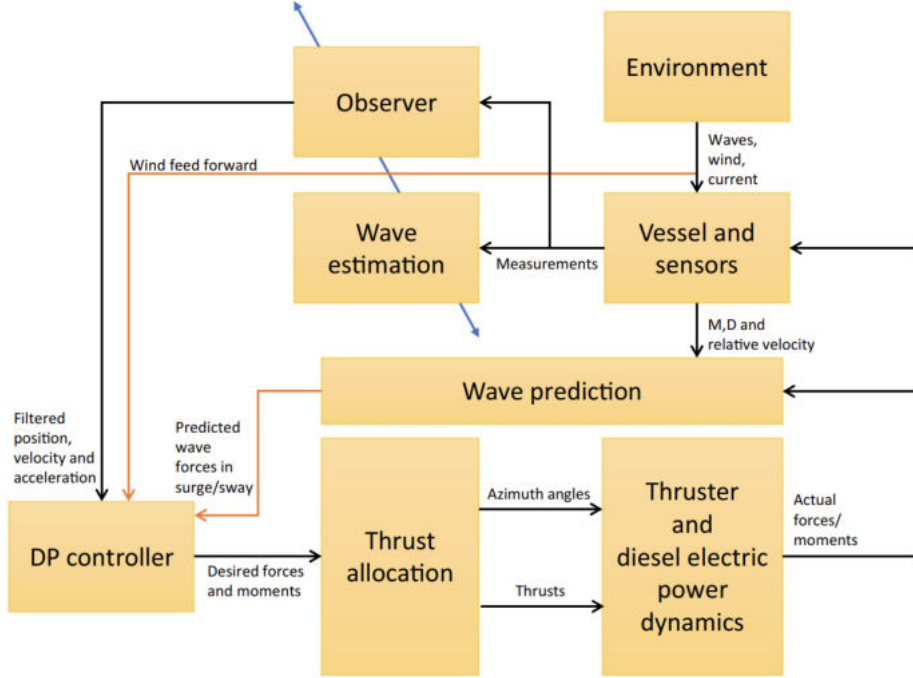


FIGURE 2.2: Block diagram of a control architecture incorporating wave predictions and load estimations [65].

state feedback linearisation [67], but problems such as response time have still been noted [68]. However, the improved performance of LQRs over PIDs [69] coupled with their computational lightweight nature (due to the optimal feedback gain structure) make them ideal for cases with slow dynamics. The study in [65] also demonstrated that performance can be improved by incorporation of wave prediction algorithms; an example of the control architecture for this method is shown in Fig. 2.2, with specific prediction methods being the subject of the review in Section 2.2.

Alternatively, there has been significant interest in recent times on the development of predictive control methods, with one such method being the use of Model Predictive Control (MPC) and its variations. Generally, the major difference between the MPC and LQR approach relates to the optimisation stage, which in MPC is performed over a receding time horizon with a new solution calculated recursively [23]. Previously, the capability to perform this online optimisation at a speed suitable for real-time applications was not possible, but with the improvement of computing power and development of advanced optimisation tools [70, 71] this is now becoming an increasingly viable solution. Applicability has been demonstrated across a multitude of other scenarios such as (but not limited to) ground vehicles, [72, 73], aerial vehicles [74] and industrial processes [75], with desirable traits such as the handling of inequality constraints, nonlinear dynamics and Multiple-Input-Multiple-Output (MIMO) systems being the major reasons for the drive to wider deployment.

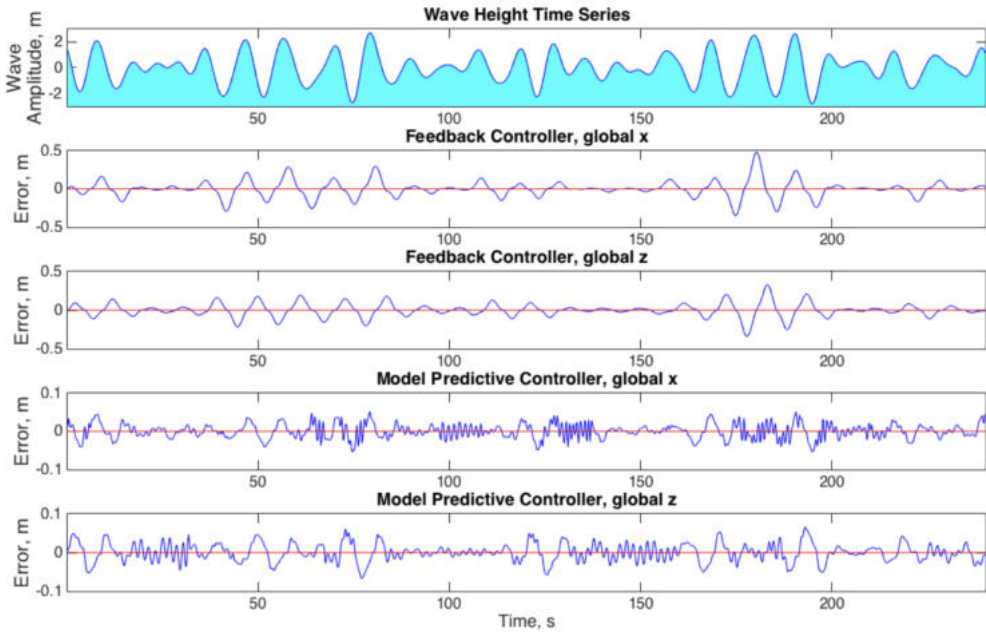


FIGURE 2.3: Example of the performance improvement potential of an MPC structure with embedded wave-induced disturbance considerations [21].

Early demonstrations of MPC deployment on underwater vehicles focused on simplified control tasks, such as the control of only a single DoF [76, 77, 78], typically the yaw angle or depth of the vehicle. A major advantage of MPC is the ability to incorporate constraints on the state within the control structure; this is highly desirable in cluttered environments where the position of obstacles can be explicitly considered, such as those in [79]. Similarly, constraints and dynamic responses relating to the control variables can also be specified [80, 81, 82], which greatly improves the performance of the control and allows for an optimal action to be performed. As with the LQR approach, this results in significant reduction in error over classical control methods such as PID and associated variations [21, 66]; see Fig. 2.3. One factor which is lacking in many of the aforementioned works is the consideration of environmental disturbances, or when they are considered such as in [21] they do not provide a methodology for predicting or estimating their impact, assuming this knowledge is known. This is a critical element for implementation of the methodology, and as discussed in [83, 84] if environmental disturbances are not considered appropriately, this can have a detrimental effect on the MPC performance.

In an ocean environment, the presence of waves and currents can have significant impact on the vehicle dynamics when operating in shallow waters or within the upper section of the water column, therefore must be addressed. Several works have examined this, varying from considering constant ocean currents [85] to incorporating ocean forecasts directly within the control structure [86]. The approach of including a preview of the oncoming wave-induced disturbances shows promise in further enhancing the performance of the control [87, 88, 89], differing from the typical approach of

handling disturbances in MPC which assumes information of the disturbance is not directly available and generalises the mitigation process. As noted in [25], this can potentially lead to instabilities when larger disturbances are encountered. This is an interesting concept, as exploiting forecasting tools [90] can be used to both improve performance and reduce energy consumption simultaneously - the limitation here relates to computation time when dealing with large amounts of data, in conjunction with the reliability of the produced forecast. One solution is to limit the forecast to only the immediate operational area of the plant [91], whilst also adopting tailored search algorithms to reduce the search time during the optimisation stage of the MPC, shown to be effective in several works [92, 93, 94]. Similarly, ocean current/wave disturbances can be estimated *in-situ* through sensor fusion [95], direct force measurement [96, 97] or using state estimation techniques [98] to predict the vehicle response and perform corrective action accordingly. These approaches, reliant on cross-platform deployment, become dependent on each system being fitted with sufficient sensors for the hydrodynamic load estimation to be obtainable. This point was raised in [98], which considered ocean current disturbances in the form of a velocity within the vehicle dynamics instead of attempting to directly measure forces (owing to this parameter being easier to measure). Similar results are presented through the approaches in [99, 100] for trajectory tracking, but without considering the ocean current/wave disturbances to be measured. In relative terms the trajectory tracking is accurate, but this is largely due to the task being performed over larger distances (tens of metres); for alternative tasks such as station keeping/state regulation where positional error is of upmost importance, the average errors of  $\approx 0.3\text{m}$  can occasionally be too large. Particularly if the vehicle is required to complete contact tasks (e.g. Non-Destructive Testing (NDT) or fine manipulation), this would be deemed excessive and hazardous. The disturbance and measurement noise are also not considered simultaneously, casting doubt on the robustness of the proposed controller in real-world operations. Typically, the incorporation of ocean wave disturbances directly within the control structure has largely been tailored towards Wave Energy Converter (WEC) efficiency improvement [91, 101, 102], with little literature existing dealing with both the wave prediction and control elements for underwater vehicles in unison.

Various alternative approaches and adaptations to the standard MPC structure have been proposed in the literature, such as Multi-objective MPC (MOPC) [104] which can account for scenario dependent control specifications and vary the objective function accordingly. For very complex control tasks this can be advantageous, but for state regulation around a set-point this is often not necessary. Robust MPC (RMPC) [105, 106, 107] has also been proposed, designed to handle increasing levels of uncertainty in a stable manner. This is highly desirable, particularly when the system dynamics are not well-defined (or simplified, for example linearised). However,

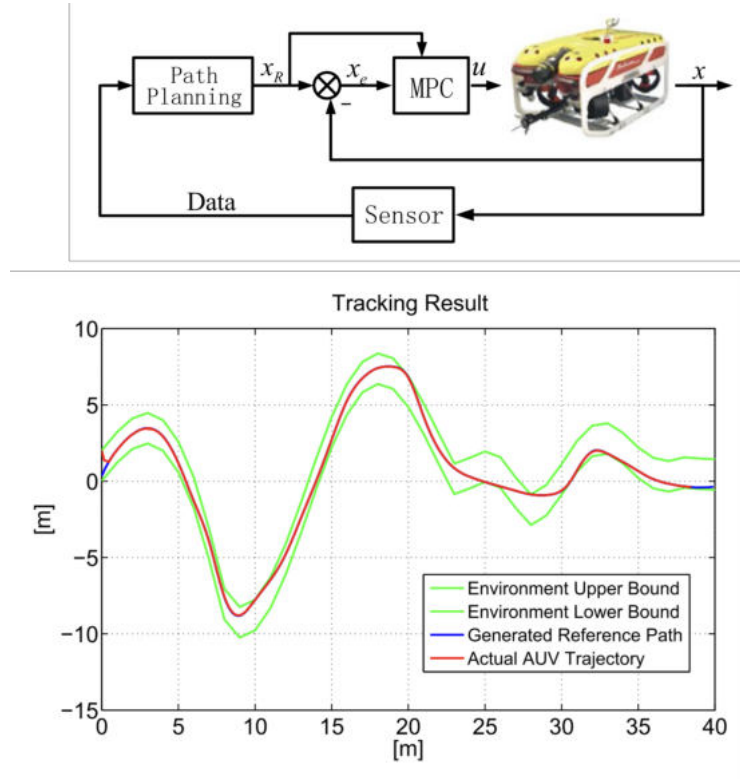


FIGURE 2.4: An example of an integrated path planning and MPC-based tracking control scheme, as proposed in [103]. As can be seen, no active environmental disturbances are considered.

as noted in [108] these methods can lead to computationally challenging optimization problems, ultimately affecting performance negatively. Amongst other proposals is Lyapunov-based MPC [109, 110], but (as with those previously mentioned) most approaches tend to deal with the trajectory tracking problem [107, 111, 103, 112] as opposed to the station keeping or state regulation task [21, 30]; see Fig. 2.4 for an example of the applied scheme in [103], integrating a spline-based path planner with a MPC tracking law. In conjunction, the majority of these alternative approaches have been tailored towards unexpected disturbances, which MPC is known to be susceptible to [22]. In terms of underwater vehicles, RMPC or Robust Nonlinear MPC (RN-MPC) is often deployed, ensuring constraints are met under bounded disturbances to the system; the drawback as with most modified MPC structures and as alluded to previously, is the added computation cost. Similarly, Explicit Model Predictive Control (Ex-MPC) could offer a solution to significantly reduce the computational burden by computing the control law off-line for a specified range of parameters, only requiring a function evaluation online which is usually piece-wise affine [113]. The literature available addressing this issue is sparse, with only few examples [114] showing promise. Ex-MPC has also been applied to spacecraft which share some analogous traits to underwater vehicles from a modelling and control perspective [115]. An interesting approach outwith these variations is to explicitly model the disturbances in real-time, directly forming an additional input to the controller for consideration

when generating control actions - computation time then becomes solely dependent on the optimisation search algorithm. Alternative attempts have examined the feasibility of combining an MPC structure with visual servoing techniques, with the goal of providing a more complete solution for the vast array of conditions the vehicle may encounter [116, 117]. As with incorporating forecasting techniques, computation power requirements naturally increase, but this can be tackled through the use of self-triggering mechanisms [116] or actively switching between cost functions [118].

An alternative method to add robustness to the system control (similar to the purpose of using SMC) is using  $H_\infty/H_2$  control techniques, which have been proposed for depth control [119, 120], trajectory tracking [121] and to improve robustness with reference to the coupled dynamics inherent to underwater vehicles [122, 123] amongst others. There have also been works that have dealt with the stabilisation problem under the influence of wave disturbances [124], although limited in scope by the small magnitude of the wave disturbance compared to those frequently encountered in the field. An interesting avenue of exploration could be to combine  $H_\infty$  and feed-forward elements (using disturbance estimations to calculate informed mitigation control actions), enhancing the robustness to disturbances commonly associated with  $H_\infty$  control. This concept was proposed in [125] in the context of handling communication delays as opposed to environmental load disturbances. Similarly, combining  $H_\infty/H_2$  with a predictive control layer was proposed in [126] for tackling instability issues with decoupled control, which is an interesting proposition and could offer solutions to some issues associated with MPC. The drawback of employing these techniques uniquely, as with others, relates to the inability to deal with system constraints as well as being impractical for systems with large dimensions [127].

As with most fields in recent times, the use of Artificial Intelligence (AI) and machine learning techniques have also been proposed [128], with early proposals of using Reinforcement Learning (RL) demonstrated in [129, 130] for vehicle navigation. RL has been proposed for several different key tasks relating to underwater vehicle control, such as trajectory tracking [131], autonomous docking [132] and target tracking [133, 134], all aimed at improving the level of autonomy currently available. While these techniques offer good performance, their response to external disturbances is minimal or neglected in most works, for example [132] disregards disturbances entirely and in [131], the only disturbance considered is a basic environmental noise which is commonly filtered. A recent proposal in [135] does consider ocean currents (1m/s) and is shown to effectively employ RL for path planning in unknown environments within simulation (Fig. 2.5); the limitation here is that the disturbance is constant in magnitude and only affected by the vehicle pose, thus it is uncertain how drastically time-varying disturbance magnitudes (such as ocean waves) would affect the learning element. The interaction of waves and currents is an interesting topic, as this can affect the magnitude of oscillations and therefore disturbances on the vehicle. This is one area where RL could prove useful, or similarly when the

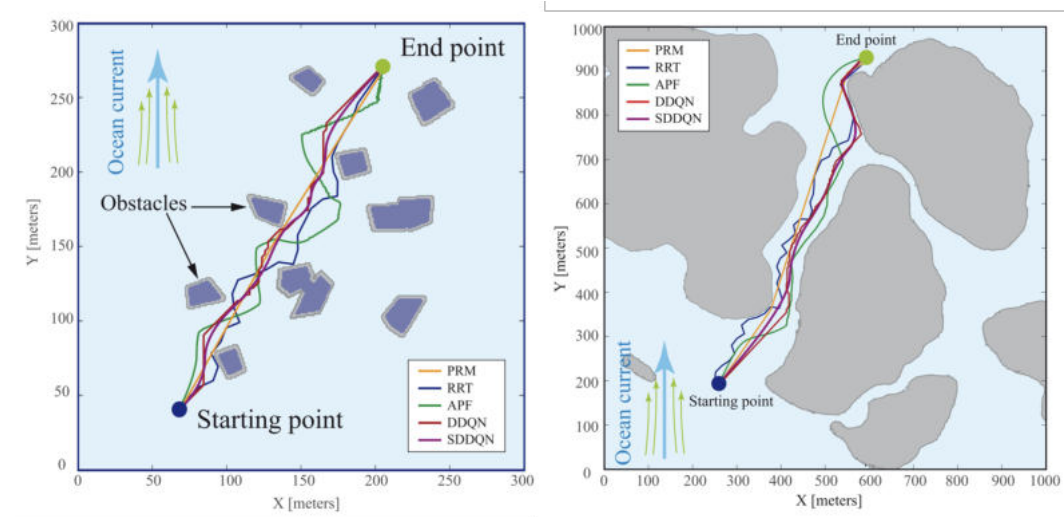


FIGURE 2.5: Using deep reinforcement learning for vehicle path planning under constant ocean currents of 1m/s [135]. Here, the algorithms tested were probabilistic roadmap (PR), rapidly exploring random tree (RRT), artificial potential field (APF), double deep Q Network (DDQN) and smooth DDQN (SDDQN).

vehicle is in the wake of a fixed structure; here, problem becomes extremely complex and thus RL may excel, but this has also been studied extensively with model-based approaches which are computationally lighter. A vehicle sitting behind a fixed or quasi-static structure where both are invested by a current represents a classic case of vortex induced vibrations [136], where the shedding of coherent fluid structures from the fixed structure impacts the downstream vehicle. Interaction of a body with vortices has been studied extensively from a dynamical perspective. By knowing the current speed, it is possible to estimate the frequency of shedding and therefore the time-history of how these vortices impact on the downstream body. While there is not much in literature with respect to vehicle control, there are low-order models [137, 138] which have recently been formulated and which would lend themselves to the incorporation of hydrodynamic disturbances from shed vortices in the control of the vehicle.

Similarly, RL may excel in the presence of uncertainties, a point highlighted in [139]. Indeed, the model-free structure removes the ambiguity associated with the hydrodynamic parameters, although this is at the expense of increased overhead on the learning side. Admittedly, this could represent useful support in determining the initial model of the vehicle, whilst later deploying a more intuitive control structure such as RMPC. This has been proposed in [140], which deploys a Neural Network (NN) to obtain a data-driven model for use in predictive control of an underwater manipulator. NNs have also been proposed for underwater vehicle control to compensate for un-modelled dynamics and disturbances (amongst other factors) [141, 142, 143], with some efforts also incorporating RL within the formulation [144]. In some instances these techniques have also been used to improve the performance of classical

control methods such as SMC [145]. In many cases these approaches can offer guaranteed optimality, but the current question relates to practical implementation and how transferable these proposed methods are into an industrial setting, or whether the additional effort required to formulate the controller in contrast to other standard methods provide analogous improvement in performance. This also concerns the level of perception required on the robot side in order to make appropriate decisions and generate effective control actions. Promisingly, the deep reinforcement learning-based method in [146] did demonstrate experimentally the applicability of the approach with minimal prior knowledge of the system, offering promise on the deployment aspect. The point remains that although these techniques are suitable for obtaining a reliable representation of the vehicle parameters, they don't yet provide accurate enough representations of oncoming, time-varying disturbances; this places the scope of these methods outwith providing preview information to the controller.

### 2.1.3 Sensing for Control of Underwater Vehicles

Controlling the behaviour of an underwater robot requires some form of state feedback of the robot, often acquired by various sensing mechanisms. This provides a reference between the robot state and the desired state, facilitating convergence towards the specified goal. Here, a brief review on different state sensing techniques for underwater robots will be discussed, covering typical methods such as the use of optical, acoustic and other forms of measurements, highlighting advantages and limitations of each methods and applicability in these scenarios.

Using visual feedback can be a solution when operating in the vicinity of structures, as these can act as reference points to perform posture regulation. In [147, 148, 149, 150], a method is proposed which directly calculates the relative 3D displacements using the spatio-temporal derivatives of image pairs. The drawback in this work as noted by the authors related to the assumption of small height variations in average distance to the ocean floor, which isn't always valid. The approach also requires small motions between image pairs, so large disturbances will reduce effectiveness. A more common approach to tackle the problem is using texture tracking. This method can prove useful in highly textual areas (an image with contrasting features), but it can encounter difficulties locking onto a target with insufficient texture or sloped surfaces [151]. Other techniques could be used in conjunction with a simple texture tracking system to improve performance, such as the inclusion of image stabilisation and motion models [152, 153, 154]. On the contrary, the performance of a texture tracking system can be affected by something as intuitive as poor lighting. This problem is common, but can be tackled somewhat by using filtering and correlation techniques to increase the contrast within the image [155]. This approach has been seen to be robust even in poor lighting conditions; however, the effect of disturbances were only tested under a single pole induced disturbance, not a complex wave field.

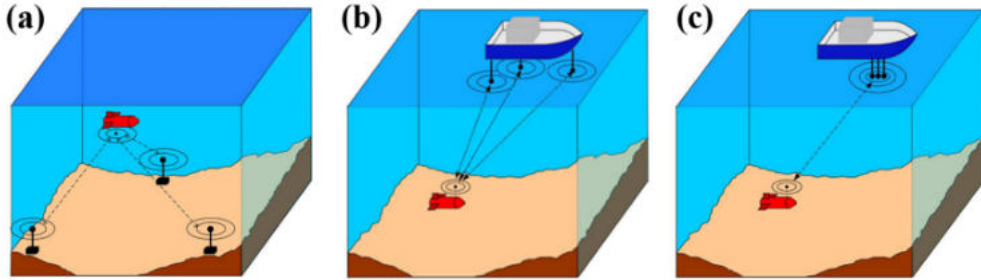


FIGURE 2.6: Example of different types of acoustic navigation configurations, showing (a) Long-Baseline, (b) Short-Baseline and (c) Ultra-Short Baseline [163].

The problem still remains that a lack of image features may influence performance substantially, which [156] aims to resolve. The authors propose using region matching and selective texture analysis, using regional textural operators to improve the accuracy of image correspondence. Although the system performed in real time, the algorithm was executed on an off-board computer which in real scenarios could hinder applicability. Tracking of features is described in [157, 158], where firstly a station keeping solution is presented followed by control of a vehicle in the horizontal plane. The algorithm was tested in a tank and subject to disturbances, however, these disturbances never exceeded 0.5m/s; in a shallow ocean environment this value is often exceeded. Similar to texture tracking, there is the method of tracking objects. This method is utilised in [159], demonstrating applicability for both station keeping and following a moving target, for example a diver. The image quality issue was identified prior to the experiments, so although preliminary tank results are reliable, ocean clarity and wave disturbances may greatly affect these. These problems could be averted by utilising the image processing methodology highlighted in [155]. The target tracking approach was adapted in [160], with the addition of the system learning the target signature on-line. A clear disadvantage to using this method is that a suitable target is required for the system to lock onto. An alternative approach is detailed in [161]; a laser triangulation optical correlation sensor is deployed, which creates a square of 4 laser spots. When the vision system identifies these on the ocean floor, effective station keeping can be witnessed. This approach solves the issue of requiring an object to detect, but would only be applicable in near ocean floor applications. Robustness to noise is a main advantage for using specific object tracking, as highlighted in [162]. Compared to the other literature, the solution presented here station keeps for substantially longer with minimal positional error but as with [159], only tank tests were performed and without wave disturbances.

The main problem of using visual feedback underwater concerns the frequent occurrence of weather conditions causing poor visibility. In particular scenarios using vision as a control input can be effective, but during operations in turbulent environments or close to the sea floor, sediment can significantly hamper the robots vision

capability, causing the visual feedback to ultimately become redundant. However, recently developed techniques such as that presented in [164], which removes the effect of water on colour to greatly improve clarity and contrast of images, may potentially open new research avenues for development of powerful underwater vision and its applications in control. Regardless, the typical approach when using any visual data is to fuse this with other sensor measurements, exploiting multiple modalities to improve reliability of state estimations [165] and increase robustness.

One of these modalities worth highlighting is inertial sensing, which is often implemented through use of a Doppler Velocity Log (DVL), which exploits the Doppler effect to track the vehicle's velocity either with respect to the flow or the seabed [166]. The latter requires the robot to be within the DVL's maximum range of the seabed [167], but for applications around offshore renewable energy this is not a major concern and is usually satisfied. Small DVL's have been applied in the field [168], however some studies have noted interference can be an issue on smaller vehicles when the sensor is in close proximity to the thrusters [169]. As with optical sensing and acoustic measurements, integrating a DVL with other systems has been shown to improve accuracy, for example in [170, 171]. This feeds into the use of other dead-reckoning technologies, such as Inertial Navigation Systems (INS) which are based on Micro-Electro Mechanical Sensors (MEMS). Similar to above the surface, a problem which arises here is the effect of sensor drift [172], which over time can compound and cause large tracking errors.

The last modality that will be highlighted in this review is acoustic based measurements, which is robust to visibility conditions but can suffer from reduced resolution [173]. This method determines the relative position of the robot by using baseline transponders as reference points, calculating the vehicle position by sending and receiving signals. The three common configuration classifications are referred to as Long-Baseline, Short Baseline and Ultra-Short Baseline [163] (see Fig. 2.6), with the latter being the most suitable for inspection ROVs due to compact size and ease of setup [166]. These setups have been widely used [174, 175, 176], but can sometimes suffer from slow update frequencies leading to difficulties when using these directly for control. As previously mentioned, to overcome issues relating to particular modalities it is common to fuse multiple modalities, for example optical and acoustic data [177, 178]. This has been largely performed with different types of sonar, such as in [179] which deploys side scan data and combines this with the output of stereo camera system. Other efforts have looked at the combination of an INS, a forward looking sonar and an optical camera [180] for building environmental maps, with a similar approach documented in [181]. This approach has also been adopted but without any fusion, applied for SLAM-based navigation rather than mapping [182]. The major drawback with acoustic communication is low efficiency; water is much denser than air, causing a drop in signal speed, coupled with potential reflections and scattering amongst other problems [183]. When fusing acoustic and optical data,

the additional problem of complex calibration is raised [173], with a good calibration being paramount to achieving sufficient performance for feature matching. Still, being agnostic to visibility conditions makes it one of the most popular methods of communication currently, along with a DVL.

This section of this literature review has discussed different forms of providing state feedback to the control system, highlight the benefits and drawbacks of each. Although not the focus of this thesis, from an implementation perspective it is key to be aware of the different methods which can facilitate the proposed solution. It is also a critical factor in being able to control the vehicle position effectively, particularly when attachments such as manipulators are in use. If state feedback is not accurate, the control may cause the vehicle to perform unwanted motions and in some cases cause collisions with nearby structures; from a robustness point of view, this is where manipulator design and associated control becomes paramount to limit this risk. This leads nicely into the next part of this review, which discusses the control methodologies for non-traditional manipulators with highly nonlinear dynamics.

#### 2.1.4 Control of Soft Manipulators

The definition of what constitutes a "soft" robot is still a contentious subject; for the purpose of this review, any robot/manipulator which is not restricted to low degrees of freedom by long rigid-links is considered soft. This is inclusive of examples such as continuum manipulators and hyper-redundant manipulators, which display similar behavioural properties to physically soft robots [184]. This allows an application of the term "soft" to be extended to the behavioural properties of the robot, which offers several advantages in itself over classical manipulator control and design. Following [20], a common denominator between soft robot controllers is whether they are model-based or model-free. As the work in this thesis focused on exploring the incorporation of modelled disturbances within the control strategy explicitly, this review will cover model-based approaches and their applications to generic soft robotic manipulators.

In conjunction with many dynamic control applications, the use of strategies derived from PID principles has been examined throughout the literature [185, 186] for application to soft manipulators; see Fig. 2.7. Robustness of a PD control law was achieved through combination with SMC principles in [187], showing improved tracking performance over a standard PD controller. SMC has also been proposed and experimentally validated for a planar three section arm [188, 189, 190], showing through improvement over PD control that significant uncertainties were present in the system. Likewise, adaptive control has also been shown to substantially improve performance over typical PID approaches [191, 192], analogous to the findings for vehicle control, with various methods proposed such as combination with visual servoing [193] or feed-forward elements [194] to aid in driving the robot to the desired configuration. Using feed-forward elements is a fairly intuitive method that has been

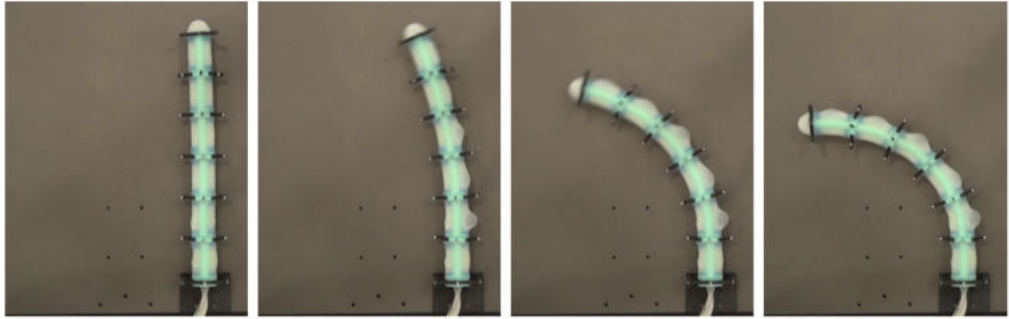


FIGURE 2.7: Example of controlling the configuration of a soft robot [185].

applied widely for controlling soft robots [195, 196, 197], and has been shown to be an effective method for controlling soft robots in controlled environments with experimental validations presented in [198, 199]. The variables required for these strategies are often easily measurable or can be calculated, making their general implementation intuitive. However, due to only exploiting knowledge of the robot characteristics and/or state, disturbances can significantly effect the robot dynamical behaviour if no compensation is considered [20, 200]. Knowledge of the robot state is also required for the majority of these approaches which can hamper performance if inaccurate, especially if routinely disturbed. Methods have been proposed for estimating the robot state, such as leveraging typical approaches through Kalman filters [201], Inertial Measurement Unit (IMU) data [202, 203] or visual feedback [193], but there is no generally accepted approach to this problem currently and it remains an open question. Other approaches have aimed to operate with only partial knowledge of either the position or velocity of the joint angles [204], or have used more advanced techniques such as Recurrent Neural Networks (RNN)s to estimate the robot state under external forces [205]. As is the case with vehicle control, the use of modern forms of control have been gaining traction. MPC for soft robots is one topic that has seen a rise in attention [206, 207], with different approaches improving the speed of execution, such as the use of Koopman Operator theory [208, 209] or exploiting Graphic Processing Units (GPUs) [210]. As mentioned in Section 2.1.2, MPC can inherently consider constraints during generation of control actions which is of large importance when controlling soft robots; these constraints can determine pressure dynamics, applicable cable torques or fluid flow rates which are all key elements to the robot response [211, 212]. These constraints can also be mapped to represent obstacles in the robot workspace, such as in [213] which explored RMPC for this purpose. Alternatively, proposals of utilising NNs has also showed the ability to improve control [214] along with reinforcement learning [215], particularly in the presence of uncertainties due to the inherent learning characteristic they possess. Alternative forms of modern control can relate to the ability of the robot to vary its characteristics thus offering a variety of achievable stiffness states depending on the task. Several

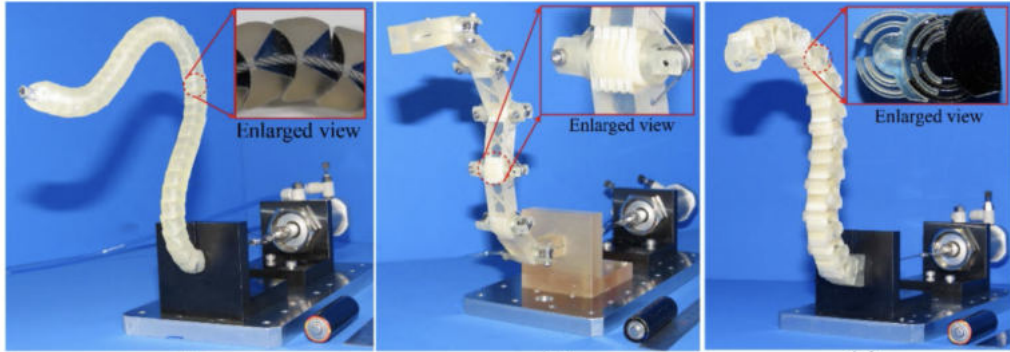


FIGURE 2.8: Variations of jamming techniques developed to control the stiffness capabilities of a wire-driven manipulator mechanism [220].

different methods have been proposed for achieving these *tuneable stiffness* properties, one being the concept of *jamming* or *granular/particle jamming*. In [216], this is achieved by compressing identically designed beads together to increase the frictional contact and solidify the state of the manipulator, using a wire-driven mechanism like that shown in Fig. 2.8. This concept was also applied in [217], using a pneumatic McKibben muscle [218] to contract the beads together instead of a cable. In both the manipulator was shown to possess good holding force relatively to its physical size, however the manipulator operated passively and positioned manually with no control applied. Other uses of a wire-driven method to achieve a state-transition can be seen in [219, 220, 221], adopting different forms of mechanism which all stem from the concept of granular jamming [222]. The drawback with these approaches over pure control is that the robot must remain in this state to mitigate disturbances, however this can constitute a useful trait for some applications or instances during operation. Adding the ability to become rigid when desired vastly improves the load-bearing capability of the "soft" robot, widening applicability for underwater tasks; current designs have been almost exclusively restricted to applications requiring delicate handling [223, 224, 225, 226, 227]. Although this is an advantage in instances such as biological sampling, this presents a major limitation within the marine energy industry, where it is desirable to place sensors at the tip of the manipulator or manoeuvre heavier objects.

Over typical feedback/feed-forward control, these methods share some key motivations but all focus on improved performance in general and improved ability to mitigate disturbances and state perturbations. Although there have been works dealing with the estimation of generalised disturbances *in-situ* [228, 229], there is little to no literature which explores actively controlled disturbance rejection of dynamically varying loading. Considering a marine environment, ocean waves have a certain degree of associated predictability; an interesting avenue would be whether it is viable to incorporate this trait into the control strategy to useful effect for maintaining an end-effector position. The inherent increased dynamical behaviour of soft robots compared to rigid robots implies this could vastly improve control performance. There

has been some notable exploration of modelling the fluid induced forces arising due to drag and added mass [230, 231, 232, 233], but these do not consider cases when both the body and the fluid is actively moving and varying, as it is when operating under waves or currents. It can also be noted that these models have almost exclusively been applied to locomotive bodies of tentacle like structures [232, 233, 234] and not for precise end-effector control of a manipulator. A more suitable design for the case of physical manipulation would be to adopt a continuum [235, 24, 236, 237] or hyper-redundant [238] structure, which offers increased loading capacity [239] and can be controlled to a higher degree of accuracy.

### 2.1.5 Challenges in Underwater Robot Control

Firstly, as the reviews in Sections 2.1.1-2.1.2 show, there have been extensive efforts at dealing with the motion control problem for underwater vehicles from a multitude of perspectives; however, most approaches do not aim to model impending wave disturbances as a reconstructed time series evolution. Typically when wave disturbances are considered, they are often in a time-averaged or statistical form of a "possible" disturbance, with most mitigation control schemes not attempting to match the temporal form of the disturbance and act explicitly. Throughout the works that do consider and attempt this, such as [21], the disturbances are either treated as given and well-known or the proposed method does not provide a means for vehicle localisation and obtaining the wave parameters to subsequently estimate the disturbances. These elements are of particular importance when considering the motivation behind deploying underwater vehicles; performing tasks in environments that are undesirable to place humans. Given that the majority of recent works focus on modern control, there is a relatively sparse body of literature which considers the prediction of dynamic disturbances *in-situ* and explicitly accounts for these within the vehicle control. However, as demonstrated by works such as [21, 89, 25], if accurate predictions can be provided and incorporated within the optimisation phase of an MPC loop, this may represent an effective solution.

Similarly from the review in Section 2.1.4, there have been some key findings which form the basis for the specification of Research Objective 3. The control problem related to soft robots is still an open question, with model-based approaches seemingly becoming the accepted norm as the most effective. In controlled environments, this has few issues apart from determining the robot physical parameters, but in a dense and active medium (such as water) this becomes more complex. Typical feedback and feed-forward approaches tend to degrade in performance in these situations, as there is no knowledge of the environmental interactions occurring - this point is where the application of a predictive control architecture can prove useful. With regards to this, the work that exists in relation to mitigating disturbances with active control is sparse at best. Deploying predictive control schemes for the control of soft robots appears to

offer an upturn in performance generally; the additional computation requirements can also be offset using general techniques which presents a viable option. These can be extremely effective for mitigating the effect of predictable state perturbations, which are particularly predominant in an underwater setting (as highlighted in Section 2.1). State estimation techniques are becoming more accurate, which can be leveraged in these instances and coupled with one of the wave prediction techniques discussed in the following Section 2.2 to provide a widely applicable solution to a variety of soft robots.

The conjecture from these reviews is that even with coarse hydrodynamic load predictions, an improvement in controller performance can be attained over a broad generalisation of conditions, avoiding the computational burden that is inherent in approaches such as reinforcement learning. These findings fuel the contributions of this thesis related to objectives 1-3, with the common objective of improving control performance under the influence of wave disturbances.

## 2.2 Ocean Wave Forecasting

The implementation of a large bulk of modern control methods rely heavily on the ability to model and estimate disturbances in a general sense, however as shown by the reviewed works in Section 2.1.2, embedding this ability within the control system has the potential to greatly improve performance with respect to attaining or regulating the system towards the prescribed goal. With these control methods, the major factor affecting performance shifts from the dynamic response of the control to how accurate disturbances can be estimated or predicted. In reference to ocean wave disturbances, it is convenient to categorise these into long-term and short-term forecasts for this review. These are both depicted in Fig. 2.9, where the long-term statistical properties are depicted by the arrows and an enlarged version of the local temporal evolution these are derived from.

Multiple systems have been developed to provide extensive forecasts of particular ocean areas for a specified time period into the future, typically for no longer than 48 hours for sufficient accuracy; one very well known example of this category of system is the Regional Ocean Modelling System (ROMS) [90]. Similarly, the Coastal Ocean Forecast System [240] produces 24-hour forecasts of the U.S. East Coast, whilst a longer forecast of 10/15 days is produced by the Mediterranean Ocean Forecasting System [241, 242]. These systems use large amounts of data from a variety of different sensors at a large spatial scale to produce informed predictions at low spatial and temporal granularity. Indeed, these systems do not provide fine-detailed, local data of the wave time history, but rather produce key spectral parameters over longer time periods such as significant wave height and peak spectral period. One of the problems of using these systems is highlighted in [86], showing that forecasts can often

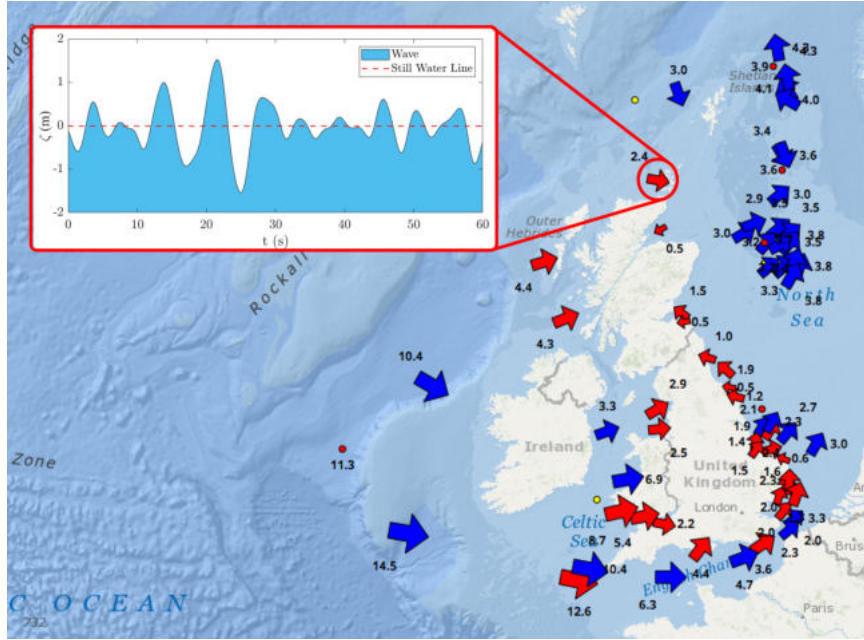


FIGURE 2.9: Visual representation of the statistical nature of long-term forecasts (each arrow indicates a wave buoy) and an enlarged view of the local temporal evolution these are derived from, simplified to a planar view for clarity [246].

differ significantly from the actual conditions encountered locally, preventing a realistic description of temporal wave elevations in a specific location. Another issue is the computing power required to handle this volume of data, likely a contributing factor as to why the station-keeping algorithm developed in [243] was ran off-board the vehicle. While wave elevation estimation is problematic, slow-varying ocean parameters can be better captured by such large-scale diagnostic models. As an example, an alternative use for these ocean models can be seen in [244, 245] whereby the data produced is used to generate a simulation of ocean currents for validating the developed path/trajectory planning algorithms. Using realistic conditions in simulations is useful to prove functionality of the algorithms, however this raises a question about the required level of prior knowledge in relation to the sea-state in order to produce the same results in a real time scenario. In contrast, short term future predictions in the magnitude of seconds can be considered to be a viable alternative, particularly in the case of dynamic positioning control. This approach has been investigated for wave energy applications in [247, 248, 249, 250, 251], discussing methods for predicting a temporal sequence of wave elevations at a specific point based on the past history of the wave, particularly the Autoregressive Model (AR) [252]. The recent literature on AR models demonstrates that no real benefits derives from using complex non-linear models [249] strengthening the case for simpler (but faster) techniques, especially for short time-frame predictions. Further work was undertaken in [250, 251] to investigate the prediction requirements with respect to the previous research conducted. One key point that is raised within these works is that the predictions are typically related to low-frequency swells, with long wave periods where non-linearities are weak;

shorter period waves were tested and ultimately displayed poorer performance [249]. More importantly, reviewing these works highlighted that a planar record of predicted wave heights are the focus due to the desire of predicting the excitation force for a wave energy converter, thus directionality is not a critical parameter and is not required [249]. This precludes the use of AR models for the purpose of robot control in waves, where a prediction algorithm capable of accounting for wave directionality is non-optional.

As mentioned previously, for many applications the exploration of machine and deep learning techniques has increased in recent times, for example using NNs [253, 254]. As is the case with traditional forecasting, most works deal with forecasting key wave parameters over time periods in the order of hours [255, 256, 257, 258]; however, for dynamic control, much shorter higher fidelity predictions are required in the order of seconds. Other methods have covered the use of Genetic Programming (GP) [259] and Model Tree's (MT)s [260], which have all been deployed to exploit continuously observed data at specific locations and produce forecasts. Other data sources have also been shown to be effective in producing reasonable forecasts, for example wind data [261], but these are limited in producing accurate short term predictions of temporal evolution of wave elevations. One particularly interesting study is given in [262], which extends the prediction step to a moving body. This work also potentially sets the groundwork for comparing the computational overhead to performance ratio with an AR or deterministic model in terms of scalability of the prediction.

Expanding on deterministic models, another well-known technique for short term wave forecasting is Deterministic Sea Wave Prediction (DSWP). DSWP uses direct measurements relating to the wave height at a prescribed location (typically wave elevation however this can be inferred from alternative parameters, such as subsurface pressure readings) to form a spectral model of the sea state. Subsequently, this is propagated through space or time to predict the wave elevation at a secondary location. Wave estimation at a distant location or at a future time-instant define two methods referred to as fixed-time and fixed-point respectively. The former considers a snapshot of the wave elevation over a specific area at an instance in time, whilst the latter considers the wave elevation at a single fixed-point over a period of time. The fundamental working principle of the fixed-point method is shown in Fig. 2.10. This is a well studied topic, proposed and developed throughout the works in [263, 264, 265, 266, 267]. Exploration into extending DSWP to account for multi-directional waves was later achieved through data obtained by a wave profiling radar system [268], making this technique superior to AR models where multi-directionality has not been fully addressed.

Further research has been conducted recently using mixed space-time wave radar data [269], later extending this work into sea trials with wave-profiling Light Detection and Ranging (LIDAR) [270] to measure in-situ wave height sequences, successfully using these measurements to form the future wave predictions. This is particularly

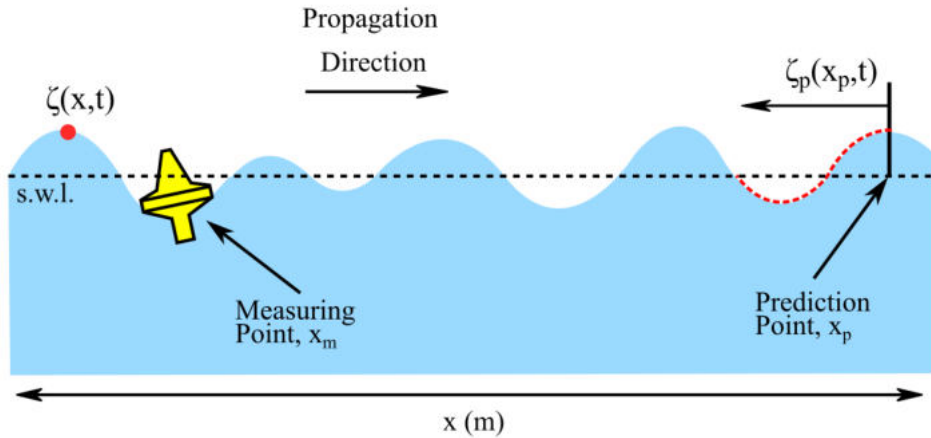


FIGURE 2.10: Basic principle of fixed-point DSWP; utilising wave elevation measurements at one location ( $\zeta(x_m, t)$ ) to predict the wave elevation at another ( $\zeta_p(x_p, t)$ ). Here, s.w.l. refers to the still water line whilst  $x$  is the space parameter.

applicable to wave rider buoys, such as in the schematic in Fig. 2.11 [265]. Similarly, the use of X-Band ship navigation radar has been explored during field campaigns, showing high enough accuracy for MPC-based control of wave energy converters [271]. Another recent development was an alternative approach of using velocity profiles for Nonlinear DSWP [272], measuring the instantaneous wave-induced velocity in the water column at a fixed position instead of the surface elevation. Whilst interesting, measurement of velocity requires dedicated reconstruction techniques, ultimately confirming that traditional DSWP remains the more attractive technique from a practical perspective at present. Combining DSWP with Artificial Neural Networks (ANN) has been explored in [273], stating the main motivation as closing the real-time gap [274]. However, it should be noted this was tailored towards nonlinear predictions of ocean surface waves; nonlinear predictions were also considered in [275] using spatio-temporal optical measurements. Using nonlinear models to re-create the sea state has the advantage of extending the range of formations that can be accurately modelled, as shown in [276]; this work does however note that for low wave steepness linear models perform on par with nonlinear ones. One benefit of adopting deterministic approaches is that a variety of different methods can be adopted to measure the sea-state [277, 278], where the only limitation is the introduction of uncertainty where transformations are applied, e.g. when using pressure reading to estimate wave elevation. A strong indicator of successful usage of DSWP for estimating the motion a free-floating system under the influence of ocean waves was provided by [279], experimentally verifying the use of a linear wave model in real-time forecasting for the motion of a ship. Although the potential is clear from this work, the fact that the system was uncontrolled and a ship has much slower dynamics to an ROV highlights the requirement for a full investigation into the application of DSWP for predictive disturbance compensation.

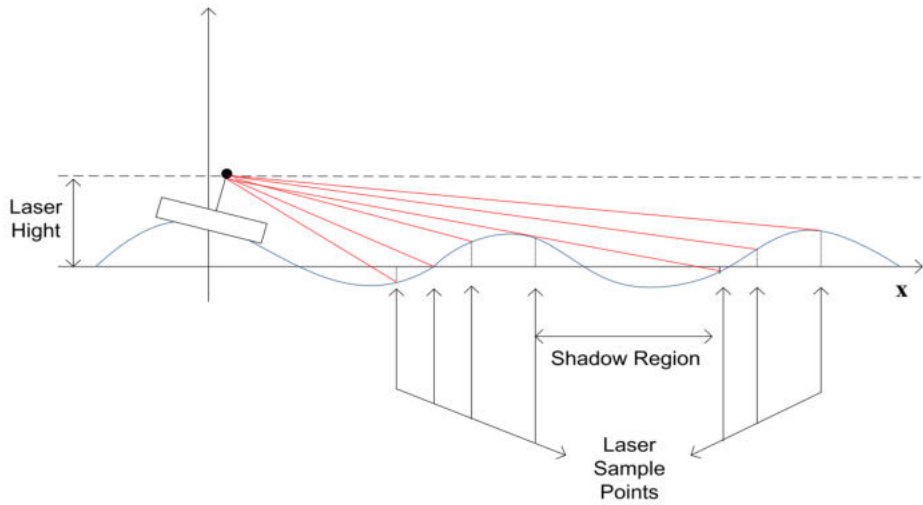


FIGURE 2.11: Example of using a wave-rider LIDAR system for the purposes of DSWP. [265].

With regards to applicability for autonomous vehicle control, short term prediction over the neighbouring area to the vehicle appears the most promising solution when using forecasting models. Predicting wave parameters based on data for a specified point removes the delay incurred when using on-board sensors, providing a means of reducing disturbances before they occur. Delays in communication can also be avoided by explicitly accounting for this in the temporal wave model. This possesses its own challenges such as obtaining data for producing accurate predictions, but is more suitable than the other methods listed for vehicle control. Accurately modelling the sea surface is still an active area of research [280, 281, 282], however the level of fidelity required varies significantly between applications, so the modelling techniques adopted can often be less detailed and still provide enough useful information. Developing algorithms for determining and predicting wave parameters for dynamic control is typically motivated by the goal of improving and optimising WEC performance [283, 284, 91, 277]. Transitioning from WEC to underwater vehicle applications has been briefly investigated in [285] with MPC, but for end-effector set-point regulation as opposed to mitigating disturbances to the vehicle position. But, applying DSWP for WEC output optimisation is a different problem with different characteristics to robot control; WEC's are less mobile, whilst [286] notes that throughout the majority of published studies, the system is assumed to only move in the heave, constraining the optimisation process to only 1DoF. In contrast a self-propelled, floating-base system (such as an ROV) is required to undertake complex maneuvering, requiring control over all 6DoFs. These additional considerations are the driving factor behind the study conducted throughout this thesis.



## Chapter 3

# Preliminaries

### 3.1 Modelling the Ocean Environment

With regards to modelling an ocean environment, a large body of literature exists which ranges from practical models that are computationally light to complex models which strive to capture the highly nonlinear behaviour observed in the real-world [282, 287, 288, 289]. The most suitable model depends highly on parameters such as ocean depth, wavelength and wave height (amongst others), which have significant influence on wave formation as the shore is approached. For this work, an additional requirement of fast computation exists, considering the model will inevitably be embedded within a control strategy for wave-disturbance estimation and mitigation. Here, the approach adopted in this thesis is presented whilst also highlighting other representations, providing justifications for the specific choices made.

#### 3.1.1 Spectral Analysis

The sea state is defined as a spectrum of individual wave components, considered to either be unidirectional or multi-directional depending on whether a 2-dimensional or 3-dimensional representation is being considered. The amplitude,  $A_i$  of each component in the spectrum is given by:

$$A_i(\omega) = \sqrt{2S(\omega_i)\Delta\omega} \quad (3.1)$$

where  $S(\omega)$  is the spectral power density,  $\omega$  is the circular frequency and  $\Delta\omega$  is the width of the frequency intervals after discretization. Often this is taken as constant but can vary in some instances, for example when using the equal area/energy approach as the discretization method [290, 291].

The spectral density function can be obtained by performing Fourier analysis to a temporal evolution of wave elevation,  $\zeta$ , from  $0 \rightarrow t$ :

$$S(\omega) = \mathfrak{F}(\zeta[0 \cdots t]) \quad (3.2)$$

which produces a spectrum such as that shown in Figure 3.1. It is possible to encounter spectra with two peak frequencies in some instances [292], however this is not

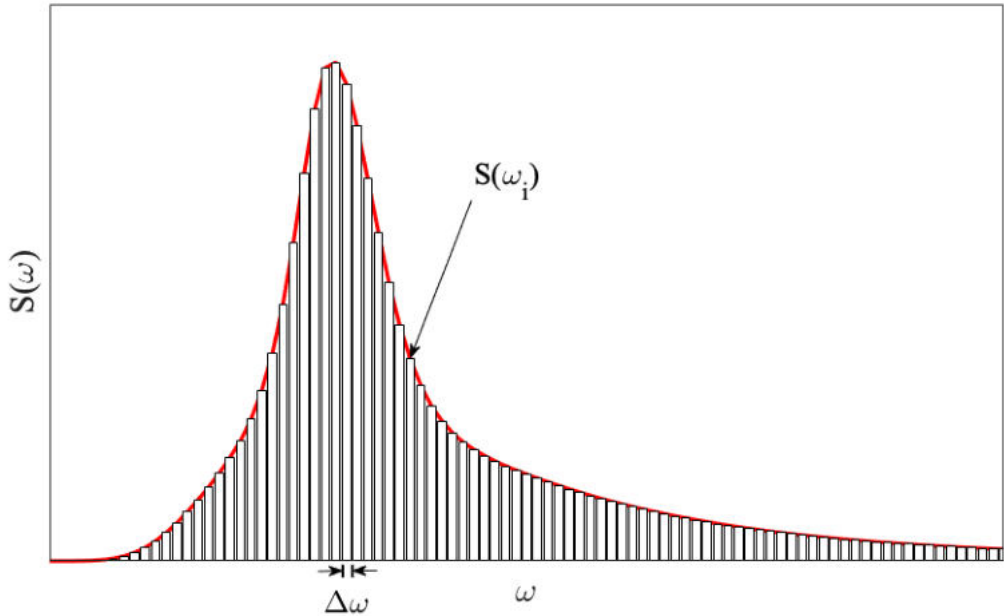


FIGURE 3.1: Discretized wave spectrum

considered in this work and only well-known representations relating to *fully-developed seas* are analysed. To provide some further insight however, different proposed representations of the ocean wave spectrum are presented below, highlighting the reasons for selecting the chosen model in this thesis.

### Bretschneider Spectrum

For unidirectional seas, an early proposal for the ocean wave spectrum is the model by Bretschneider [293], which concerns only two parameters in the form of the modal frequency,  $\omega_0$ , and the significant wave height,  $H_s$ . This representation is described by:

$$S(\omega) = \frac{1.25}{4} \frac{\omega_0^4}{\omega^5} H_s^2 \exp \left[ -\frac{5}{4} \left( \frac{\omega_0^4}{\omega} \right) \right] \quad (3.3)$$

This model was developed for the North Atlantic and features several assumptions such as no swell being present, unlimited fetch and infinite depth.

### Pierson-Moskowitz Spectrum

The Pierson-Moskowitz (PM) [294] formulation of the wave spectrum was proposed only 4 years after the Bretschneider spectrum for fully developed seas, also in the North Atlantic Ocean. The spectrum concerns wind-generated seas and is described by the function:

$$S(\omega) = \frac{\alpha_p g^2}{\omega^5} \exp \left[ -0.74 \left( \frac{g}{U_{19.5}\omega} \right)^4 \right] \quad (3.4)$$

where  $\alpha_p = 0.0081$  is known as the Phillips constant (effectively describing the *intensity* of the spectrum) [295],  $g$  is the gravitational constant and  $U_{19.5}$  is the wind speed at 19.5m above the sea surface.

### JONSWAP Spectrum

The final spectral formulation worth noting is the JONSWAP spectrum [296], which describes wave formations in the North Sea. In contrast to the Bretschneider spectrum, the JONSWAP spectrum concerns wind-generated waves when assuming a finite water depth and limited fetch. The spectral density function here is described by:

$$S(\omega) = \frac{\alpha_p g^2}{\omega^5} \exp \left[ -\frac{5}{4} \left( \frac{\omega_p}{\omega} \right)^4 \right] \gamma^\Gamma \quad (3.5)$$

where  $\omega_p$  is the spectral peak frequency and  $\gamma^\Gamma$  is a peak enhancement factor. The typical values for the constants in the JONSWAP formulation are given as:

$$\begin{aligned} \alpha_p &= 0.0081 \\ \gamma &= 3.3 \end{aligned} \quad (3.6)$$

$$\begin{aligned} \sigma &= \begin{cases} 0.07, & \text{if } \omega \leq \omega_p \\ 0.09, & \text{if } \omega \geq \omega_p \end{cases} \\ \Gamma &= \exp \left[ \frac{(\omega - \omega_p)^2}{2\omega_p^2 \sigma^2} \right] \end{aligned}$$

It should be noted that  $\alpha_p$  can range up to 0.01 depending on the wind speed and fetch length, however the value given above is the typical value used in a generic modelling scenario.

Throughout the simulations performed in Chapters 5-6, the JONSWAP spectrum was opted for as the most applicable. This is mainly due to the fact the North Sea is a target operation area and therefore the JONSWAP spectrum would represent comparable conditions the vehicle would encounter.

#### 3.1.2 Surface Wave Temporal Modelling

The information provided by the spectral formations above can be used to model the wave elevation at a point in space and time; the common assumption for a 2D case (planar, unidirectional) is that the surface wave can be modelled as a summation of  $N$  spectral components each with a unique wave amplitude,  $A$ , wave period,  $T$ , and phase offset  $\epsilon$  [292]; see Fig. 3.2. From this definition, the wave elevation  $\zeta$  at a point

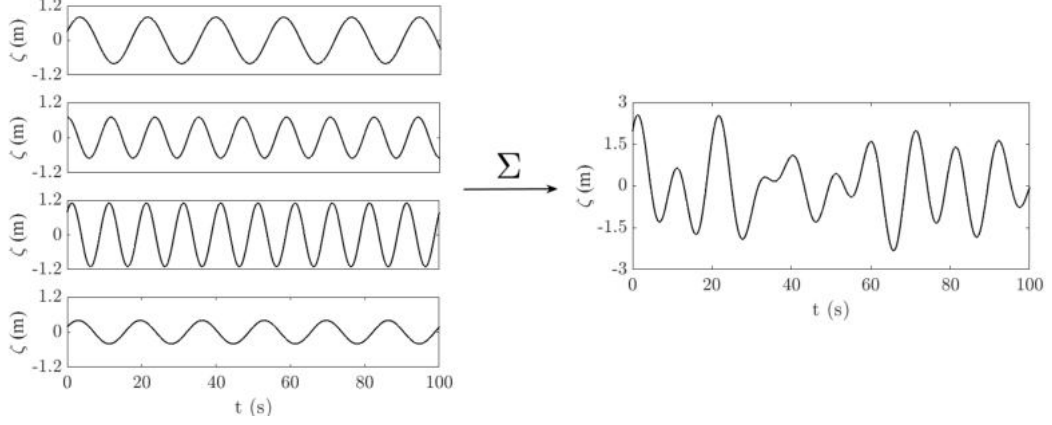


FIGURE 3.2: A polychromatic/irregular wave can be represented by a set of superimposed monochromatic/regular waves.

$x$  and time  $t$  can be obtained by:

$$\zeta(x, t) = \sum_{i=1}^N A_i \cos(k_i x - \omega_i t + \epsilon_i) + \sum_{i=1}^N \frac{1}{2} k_i A_i^2 \cos(k_i x - \omega_i t + \epsilon_i) \quad (3.7)$$

where  $k$  and  $\lambda$  represent the wave number, the angular frequency and the wavelength. These additional parameters are obtained by solving the *dispersion relation* [297]:

$$\omega = \sqrt{gk \tanh(kd)} \quad (3.8)$$

where  $d$  is the seabed depth. The above representation describes *2nd-order theory*, where the second term is included to account for the wave drift component. Spectral information also facilitates deduction of the fluid particle velocities in the global frame by considering the velocity potential; for progressive waves and finite depth, this is defined as:

$$\begin{aligned} \Phi(x, z, t) = & \sum_{i=1}^N \frac{g H_i}{2 k_i c} \frac{\cosh k_i(z+d)}{\cosh k_i d} \sin(k_i x - \omega_i t + \epsilon_i) + \\ & \frac{3}{32} c k_i H_i^2 \frac{\cosh[2k_i(z+d)]}{\sinh^4 k_i d} \sin[2(k_i x - \omega_i t + \epsilon_i)] \end{aligned} \quad (3.9)$$

where  $z$  is the evaluated depth,  $H = 2A$  is the wave height and  $c$  is the wave celerity. It should be noted that in order to result in non-trivial values of amplitude, the above representation is also subject to satisfying Eq. 3.8 which relates the angular frequency, wave number and wavelength. Obtaining the particle motions in the domain bounded by the sea surface elevation,  $\zeta$ , and the sea-bed,  $d$ , directly considers Eq. 3.9 such that:

$$u_p(x, z, t) = \frac{\partial \Phi}{\partial x}, \quad w_p(x, z, t) = \frac{\partial \Phi}{\partial z} \quad (3.10)$$

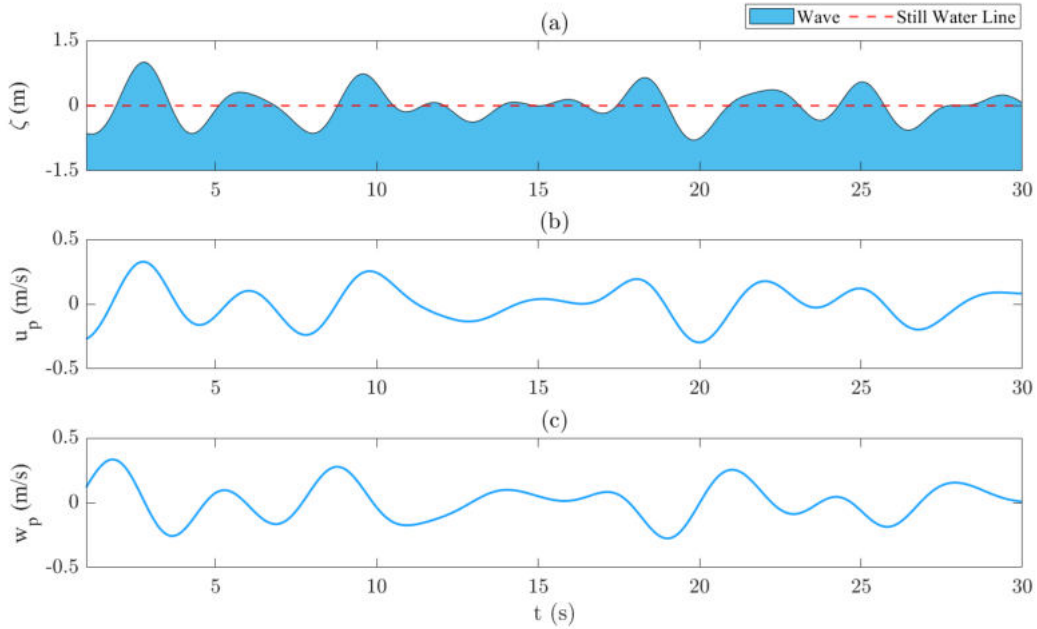


FIGURE 3.3: Evolution of the (a) wave elevation (b) surge component of particle velocity and (c) heave component of particle velocity across a 30s temporal segment for a planar case.

This yields the following 2nd-order expressions for the fluid particle's surge and heave components as [298]:

$$u_p(x, z, t) = \sum_{i=1}^N \frac{g H_i}{2c} \frac{\cosh k_i(z + d)}{\cosh k_i d} \cos(k_i x - \omega_i t + \epsilon_i) + \frac{3}{16} c k_i^2 H_i^2 \frac{\cosh[2k_i(z + d)]}{\sinh^4 k_i d} \cos[2(k_i x - \omega_i t + \epsilon_i)] \quad (3.11)$$

$$w_p(x, z, t) = \sum_{i=1}^N \frac{g H_i}{2c} \frac{\sinh k_i(z + d)}{\cosh k_i d} \sin(k_i x - \omega_i t + \epsilon_i) + \frac{3}{16} c k_i^2 H_i^2 \frac{\sinh[2k_i(z + d)]}{\sinh^4 k_i d} \sin[2(k_i x - \omega_i t + \epsilon_i)] \quad (3.12)$$

It should be noted that these representations are the general form of these equations and the definition for celerity will vary depending on the seabed depth to wavelength ratio [297].

$$c(\omega) = \begin{cases} \sqrt{\frac{g\lambda}{2\pi}}, & \text{if } d/\lambda \geq 0.5 \\ \sqrt{gd}, & \text{if } d/\lambda \leq 0.05 \\ \sqrt{\frac{g}{k} \tanh kd}, & \text{if } 0.5 > d/\lambda > 0.05 \end{cases}$$

Similarly, the particle accelerations can be deduced by considering the derivatives of Eq. 3.11-3.12. The solutions of the above equations are used primarily to model the orbital motions of the particles beneath the sea surface, from which the influence of

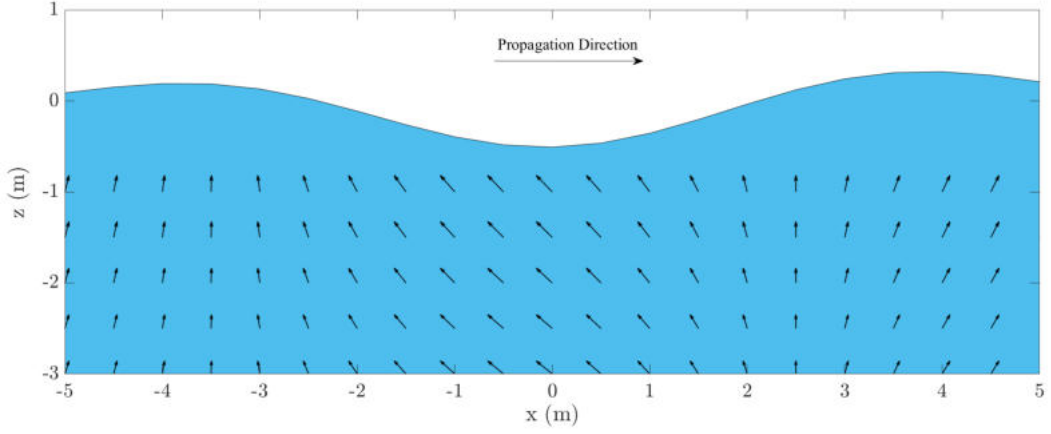


FIGURE 3.4: Vector representation of the fluid particle velocities beneath the surface wave elevation.

the surface waves on a body at a specified depth beneath the surface can be inferred. A temporal snapshot of the particle velocity evolution's are shown in Fig. 3.3 (at a depth of  $z = 5m$ , showing a  $90^\circ$  phase difference) whilst a vector representation is depicted in Fig. 3.4, demonstrating how the surge and heave components vary with respect to the surface elevation and each other.

### Linear Wave Theory

With regards to Eq. 3.7, the Linear Wave Theory (LWT) or Airy Theory representation only considers a 1st-order approximation and thus the 2nd-order term is neglected, deemed as not having significant effect on the output waveform. The wave elevation is therefore simply described by:

$$\zeta(x, t) = \sum_{i=1}^N A_i \cos(k_i x - \omega_i t + \epsilon_i) \quad (3.13)$$

Analogously, the velocity potential is reduced to only consider the primary term in Eq. 3.9

$$\Phi(x, z, t) = \sum_{i=1}^N \frac{g H_i}{2k_i c} \frac{\cosh k_i(z + d)}{\cosh k_i d} \sin(k_i x - \omega_i t + \epsilon_i) \quad (3.14)$$

Similar to the 2nd-order representation above, using the information from the wave frequency spectrum the orbital motions of fluid particles can be deduced at a point beneath the surface, returning a lower order approximation. The two components of fluid velocity in the global frame according to Eq. 3.9 and Eq. 3.10 are defined as:

$$u_p(x, z, t) = \sum_{i=1}^N \frac{g H_i}{2c} \frac{\cosh k_i(z + d)}{\cosh k_i d} \cos(k_i x - \omega_i t + \epsilon_i) \quad (3.15)$$

$$w_p(x, z, t) = \sum_{i=1}^N \frac{g H_i}{2c} \frac{\sinh k_i(z + d)}{\cosh k_i d} \sin(k_i x - \omega_i t + \epsilon_i) \quad (3.16)$$

and the two components of acceleration are again described by their derivatives. As the main concern of this thesis is to analyse the effect of wave forces on a submerged vehicle and apply control to mitigate these, the wave forces must be estimated quickly at a speed useful for real-time applications. To this end, LWT is adopted for the wave disturbance model and initial analysis in Chapter 4. Within the extended simulation study in Chapter 5, 2nd order theory is adopted to include the effects of wave drift on the vehicle and add an additional layer of realism. It should be noted that the above are the general form of these equations and these will vary depending on the classification of the wave (deep, intermediate or shallow) [298].

### Directional Spectra

As this thesis deals specifically with plane waves with unidirectional propagation, the two representations for the sea-surface given in Eq. 3.7-3.13 are only dependent on the longitudinal position  $x \in \mathbb{R}$  and point in time  $t \in \mathbb{R}$ . However, it is worth detailing the process to expand these definitions into the spatial domain as this is intended work for the future using the same framework. The extension to describe the wave height at a position  $(x, y) \in \mathbb{R}^2$  can be achieved by considering each wave direction and performing a double summation over  $M$  directional components and  $N$  frequency components; for the LWT representation the wave elevation is therefore modified and defined as:

$$\zeta(x, y, z, t) = \sum_{j=1}^M \sum_{i=1}^N A_{ij} \cos(k_j [x \cos \Theta_i + y \sin \Theta_i] - \omega_j t + \epsilon_{ij}) \quad (3.17)$$

where for a fixed value of  $j \in \{1, \dots, M\}$  the summation describes one particular wave front. In the above,  $\Theta$  describes the wave directionality. However, as noted in [282], phase-locking can occur due to waves of equal frequency in varying directions interacting, resulting in spatial interference patterns and subsequently non-ergodic wave fields.

Alternatively, and to avoid this effect during experimental testing, a single summation method can be applied; this is the process used at the wave tank facility discussed in Chapters 4-5. When applied, the sea state is instead constructed by considering each frequency component associated with a unique propagation direction, which reduces the wave elevation equation to a single summation [282]:

$$\zeta(x, y, z, t) = \sum_{i=1}^N A_i \cos(k_i [x \cos \Theta_i + y \sin \Theta_i] - \omega_i t + \epsilon_i) \quad (3.18)$$

With respect to the velocity potential, a similar modification can be made to Eq. 3.14 along with the introduction of an additional component of velocity, such that:

$$\Phi(x, y, z, t) = \sum_{i=1}^N \frac{A_i \omega_i}{k_i} \frac{\cosh k_i(z + d)}{\cosh k_i d} \sin(k_i [x \cos \Theta_i + y \sin \Theta_i] - \omega_i t + \epsilon_i) \quad (3.19)$$

$$v_p(x, y, z, t) = \frac{\partial \Phi}{\partial y} \quad (3.20)$$

where  $v_p$  is the y-component of the particle velocity vector. Explicitly, this results in the following expressions for the three components of particle velocity at the specified position  $(x, y, z)$  bounded by the sea-bed and sea surface:

$$u_p(x, y, z, t) = \sum_{i=1}^N A_i \omega_i \cos(\Theta) \frac{\cosh k_i(z + d)}{\cosh k_i d} \cos(k_i [x \cos \Theta_i + y \sin \Theta_i] - \omega_i t + \epsilon_i) \quad (3.21)$$

$$v_p(x, y, z, t) = \sum_{i=1}^N A_i \omega_i \sin(\Theta) \frac{\cosh k_i(z + d)}{\cosh k_i d} \cos(k_i [x \cos \Theta_i + y \sin \Theta_i] - \omega_i t + \epsilon_i) \quad (3.22)$$

$$w_p(x, y, z, t) = \sum_{i=1}^N A_i \omega_i \frac{\sinh k_i(z + d)}{\cosh k_i d} \sin(k_i [x \cos \Theta_i + y \sin \Theta_i] - \omega_i t + \epsilon_i) \quad (3.23)$$

The particle accelerations are obtained analogously to the uni-directional case by considering the time-derivative. As above, a snapshot of the particle velocity evolution's are shown in Fig. 3.5 for constant depth, demonstrating how the particle velocities vary when considering the wave directionality,  $\Theta$ .

The disadvantage of adopting a single summation approach is the requirement for an increased number of components to be considered, but this does reduce the aforementioned effects during wave construction which is highly desirable in experimental testing. As the only parameter which varies in these representations is the position, it is intuitive that an analogous modification determines the adjustment to both the wave elevation and the fluid motions beneath the surface, with reference to the wave direction,  $\Theta$ . Although not considered in this work, it is worth mentioning that wave data inclusive of directionality can be obtained through the use of devices such as advanced wave buoys, with data-sets available through several online repositories for testing purposes [246].

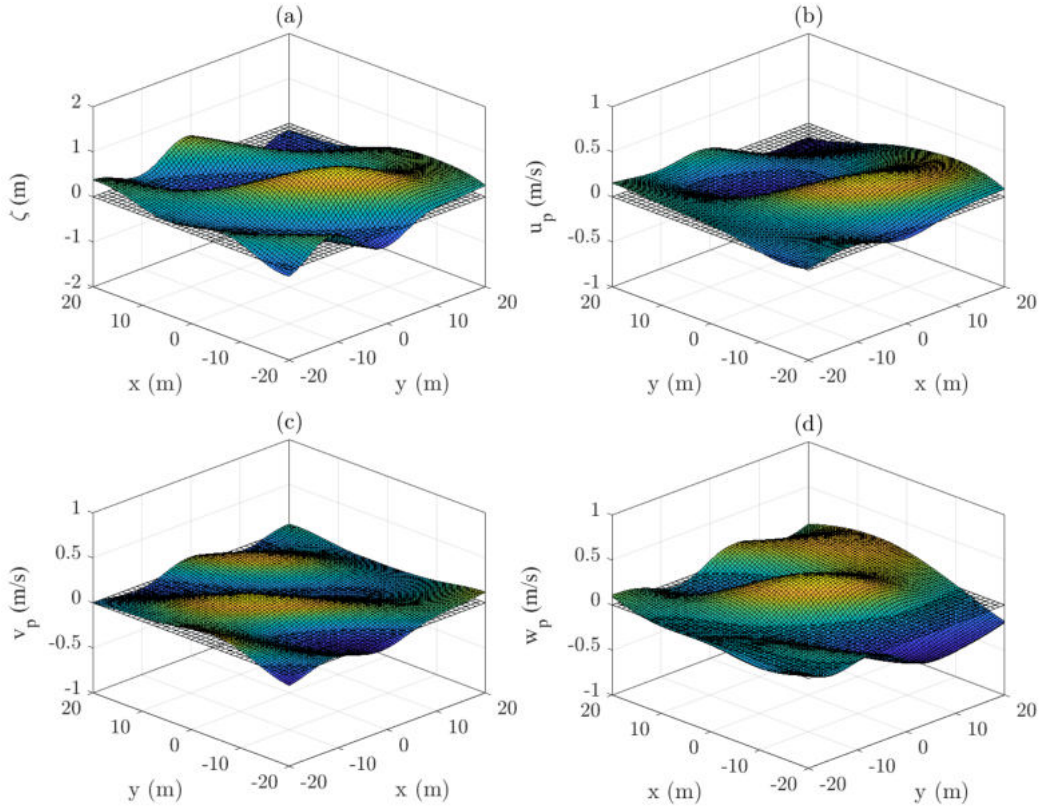


FIGURE 3.5: Evolution of the (a) wave elevation (b) surge component of particle velocity (c) yaw component of particle velocity and (d) heave component of particle velocity at a point in time  $t$  for a multi-directional case. These were generated in MATLAB via implementation of Eq. 3.18 and Eq. 3.21-3.23.

## 3.2 Modelling of Underwater Vehicles

In this section, the theoretical modelling of an underwater vehicle using rigid-body dynamics is presented, closely following the methodology outlined in [292] and [299]. Firstly, the notation adopted and vehicle kinematics are presented, followed by a description of the vehicle dynamics and the associated hydrodynamic forces, before finally summarising the full 6DoF equations of motion for an underwater vehicle. In the final section, the theoretical representation of the model adopted for control is described when employing several assumptions and simplifications, partnered with the vehicle-specific definitions for the BlueROV2 Heavy [300] (the vehicle considered throughout this thesis). The theory detailed here is the basis for the work undertaken throughout Chapter 4 and Chapter 5.

### 3.2.1 Kinematics

The most commonly used notation within the maritime engineering sector for marine vessels is SNAME notation; Fig. 3.6 shows a visual representation of this notation in 6DoF with the associated parameters also listed in Table 3.1.

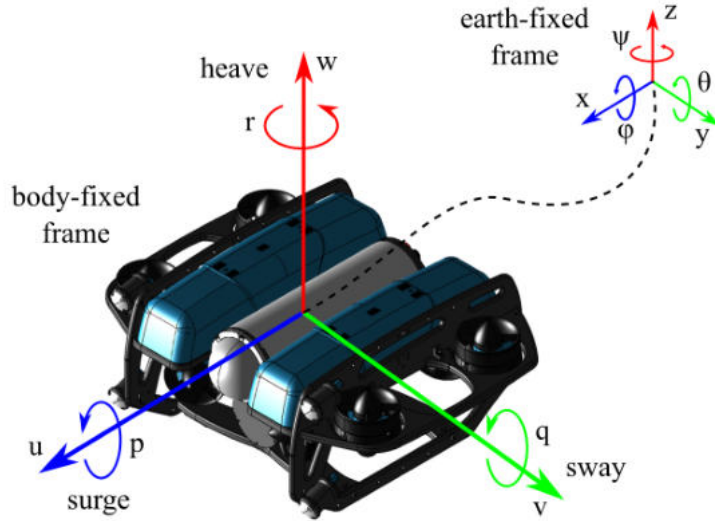


FIGURE 3.6: Visual representation of the earth-fixed and body-fixed co-ordinate frames and the associated parameters.

When modelling marine vehicles, it is convenient to define two co-ordinate systems for the position and motion of the body. The body-fixed frame is attached to the vehicle and therefore moves with the vehicle, as opposed to the earth-fixed frame which remains constant. As shown in Fig. 3.6, the position and orientation of the vehicle is given relative to the earth-fixed frame whilst the linear and angular velocity of the vehicle is given relative to the body-fixed frame. These are defined by the vectors  $\boldsymbol{\eta} \in \mathbb{R}^6$  and  $\boldsymbol{v} \in \mathbb{R}^6$  such that:

$$\boldsymbol{\eta} = \begin{bmatrix} x \\ y \\ z \\ \phi \\ \theta \\ \psi \end{bmatrix} \quad \boldsymbol{v} = \begin{bmatrix} u \\ v \\ w \\ p \\ q \\ r \end{bmatrix} \quad (3.24)$$

where  $x$ ,  $y$  and  $z$  describe the position of the vehicle in Cartesian co-ordinates and  $\phi$ ,  $\theta$  and  $\psi$  describe the orientation of the vehicle in Euler angles. All definitions can be found in Table 3.1.

TABLE 3.1: SNAME notation, commonly used for marine vehicles. The associated axis is listed with the Degree of Freedom.

Degree of Freedom	Positions/Angles	Linear/Angular Velocities	Forces/Moments
Surge, x-axis	$x$	$u$	$X_\tau$
Sway, y-axis	$y$	$v$	$Y_\tau$
Heave, z-axis	$z$	$w$	$Z_\tau$
Roll, x-axis	$\phi$	$p$	$K_\tau$
Pitch, y-axis	$\theta$	$q$	$M_\tau$
Yaw, z-axis	$\psi$	$r$	$N_\tau$

In general, the transformation between these reference frames is defined by the kinematics of the system relating the two vectors,  $\boldsymbol{\eta}$  and  $\boldsymbol{\nu}$ , which in compact form is defined as:

$$\dot{\boldsymbol{\eta}} = \mathbf{J}(\boldsymbol{\eta})\boldsymbol{\nu} \quad (3.25)$$

As the above formulation describes both a linear and angular velocity transformation, it is useful to consider the expanded form. With respect to this, Eq. 3.25 can be expressed as:

$$\begin{bmatrix} \dot{\boldsymbol{\eta}}_1 \\ \dot{\boldsymbol{\eta}}_2 \end{bmatrix} = \begin{bmatrix} \mathbf{J}_1(\boldsymbol{\eta}_2) & \mathbf{0}_{3 \times 3} \\ \mathbf{0}_{3 \times 3} & \mathbf{J}_2(\boldsymbol{\eta}_2) \end{bmatrix} \begin{bmatrix} \boldsymbol{\nu}_1 \\ \boldsymbol{\nu}_2 \end{bmatrix} \quad (3.26)$$

where

$$\boldsymbol{\eta}_1 = \begin{bmatrix} x \\ y \\ z \end{bmatrix} \quad \boldsymbol{\eta}_2 = \begin{bmatrix} \phi \\ \theta \\ \psi \end{bmatrix} \quad (3.27)$$

$$\boldsymbol{\nu}_1 = \begin{bmatrix} u \\ v \\ w \end{bmatrix} \quad \boldsymbol{\nu}_2 = \begin{bmatrix} p \\ q \\ r \end{bmatrix} \quad (3.28)$$

$$\mathbf{J}_1(\boldsymbol{\eta}_2) = \begin{bmatrix} \hat{c}\phi\hat{c}\theta & -\hat{s}\psi\hat{c}\phi + \hat{c}\psi\hat{s}\theta\hat{s}\phi & \hat{s}\psi\hat{s}\phi + \hat{c}\psi\hat{c}\phi\hat{s}\theta \\ \hat{s}\phi\hat{c}\theta & \hat{c}\psi\hat{c}\phi + \hat{s}\psi\hat{s}\theta\hat{s}\phi & -\hat{c}\psi\hat{s}\phi + \hat{s}\psi\hat{c}\phi\hat{s}\theta \\ -\hat{s}\theta & \hat{c}\theta\hat{s}\phi & \hat{c}\phi\hat{c}\theta \end{bmatrix} \quad (3.29)$$

$$\mathbf{J}_2(\boldsymbol{\eta}_2) = \begin{bmatrix} 1 & \hat{s}\phi\hat{t}\theta & \hat{c}\phi\hat{t}\theta \\ 0 & \hat{c}\phi & -\hat{s}\phi \\ 0 & \hat{s}\phi/\hat{c}\theta & \hat{c}\phi/\hat{c}\theta \end{bmatrix} \quad (3.30)$$

with  $\hat{c}$ ,  $\hat{s}$  and  $\hat{t}$  representing shorthand form of cos, sin and tan. It should be noted that  $\theta = \pm 90^\circ$  represents a singularity which can be avoided by either using a quaternion representation or two euler angle representations with different singularities [292], although the vehicle is highly unlikely to operate near these points and so is not considered.

In the following sections, the kinematic description above will be considered when deriving the nonlinear dynamic equation of motion for an underwater vehicle, resulting in the form:

$$\mathbf{M}\dot{\boldsymbol{\nu}} + \mathbf{C}(\boldsymbol{\nu})\boldsymbol{\nu} + \mathbf{D}(\boldsymbol{\nu})\boldsymbol{\nu} + \mathbf{g}(\boldsymbol{\eta}) = \boldsymbol{\tau}_P + \boldsymbol{\tau}_E \quad (3.31)$$

where  $\mathbf{M}$ ,  $\mathbf{C}(\boldsymbol{\nu})$ ,  $\mathbf{D}(\boldsymbol{\nu})$  and  $\mathbf{g}(\boldsymbol{\eta})$  are the inertia matrix, Coriolis/centripetal matrix, Damping matrix and a vector of restoring forces respectively. Also,  $\boldsymbol{\tau}_P$  and  $\boldsymbol{\tau}_E$  describe propulsive and environmental forces respectively.

### 3.2.2 Rigid-Body Dynamics

The common approach when deriving the equations of motion for a typical underwater vehicle is to assume that the body is rigid and behaves as such, which is widely accepted as the reasonable approach. This gives rise to the following rigid-body equation of motion:

$$\mathbf{M}_{RB}\dot{\boldsymbol{\nu}} + \mathbf{C}_{RB}(\boldsymbol{\nu})\boldsymbol{\nu} = \boldsymbol{\tau}_{RB} \quad (3.32)$$

where  $\mathbf{M}_{RB} \in \mathbb{R}^{n \times n}$  is the rigid-body inertia matrix,  $\mathbf{C}_{RB} \in \mathbb{R}^{n \times n}$  is the rigid-body Coriolis and centripetal matrix and  $\boldsymbol{\tau}_{RB} \in \mathbb{R}^n$  is a vector of external forces and moments such that:

$$\boldsymbol{\tau}_{RB} = \boldsymbol{\tau}_H + \boldsymbol{\tau}_E + \boldsymbol{\tau}_P \quad (3.33)$$

where  $\boldsymbol{\tau}_H \in \mathbb{R}^n$ ,  $\boldsymbol{\tau}_E \in \mathbb{R}^n$ ,  $\boldsymbol{\tau}_P \in \mathbb{R}^n$  are used to denote the hydrodynamic, environmental and propulsive forces and moments respectively. These contributions will be derived in the following sections. In these definitions,  $n \in \mathbb{Z}^+$  refers to the number of DoF considered in the model where  $0 < n \leq 6$ .

In general compact form, the rigid-body inertia matrix (for  $n = 6$ ) is defined as:

$$\mathbf{M}_{RB} = \begin{bmatrix} m\mathbf{I}_{3 \times 3} & -m\mathbf{S}(\mathbf{r}_G) \\ m\mathbf{S}(\mathbf{r}_G) & \mathbf{I}_0 \end{bmatrix} \quad (3.34)$$

where  $m$  is the vehicle dry mass,  $\mathbf{I}_0$  is the inertia tensor and  $\mathbf{r}_G$  is the centre of gravity;  $\mathbf{S}(-)$  is a skew-symmetric matrix given in Definition 3.2.1. For a 6DoF system, rigid-body inertia matrix can be shown in expanded component form as:

$$\mathbf{M}_{RB} = \begin{bmatrix} m & 0 & 0 & 0 & mz_G & -my_G \\ 0 & m & 0 & -mz_G & 0 & mx_G \\ 0 & 0 & m & my_G & -mx_G & 0 \\ 0 & -mz_G & my_G & I_x & -I_{xy} & -I_{xz} \\ mz_G & 0 & -mx_G & -I_{yx} & I_y & -I_{yz} \\ -my_G & mx_G & 0 & -I_{zx} & -I_{zy} & I_z \end{bmatrix} \quad (3.35)$$

**Definition 3.2.1** A skew symmetric matrix is one that satisfies  $\mathbf{S}(-) = -\mathbf{S}(-)^T$ . Therefore, considering the candidate vector  $\mathcal{X} = [\mathcal{X}_1, \mathcal{X}_2, \mathcal{X}_3]^T$  it follows that

$$\mathbf{S}(\mathcal{X}) = \begin{bmatrix} 0 & -\mathcal{X}_3 & \mathcal{X}_2 \\ \mathcal{X}_3 & 0 & -\mathcal{X}_1 \\ -\mathcal{X}_2 & \mathcal{X}_1 & 0 \end{bmatrix} \quad (3.36)$$

**Property 3.2.1** The rigid-body inertia matrix is positive and symmetric:  $\mathbf{M}_{RB} > 0$ ,  $\mathbf{M}_{RB} = \mathbf{M}_{RB}^T$ .

With respect to the rigid-body Coriolis and centripetal matrix, several parametrizations can be derived [292], one of which is:

$$\mathbf{C}_{RB} = \begin{bmatrix} m\mathbf{S}(\boldsymbol{\nu}_2) & -m\mathbf{S}(\boldsymbol{\nu}_2)\mathbf{S}(\mathbf{r}_G) \\ m\mathbf{S}(\mathbf{r}_G)\mathbf{S}(\boldsymbol{\nu}_2) & -\mathbf{S}(\mathbf{I}_0\boldsymbol{\nu}_2) \end{bmatrix} \quad (3.37)$$

**Property 3.2.2** *The rigid-body Coriolis and centripetal matrix can be defined so that it is skew-symmetric:  $\mathbf{C}_{RB} = -\mathbf{C}_{RB}^T$ .*

### 3.2.3 External Forces and Moments

When evaluating the vehicle dynamic response, consideration of the various sources of external hydrodynamic forces and moments is required in conjunction with the above rigid body dynamics. The standard assumption is that these are linearly superimposed [301] and the major contributions arise from radiation-induced forces (added mass effects, various forms of potential damping and restoring forces and moments), environmental disturbances (arising from ocean currents, waves and wind) and propulsive forces (including control surfaces such as rudders).

#### Added Mass

The effects arising from added mass can be separated into the added inertia matrix and the hydrodynamic Coriolis and centripetal matrix,  $\mathbf{M}_A \in \mathbb{R}^{n \times n}$  and  $\mathbf{C}_A \in \mathbb{R}^{n \times n}$  respectively. Derivation of these matrices using Kirchoff's equations and their full representation can be found in [292]. The resulting added inertia matrix for a 6DoF system takes the form:

$$\mathbf{M}_A = - \begin{bmatrix} X_{\dot{u}} & X_{\dot{v}} & X_{\dot{w}} & X_{\dot{p}} & X_{\dot{q}} & X_{\dot{r}} \\ Y_{\dot{u}} & Y_{\dot{v}} & Y_{\dot{w}} & Y_{\dot{p}} & Y_{\dot{q}} & Y_{\dot{r}} \\ Z_{\dot{u}} & Z_{\dot{v}} & Z_{\dot{w}} & Z_{\dot{p}} & Z_{\dot{q}} & Z_{\dot{r}} \\ K_{\dot{u}} & K_{\dot{v}} & K_{\dot{w}} & K_{\dot{p}} & K_{\dot{q}} & K_{\dot{r}} \\ M_{\dot{u}} & M_{\dot{v}} & M_{\dot{w}} & M_{\dot{p}} & M_{\dot{q}} & M_{\dot{r}} \\ N_{\dot{u}} & N_{\dot{v}} & N_{\dot{w}} & N_{\dot{p}} & N_{\dot{q}} & N_{\dot{r}} \end{bmatrix} \quad (3.38)$$

following the notation of SNAME previously mentioned (Table 3.1). For clarity, the above coefficients represent added mass forces due to accelerations in different directions, for instance  $X_{\dot{u}} = \partial X / \partial \dot{u}$ . In terms of the hydrodynamic Coriolis and centripetal effects, the corresponding matrix considers Eq. 3.38 in short form as:

$$\mathbf{M}_A = \begin{bmatrix} \mathbf{A}_{11} & \mathbf{A}_{12} \\ \mathbf{A}_{21} & \mathbf{A}_{22} \end{bmatrix} \quad (3.39)$$

resulting in

$$\mathbf{C}_A(\boldsymbol{\nu}) = \begin{bmatrix} \mathbf{0}_{3 \times 3} & -\mathbf{S}(\mathbf{A}_{11}\boldsymbol{\nu}_1 + \mathbf{A}_{12}\boldsymbol{\nu}_2) \\ -\mathbf{S}(\mathbf{A}_{11}\boldsymbol{\nu}_1 + \mathbf{A}_{12}\boldsymbol{\nu}_2) & -\mathbf{S}(\mathbf{A}_{21}\boldsymbol{\nu}_1 + \mathbf{A}_{22}\boldsymbol{\nu}_2) \end{bmatrix} \quad (3.40)$$

### Damping

In terms of hydrodynamic damping, multiple effects require consideration. Radiation-induced potential damping,  $-\mathbf{D}_P(\boldsymbol{\nu}) \in \mathbb{R}^{n \times n}$ , effects from skin friction,  $-\mathbf{D}_S(\boldsymbol{\nu}) \in \mathbb{R}^{n \times n}$ , wave drift damping,  $-\mathbf{D}_W(\boldsymbol{\nu}) \in \mathbb{R}^{n \times n}$ , and damping due to vortex shedding,  $-\mathbf{D}_M(\boldsymbol{\nu}) \in \mathbb{R}^{n \times n}$ , all affect the vehicle behaviour. Typically these are considered as a summation and the total damping matrix is defined as:

$$\mathbf{D}(\boldsymbol{\nu}) = \mathbf{D}_P(\boldsymbol{\nu}) + \mathbf{D}_S(\boldsymbol{\nu}) + \mathbf{D}_W(\boldsymbol{\nu}) + \mathbf{D}_M(\boldsymbol{\nu}) \quad (3.41)$$

which consists of both linear damping terms and quadratic damping terms. This is a convenient way of expressing the damping, grouping the contributions into two coefficients:

$$\mathbf{D}(\boldsymbol{\nu})\boldsymbol{\nu} = \{\mathbf{D}_L(\boldsymbol{\nu}) + \mathbf{D}_Q(\boldsymbol{\nu}) \odot |\boldsymbol{\nu}|\}\boldsymbol{\nu} \quad (3.42)$$

where  $\mathbf{D}_L(\boldsymbol{\nu}) \in \mathbb{R}^{n \times n}$  and  $\mathbf{D}_Q(\boldsymbol{\nu}) \in \mathbb{R}^{n \times n}$ . Here,  $\odot$  represents the Hadamard product where each row of the matrix  $\mathbf{D}_Q(\boldsymbol{\nu})$  is multiplied by the corresponding element in the vector  $\boldsymbol{\nu}$ .

### Restoring Forces and Moments

All forces arising from gravitational and buoyancy forces are grouped into a column vector dependent on the position of the vehicle centre of gravity,  $\mathbf{r}_G = [x_G, y_G, z_G]^T$ , the vehicle centre of buoyancy,  $\mathbf{r}_B = [x_B, y_B, z_B]^T$  and the orientation of the vehicle. The resulting vector is given as:

$$\mathbf{g}(\boldsymbol{\eta}) = \begin{bmatrix} (W - B) \sin \theta \\ -(W - B) \cos \theta \sin \phi \\ -(W - B) \cos \theta \cos \phi \\ -(y_G W - y_B B) \cos \theta \cos \phi + (z_G W - z_B B) \cos \theta \sin \phi \\ -(z_G W - z_B B) \sin \theta + (x_G W - x_B B) \cos \theta \cos \phi \\ -(x_G W - x_B B) \cos \theta \sin \phi - (y_G W - y_B B) \sin \theta \end{bmatrix} \quad (3.43)$$

where  $W$  and  $B$  are the vehicle weight and buoyancy.

The total vector of hydrodynamic forces and moments in Eq. 3.33 can now be obtained through Eq. 3.38 - 3.43, producing:

$$\boldsymbol{\tau}_H = -\mathbf{M}_A \dot{\boldsymbol{\nu}} - \mathbf{C}_A(\boldsymbol{\nu})\boldsymbol{\nu} - \mathbf{D}(\boldsymbol{\nu})\boldsymbol{\nu} - \mathbf{g}(\boldsymbol{\eta}) \quad (3.44)$$

## Propulsive Forces

Generally, any forces or moments generated from thrusters, propellers, control surfaces or similar means are grouped into a vector of control forces denoted as  $\tau_P$ . A common representation of this generalised vector is to consider an allocation matrix  $\mathbf{B}_P \in \mathbb{R}^{n \times n_p}$ , where  $n_p$  is the number of propulsion sources. This defines the contributions of each control action for each DoF such that:

$$\tau_P = \mathbf{B}_P \mu \quad (3.45)$$

where  $\mu \in \mathbb{R}^{n_p}$  is a column vector of control inputs which scales relative to the number of propulsion sources. Within this representation, the allocation matrix implements the transformation from control input to output propulsion force, for example considering the thruster geometry or dynamic response.

## Environmental Disturbances

The final element to consider in Eq. 3.31 and Eq. 3.33 is the effect of environmental disturbances on the vehicle behaviour. As has been alluded to previously, these are considered as a superposition where the main sources considered are ocean waves,  $\tau_\zeta \in \mathbb{R}^n$ , ocean currents,  $\tau_C \in \mathbb{R}^n$ , and wind,  $\tau_W \in \mathbb{R}^n$ . It follows that:

$$\tau_E = \tau_\zeta + \tau_C + \tau_W \quad (3.46)$$

which for  $n = 6$  results in the full generalised form:

$$\tau_E = [X_E \ Y_E \ Z_E \ K_E \ M_E \ N_E]^T \quad (3.47)$$

Each of these sources can be modelled to various degrees of complexity and accuracy depending on application; intuitively, for an underwater vehicle  $\tau_W = 0$  is a valid assumption and these disturbances can be considered as wind-generated waves instead. In terms of ocean currents, incorporation relies on the assumption that Eq. 3.31 can be defined according to a relative velocity,

$$\nu_r = \nu - \nu_c \quad (3.48)$$

$$\nu_c = [u_c, v_c, w_c, 0, 0, 0]^T$$

Generally the assumption is also made that  $\nu_c$  is constant or slowly varying.

With respect to this work, the focus was purely on the prediction and rejection of wave disturbances and therefore only contributions from ocean waves were considered. A detailed description of the adopted ocean model is provided in Section 3.1,

whilst the method for estimating wave-induced loading for the considered application is given in Section 4.2.1.

### 3.2.4 Nonlinear Dynamic Model for BlueROV2 Control

The definitions presented in Section 3.2.1-3.2.3 are in relation to a general dynamic model, based on the framework of Fossen [292, 299]. This model can be adapted and simplified on a case-by-case basis under various assumptions, hence it is useful to define the model adopted in this work and the assumptions employed in deriving this representation.

**Assumption 3.2.1** *The centre of gravity (CoG) of the vehicle is aligned with the origin:*

$$\mathbf{r}_G = [x_G, y_G, z_G]^T = [0, 0, 0]^T \quad (3.49)$$

**Assumption 3.2.2** *The centre of buoyancy (CoB) of the vehicle is assumed to be aligned with the origin in the longitudinal and lateral axes:*

$$\mathbf{r}_B = [x_B, y_B, z_B]^T = [0, 0, z_B]^T \quad (3.50)$$

**Assumption 3.2.3** *The vehicle is considered to possess two planes of symmetry, fore-aft and port-starboard. Although not perfectly symmetrical, this assumption is considered valid as most off-diagonal terms will be negligible in magnitude compared to major diagonal terms [299]. Therefore a reduced form of the added inertia matrix is considered and the damping matrix is considered to be purely diagonal:*

$$\mathbf{M}_A = - \begin{bmatrix} X_{\dot{u}} & 0 & 0 & 0 & X_{\dot{q}} & 0 \\ 0 & Y_{\dot{v}} & 0 & Y_{\dot{p}} & 0 & 0 \\ 0 & 0 & Z_{\dot{w}} & 0 & 0 & 0 \\ 0 & K_{\dot{v}} & 0 & K_{\dot{p}} & 0 & 0 \\ M_{\dot{u}} & 0 & 0 & 0 & M_{\dot{q}} & 0 \\ 0 & 0 & 0 & 0 & 0 & N_{\dot{r}} \end{bmatrix} \quad (3.51)$$

$$\mathbf{D}(\boldsymbol{\nu}) = -\text{diag}\{X_u, Y_v, Z_w, K_p, M_q, N_r\} \quad (3.52)$$

$$-\text{diag}\{X_{u|u}|u|, Y_{v|v}|v|, Z_{w|w}|w|, K_{p|p}|p|, M_{q|q}|q|, N_{r|r}|r|\}$$

**Assumption 3.2.4** *As this work is purely concerned with the mitigation of wave-induced disturbances, all other environmental disturbances are assumed to be null or negligible in comparison:*

$$\boldsymbol{\tau}_C, \boldsymbol{\tau}_W = 0, \quad \therefore \quad \boldsymbol{\tau}_E = \boldsymbol{\tau}_\zeta \quad (3.53)$$

Similarly, in conjunction with the assumptions stated above, the scenario we are concerned with is restricted to 3DoF planar control in the surge, heave and pitch

motions. Kinematically, these assumptions affect the form of the transformation matrix  $\mathbf{J}(\boldsymbol{\eta})$ , which reduces to a single rotation about the  $y$ -axis affecting the surge and heave:

$$\mathbf{J}(\boldsymbol{\eta}) \rightarrow \mathbf{R}_y = \begin{bmatrix} \cos \theta & \sin \theta & 0 \\ -\sin \theta & \cos \theta & 0 \\ 0 & 0 & 1 \end{bmatrix} \quad (3.54)$$

This reduces the matrix dimensions and results in the following for the BlueROV2 Heavy configuration:

$$\mathbf{M} = \begin{bmatrix} m - X_{\dot{u}} & 0 & -X_{\dot{q}} \\ 0 & m - Z_{\dot{w}} & 0 \\ -M_{\dot{u}} & 0 & I_y - M_{\dot{q}} \end{bmatrix} \quad (3.55)$$

$$\mathbf{D}_L(\boldsymbol{\nu}) = - \begin{bmatrix} X_u & 0 & 0 \\ 0 & Z_w & 0 \\ 0 & 0 & M_q \end{bmatrix} \quad (3.56)$$

$$\mathbf{D}_Q(\boldsymbol{\nu}) = - \begin{bmatrix} X_{u|u|} & 0 & 0 \\ 0 & Z_{w|w|} & 0 \\ 0 & 0 & M_{q|q|} \end{bmatrix} \quad (3.57)$$

Likewise, as the only angular motion considered is  $\theta$  (i.e.  $\phi = \psi = 0$ ) and the CoG and CoB are aligned on the vehicles longitudinal axes, the vector of restoring forces and moments is reduced to:

$$\mathbf{g}(\boldsymbol{\eta}) = \begin{bmatrix} (W - B) \sin \theta \\ -(W - B) \cos \theta \\ -(z_G W - z_B B) \sin \theta \end{bmatrix} \quad (3.58)$$

Finally, the propulsion allocation matrix can be derived from the vehicle geometry (see Fig. 3.7) and thruster parameters. An affine model is adopted similar to Eq. 3.45, with the addition of a first order response to model the delay between the control command and the produced forces and moments. Considering the 3DOF of the vehicle and the 8 available thrusters, the propulsion vector is defined by:

$$\boldsymbol{\tau}_P = \left(1 - e^{-\Delta t/t_m}\right) \mathbf{B}_P \mathbf{K}_\tau \boldsymbol{\mu} \quad (3.59)$$

where  $t_m \approx 0.1s$  is the thruster motor time constant,  $\Delta t$  is a discrete time-step,

$\boldsymbol{\mu} = [\mu_1 \ \mu_2 \ \mu_3 \ \mu_4 \ \mu_5 \ \mu_6 \ \mu_7 \ \mu_8]^T$  and

$$\mathbf{B}_P = \begin{bmatrix} \cos(\alpha_1) & \cos(\alpha_2) & -\cos(\alpha_3) & -\cos(\alpha_4) & 0 & 0 & 0 & 0 \\ 0 & 0 & 0 & 0 & 1 & 1 & 1 & 1 \\ 0 & 0 & 0 & 0 & l_x & l_x & -l_x & -l_x \end{bmatrix} \quad (3.60)$$

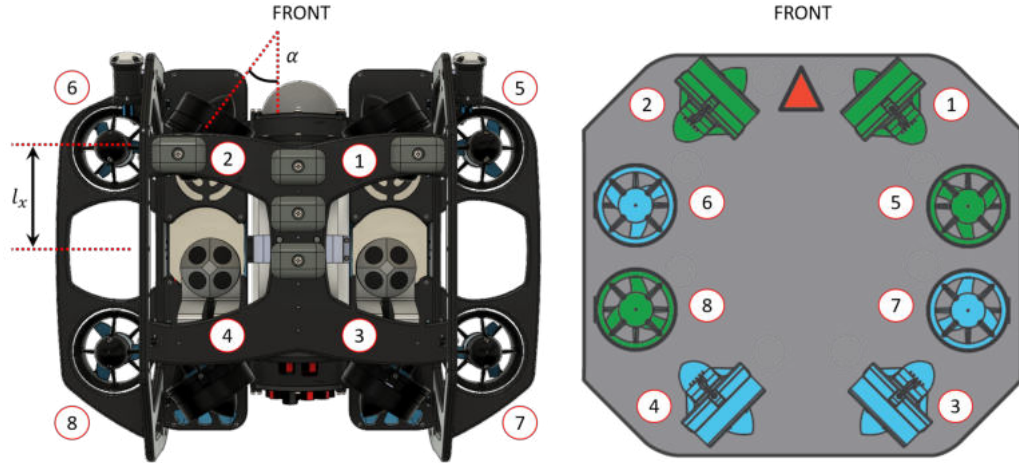


FIGURE 3.7: Thruster layout of the BlueROV2 Heavy, showing numbering assignments and key parameters.

Here,  $\alpha$  and  $l_x$  refer to the angular offset of the horizontal thrusters and moment arm of the vertical thrusters with respect to the vehicle's local longitudinal axes; it should be noted the vertical thrusters possess zero angular offset. Also,  $\mathbf{K}_\tau = \text{diag}(T_{max}) \in \mathbb{R}^{8 \times 8}$  is a force co-efficient matrix describing the capability of the thrusters where  $T_{max}$  is the maximum force producable per thruster.

As the BlueROV2 Heavy is actuated in all DoF and control of the heave and pitch is coupled through corresponding thrusters (5-8), a thrust allocation method was incorporated to transmit the required control actions accordingly. Regarding this, a similar strategy was adopted as in [299, 65] using a pseudo-inverse approach; this simplifies the control calculations by considering a set generalised control actions  $\boldsymbol{\mu}_g \in \mathbb{R}^3$  and producing a solution for  $\boldsymbol{\mu} \in \mathbb{R}^8$  as the input for Eq. 3.59. Consequently, the control vector is determined through:

$$\boldsymbol{\mu} = \left[ \left( 1 - e^{-\Delta t/t_m} \right) \mathbf{K}_\tau^{-1} \right] \mathbf{B}_P^\dagger \boldsymbol{\tau}_P \quad (3.61)$$

where  $\mathbf{B}_P^\dagger$  is the Moore-Penrose pseudo-inverse of  $\mathbf{B}_P$  and  $\boldsymbol{\tau}_P = \boldsymbol{\tau}_{max} \odot \boldsymbol{\mu}_g$  where  $\boldsymbol{\tau}_{max} \in \mathbb{R}^3$  is the maximum force or moment producible in each DoF.

This defines the dynamics of the BlueROV2 Heavy ROV and constitutes the model used in the simulations presented in Chapter 5, where all numerical values are specified in Table 5.6.

### 3.3 Modelling of Soft Manipulators

As discussed previously in Section 2.1.4, several models exist for modelling the behaviour of soft robots to varying degrees of accuracy; the adopted model is typically

dependent on application. In this work, the model implemented is a Piecewise Constant Curvature (PCC) model which effectively only considers the behaviour of the central backbone of the manipulator. As the concept of the physical manipulator is designed to be modular and each element within the structure is assumed to be identical from a theoretical standpoint, this was considered sufficiently accurate and applicable with respect to formulating the manipulator control. This facilitated the use of well-established continuum mechanics theories that can be found throughout the literature [197].

This section presents the mathematical description related to the PCC model, following a similar structure to the previous section by stating assumptions and properties throughout the derivation. Similarly, the model that is adopted for control purposes is defined here and is subsequently applied throughout the work presented in Chapter 6. The modelling approach closely follows the theory described in [197] and relates to the planar motion case, such that the absolute position of the manipulator end-effector is always considered as a point in space in  $\mathbb{R}^2$ .

### 3.3.1 Kinematics

In terms of the kinematics of the soft robot, the PCC approach considers a set of nodes along the backbone of the robot connected by arcs of constant radius; these arcs will be referred to as *segments* from here on-wards. Considering a soft robotic manipulator consisting of  $n$  DoF, the configuration of the robot is described by a vector of joint angles,  $\mathbf{q} \in \mathbb{R}^n$ ; the transformation into a Cartesian space representation is performed according to:

$$\dot{\mathbf{x}}_s(s, \mathbf{q}) = \mathbf{J}(s, \mathbf{q})\dot{\mathbf{q}} \quad (3.62)$$

where  $\mathbf{x}_s$  is defined as the posture relative to the segment abscissa  $s \in [0, 1]$  where 0 represents the base of the segment and 1 represents the tip. Refer to Fig. 3.8 for a visual representation of this parameter. The Jacobian in Eq. 3.62 is evaluated as:

$$\mathbf{J}(s, \mathbf{q}) = \frac{\partial \mathbf{h}(s, \mathbf{q})}{\partial \mathbf{q}} \quad (3.63)$$

with  $\mathbf{h}(s, \mathbf{q})$  describing the forward kinematics of the manipulator. The forward kinematics are described by considering the geometry of the manipulator, which for a single segment at a specified point in time is defined as:

$$\mathbf{x}_s(s, t) = \mathbf{h}(s, \mathbf{q}(t)) = \mathcal{L} \begin{bmatrix} \sin(sq(t)) & \frac{1-\cos(sq(t))}{q(t)} & \frac{sq(t)}{\mathcal{L}} \end{bmatrix}^T \quad (3.64)$$

where  $\mathcal{L}$  is the segment length. In this representation, the first two terms relate to the Cartesian position of the point  $s$  whilst the third simply describes the relative joint angle of  $s$  (for  $s = 1$  this reduces to  $q(t)$ ). It follows that  $\mathbf{J}(s, \mathbf{q})$  can be evaluated

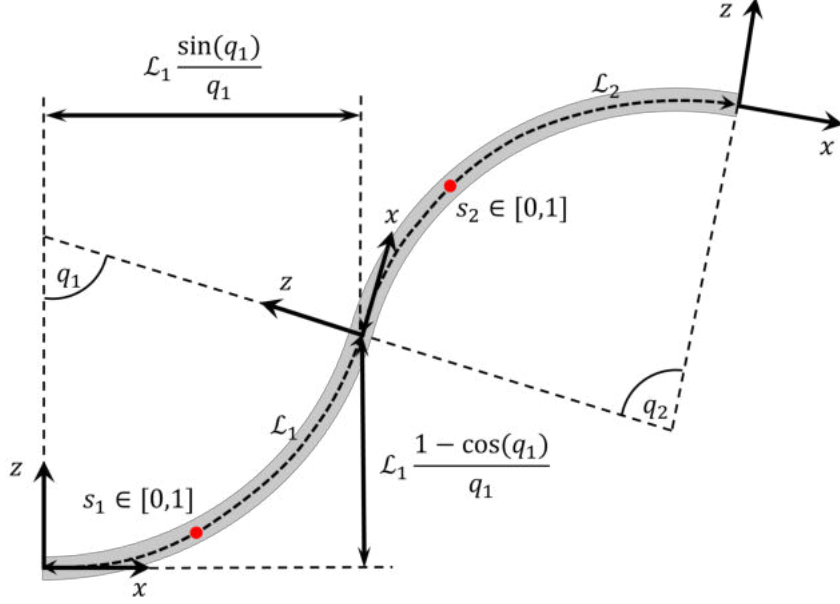


FIGURE 3.8: Schematic representation of the PCC geometry for a two segment robot.

according to Eq. 3.63 as:

$$\mathbf{J}(s, \mathbf{q}) = \mathcal{L} \begin{bmatrix} \frac{sq \cos(sq) - \sin(sq)}{q^2} & \frac{(\cos(sq) - 1) + sq \sin(sq)}{q^2} & \frac{s}{\mathcal{L}} \end{bmatrix}^T \quad (3.65)$$

These are the basic ingredients which facilitate the derivation of the nonlinear dynamic equation for the soft robot:

$$\mathbf{M}(\mathbf{q})\ddot{\mathbf{q}} + \mathbf{C}(\mathbf{q}, \dot{\mathbf{q}})\dot{\mathbf{q}} + \mathbf{G}(\mathbf{q}) + \mathbf{D}(\mathbf{q})\dot{\mathbf{q}} + \mathbf{K}(\mathbf{q}) = \boldsymbol{\tau} + \boldsymbol{\tau}_E \quad (3.66)$$

where \$\mathbf{M}(\mathbf{q})\$, \$\mathbf{C}(\mathbf{q}, \dot{\mathbf{q}})\$, \$\mathbf{G}(\mathbf{q})\$, \$\mathbf{D}(\mathbf{q})\$ and \$\mathbf{K}(\mathbf{q})\$ are the configuration dependent inertia matrix, Coriolis and Centrifugal matrix, gravitational vector, damping matrix and stiffness vector respectively. As in the ROV model, \$\boldsymbol{\tau}\$ and \$\boldsymbol{\tau}\_E\$ are vectors of generalised control torques and environmental disturbances respectively. The derivation of these introduced terms will be detailed in the following section in generalised form.

### 3.3.2 General Parameter Derivation

As the dynamics are given relative to the joint space and each parameter is configuration dependent, it is important to understand the mathematical derivations which lead to the formulation in Eq. 3.66. This section will therefore specify the definitions of each parameter and the relation to the body dynamics.

#### Inertia Matrix

To evaluate the inertia matrix relative to the joint-space, the mass and inertia distribution, \$\mathbf{M}\$, of each segment is considered. Considering the Jacobian of each segment,

the inertia matrix can be calculated according to:

$$\mathbf{M}(\mathbf{q}) = \sum_{i=1}^n \int_0^1 \mathbf{J}_i^T(s, \mathbf{q}) \mathcal{M}_i \mathbf{J}_i(s, \mathbf{q}) ds \quad (3.67)$$

which results in  $\mathbf{M}(\mathbf{q}) \in \mathbb{R}^{n \times n}$  as a square matrix. For a body moving within a medium of density much lower than that of the body itself ( $\rho_f \ll \rho_s$ , e.g. air) and is symmetrical in all planes, the inertia matrix is simply defined as:

$$\mathcal{M} = \mathcal{M}_S = \begin{bmatrix} m_s(s) & 0 & 0 \\ 0 & m_s(s) & 0 \\ 0 & 0 & \mathcal{J}_s(s) \end{bmatrix} \quad (3.68)$$

where,  $m_s(s)$  and  $\mathcal{J}_s(s)$  are mass and moment of inertia respectively relating to the segment composition. When operating in a dense medium (e.g. water), consideration of the added inertia is also required as this will have significant effect on the body dynamics. This is simply implemented by considering a matrix of added inertia's to be superimposed with Eq. 3.68, producing:

$$\mathcal{M} = \mathcal{M}_S + \mathcal{M}_A = \begin{bmatrix} m_s(s) & 0 & 0 \\ 0 & m_s(s) & 0 \\ 0 & 0 & \mathcal{J}_s(s) \end{bmatrix} + \begin{bmatrix} X_{\dot{u}}(s) & 0 & 0 \\ 0 & Z_{\dot{w}}(s) & 0 \\ 0 & 0 & M_{\dot{q}}(s) \end{bmatrix} \quad (3.69)$$

Due to the inertia matrix being configuration dependent, the dynamics are affected by centrifugal forcing which is derived accordingly. It should also be noted that as previously mentioned, the above definitions refer to the planar case where the end-effector position is described as  $[x, z]$ . Commonly, the thin-rod assumption is employed which results in  $\mathcal{J}_s(s), M_{\dot{q}}(s) = 0$  thus simplifying Eq. 3.69 further.

### Coriolis and Centrifugal Matrix

Evaluating the Coriolis and Centrifugal contributions can be performed using standard mathematical approaches, with many different forms of this matrix producing equivalent dynamics. One such approach is the use of Christoffel symbols [302, 197], a technique widely covered in literature and employs the assumption that elongation is negligible, which for the cases of interest in this work constitutes a reliable assumption.

Following this approach, each Christoffel symbol (of the first kind) is defined by:

$$\Gamma_{ijk}(\mathbf{q}) = \frac{1}{2} \left[ \frac{\partial M_{ij}}{\partial q_k} + \frac{\partial M_{ik}}{\partial q_j} - \frac{\partial M_{jk}}{\partial q_i} \right] \quad (3.70)$$

where  $M$  denotes an entry of the inertia matrix and the subscripts represent the Coriolis effect induced on a joint angle by the velocity of another. This definition

allows the elements of the Coriolis and Centrifugal matrix to be expressed according to:

$$[\mathbf{C}(\mathbf{q}, \dot{\mathbf{q}})]_{ij} = \sum_{k=1}^n \Gamma_{ijk}(\mathbf{q}) \dot{q}_k \quad (3.71)$$

which are used to construct the complete matrix  $\mathbf{C}(\mathbf{q}, \dot{\mathbf{q}})$ . It should be noted here that  $\Gamma_{ijk} = \Gamma_{ikj}$  is satisfied due to the inertia matrix being symmetric.

### Gravitational Vector

The effects due to the presence of gravity are evaluated by considering the gravitational potential energy, obtained by integrating the contributions of each infinitesimal element along the spatial coordinate. Within a medium such as air which is considered to have low density, this is simply evaluated as:

$$\mathbf{G}(\mathbf{q}) = \frac{\partial U_G}{\partial \mathbf{q}} = \frac{\partial}{\partial q_i} \sum_{i=1}^n \int_0^1 U_{G,i}(s) ds \quad (3.72)$$

Here,  $U_G$  is the gravitational potential energy of each segment of the manipulator such that:

$$U_G(s) = -mg_0^T \mathbf{r}_0(s) \quad (3.73)$$

where  $\mathbf{g}_0 \in \mathbb{R}^2$  and  $\mathbf{r}_0(s) \in \mathbb{R}^2$  ( $\mathbb{R}^2$  stemming from the consideration of a planar case) are the gravitational acceleration vector and the centre of mass of the point  $s$  along the robot arm respectively. When the soft robot is situated within a fluid such as water, effects from buoyancy must be considered by modifying Eq. 3.73 to consider the density ratio of the robot body material and fluid. In this instance, the gravitational potential energy is defined as:

$$U_G(s) = \left(1 - \frac{\rho_f}{\rho_s}\right) m_s \mathbf{g}_0^T \mathbf{r}_0(s) \quad (3.74)$$

where  $\rho_f$  is the density of the submerging fluid and  $\rho_s$  is the density of the segment.

### Stiffness Vector

Similar to the gravitational vector, effects due to the stiffness of the body are evaluated by considering the elastic potential energy along the spatial coordinate. The stiffness vector is therefore defined as:

$$\mathbf{K}(\mathbf{q}) = \frac{\partial U_K}{\partial \mathbf{q}} = \frac{\partial}{\partial q_i} \sum_{i=1}^n \int_0^1 \frac{1}{2} \kappa_i(s) q_i^2 ds \quad (3.75)$$

where  $\kappa(s) \in \mathbb{R}$  is the local stiffness in the structure element  $s$  that is assumed to be approximately constant when adopting the constant curvature assumption. This value will vary depending on the material and structure of the segment.

### Damping Matrix

The other dissipative term within the dynamics is the damping matrix, which describes any internal viscous losses within the structure. These can be evaluated by considering a proportional relationship with the variation in curvature, such that:

$$\mathbf{D}(\mathbf{q}) = \text{diag}_{i=0}^n \int_0^1 s d_{s,i}(s) ds \quad (3.76)$$

where  $d_s(s) \in \mathbb{R}$  is the local damping in the structure element  $s$ . The above representation is an equivalent form to considering each infinitesimal contribution along the segment length [197].

### Actuation Vector

Finally, one common approach to modelling the actuation forces is by considering a mapping matrix  $\mathbf{A}(\mathbf{q})$  in conjunction with the torque applied to the robot,  $\boldsymbol{\tau}_A$ . The mapping matrix dictates the transmitted torque to each robot segment, whereas the applied torque is dependent on the actuation method and will typically involve a transformation (for example a pressure to torque transformation for pneumatically actuated robots or tension to torque for tendon-driven robots). The actuation vector is therefore defined as:

$$\boldsymbol{\tau} = \mathbf{A}(\mathbf{q})\boldsymbol{\tau}_A \quad (3.77)$$

It should be noted that throughout this work the actuation torque is considered as a generalised input to the system dynamics and a pure moment applied at the tip. The specifics of the actuation method (i.e. tendon-driven, pneumatic, hydraulic, etc.) is not considered and thus the control concerns this value directly as opposed to some other control variable (e.g. a pressure or flow rate).

#### 3.3.3 Soft Robot Model for Control

The presented theory in Section 3.3 covers the generalised case for modelling soft robots, giving an overview of the PCC model and the derivations of each parameter. In the work undertaken in Chapter 6, the case considered is where the manipulator is restricted to planar motion ( $\mathbf{x}_s \in \mathbb{R}^3$  inclusive of joint angle) and consists of 3 independently actuated segments ( $n = 3$ ); considering this, the specific properties of the model relating to our case is presented here. For conciseness, the dependencies are dropped in the following definitions.

**Assumption 3.3.1** *Each actuated segment has identical physical and geometrical properties and are assumed symmetrical along each cross-section, thus can all be modelled using the same form.*

**Assumption 3.3.2** *The soft robot is assumed to have a uniform mass distribution along the entire length of the robot and can be treated as a very thin rod.*

$$m(s) = m \quad \mathcal{J}_s(s), M_{\dot{q}}(s) \approx 0$$

**Assumption 3.3.3** *Due to Assumption 3.3.1 with each robot segment assumed to be axisymmetric, the matrices relating to contributions arising from added mass and drag effects are purely diagonal with no cross coupling.*

This leads to the mass and inertia distribution being described by mass components only, which for the planar case where  $\mathbf{x}_s \in \mathbb{R}^2$  relates to:

$$\mathcal{M}_i = \mathcal{M} = \begin{bmatrix} m + X_{\dot{u}} & 0 & 0 \\ 0 & m + Z_{\dot{w}} & 0 \\ 0 & 0 & 0 \end{bmatrix} \quad (3.78)$$

for each segment. The value of both the segment mass  $m$  and the hydrodynamic added mass parameters  $X_{\dot{u}}, Z_{\dot{w}}$  will vary depending on materials and dimensions of the robot, but given that a generalised case is presented here the hydrodynamic added mass parameters are numerically defined in Section 6.3 for the simulations performed.

In terms of other parameters, the manipulator is assumed to possess identical segments and is therefore homogeneous in terms of stiffness and damping coefficient's:

$$d_{s,i}(s) = d_s \quad \kappa_i(s) = \kappa \quad (3.79)$$

Likewise, the robot is assumed to have direct independent actuation in order to maintain a sense of generality, therefore:

$$\mathcal{A}(\mathbf{q}) = \mathbf{I}^{n \times n} \quad (3.80)$$

where  $\mathbf{I}$  is the identity matrix. All other values for the properties of the robot (both geometric and hydrodynamic) are numerically defined in Table 6.1. Similarly, details of the control and the implementation of the assumptions discussed in this section are expanded upon and implemented in Chapter 5.

## Chapter 4

# Parametric Analysis of Wave-Vehicle Interactions for Station Keeping Control

### 4.1 Introduction

The investigation of deploying predictive control techniques on underwater robots for wave-induced disturbance rejection begins by focusing on the estimation and modelling aspect of wave-vehicle interactions. The aim here is to assess the validity of deploying low-order models which are computationally light and generally applicable for control purposes, specifically in the context of station keeping in wave-dominated environments. Firstly, the proposed model is presented along with key assumptions, in conjunction with an experimental study which centres on validating the model for the intended application; the obtained results provide a rigorous assessment evaluating the accuracy of the model. Following this, the development of an analytical model for predicting the performance of typical feedback control is detailed. The goal of this extension is to generalise the behaviour of underwater vehicles under wave disturbances, thus presenting a basis for a pre-assessment of control requirements without the necessity of performing fully constructed numerical simulations.

This preliminary work forms the basis of justifying the requirements of deploying predictive control methods for control of an underwater vehicle, by providing a disturbance model which can be deployed in tandem with a prediction algorithm. Likewise, in developing an analytical model of the station keeping performance using traditional feedback methods, assessment can be made based on the environmental conditions as to whether more complex control is required through this tool. Concluding remarks are finally given with regards to future work and connections to the following chapters.

## 4.2 Disturbance Estimation

A major limiting factor in applying a predictive control method such as MPC is the computational overhead required to perform the optimisation online at a speed applicable for real-time situations. This is exacerbated in a marine environment, which is often highly dynamic in nature and features nonlinear behaviour which further increases system requirements if no linearisation techniques are applied. Where model-order reduction techniques are applied, the question is then raised as to whether the simplified control model is representative of the real-world system and how the disparity affects the control performance.

With respect to Research Objective 1, this section focuses on exploring the use of low-order modelling of ocean wave disturbances on a submerged body with the intention of applying these estimations explicitly within an NMPC scheme. A model is proposed and developed, coupled with an experimental validation of said model, concluding by evaluating the overall performance and applicability.

### 4.2.1 ROV Wave Disturbance Model

Estimation of the linear drag and inertial fluid forces on the vehicle is intuitive, as these forces are considered a simple superposition and can be assumed to be constant across the body due to the rigid body assumption. Only the flow velocity and acceleration at the vehicle centre is therefore required to be evaluated. However, computation of the pitching moment exerted by the wave on the body requires an alternative treatment as the motion is induced due to the variation of the force over the body.

Owing to the consideration for a fast prediction, the proposed model is developed by considering the force variation over the body as a product of the uneven fluid flow, adopting an *ad-hoc* treatment. Alternative methods were considered such as the application of RAOs, a frequency domain method, however these do not generally suit predictive corrective control where a more precise impression of the vehicle response to a particular disturbance is critical. In contrast to the approach detailed here, the intention is that typically available hydrodynamic coefficients can be directly exploited instead to provide fine-granularity temporal wave disturbance estimations. The resulting moment is considered to be only produced by the normal force to the body along the vehicle sagittal plane, and any tangential component of fluid motion is disregarded as having a significant effect; see Fig. 4.1. This is a fair assumption due to the area of the vehicle in the heave plane being significantly larger than the surge, coupled with higher inertial and drag properties. This approach is also closely linked to Morison theory [303] for submerged piles which shares this assumption; whilst this stretches the validity of slender body theory (as the ROV is considered a bluff body), it enables a degree of prediction within a time-frame suitable for real-time control and therefore the validity of the approach was of interest.

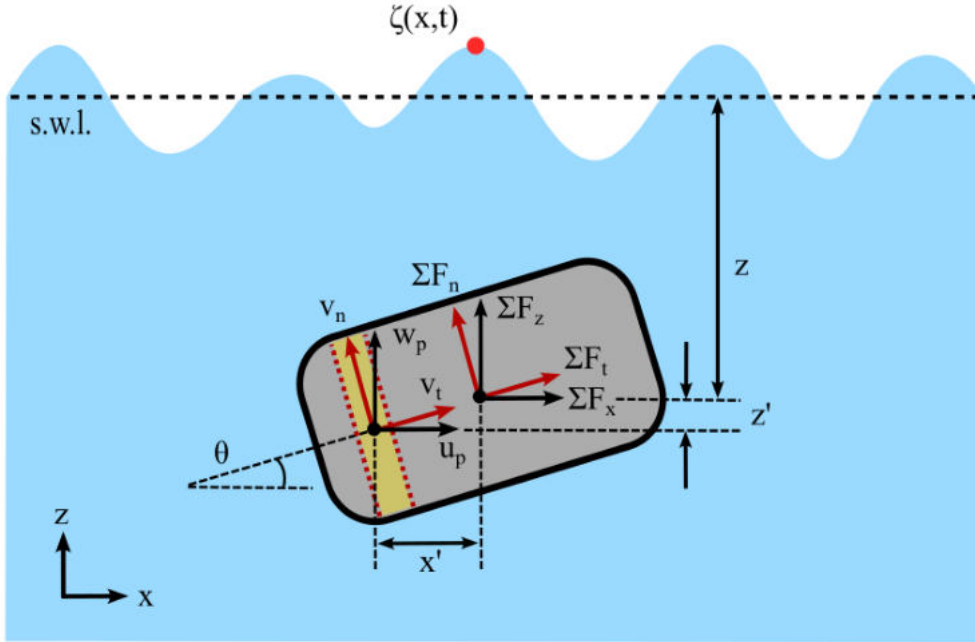


FIGURE 4.1: Particle velocities and resultant forces acting on the vehicle in both the local and global co-ordinate frame, depicting the different components acting along the vehicle sagittal plane with reference to the vehicle pitch,  $\theta$ .

Considering a fluid velocity vector in the global co-ordinate frame defined as  $\nu_p = [u_p \ w_p \ 0]^T$  where  $u_p$  and  $w_p$  are evaluated through the theory detailed in Section 3.1.2, with the dependencies dropped for the sake of clarity. As the vehicle velocities are defined in the local co-ordinate frame, the fluid velocity in the local frame is obtained by a single rotation of  $\nu_p$  such that:

$$\nu_{p,r} = \mathbf{R}_y \nu_p = [\nu_n \ \nu_t \ 0]^T \quad (4.1)$$

where  $\nu_n$  and  $\nu_t$  are the fluid velocity components normal and tangential to the body.

As the pitch moment requires slightly different consideration to the surge and heave loading, this is discussed first. If we define  $x'$  and  $z'$  as body-fixed co-ordinates which vary along the axial centre-lines of the vehicle, as shown in Fig. 4.1, substitution into Eq. 3.15-3.16 allows  $\nu_{p,r}$  to be deduced at varying locations along the vehicle sagittal plane. According to Morison theory, the following expressions can be applied to calculate the normal force component on an infinitesimal section of the vehicle's  $x'$  axis:

$$F_n(x', z', t) = \rho_f V C_M \dot{\nu}_n(x', z', t) + \frac{1}{2} \rho_f C_D A_f \nu_n(x', z', t) |\nu_n(x', z', t)| \quad (4.2)$$

where  $V$  is the spanwise volume of the section,  $C_M$  is an inertial coefficient,  $C_D$  is a drag coefficient and  $A_f$  is the projected area to the flow. Integration of these force elements along the vehicle length produces a model for estimating the wave-induced

moment exerted on the vehicle:

$$M_E = \int_{-L/2}^{L/2} x' F_n(x', z', t) dx' \quad (4.3)$$

where  $L$  is the vehicle longitudinal length. As for the surge and heave forces, these are obtained by considering  $\nu_{p,r}$  at the centre of the vehicle and evaluating the inertial and drag forces as constant across the body. It therefore follows that the wave-induced disturbances can be described by:

$$\boldsymbol{\tau}_E = \begin{bmatrix} X_E \\ Z_E \\ M_E \end{bmatrix} = \begin{bmatrix} X_u \dot{\nu}_{p,x} + (X_u + X_{u|u}| \nu_{p,x} |) \nu_{p,x} \\ Z_w \dot{\nu}_{p,z} + (Z_w + Z_{w|w}| \nu_{p,z} |) \nu_{p,z} \\ \int_{-L/2}^{L/2} x' F_n(x', z', t) dx' \end{bmatrix} \quad (4.4)$$

which is analogous to the form in Eq. 4.4. To summarise, this representation effectively considers a perpendicular force acting at discrete points along the vehicle as causing a pitching motion, allowing the net moment to be calculated quickly and efficiently. These estimations are key for providing the vehicle controller with a swiftly computed preview of the wave disturbances, thus allowing anticipatory mitigating control.

#### 4.2.2 Key Assumptions

To deploy the model in Eq. 4.4, knowledge of the wave spectra is required at the vehicle location. To acquire this knowledge, the vehicle position and orientation in space and time must be known. These are both assumed to be known in Section 4.3, but methods to acquire this information are detailed in Chapter 5 where the integrated solution is presented.

Rather than using *in-situ* measurements, the focus with this work was on formulating a disturbance model purely with hydrodynamic parameters. Considering this, the assumptions relating to this method are as follows:

**Assumption 4.2.1** *The effects due to the presence of surface waves can be modelled according to LWT and additional effects are considered negligible and assumed to be null.*

**Assumption 4.2.2** *The wave-induced pitching moment is purely a product of the normal component of velocity and the frictional effects caused by the tangential component are considered negligible.*

$$F_t(x', z', t) \approx 0 \quad (4.5)$$

**Assumption 4.2.3** *The position of the vehicle and wave parameters at this position can be evaluated and therefore an estimate of Eq. 4.1 is obtainable.*

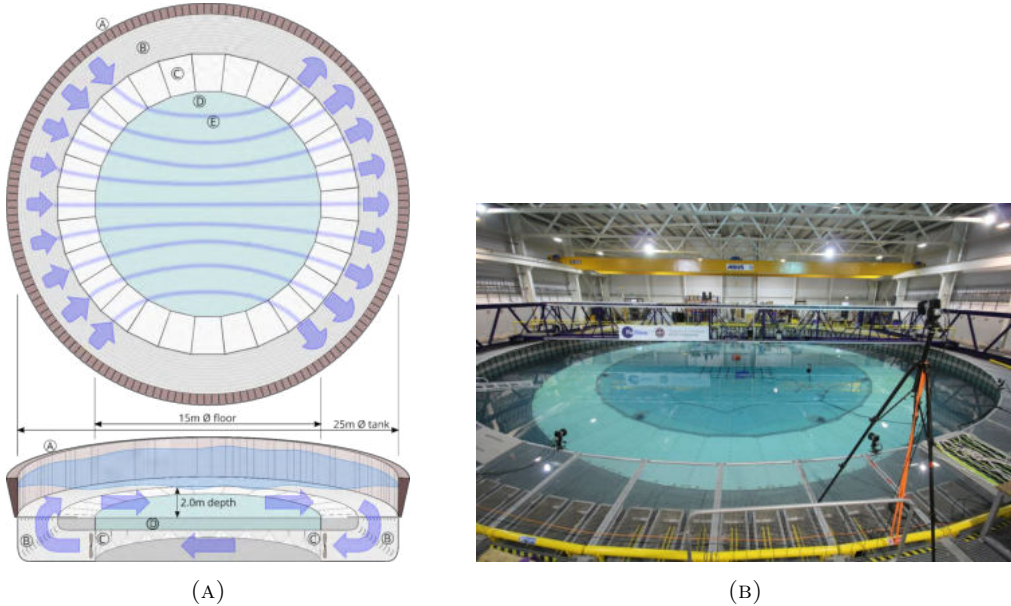


FIGURE 4.2: The FloWave Ocean Research Facility, showing (A) a schematic representation of the tank operation and (B) the tank itself with the water in an equilibrium state.

### 4.3 Experimental Study

As the model presented above is based on a low-order description of the wave-body interactions, an experimental study was designed and undertaken to validate the modelled hydrodynamic loads against those experienced by the submerged vehicle; this was purely due to the presence of surface waves with no currents enforced. The overall goal of the study was to record the forces and torques exhibited by the vehicle for varying wave formations, subsequently reconstructing the experimental cases within a simulated numerical environment to analyse the accuracy of our proposed model.

The experiments were undertaken at the FloWave Ocean Energy Research Facility [304] (referred to as FloWave for henceforth) at the University of Edinburgh and concerned the same ROV used throughout this thesis, namely the BlueROV2 produced by Blue Robotics [300]. The tank at FloWave is unique in that it is a circular tank with 168 wave-makers around the entire circumference, in comparison to a typical wave basin which is rectangular and usually propagates waves longitudinally from wave-makers at one end. This adds the capability of  $360^\circ$  current generation, in conjunction with being able to produce both uni-directional and multi-directional wave formations; these experiments focused solely on uni-directional waves. The waves are generated at one-end of the tank and the wave-makers at the opposite end are configured to absorb these, minimising any reflections and minimising these effects on the recorded data. For a schematic representation of how the FloWave tank operates and the tank itself, see Fig. 4.2; the tank is 25m in diameter and has a 2m total water depth with a raisable floor.

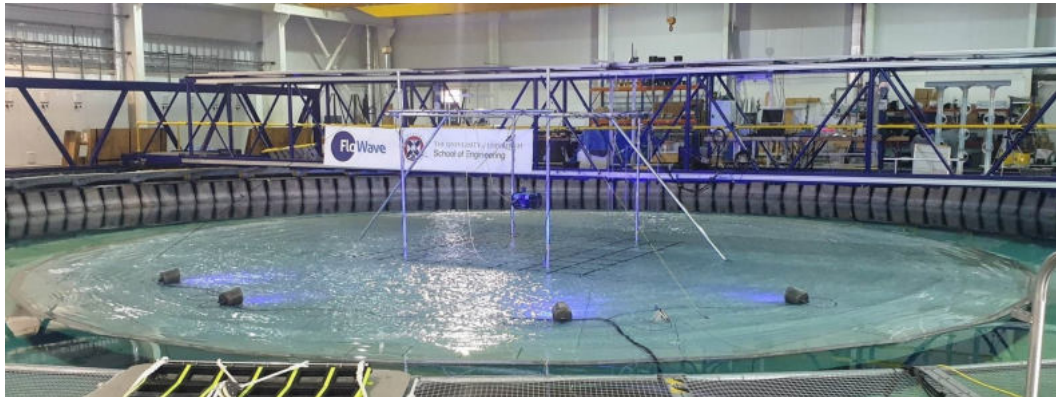


FIGURE 4.3: The ROV suspended in the purpose-built frame with the tank floor raised and the vehicle above the still water line.

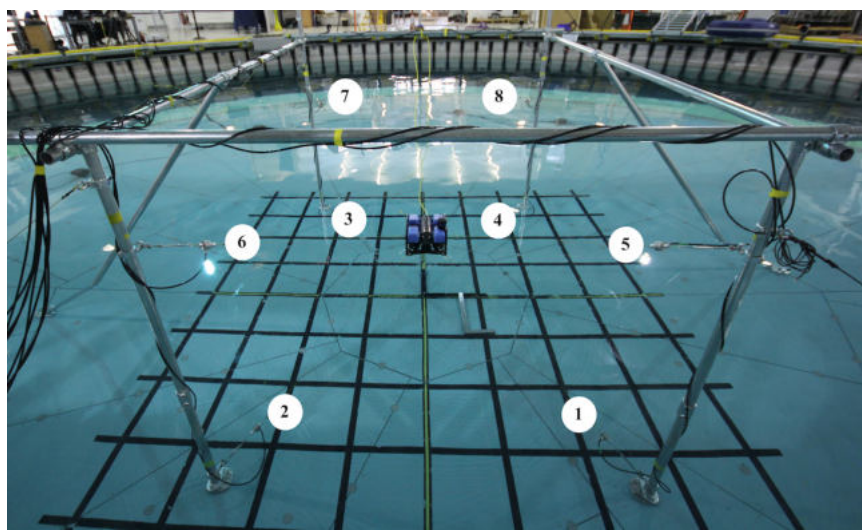


FIGURE 4.4: Numbering scheme adopted for the load cells.

#### 4.3.1 Methodology

In order to accurately record the forces and torques produced by the presence of the waves on the vehicle, the vehicle was suspended within a purpose built-frame by eight tethers, each fitted with an inline load cell (LC). The arrangement is shown in Fig. 4.3 with the floor raised and the ROV suspended in the frame. The frame was designed and manufactured specifically for this study to minimise the interference with the flow around the vehicle by using galvanised tubes with an outer diameter of 48.3mm. The frame was 3.47m long in the x-plane, 2.52m wide in the y-plane and  $\approx 2.5\text{m}$  in height with the top of the frame piercing the water surface. The frame was fixed to the base of the tank with the ROV located at the centre of the tank and at a depth of 1m; the wave formations generated by the tank software refer to a fully developed sea-state at the centre of the tank. In doing so, the loads experienced are as representative of the same point in space and time as possible and recordings are not skewed by vehicle motion. The frame and suspended ROV are shown in Fig. 4.4 when the floor of the tank is raised, also displaying the load cell numbering scheme.

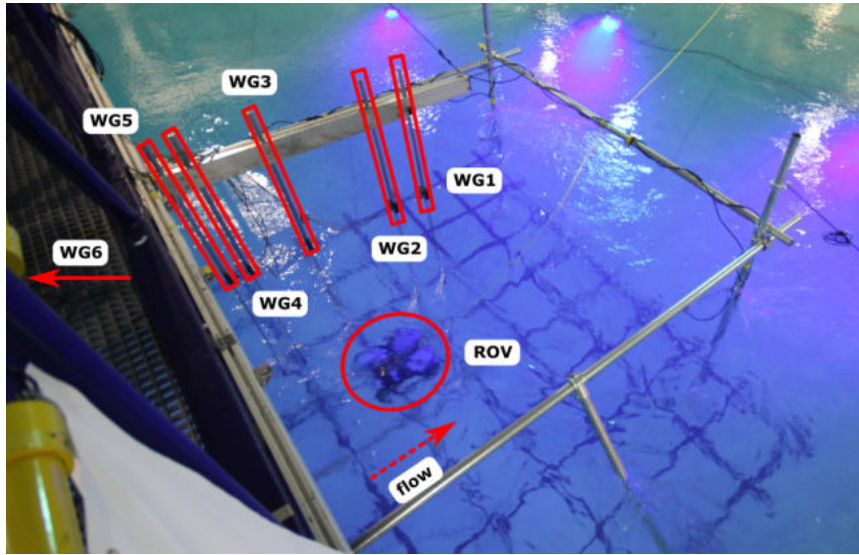


FIGURE 4.5: The submerged ROV within the frame, showing the numbering scheme adopted for the wave gauges (WG) and the propagation direction of the waves.

TABLE 4.1: Experimental parameters for the test cases considered. For cases R01-R03, the peak spectral period refers to the period.

Case Reference	Significant Wave Height, $H_s(m)$	Peak Spectral Period, $T_p(s)$
R01	0.1	2
R02	0.2	2
R03	0.4	2
JS01	0.2	2
JS02	0.4	2
JS03	0.6	2

To monitor the disparity between the *ideal* wave generated by the software and the actual wave produced by the wave-makers, a six-point wave gauge (WG) array was also installed over the ROV after it was submerged in the main wave direction (orthogonal to the gantry), as shown in Fig 4.5. This was purely for cross-checking of the encountered waves against the loads experienced when performing the validation stage using our proposed numerical model. With regards to the wave parameters of the different test cases, a mixture of both monochromatic waves and JONSWAP spectra were analysed ranging from 0.1m to 0.6m in significant wave height where the height refers to peak-to-trough. For all cases, the period or peak spectral period was specified as 2s, as this is an optimal operating point of the tank which allows larger wave heights to be generated. The full specification for all cases and assigned case references are displayed in Table 4.1, with a visual frequency and temporal representation of the JONSWAP cases shown in Fig. 4.6; this clearly displays the variation in wave height across the different test cases.

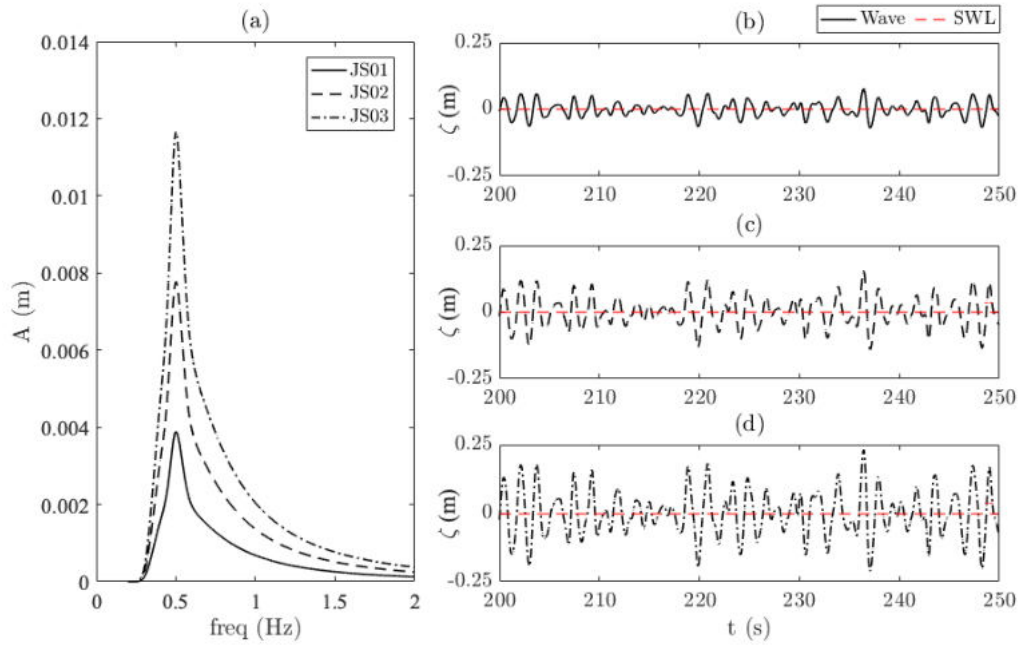


FIGURE 4.6: JONSWAP cases tested throughout the experimental study, showing (a) the frequency spectrum of each (constant peak period, varying significant height) and a temporal segment of the wave for case (b) JS01, (c) JS02 and (d) JS03. Here, SWL refers to the still water line.

### 4.3.2 Instrumentation and Setup

In total, three different systems were deployed to take measurements of the system. Two have been previously mentioned in the form of the LCs and WGs; the other system concerns an underwater motion capture system (MoCAP) which monitored any small motions the vehicle underwent which the frame failed to mitigate completely. As with the WGs, this was used as a corrective measure to cross-check against the intended position of the vehicle. To synchronise the different sources of data acquisition, a digital pulse was used that is output by the tank control system. All instrumentation provided measurements at a frequency of 128Hz.

#### Motion Capture System

To monitor any minimal motions that occurred during the experiments due to the frame not being able hold the vehicle perfectly stationary, an array of four underwater cameras provided by Qualisys were deployed. These were mounted to the edge of the tank floor and operate by tracking reflective markers placed on the system of interest. In this instance, seven reflective markers were placed on the vehicle body and an additional eight were placed on the tethers (one on each), close to the mounting point of the load cells. The placement of the cameras relative to the frame can be seen in Fig. 4.7, which uses blue light to track the markers.

To ensure the accuracy of the system of all experiments ( $< 1\text{mm}$ ), standard refinement calibration procedures were followed [27, 28]. The markers on the vehicle

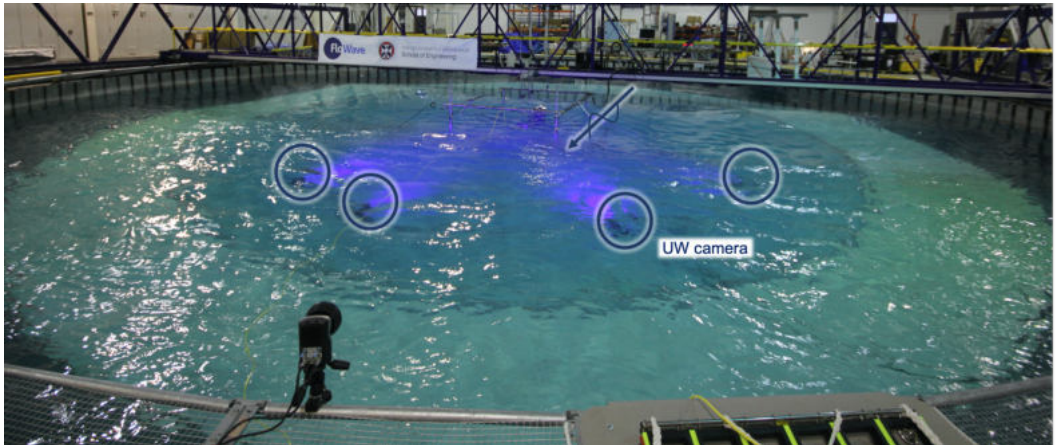


FIGURE 4.7: Positions of the underwater cameras associated with the motion capturing system when the frame and vehicle are submerged, also showing the direction of the flow.

body provided results in all 6DoF, allowing cross-analysis of the vehicle location relative to the centre of the tank and the point of wave generation. The system was also used to observe the motion and potential deformation of the frame itself under different waves.

### Load Cells

To connect the vehicle to the frame, 8 tethers were used made of a lightweight Dyneema rope each fitted with an in-line LC as well as a single turnbuckle; this allowed pre-load to be applied to the structure and the vehicle to be aligned precisely within the centre of the frame. It should be noted that this process could only be undertaken when the floor was raised and in dry conditions before the vehicle was submerged. Six of the LCs were rated up to 100N in load capacity whilst the remaining two were rated up to 500N; these higher rated LCs are LC7 and LC8 in Fig. 4.4. Due to the higher rating of LC7 and LC8, the measurements are comparably noisier when considering lower forces [305]; therefore, a Savitzky-Golay filter [306] was applied to the experimental data to smooth the signal and reduce this where possible. As per the manufacturer specifications, the accuracy is given as  $< \pm 0.15\%$  of the rated capacity with a typical value of  $\pm 0.05\%$  [305].

Given the position of the ROV, the mounting points of the tethers to the vehicle frame could be calculated as virtual points; the resulting force vector and decomposed force components could then be resolved in three-dimensional space and small variations could be taken into account. Using the MoCAP, eight reflective markers were mounted to the tethers at a specified mounting point (MP). Using the measured frame marker point (FP), the direction of the load cell vector could be determined as:

$$\vec{V} = \vec{FP} - \vec{MP} = [V_x \quad V_y \quad V_z] \quad (4.6)$$

TABLE 4.2: Locations of the mounting points (MP) relative to the centre of the vehicle body during the wave-induced loading experimental trials.

Plane	MP1	MP2	MP3	MP4	MP5	MP6	MP7	MP8
x(mm)	129.6	129.6	-130.4	-130.4	129.6	129.6	-130.4	-130.4
y(mm)	-167.8	167.8	167.8	-167.8	-167.8	167.8	167.8	-167.8
z(mm)	112.0	112.0	112.0	112.0	-80.0	-80.0	-80.0	-80.0

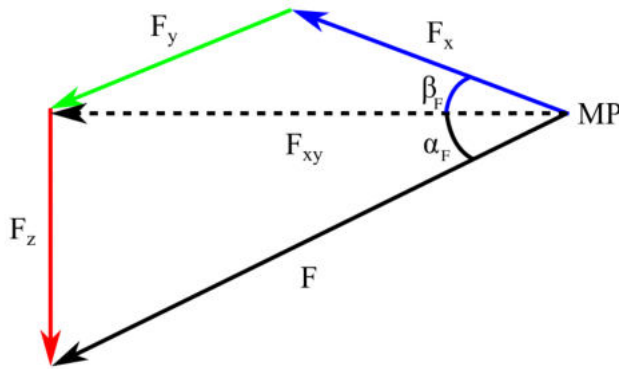


FIGURE 4.8: Visual representation of how the measured force vector is decomposed into the main components in three-dimensions.

where  $V_x$ ,  $V_y$  and  $V_z$  are the individual vector components. The locations of the MPs relative to the centre of the ROV body is given in Table 4.2.

Decomposition of the measured force ( $F$ ) into their main components is then performed through:

$$F_x = F_{xy} \cos \left( \arctan \left[ \frac{V_y}{V_x} \right] \right) \quad (4.7)$$

$$F_y = F_{xy} \sin \left( \arctan \left[ \frac{V_z}{(V_x^2 + V_y^2)^{0.5}} \right] \right) \quad (4.8)$$

$$F_z = F \sin \left( \arctan \left[ \frac{V_z}{(V_x^2 + V_y^2)^{0.5}} \right] \right) \quad (4.9)$$

where

$$F_{xy} = F \cos \left( \arctan \left[ \frac{V_z}{(V_x^2 + V_y^2)^{0.5}} \right] \right) \text{dir}(i) \quad (4.10)$$

and

$$\text{dir} = [1, 1, -1, -1, 1, 1, -1, -1] \quad (4.11)$$

is a correction vector applied to the horizontal forces due to all LCs returning positive values, when in reality four are in the opposite direction. A visualisation of this force vector is displayed in Fig. 4.8 for clarity, where the substitutions  $\alpha_F = \arctan [V_z/(V_x^2 + V_y^2)^{0.5}]$  and  $\beta_F = \arctan [V_y/V_x]$  are used.

TABLE 4.3: Longitudinal (x) locations of the wave gauges (WG) with respect to the centre of the tank and ROV in the global co-ordinate frame (0.000m).

WG1 (m)	WG2 (m)	ROV (m)	WG3 (m)	WG4 (m)	WG5 (m)	WG6 (m)
-0.495	-0.313	0.000	0.141	0.414	0.505	2.105

### Wave Gauges

As shown in Fig. 4.5, the WG array was placed coincident to the main direction of flow and wave direction and was positioned above the ROV after the floor had been lowered and the vehicle submerged. The accuracy of the conductive WG in measuring the surface height is  $\leq 1\text{mm}$  and an additional calibration procedure was followed to ensure consistency of this degree of accuracy [28].

With respect to the spacing of the array, WG1-5 were specified as part of a reflection array based on a Golomb ruler with an order of 5 (marks [11 9 4 1 0]; base length of 1m). As for the remaining gauge, this was installed on the opposite side of the gantry and is the only gauge to be situated outside of the frame perimeter. The direction of the waves was maintained constant for all experiments, thus WG6 encountered the wave first and WG1 last. Also, the ROV was situated between WG4 and WG2, with WG3 the closest to the centre of the tank. The specific longitudinal locations of each WG is provided in Table 4.3 with respect to tank and ROV centre, where the vertical and lateral locations are equal to 0m (sea surface and centre aligned).

#### 4.3.3 Model Validation

The validation procedure first involved emulating the sea state created by the wave-makers in a numerically simulated environment through application of the theory in Section 3.1.2. This facilitates estimation of the fluid particle velocities and accelerations at the vehicle location beneath the surface; the model presented in Section 4.2.1 was then applied to estimate the wave-induced hydrodynamic loads. These estimated loads were directly compared to the processed data collected during the experiments. As the waves considered in this study are uni-directional, the analysis concerns only the forces and torques in the surge, heave and pitch; this directly relates to the reduced vehicle dynamical model presented in Section 3.2.4. For the JONSWAP cases, it was possible to extract the ideal frequency spectrum from the tank software thus the component parameters to reconstruct the wave field at the centre of the tank. This ideal reconstruction was compared to the observed wave recorded by the WG array to analyse the errors incurred and how valid the LWT approach was. Alternatively, the WG data could be directly exploited using Fourier analysis, however as there was no recording directly at the centre of the tank the former approach was considered more appropriate to remove any additional minor errors associated with shifting the waveform.

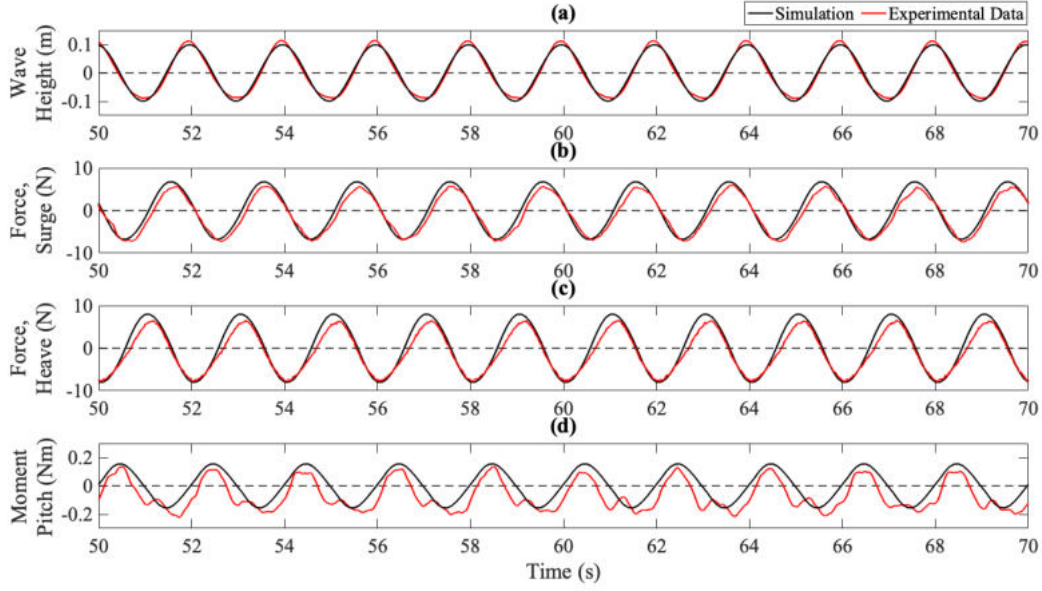


FIGURE 4.9: Comparison between simulation and experimental data for case R02, showing the time segment 50 – 70s. The sub-plots display the (a) wave height, (b) surge force, (c) heave force and (d) pitching moment.

Considering the above, the additional assumptions adopted during the validation process are therefore as follows:

**Assumption 4.3.1** *The vehicle pose is assumed to be perfectly stationary for the entire simulation and any small motions are neglected; all processed data is assumed to refer to:*

$$\boldsymbol{\eta} = [0, 0, -1, 0, 0, 0]^T$$

$$\boldsymbol{\nu} = [0, 0, 0, 0, 0, 0]^T$$

**Assumption 4.3.2** *The vehicle is assumed to be configured perfectly head-on with the encountered wave and therefore the only forces and torques experienced relate to the surge, heave and pitch.*

$$\boldsymbol{\tau}_E = [X_E, 0, Z_E, 0, M_E, 0]^T$$

**Assumption 4.3.3** *The floor of the tank is assumed to have negligible impact on the wave formation, thus LWT and the surface wave/particle trajectories can be emulated using only a 1st-order approximation.*

## Results Discussion

Analysing the data qualitatively, a temporal snapshot of one of the monochromatic cases R02 is displayed in Fig. 4.9 whilst the same snapshot is shown for cases JS01-JS03 are displayed in Fig. 4.10-4.12.

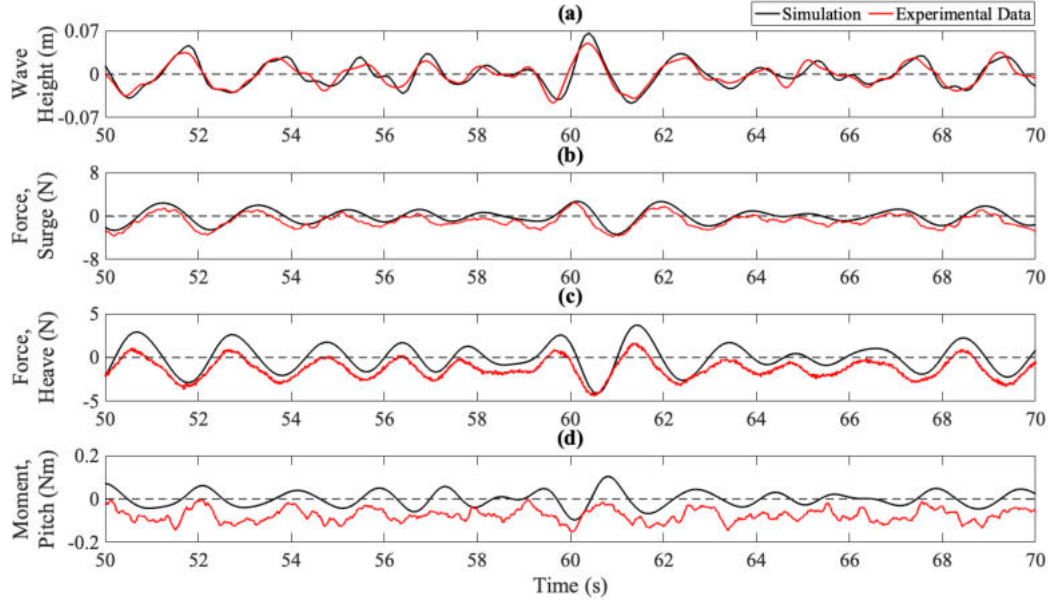


FIGURE 4.10: Comparison between simulation and experimental data for case JS01, showing the time segment 50 – 70s. The sub-plots display the (a) wave height, (b) surge force, (c) heave force and (d) pitching moment.

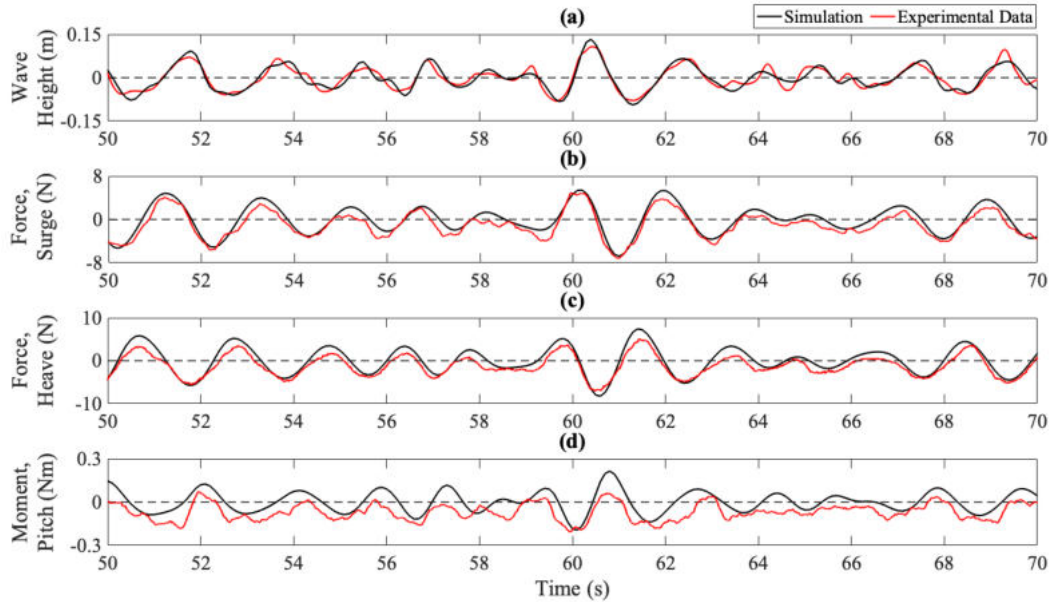


FIGURE 4.11: Comparison between simulation and experimental data for case JS02, showing the time segment 50 – 70s. The sub-plots display the (a) wave height, (b) surge force, (c) heave force and (d) pitching moment.

All of these plots show that the general behaviour of the simulated loads and recorded loads are followed closely, with the pitch moment showing the most disparity. Good correlation between the estimations and the experimentally collected data is displayed, demonstrating that the lower order model can provide a fair representation of the particle motions and resulting forces induced by surface waves. Although the data was filtered to reduce the effect of sensor noise, all plots still show some effect of noise on the resulting trace. This is mainly due to 2 of the load cells being rated higher,

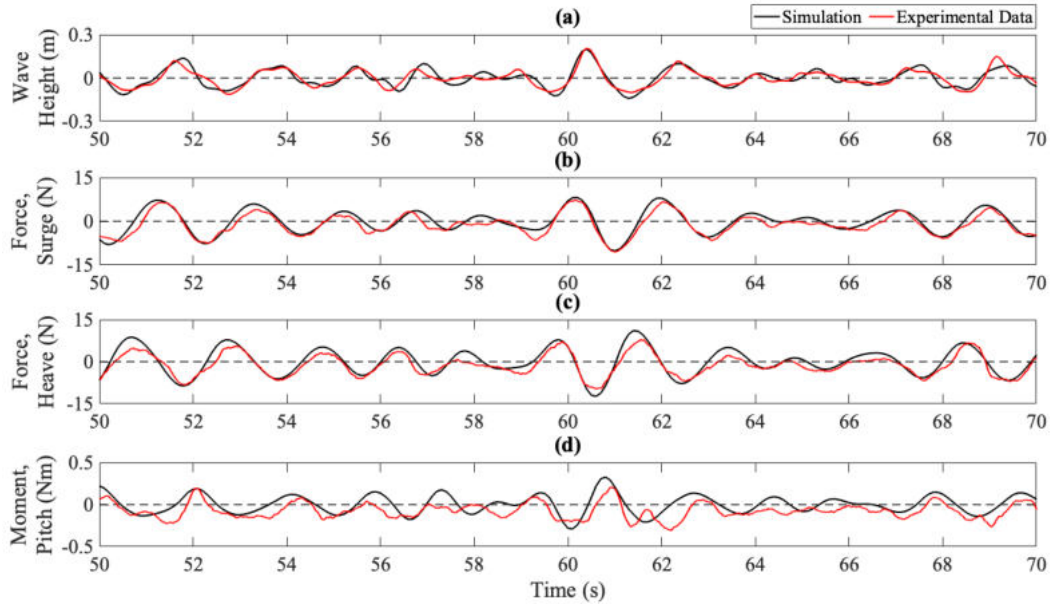


FIGURE 4.12: Comparison between simulation and experimental data for case JS03, showing the time segment 50s – 70s. The sub-plots display the (a) wave height, (b) surge force, (c) heave force and (d) pitching moment.

causing low magnitude wave elevations to be affected by a higher degree of background sensor fluctuation. There may also be components operating at a frequency similar to that of the wave associated with the frame and measurement gauges, which are difficult to segregate from the force signal. However, the overall behaviour can still be seen as consistent, particularly for case JS02 and JS03 where the significant heights are larger. This is an interesting point as the proposed method in Chapter 5 is focused on mitigating large magnitude wave disturbances, so if reasonably accurate estimations can be obtained then the disparity for lower magnitude waves is of less importance.

The correlation coefficients between the estimated forces and the data collected during the experiments were also evaluated, showing good agreement for the majority of cases, detailed in Table 4.4. A noticeable decrease was noticed for case R03, the monochromatic case with the largest wave height. However, as the wave height here is comparable to case JS02 it is suspected that this is not the reasoning for the increase disparity and the problem is related to the apparatus, possibly that the vehicle was not positioned correctly for the entirety of the experiments. This is also reflected in the fact the wave itself showed a drop in correlation, likely due to operating near the FloWave tank physical limits. Even when including this case, the mean correlation coefficients for the surge and heave forces are 0.9123 and 0.9061 whilst the pitch moment returned a coefficient of 0.7117. When neglecting this specific case, the coefficients increase substantially to 0.9506, 0.9559 and 0.7627 for the surge, heave and pitch respectively. In some cases, the correlation is as high as 0.9882 (heave, case R02); this again highlights the capability of the model to estimate the investigated

TABLE 4.4: Correlation coefficients between the estimated forces and the experimental data for the wave height,  $\zeta$ , surge force,  $F_x$ , heave force,  $F_z$  and pitching moment,  $M_\theta$ .

Variable	Wave Case					
	R01	R02	R03	JS01	JS02	JS03
$\zeta$	0.9671	0.9423	0.8484	0.9403	0.9259	0.8585
$F_x$	0.925	0.9811	0.7207	0.9349	0.9661	0.9459
$F_z$	0.9205	0.9882	0.6567	0.9688	0.9707	0.9317
$M_\theta$	0.8728	0.8796	0.4570	0.6571	0.7637	0.6402

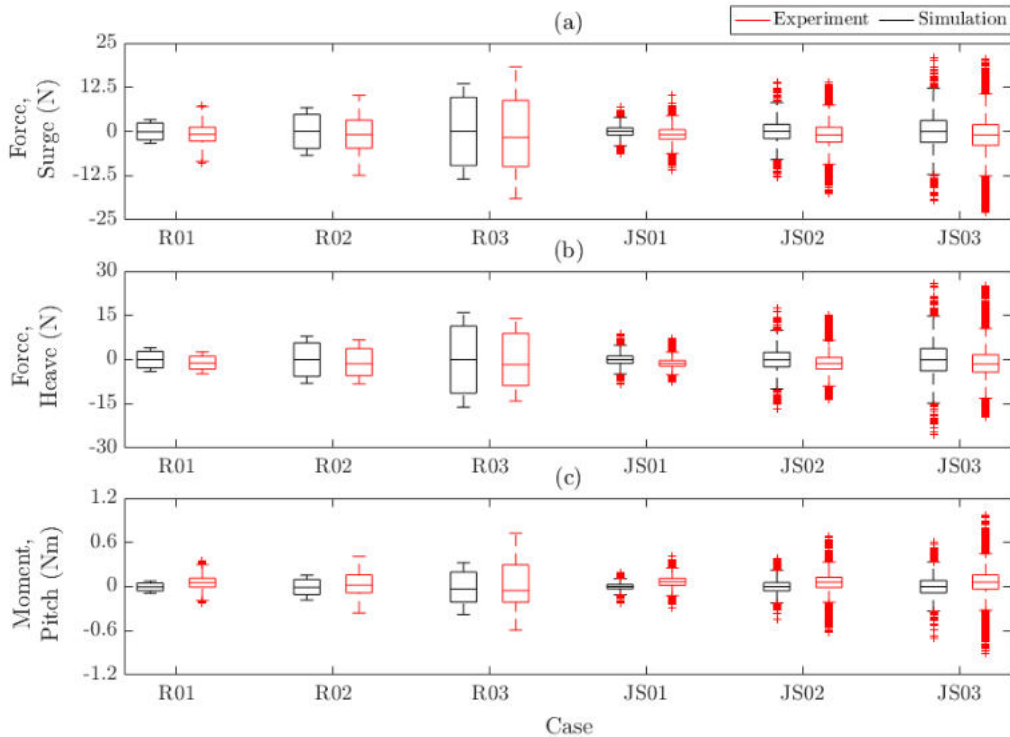


FIGURE 4.13: Distribution of the experimentally collected data compared to the simulated data obtained using the disturbance model.

parameters offering high confidence in its future usage for control purposes.

With reference to Fig. 4.13, the moment value, Fig. 4.13(c) displays the largest deviation in range between the datasets, correlating with the results displayed in Fig. 4.14 and suggesting the angular torques feature higher uncertainty. Due to the error analysis being a timewise point-to-point comparison there will be occasions where the lower-order model and the experimental data largely differ, which will produce a larger error range. This is demonstrated in Fig. 4.14, however the overall model output closely follows the unsteady behaviour of the systems with remarkable accuracy with the majority of the data falling within a small normalised error range. It can also be seen that the mean error is slightly positive which could indicate some experimental errors, supported by a slight constant y-offset witnessed in Fig. 4.9-4.12, particularly Fig. 4.10. For all cases, the normalised mean error recorded is  $< 0.35$  showing that the model is a fair general representation of the wave induced forces

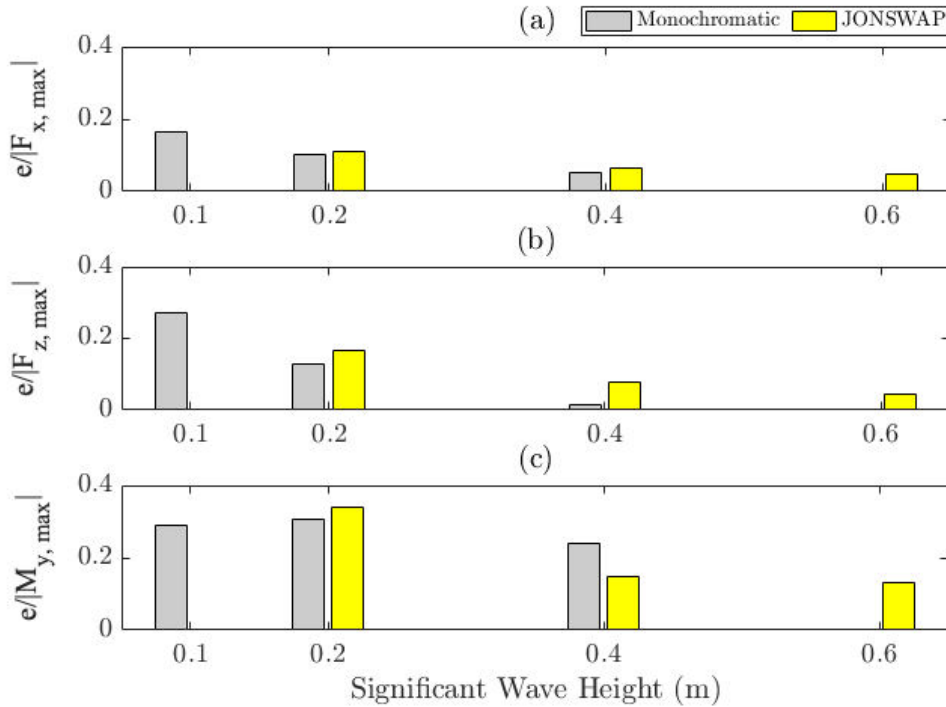


FIGURE 4.14: Normalised error relative to significant wave height for all cases.

and moments.

### Error Considerations

It is suspected that some of the errors recorded are attributed to modelling assumptions, i.e. only considering the effects arising from added mass and viscous damping. All other wave-body interaction forces are considered negligible; in reality (even though minor), there will still be an effect on the data recorded during the experiments. Furthermore, the MoCap documented very small rotations and translations, which are not reproduced in the LWT approach due to the assumption of a perfectly still geometry. The restraining cables were chosen as in-extensible, lightweight Dyneema rope, however there will still be some effect on the recorded moment due to it being impossible to hold the vehicle perfectly stationary. Additionally, it is possible that imperfect pre-tensioning or momentaneous misalignment of the supporting rig will cause discrepancies, as these could allow room for some unwanted small angular motions. This could explain why the comparison of recorded and simulated moments in Fig. 4.9(d)-4.12(d) do not match as closely as the linear forces, but the overall behaviour exhibited still shows good consistency. A clear factor effecting the correlation is that the emulated wave is not an identical match to the wave generated by the wave makers; the experimental case will feature imperfections and this will therefore cause deviations before any approximations are even considered. Throughout these experiments, it was assumed that the floor of the tank would have negligible impact on the wave formation, which in these cases was valid. However, for waves which

vary from a sinusoidal composition and display effects of non-linearity (i.e. are transitioning into breaking waves), the validity of these assumptions would have to be addressed.

Even when considering all of the above, the estimated forces validated in these experiments still present a good approximation relative to the degree of complexity and computational burden required. These estimations can not only provide an understanding of the dynamic response of a vehicle subject to surface wave disturbances, but can be exploited to assist in developing suitable control methodologies to effectively perform tasks such as station keeping in harsh environments. Using disturbance estimations explicitly within the control in a preview style manner, the disturbance rejection ability of the control can be largely improved and a broader range of operational conditions can be achieved.

#### 4.3.4 Concluding Remarks

In this section, a model for low-order disturbance estimations in three dimensions was presented based on the hydrodynamic properties of a commercially available ROV. The model considers the linear hydrodynamic forces as a simple summation of added mass and drag forces, whilst the angular torque is evaluated as a piece-wise integration along the vehicle plane coincident to the propagation direction of the wave. An experimental study was also presented which validated the proposed model and showed it was capable of producing relatively accurate disturbance estimations, particularly when considering the level of approximations that are adopted. In conjunction with this, the model was executed in a time frame applicable to real-time scenarios; this is a key factor of the analysis when considering the proposed application is to provide disturbance estimations for use within a predictive control architecture. A 20s time history is analysed in  $\approx 5\text{s}$  using MATLAB on a laptop with a 1.6GHz Dual-Core Intel Core i5 processor, which would be substantially improved when translating into a more applicable lower level coding language. This strengthens the case for use in dynamic control applications, with these findings forming the foundations of the work detailed in Chapter 5, in which they are exploited through this low-order model directly within a predictive control framework for disturbance mitigation.

As discussed above, there exist some sources of error which require careful consideration during deployment, however these typically relate to the experimental apparatus that was utilised and it would be interesting to investigate the effect on the estimations when the vehicle is allowed to freely move under the influence of the waves. Due to the formulation adopted it is expected this would have little detrimental effect, as only slight modification to consider relative motions would be required. Nevertheless, it would be an interesting avenue to explore and one that may be considered in future, provided a reasonable experimental method of performing this analysis can be formulated.

## 4.4 Simulation Study: Feedback Controlled Station Keeping

Given the scope of this chapter, an extensive simulation study was undertaken to collect a large data-set for analysing the vehicle behaviour under a wide variety of different conditions. First and foremost, this provides a comprehensive picture of how a standard feedback controller performs under the influence of significant and varying wave disturbances; critically, this immediately demonstrates under what conditions more complex and higher performing control is required. Secondly, this accumulated data can be used as a reference of how the vehicle is expected to behave when developing analytical models, as is discussed in Section 4.5, allowing informed adjustments to be made in line with the underlying dynamical principles of the wave-body interactions occurring. Considering these two points, the aim of this section was to quantify the performance of Proportional-Derivative (PD) control for station keeping an ROV, encapsulating the broadest available range of realistic environmental conditions and evaluating the maximum positional error the ROV is expected to experience, before developing general analytically derived scaling laws in accordance. This section details the findings of these simulated cases with regards to station keeping performance and the full derivation of the associated analytical model.

### 4.4.1 Parameter Identification

The analysis throughout this section relies heavily on the availability of the hydrodynamic properties of the vehicle. These can be obtained by various different experimental procedures such as towing tank tests or open water self-propelled tests [307], but as the BlueROV2 Heavy is a relatively widely used experimental platform there were several works which provided a large portion of these parameters [46, 165, 308]. The available parameters concerned the centre of gravity to centre of buoyancy vector, along with the major parameters of added mass and hydrodynamic drag (the diagonal elements), with the typical assumption being that the vehicle can be considered to be symmetrical in all planes. For the BlueROV2 Heavy, this assumption is stretched somewhat owing to a reasonable asymmetry present between the top and bottom half of the vehicle, introducing a coupling between the surge and pitch.

To avoid any unwanted disparities during the analytical modelling, the additional elements of added mass ( $X_{\dot{q}}$ ,  $M_{\dot{u}}$ ) were estimated using WAMIT [309], a well known software tool which adopts potential flow theory for estimating the hydrodynamic properties of offshore structures in waves. Only these parameters were required due to the Assumption 3.2.3, however it is worth stating that the additional parameters,  $Y_{\dot{p}}$  and  $K_{\dot{v}}$ , were also evaluated following the standard procedure in the WAMIT manual, mainly for convenience when extending this work into higher dimensions.

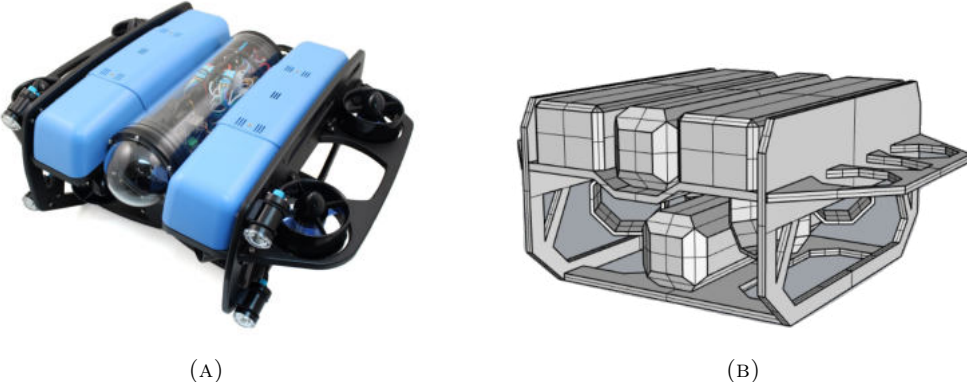


FIGURE 4.15: The (a) BlueROV2 Heavy and the (b) simplified BlueROV2 Heavy model, designed within Rhinoceros 3D for determination of added mass coefficients in WAMIT.

Given that the proposition here is to evaluate these metrics from an analytical standpoint, the requirement for experimental studies was undesirable and would be a major drawback to adopting this framework, hence WAMIT was used as a tool to validate the values sourced from literature and obtain missing parameters.

As the CAD model provided by Blue Robotics is a fully complete version of all components of the BlueROV2 Heavy (including screws, seals etc.), a simplified model was constructed in Rhinoceros 3D to avoid complications during WAMIT execution, shown in Fig. 4.15b(b). WAMIT operates by considering the input shape as a set of geometric panels, therefore this stage was necessary to obtain realistic results and mitigate processing failures. Similarly and as noted in [310], WAMIT can often output asymmetric results as a by product of this process, even when it is well known that the added-mass matrix should be symmetric. This has been noted as an issue with WAMIT which can even occur for simple shapes such as cuboids. Therefore, the resulting matrix was symmetrised according to the methodology in [310] using the provided processing script in Appendix B.1; the returned values are non-dimensionalised and in the form  $A_{ij}$  where  $i$  and  $j$  refer to the position within the added mass matrix. To obtain the vehicle specific values, these are scaled according to:

$$\bar{\Lambda}_{ij} = \frac{\Lambda_{ij}}{\rho_f L_k} \quad (4.12)$$

where  $k$  varies according to the index as stated in WAMIT user manual [309]. The scaled output values of this script are given below as Eq. 4.13. The values returned by WAMIT after processing aligned relatively closely with those reported by other works [46, 165, 308], therefore the sourced values were deemed sufficient. The major values (diagonal values) obtained from WAMIT were not adopted due to the use of a simplified model, thus were only used as a validation that other works had reported reasonable results and were not largely inaccurate. However, the additional values unavailable within literature relating to cross-coupled terms were exploited to simulate this influence on the vehicle dynamics.

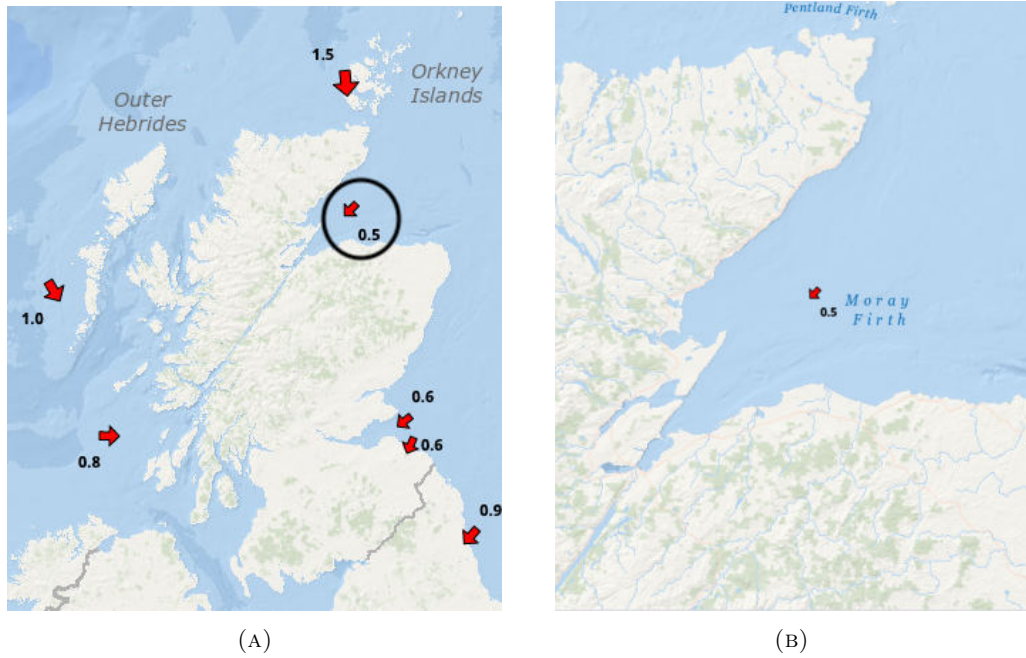


FIGURE 4.16: Map showing the (a) various locations of buoys around Scotland, circling the buoy selected for this analysis and (b) an enlarged map of the Moray Firth buoy location.

$$M_A = \begin{bmatrix} 6.72 & 0 & 0.66 & 0 & -0.67 & 0 \\ 0 & 21.27 & 0 & -0.20 & 0 & 0.03 \\ 0.66 & 0 & 22.79 & 0 & -0.53 & 0 \\ 0 & -0.20 & 0 & 0.33 & 0 & -0.04 \\ -0.67 & 0 & -0.53 & 0 & 0.36 & 0 \\ 0 & 0.03 & 0 & -0.04 & 0 & 0.26 \end{bmatrix} \quad (4.13)$$

#### 4.4.2 Scenario Configuration

Obtaining positional data to develop and compare against the analytically derived model required simulating an operational environment, aligning as closely as possible with conditions the vehicle may encounter. To this end, real-world data was sourced which spanned the testing parameters (i.e. significant wave height and spectral peak period) over a representative range of climate conditions. This ensures a clear representation of vehicle performance in a realistic range of scenarios is examined and the model is applicable to a broader range of conditions, rather than being constrained to an idealised set. Wave data was obtained from the online repository of the Centre for Environment Fisheries and Aquaculture Science (Cefas). The data was collected using a wave buoy situated within the Moray Firth, an inlet off the coast of Inverness, Scotland. The location of the buoy is shown in Fig. 4.16, where  $d = 54\text{m}$ ; the majority of offshore wind farms are typically located in areas of this depth or below [311, 312] and an offshore wind development is currently under construction at this

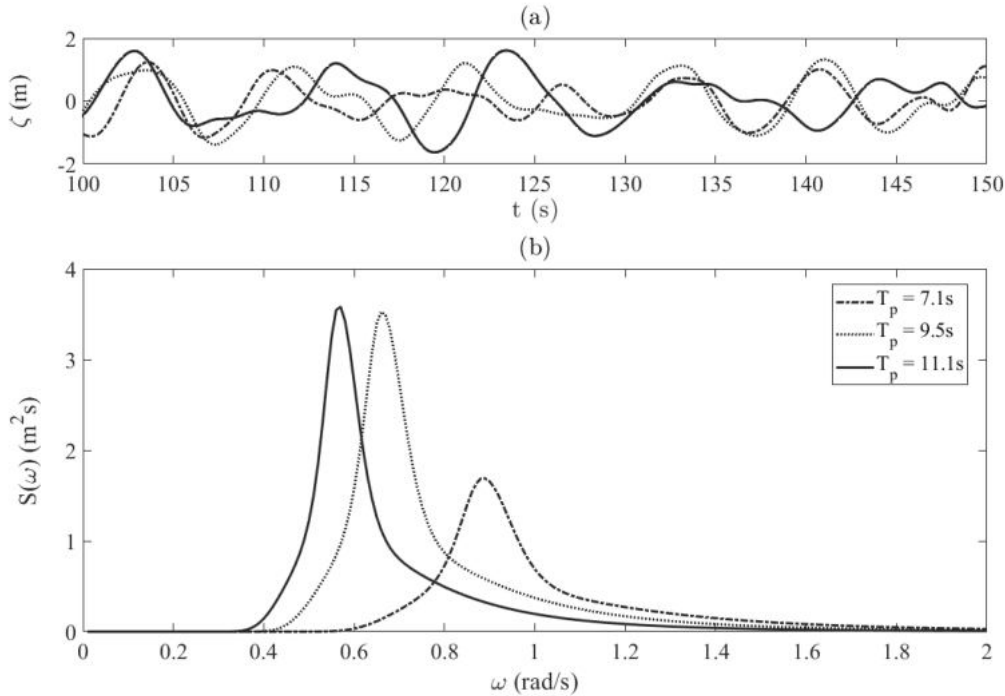


FIGURE 4.17: Tested wave spectra, showing (a) a temporal segment of the 3 different waves and (b) the frequency spectrum for the 3 different waves.

location [313], thus making the dataset suitable for simulating a typical inspection/- maintenance task.

To provide a broad understanding of how different wave parameters affect vehicle behaviour, three different spectra were selected with  $T_p = 5.4\text{s}$ ,  $T_p = 8\text{s}$  and  $T_p = 11.1\text{s}$ . For each of the spectra, tests were performed across a range of significant wave heights. The non-dimensional wave height was varied within the range of  $0.5 \leq H_s/L \leq 7$  (where  $L = 0.457\text{m}$  represents the reference dimension of the BlueROV2 Heavy). With these initial parameters, a 300s time history was reconstructed by application of the theory detailed in Section 3.1.2. A section of these time histories is depicted in Fig. 4.17(a) alongside the frequency spectra in Fig. 4.17(b) formed using the frequency components provided via the database. Subsequently, the loads acting on the vehicle were estimated via Eq. 4.4 and implemented within the vehicle dynamics via Eq. 3.31, allowing the response of the vehicle to be determined by solving via a fourth order Runge-Kutta method. By spanning over significant wave height, peak period and depth, these test cases cover a wide range of sea states and operational conditions. For all non-dimensional wave height analysis, the unique frequency components of the selected 300s temporal segment were scaled in magnitude consistently to retain the wave formation; the measured displacement is therefore a direct product of the varying wave height. The vehicle response was evaluated across a portion of the water column spanning the range of  $0.05 \leq z/d \leq 0.95$ . In terms of how realistic these conditions are, Fig. 4.18 displays the recorded data and associated mean values spanning the time period 01 Nov. 2019 - 01 Nov. 2020. This

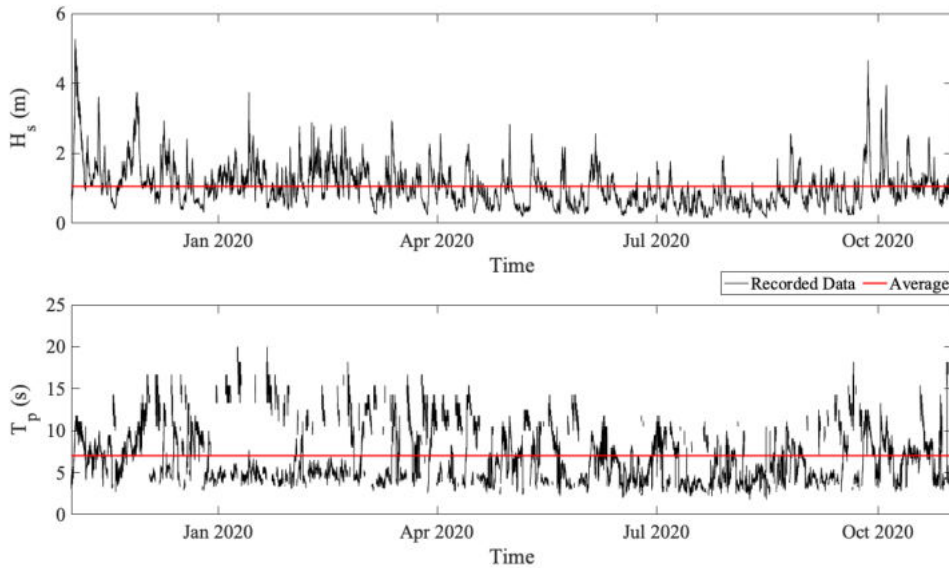


FIGURE 4.18: Recorded data and associated mean values from the Moray Firth WaveNet Site spanning the time period 01 Nov. 2019 - 01 Nov. 2020.

TABLE 4.5: Control parameters for the ROV during the station keeping mission.

Parameter	Nomenclature	Value
Proportional Gain	$\mathbf{K}_p$	diag(1.2,1.2,0.5)
Derivative Gain	$\mathbf{K}_d$	diag(3,3,1)

data supports the selected range of test cases being representative of conditions the ROV could encounter, allowing for a fair impression of controller performance to be achieved. The controller was specified as a typical feedback PD control law according to:

$$\boldsymbol{\mu}_{PD} = \mathbf{K}_p \mathbf{e} + \mathbf{K}_d \dot{\mathbf{e}} \quad (4.14)$$

where  $\mathbf{e}$ ,  $\mathbf{K}_p$  and  $\mathbf{K}_d$  are the positional error between the reference set-point and current vehicle state, the proportional gain and the derivative gain respectively. These parameters are defined numerically in Table 4.5 and were tuned heuristically.

#### 4.4.3 Simulation Results

For the spectrum of cases given above, the maximum magnitude of positional error which occurred due to the presence of surface waves is reported in Fig. 4.19 whilst the vehicle attempted to perform PD-controlled station keeping. The results presented focus on shallower depths and larger wave heights as these scenarios are of higher interest with regards to controller performance. More precisely, the data shown encompasses all cases where the positional error in both surge and heave exceeded 0.05m for all spectra, ranging up to the maximum wave height tested.

In terms of control performance, for the extreme test case examined with  $H_s/L = 7$ ,  $z/d = 0.05$  which refers to  $H_s = 3.2\text{m}$ ,  $z = 2.7\text{m}$ , shows positional errors  $> 0.36\text{m}$

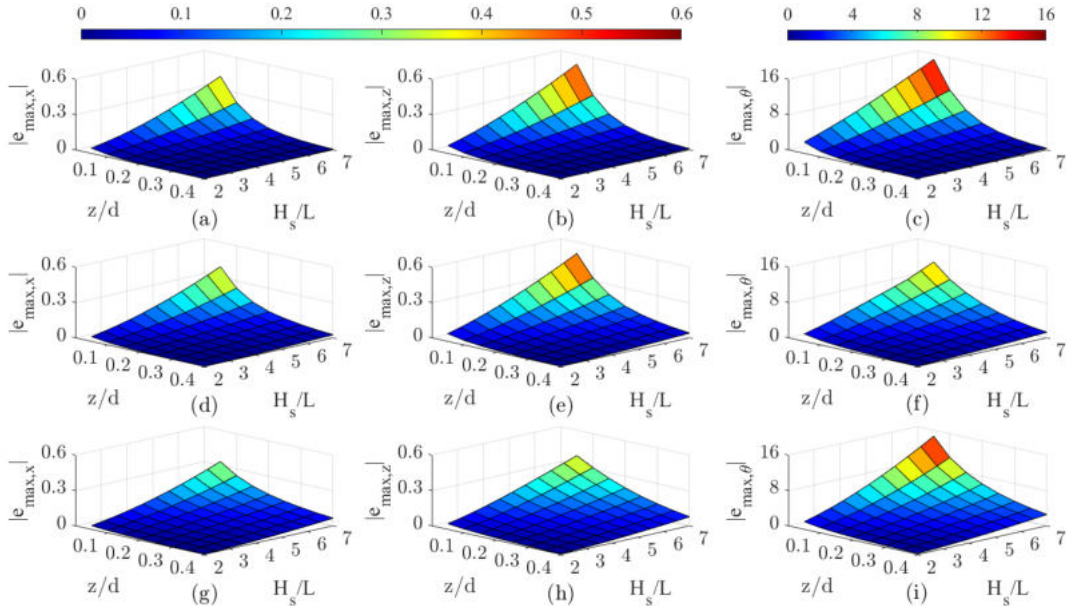


FIGURE 4.19: Vehicle maximum displacement from the desired station keeping position while subject to a wave with (a)-(c)  $T_p = 5.4\text{s}$ , (d)-(f)  $T_p = 8\text{s}$  and (g)-(i)  $T_p = 11.1\text{s}$  as a function of non-dimensional wave height  $H_s/L$  and operational depth  $z/d$ . Results depicted refer to maximum positional error in the (a), (d), (g) surge, (b), (e), (h) heave and (c), (f), (i) pitch but for clarity the plots are restricted to only show the cases closer to the surface where error is significant

for surge and heave and  $> 9^\circ$  for the pitch were recorded across all spectra. For station keeping at close quarters to submerged structures this error would be considered unsafe, due to its likelihood of causing collisions or exerting hazardous torques on a robot arm during manipulation. Inspecting the data from the perspective of a safe tolerance, if we consider an acceptable error margin to be 0.1m and assume this must be maintained throughout the period of operation, for all spectra and all operating depths this can only be attained in both surge and heave when  $H_s/L \approx 2.4$ , corresponding to  $H_s \approx 1.1\text{m}$ . This wave height is frequently exceeded in areas where marine renewable devices are located, as supported by the data in Fig. 4.18; 40% of the recorded wave heights exceed 1.1m and the average wave height across the year is 1.06m. This immediately highlights that for a significant range of operating conditions a more sophisticated control strategy is necessary when precise station keeping is required at shallow depths. For the largest wave height tested, 3.2m, the same error margin can only be satisfied for all spectra when the vehicle's operational depth exceeds 20m, again showing how the range of operating conditions is limited by the performance of the controller. It is worth highlighting that this value varies depending on the peak period of the spectra, as the magnitude of particle motions decay exponentially with depth. For the spectra with  $T_p = 5.4\text{s}$ , the error margin of 0.1m for the same wave height could be satisfied at a depth of  $\approx 10.5\text{m}$ , which would still restrict operations near the free surface. Similarly, for the spectra with  $T_p = 8\text{s}$  the operating depth required to satisfy the error margin was  $\approx 18\text{m}$ .

#### 4.4.4 Concluding Remarks

From these initial findings when utilising feedback driven control, it is evident that ocean wave disturbances present a significant hindrance to the station keeping ability of the vehicle. Not only are the lateral motions affected largely by wave loading, but the rotational pitch motion of the vehicle is also seen to undergo significant excitation. In turn this has a detrimental effect on feedback control, owing to the constrained knowledge of the system dynamics (a PD controller is completely unaware of wave-disturbances and how the vehicle responds to control inputs for example). Alternatively, the process of performing the extensive simulation study took considerable time when analysing a large breadth of cases; the entire methodology was also rather arduous. This leads into the focus of the following section, which aims to reduce this process to a set of simple analytical expressions for obtaining critical metrics (namely the anticipated maximum state error) which define a safe operational region for the vehicle.

### 4.5 Generalised Analytical Modelling

In general, the formulation in the previous sections is anticipated to scale analytically due to the fact it is largely based on the vehicle hydrodynamic and geometric parameters, which will vary accordingly depending on the vehicle structure. The typical approach to then evaluate control performance is to undertake an extensive simulation study under a large and broad range of different conditions, aiming to determine boundary conditions for safe operational environments, similar to the process undertaken in the previous section. Given the nature of the disturbances considered in this thesis, the question was posed as to whether these low order analytical approximations can be extended to also consider the control strategy. In essence posing the question: is it possible to evaluate the suitability and station keeping performance of a traditional feedback control method and whether its sufficiency without resorting to recursive numerical testing and experiments?

To achieve this, it becomes necessary to derive scaling laws that provide an insight to key performance metrics. In this thesis the focus is purely on station keeping under the influence of wave-induced disturbances. Scaling laws of this nature define a metric for immediate estimation of the positional error of a vehicle, offering a valuable tool for vehicle end-users to determine mission feasibility with feedback control. Typically, the standard metrics which are of the greatest concern are the positional RMSE of the vehicle with reference to a goal pose and the maximum positional error the vehicle experiences. The former presents a general overview of how the vehicle performs over an extended time period, but it could be argued that the latter is often of greater importance. In terms of determining a safe operational range, this is the

critical parameter of interest to avoid collisions with nearby structures when in the immediate vicinity. Ultimately, this determines the suitability of the control.

With reference to the above, this section presents the derivation of a proposed simplified analytical model for convenient (but accurate) estimation of maximum station keeping positional error when subject to a waveform with a particular significant height and peak period. This can be useful when an initial estimation of performance is desired without the requirement to program and perform a range of full dynamic simulations. The derived model is compared to the results obtained when performing numerically modelled simulations, showing that it is possible to obtain accurate estimations using only basic geometric vehicle parameters and statistical wave parameters. The derived scaling laws are tested when adopting a standard PD feedback controller, demonstrating that such metrics can be deployed for a well-known control strategy, allowing an informed decision to be made on architecture suitability. The overall aim of this additional section of this chapter is to propose an easily implementable method to obtain metrics which can act as a point of comparison between control strategies.

#### 4.5.1 Analytical Model Derivation

The results presented in Section 4.4.3 provide a basis for the inference of general scaling laws of the positional error of feedback-controlled ROVs in waves. As this is a preliminary attempt to develop scaling laws applicable to feedback controlled vehicles, several assumptions were adopted to simplify the complexity of the model. This allowed a direct derivation to be attained with the aim of expansion in future work under relaxed assumptions.

**Assumption 4.5.1** *The vehicle dynamics are restricted to only 2DoF, namely the surge and heave and effects from the vehicle pitch are neglected in the analytical model. The contribution from the rotational excitation is therefore considered approximately null. As the vehicle is self-righting, this was deemed appropriate.*

$$\theta, q, \dot{q} \approx 0 \quad (4.15)$$

**Assumption 4.5.2** *Disturbances to the vehicle state are a pure product of wave-induced effects and comprise of quadratic hydrodynamic drag and added mass forces, owing to the simulated wave field being modelled according to LWT. Additional effects arising from fluid-body wave interactions (such as the Froude-Krylov force) are considered negligible and are disregarded.*

$$\begin{bmatrix} X_E \\ Z_E \end{bmatrix} = \begin{bmatrix} X_{\dot{u}} \dot{\nu}_{p,x} + X_{u|u|} \nu_{r,x} \\ Z_{\dot{w}} \dot{\nu}_{p,z} + Z_{w|w|} \nu_{r,z} \end{bmatrix} \quad (4.16)$$

The key term of this analysis concerns the maximum absolute displacement,  $|e_{max}|$ , that a vehicle experiences when subjected to a particular sea state, defined by a statistically representative significant wave height,  $H_s$ , and peak period,  $T_p$ . Similarly, the vehicle actuation is generated by a classic feedback-based control in the form of a PD controller. The reason for focusing on this parameter is that it ultimately can be used to define a minimum permissible range where feedback based control can still provide performance that is deemed safe. Outwith these boundaries, an alternative form of control is required to effectively counter wave-induced disturbances.

Broadly speaking, the dynamic behaviour can be recast and formulated as a generalised force balance function, whereby:

$$|e_{max}| \sim \frac{\tilde{F}}{m} \tilde{t}^2 \quad (4.17)$$

where  $\tilde{F} = F_d + F_a + F_t$ , with  $F_d$ ,  $F_a$  and  $F_t$  respectively representing the viscous, inertial and thrust forces experienced by the vehicle and  $\tilde{t}$  a characteristic time constant of the vehicle response to perturbation. The term  $m = m_d + m_a$  is the effective inertia of the vehicle, where  $m_d$  and  $m_a$  are used to describe the dry mass and added inertia here in generalised analytical form; expanding leads to approximated definitions of  $m_d \sim \rho_f L^3$  and  $m_a \sim \rho_f \pi L^3$  for a vehicle with characteristic length scale  $L$ . Disregarding hydrodynamic coupling, the drag and added-mass forces along the surge can be written as,

$$F_d = \frac{1}{2} \rho_f L^2 C_D \nu_p^2 \quad (4.18)$$

$$F_a = m_a \dot{\nu}_p \quad (4.19)$$

These forms are applicable to both surge and heave directions, with the variation being related to the hydrodynamic properties and the evaluation of fluid velocity and acceleration; Eq. 3.15-3.16.

By further assuming  $d \rightarrow \infty$  and the particle motions are approximately spherical beneath the surface (i.e. surge and heave components follow analogous magnitude relationships distinguished by a phase difference) ensures that the hyperbolic term in Eq. 3.15-3.16 simplifies to  $\frac{\cosh k(z+d)}{\cosh(kd)}, \frac{\sinh k(z+d)}{\cosh(kd)} \sim e^{kz}$ . Also,  $\cos(\cdot), \sin(\cdot) \sim 1$  represents a reliable upper bound for the RHS term. Given the context of this analysis is tackling wave-induced disturbances, it is reasonable to assume operation at close proximity with the free surface where disturbances are higher; this reduces the exponential relation to  $e^{kz} \sim (1+kz)$  for  $z \rightarrow 0$ . Considering these additional assumptions allows the fluid motions  $\nu_p$  and  $\dot{\nu}_p$  to be recast as,

$$\nu_p(z) \sim \frac{H_s \omega_p}{2} (1 + k_p z) \quad (4.20)$$

$$\dot{\nu}_p(z) \sim \frac{H_s \omega_p^2}{2} (1 + k_p z) \quad (4.21)$$

where  $k_p$  and  $\omega_p$  refer to the wave number and circular frequency of the peak spectral component (referred to as peak wave number and peak frequency for the remainder of this paper). This enables the inference of a simple scaling for inertial and viscous forces of a stationary vehicle subject to the specified wave train uniquely based on the wave parameters, vehicle's body length and depth:

$$F_d \sim \frac{1}{8} \rho_f C_D L^2 H_s^2 \omega_p^2 (1 + 2k_p z + k_p^2 z^2) \quad (4.22)$$

$$F_a \sim \frac{1}{2} m_a H_s \omega_p^2 (1 + k_p z) \quad (4.23)$$

The other force that must be considered in this analysis arises due to activation of the thrusters during corrective control action,  $F_t$ , which are generated by a PD controller in this formulation. Unlike the hydrodynamic forces, the thrust force is calculated according to the vehicle displacement as the controller actively attempts to maintain a steady vehicle position. Based on a PD controller, it is proposed the force produced by the thrusters at the point of maximum displacement can be approximated to:

$$F_t = \tau_{max} \mu = \tau_{max} (K_p e_{max} + K_d \dot{e}_{max}) \quad (4.24)$$

where  $\dot{e}_{max} \sim e_{max}/\tilde{t}$  and  $K_p, K_d$  are a set of PD gains.

An estimate for the characteristic timescale,  $\tilde{t}$ , of the vehicle's response when subject to a wave disturbance of arbitrary amplitude  $A$  and frequency  $\omega_p = T_p^{-1}$  and affected by a proportional feedback control  $K_p$  is the remaining parameter to be inferred. Considering the dynamic relation of the system, a suitable approximation is to consider a harmonically forced, undamped oscillator  $m\ddot{x} + K_p x = A \sin(t/T_p)$ . The estimation of the timescale neglects viscous effects, limiting the hydrodynamic forcing to inertial, i.e. added-mass, terms. This assumption implicitly restricts the validity of this analysis to an inertia-dominated regime, which for bluff bodies subject to waves is characterized by Keulegan-Carpenter (KC) numbers,  $KC = T_p \bar{u}_p / L < 8$  [314, 298]. By imposing initial conditions  $x(t=0) = 0$  and  $\dot{x}(t=0) = 0$ , this yields an expression for the vehicle velocity,

$$\dot{x} = \omega_n \left( -\frac{\omega_p}{\omega_n} \frac{A}{\omega_n^2 - \omega_p^2} \right) \cos(\omega_n t) + \omega_p \frac{A}{\omega_n^2 - \omega_p^2} \cos(\omega_p t) \quad (4.25)$$

which allows inference of the time at which the vehicle comes to a halt after the initial wave perturbation, by solving for  $\dot{x}(t) = 0$ . This simplifies Eq. 4.25 to,

$$t|_{\dot{x}=0} \equiv \tilde{t} = \frac{2\pi}{\omega_n + \omega_p} \quad (4.26)$$

which indicates that for long waves, the characteristic vehicle response is dominated

by the vehicle's own natural frequency, i.e.  $\tilde{t} \sim 2\pi\omega_n^{-1}$ . Also,  $\omega_n$  is a direction-dependent, vehicle natural frequency where the control tuning acts as a stiffness-equivalent term,  $\omega_n = \sqrt{\tau_{max}K_p/m}$ .

By substitution and rearrangement to isolate the displacement, Eq. 4.17 can be explicitly described as:

$$|e_{max}| \sim \frac{(F_d + F_a)\tilde{t}^2}{m + (K_p\tilde{t} + K_d)T_{max}\tilde{t}} \quad (4.27)$$

This simplistic analytical equation can be exploited to provide a first order estimate of station keeping performance in waves under PD control, where the only knowledge required are the dominant wave parameters of the spectrum and the vehicle characteristics. If the proportional feedback term is retained as the leading control input, Eq. 4.27 can be further simplified to distinguish between the strictly inertia-dominated flow regime, i.e. for  $KC \ll 8$ , where,

$$|e_{max}| \sim \frac{m_a H_s \omega_p^2}{m \omega_n^2 + K_p \tau_{max}}$$

and the drag-dominated regime, where,

$$|e_{max}| \sim \frac{\rho_f C_D L^2 H_s^2}{m \omega_n^2 + K_p \tau_{max}}$$

These derived expressions are analysed below with respect to the data collected throughout the study in Section 4.4, providing a direct comparison of model suitability.

### 4.5.2 Analytical Model Comparison

As alluded to during the derivation, the interest here is on the vehicle performance near the free surface and therefore all results shown in Fig. 4.20- 4.21 correspond to the lowest depth from our previous analysis,  $z = 2.7\text{m}$  where  $z/d = 0.05$  ( $d = 54\text{m}$ ). Likewise, consistency was retained with regards to the tested spectra with varying peak periods of 5.4s, 8s and 11.1s which correspond to subplots (a)-(c) respectively in each figure. As shown in the different plots and for the majority of significant wave heights in all cases, the model is capable of replicating the maximum displacement the vehicle will exhibit with remarkable accuracy given the level of approximations employed. The lowest RMSE exhibited for surge and heave were 0.029m and 0.025m respectively, whilst the largest deviations were 0.059m and 0.052m. When considering how drastically the level of computation required has been reduced, an RMSE of  $< 6\text{cm}$  across all cases is a good result and could be utilised as a first approximation when evaluating different control schemes or safe operational constraints.

The largest absolute deviation between the model and the simulation was 0.103m and 0.132m for the surge and heave respectively. Both of these values relate to the

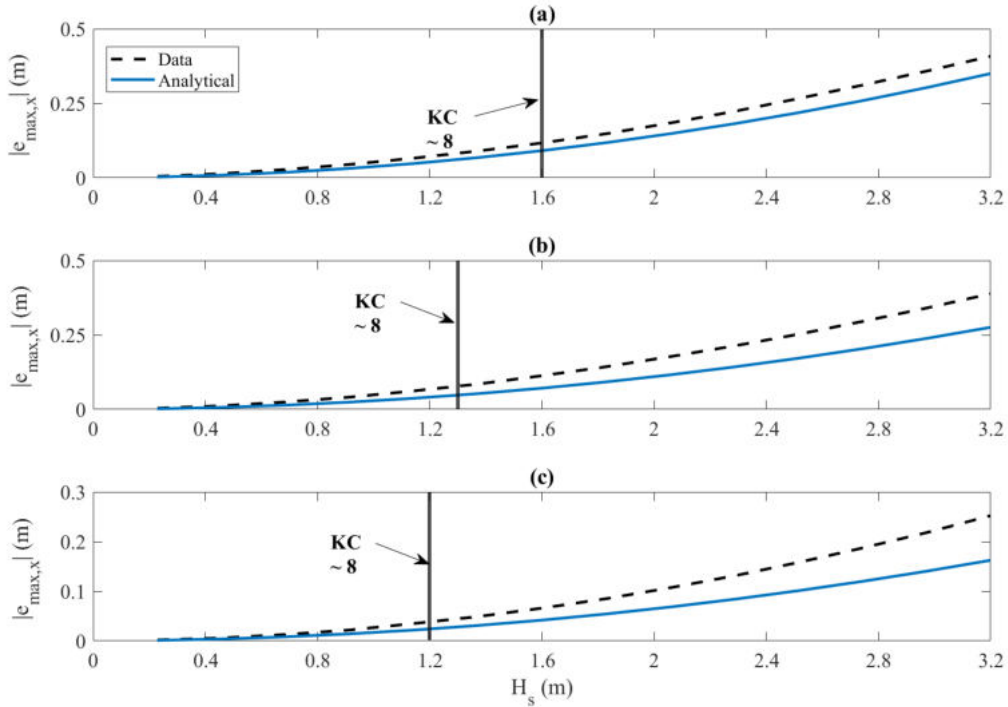


FIGURE 4.20: Analytical model results for the surge when considering a wave with a peak spectral period of (a)  $T_p = 5.4\text{s}$ , (b)  $T_p = 8\text{s}$  and (c)  $T_p = 11.1\text{s}$ .

test case with the largest significant wave height, showing that the magnitude of disturbance has an effect on the performance of the model, particularly in the surge where we see the model begin to diverge progressively as the wave height increases. This is likely due to the vehicle pitching more aggressively as wave height increases; our approximated model doesn't account for this motion and this can therefore be seen in the results obtained. Another key observation (as labelled) is that for KC numbers greater than 8 the model begins to diverge in most cases, particularly for the surge;  $KC \approx 8$  defines the boundary at which drag effects become more dominant than inertial effects [298]. Quite simply, this indicates that the model can fairly accurately represent behaviour in inertia dominated regimes, however struggles past this limit; in some instances, for example Fig. 4.20(a) and Fig. 4.21(a), the model almost exactly replicate the simulated results. Both of these cases refer to the wave case with  $T_p = 5.4\text{s}$ , potentially indicating the model possessing greater suitability for wave spectra with greater frequency components. In this cases the fluid particles will follow a more spherical path compared to longer periods, which aligns with the modelling assumptions and thus it is a fair conclusion this is a key factor affecting the model accuracy.

## 4.6 Conclusions

Within this chapter, an extensive parametric study of the wave-vehicle interactions has been undertaken, analysing and experimentally validating a low-order disturbance

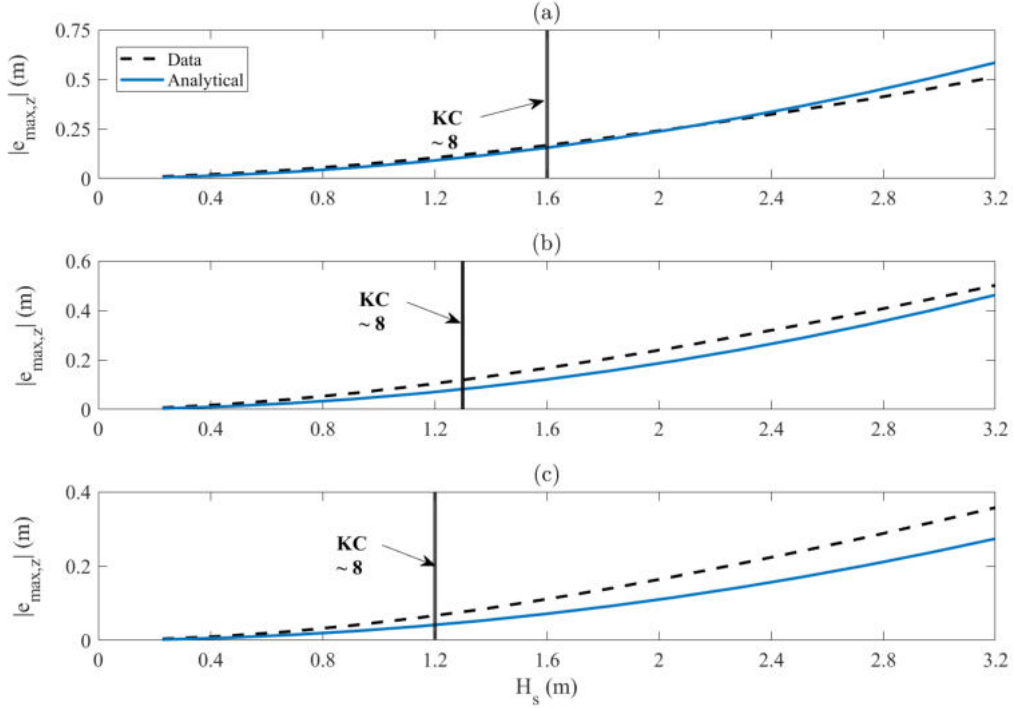


FIGURE 4.21: Analytical model results for the heave when considering a wave with a peak spectral period of (a)  $T_p = 5.4\text{s}$ , (b)  $T_p = 8\text{s}$  and (c)  $T_p = 11.1\text{s}$ .

model for the wave-induced loading on an ROV in Section 4.2-4.3. Firstly, the wave loading model was proven to produce accurate results for both linear and angular forces/torques across a variety of wave conditions; this forms a basis to perform fast and computationally inexpensive predictions, potentially suitable for use within real-time predictive control architectures. Subsequent to these findings and applying the model in simulation, an extensive feedback controlled study confirmed that for waves with  $H_s > 1.1\text{m}$ , alternative forms of control are required to sufficiently limit vehicle pose error to an accuracy range of  $0.1\text{m}$ . Given that consistent conclusions were drawn for three different wave spectra, the inference here is that knowledge of the wave profile at specific time intervals is critical to be able to effectively mitigate wave-loading effects.

Furthermore, a simplified low-order analytical model was derived and explored for estimation of maximum vehicle displacement under typical feedback control in Section 4.5, manipulating only well known and easily attainable key spectral wave parameters to produce a prediction of absolute maximum vehicle displacement. The model performed well in inertia dominated regimes but failed to capture the displacement accurately when the KC number exceeded this threshold. Although not applicable to all conditions, these findings still show potential that a simple analytical scaling law can be derived to estimate key parameters during control pre-assessment.

To summarise, these preliminary results drive the research aims of the following chapter, aiming to develop a control framework inclusive of predicted wave disturbances to mitigate vehicle pose error. Within Chapter 5, a NMPC is coupled with

a DSWP algorithm to form a short horizon temporal profile of the inbound wave, resulting in greater accuracy station keeping and trajectory tracking.



## Chapter 5

# Nonlinear Model Predictive Dynamic Positioning Exploiting Wave Disturbance Preview

### 5.1 Introduction

Having confirmed the accuracy with which time-varying wave-induced hydrodynamics loads can be estimated with a low-order dynamic model, this chapter shifts the focus to the feasibility of coupling these disturbance predictions with MPC to perform accurate station keeping of a small-scale ROV. The control background will be introduced, followed by the prediction algorithm adopted to estimate the future wave-induced disturbances based exclusively on a temporal measurement of wave elevation. An experimental study is used to validate the proposed prediction algorithm, highlighting key factors affecting forecasting performance and the overall applicability for control. Lastly, the results of a simulation study implementing the proposed methodology is presented and discussed, inclusive of a broad range of tests analysing the effect of different sources of noise and uncertainty on system performance.

This chapter presents the main contribution of this thesis in the form of a proposed end-to-end framework for predictive control of an underwater vehicle, encapsulating both the wave-induced disturbance prediction aspect and the control method postulated upon these predictions. Concluding remarks are finally given which highlight the current limitations of the work and the next steps required to extend and expand the current progress.

## 5.2 Deterministic Sea Wave Prediction

This section details the algorithm adopted for forecasting the future temporal evolution of the wave at the vehicle location based on distant measurements, namely DSWP. The theoretical background is presented, followed by the considerations required to determine applicability of the method with regards to obtaining a valid prediction of the oncoming wave. Following this, the transformation from future wave elevation to wave-induced load estimation is given, evaluating the numerical process for obtaining external forces and moments acting on the vehicle (with reference to the work undertaken in Chapter 4). For clarity, the load estimation is not explicitly part of the DSWP algorithm, but remains part of the prediction process to provide a disturbance input for the MPC optimisation, therefore the two are considered in tandem. Finally, an experimental study is presented to validate the accuracy of the DSWP algorithm. Concluding remarks are then given with reference to the applicability of this forecasting method in the context of active control for wave disturbance rejection.

### 5.2.1 Principles of Deterministic Sea Wave Prediction

As summarised nicely in [265], "*DSWP is the ability to predict the actual detailed shape of the sea surface, sufficiently far ahead in time to have practical marine applications*". This is the underlying motivation behind investigating DSWP for dynamic control of an underwater vehicle; to be used in a control scheme, a detailed description of the ocean environment in the immediate vehicle vicinity is required. Typically, wave forecasting methods and techniques focus on much longer time scales for purposes such as ship navigation or offshore renewable energy optimization; DSWP handles predictions in the order of seconds or metres (depending on whether the prediction is being made relative to time or space), which is much more suitable for dynamic control. Particularly for an MPC architecture, the prediction horizon for the control optimisation is at most a few seconds so it is undesirable to concern large areas, as an accurate picture of a precise location is what is required.

To give an overview of how the DSWP algorithm is formulated, the flow chart in Figure 5.1 is provided [266]. In its basic form, two distinct points are considered: a measurement point and a prediction point. In the first instance, the wave elevation is recorded at the measurement point for a prescribed period of time whilst undergoing techniques such as filtering to reduce the effects of noise and similar on the sensor readings. Subsequently, these measurements are used to estimate the wave spectrum, propagate this to the prediction point and form an estimation of the wave elevation profile. As the whole basis of the procedure is deterministic, a large importance is placed on the initial wave measurements and the level of pre-processing/filtering performed to remove noise artefacts in the collected data. However, the key advantage of using this technique lie in the fact that you can operate with a sliding window that

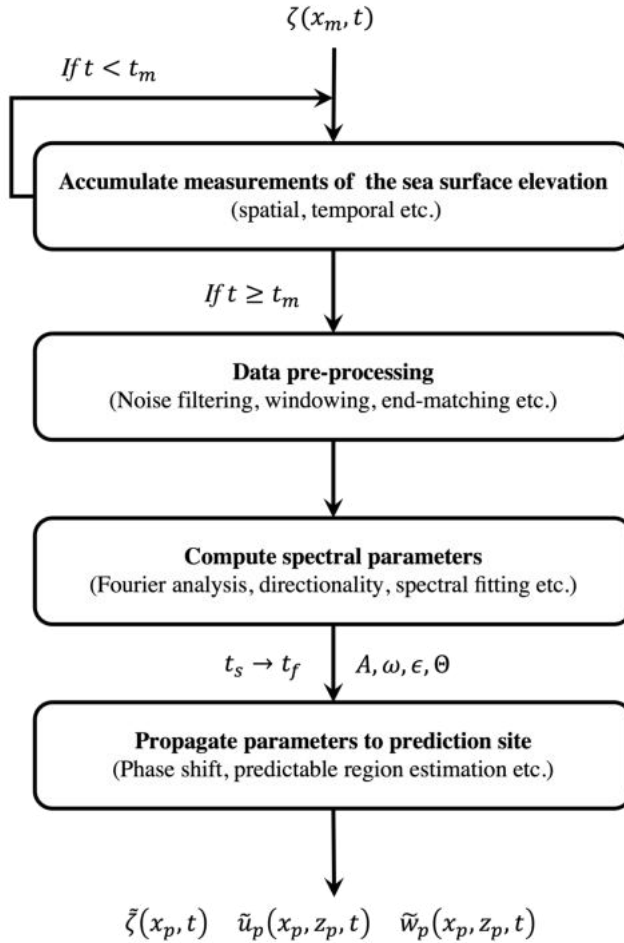


FIGURE 5.1: DSWP generalised operation flowchart.

is recurring in time, so the reconstructed sea state elevation at the prediction site is directly correlated and consistently updated with respect to these real-time measurements. This is highly advantageous as it allows the system to adapt to variations in the sea state as they occur, a key factor for the success of using predictive control for disturbance mitigation.

### 5.2.2 Estimation of Prediction Region

One of the key processes when applying the DSWP algorithm is determining what is referred to as the *predictable region*. This process involves specifying an upper and lower frequency limit from the wave power spectrum which, in conjunction with the measurement region parameters, is utilised to estimate what duration or what distance from the measurement point a valid prediction of the future wave evolution is obtainable. Two typical methods are available for this process: the *fixed-point* method and *fixed-time* method. Intuitively, the former involves taking temporal measurements from a specific location in space and propagating the prediction forward in time. In contrast, the latter involves taking spatial measurements of the sea state at a particular instant in time and predicting the wave profile according to these snapshots.

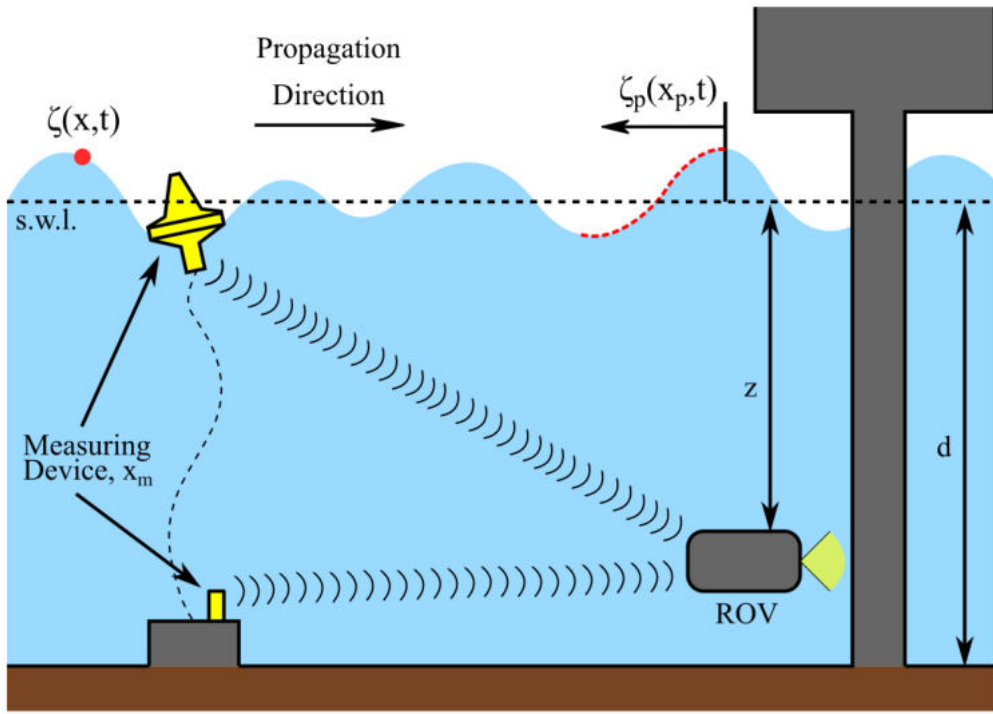


FIGURE 5.2: DSWP concept with respect to ROV control, where the measuring device is located at point  $x_m$  and the wave prediction is performed at point  $x_p$ .

For the postulated control application in this thesis, the *fixed-point* method satisfies the requirements for predictive disturbance rejection. An example is provided in Fig. 5.2, where measurements from either a wave buoy or a pressure transducer are being used to predict the wave elevation at the ROV location.

### Fixed-Point Method

Consider a measurement point on the sea surface which can be assumed to be approximately stationary at a fixed location of  $x_m = 0\text{m}$ , with a prediction point at a distance of  $x_p$  downstream from this. The fixed point method is based on recording the wave elevation  $\zeta$  at a point  $x_m$  for a period of time  $t_m$  and using this data to then predict the wave elevation at  $x_p$  for some time  $t_p$  into the future. The length of  $t_p$  for which a valid prediction can be obtained is determined by considering the space-time diagram of the frequency spectrum. The space-time diagram maps the propagation of the minimum and maximum frequency components using their celerity ( $c_{min}$  and  $c_{max}$  respectively), as shown in Fig. 5.3 for the fixed point method. When the two overlap (highlighted in red), the prediction can no longer be considered valid or accurate as the sea state is no longer considered to be statistically stationary across the region from measurement to prediction location. The example of the space-time diagram in Fig. 5.3 shows the parameters which dictate the maximum valid prediction time  $t_{p,max}$ , with the shaded area representing the region where a valid prediction is

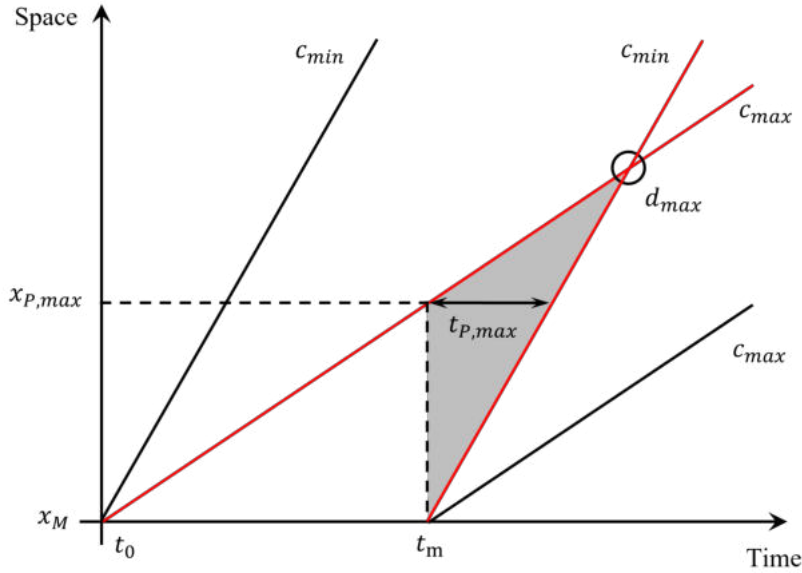


FIGURE 5.3: Space-time diagram for the fixed-point method, showing the entire predictable region shaded in grey.

obtainable. Here,  $d_{max}$  is the furthest point from the measurement site where the prediction can be considered reliable.

As the wave height recordings are accumulated as a temporal segment, the sea-state frequency spectrum can be obtained by considering a wave-height record at  $\zeta(x_m, t)$  where  $x_m = 0\text{m}$ , discretized by steps of  $\Delta t$ :

$$\mathcal{F}_n = \sum_{j=0}^{J-1} \zeta_j(0, t) \exp^{-i(2\pi \frac{jn}{J})} \quad n = (0, 1, \dots, J-1) \quad (5.1)$$

where  $J = t_m/\Delta t$  is the number of wave-height samples in the wave-height record. Given these Fourier coefficient's, the prediction model is obtained by consideration of Eq. 3.7 with the prediction location  $x_p$  as an input:

$$\begin{aligned} \tilde{\zeta}(x_p, t) &= \sum_{n=0}^N A_n \cos(k_n x_p - \omega_n t + \phi_n) \\ &\quad + \sum_{n=0}^N \frac{1}{2} k_n A_n^2 \cos 2(k_n x_p - \omega_n t + \phi_n) \end{aligned} \quad (5.2)$$

with

$$\begin{aligned} A_n &= |\mathcal{F}_n|, & \phi_n &= \angle \mathcal{F}_n, & k_n &= \omega_n^2/g \\ \omega_n &\in \left[ \frac{2\pi n}{J\Delta t}, \frac{2\pi(n+1)}{J\Delta t}, \dots, \frac{2\pi}{J\Delta t}(J-1) \right] \end{aligned}$$

For shallow water waves, the limit of the dispersion relation takes the form  $\lim_{d \rightarrow \infty} k^2 \rightarrow \omega^2/gd$ , resulting in a linear phase filter where  $k_n x_p$  is considered a phase-shifting filter parameter for propagating the wave through space. Given the amplitude spectrum,

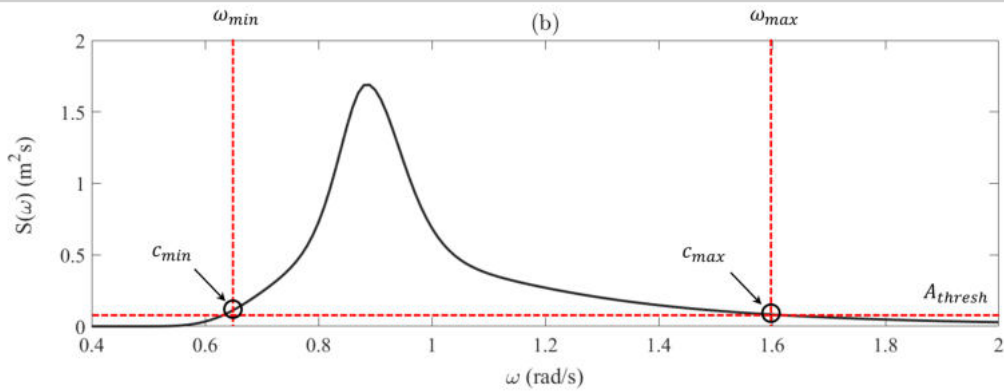


FIGURE 5.4: The wave frequency spectrum with frequency and amplitude thresholds applied to bound the components considered during wave reconstruction.

the transformation into the power density representation is straight forward:

$$S_n = \frac{A_n^2}{2\Delta\omega} \quad (5.3)$$

where  $\Delta\omega = 2\pi/J\Delta t$ .

With reference to the space-time diagram and the parameters  $c_{min}$  and  $c_{max}$ , it is appropriate to bound the spectral representation to produce a reasonable length predictable region. Extreme frequency components that are deemed to have minimal influence on the resulting waveform are disregarded, ultimately relaxing the restrictions for a prediction to be valid. This is graphically represented in Fig. 5.4, where both a frequency threshold and amplitude threshold are enforced (as is done throughout this work).

**Property 5.2.1** *The power spectrum,  $S_n$ , is bounded such that only spectral components within a specified range are considered and all others are disregarded.*

$$\omega_{min} < \omega < \omega_{max} \quad (5.4)$$

$$A < A_{max} \quad (5.5)$$

It therefore follows that the maximum valid predictable region can be determined and defined as the time-frame  $t_s \rightarrow t_f$  where:

$$t_s = \frac{x_p}{c_{min}}, \quad t_f = \frac{x_p}{c_{max}} + t_m \quad (5.6)$$

Any prediction outwith this time-frame cannot be considered reliable and therefore the prediction is deemed to be invalid.

### Fixed-Time Method

An alternative method of consideration is the fixed-time method, which, in contrast to the fixed-point method, deals with wave snapshots at an instance in time across space.

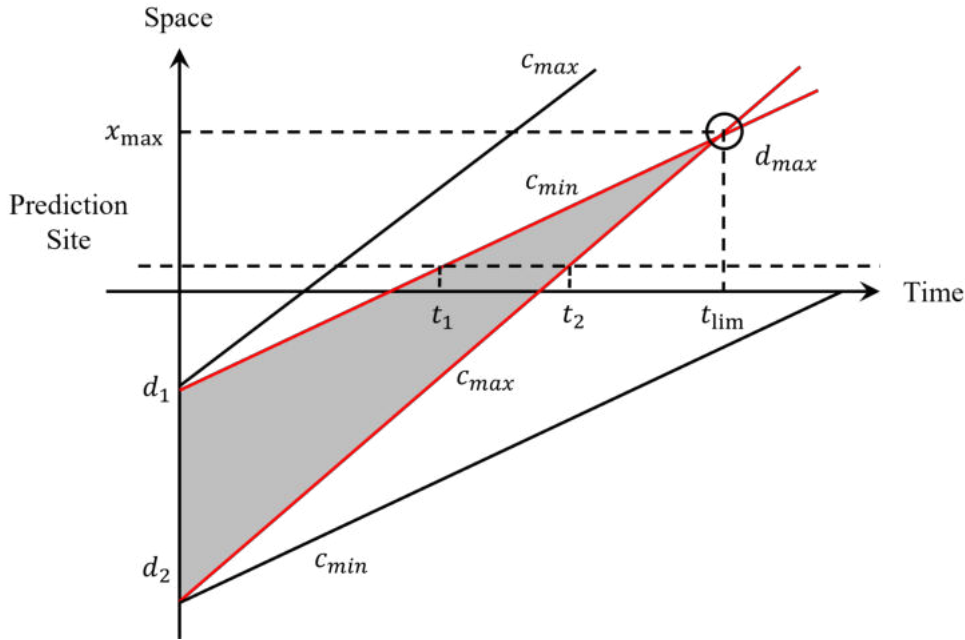


FIGURE 5.5: Space-time diagram for the fixed-time method.

With reference to Fig. 5.5, a segment of the sea surface is measured between points  $d_1$  and  $d_2$  in a negligible time in comparison to the length of time for the sea surface to vary significantly [266]. This measurement is then used to determine the profile of the sea-surface at another point in space, with the length of the valid prediction decreasing with distance. In Fig. 5.5, the point  $d_{max}$  denotes the absolute limit at which only measured information across the distance  $d_1-d_2$  is present - beyond this point, similar to the fixed-point method, there will be additional information which will invalidate the prediction.

In terms of determining the predictable region, both methods are very similar in that they are dictated by the spectrum width and the distance between the measurement and prediction sites, as well as the wave itself. Analogous to the fixed-point method, the spectral information contained within the snapshot of the measured sea surface has to propagate to the prediction site; thus, the general theoretical method presented in Eq. 5.1-5.6 remains valid with a modification to consider spatial variation as opposed to temporal [265]. It follows that the wave-height record is described at  $t = 0\text{s}$  over the distance  $d_{2,1} = d_2 - d_1$  and discretized by steps of  $\Delta d$ :

$$\mathcal{F}_n = \sum_{j=0}^{J-1} \zeta_j(d_{2,1}, 0) \exp^{-i(2\pi \frac{jn}{J})} \quad n = (0, 1, \dots, J-1) \quad (5.7)$$

where now  $J = d_{2,1}/\Delta d$  is the number of wave height samples in the wave-height record. Fundamentally the processes are the same and the variation owes to the consideration of a spatial Fourier analysis rather than a temporal. This also means the filter parameter becomes time rather than distance in this case. This method

was not adopted in this work as the fixed-point method was deemed more suitable from a logistical perspective, but is presented here for completeness with regards to the theory behind DSWP. There is also the potential of deploying mixed space-time formulations of DSWP [269], but for similar reasoning this was opted as unsuitable for the purposes of this thesis.

### 5.2.3 Key Assumptions

Given the nature of the prediction algorithm, several assumptions or requirements are given here with regards to the validity of the approach and the applications concerned in this work. These also apply to the experimental study which is discussed in Section 5.3. Although these assumptions likely apply to both forms of DSWP presented above, for completeness it should be noted that the fixed time method is adopted and is used throughout this thesis.

**Assumption 5.2.1** *An estimation of the wave-profile up-stream from the vehicle location is available, either through continuous direct measurement or reconstruction by transformation (pressure measurements for example).*

**Assumption 5.2.2** *The sea state is fully formed and can be considered effectively stationary over the measurement and propagation period:*

$$\mathfrak{F}(\zeta[0, t]) \approx \mathfrak{F}(\zeta[x_p, t]) \quad (5.8)$$

**Assumption 5.2.3** *The wave elevation is considered to be purely uni-directional and can therefore be described by the theory given in Section 3.1.2 for 2D spectra.*

### 5.2.4 Disturbance Prediction Algorithm

The model for estimating the wave-induced loads on the vehicle was presented in Section 4.2 and accompanied with an experimental validation in Section 4.3. The basic assumption to apply this model is that the wave field experienced by the vehicle is obtainable, either by direct measurement or estimated via some form of prediction. Using DSWP as a tool to predict the wave field at the vehicle location ahead of time, this basic requirement is satisfied and the predicted spectrum is the direct input for the disturbance model. Considering Eq. 3.11-3.12 with the vehicle location beneath the surface ( $x_p, z_p$ ) as the positional input, a predicted particle velocity vector can be deduced and defined as  $\tilde{\nu}_p = [\tilde{\nu}_{p,x}, \tilde{\nu}_{p,z}]$ . It follows that the predicted environmental disturbances can be obtained by considering:

$$\tilde{\tau}_E = \begin{bmatrix} \tilde{X}_E \\ \tilde{Z}_E \\ \tilde{M}_E \end{bmatrix} = \begin{bmatrix} X_u \dot{\tilde{\nu}}_{p,x} + (X_u + X_{u|u} |\tilde{\nu}_{p,x}|) \tilde{\nu}_{p,x} \\ Z_w \dot{\tilde{\nu}}_{p,z} + (Z_w + Z_{w|w} |\tilde{\nu}_{p,z}|) \tilde{\nu}_{p,z} \\ \int_{-L/2}^{L/2} x' \tilde{F}_n(x', z', t) dx \end{bmatrix} \quad (5.9)$$

---

**Algorithm 1** Fixed-point Deterministic Sea Wave Prediction with Wave-induced Disturbance Estimation Algorithm
 

---

- 1: Measure the sea surface state at each discrete sampling time  $t_k$  at a location  $x_m$
  - 2: Append each measurement to the wave height record,  $\zeta_m(k) \leftarrow \zeta(t_k)$
  - 3: At  $t_k == t_m$ , perform Fourier analysis on  $\zeta_m$   
 $(A, \omega, \epsilon) = \mathcal{F}(\zeta_m)$
  - 4: Threshold spectrum:  
 $(A, \omega, \epsilon) \leftarrow A_m > 0.05 \times \max(A)$   
 $(A, \omega, \epsilon) \leftarrow \omega_m > \omega_{min}$   
 $(A, \omega, \epsilon) \leftarrow \omega_m < \omega_{max}$
  - 5: Calculate predictable region according to:  
 $c \leftarrow c(\omega_{max})$   
 $t_p \leftarrow t(n) + x_P/c$
  - 6: Obtain fluid motions at the prediction site  $(x_P, z_P)$ :  
 $\tilde{\nu}_p(x_P, z_P, t_k) \leftarrow \text{Eq. 3.15-3.16}$
  - 7: Evaluate predicted disturbances to the vehicle:  
 $\tilde{\tau}_E \leftarrow \text{Eq. 5.9}$
  - 8: Repeat continuously for the remainder of the experiment,  $t_k > t_m$
- 

This forms the complete process from the initial recorded wave height measurements through to the propagation and evaluation of hydrodynamic loading at the vehicle location.

Given the theory presented throughout this section and the model presented in Section 4.2, Algorithm 1 was formulated and implemented within a simulated environment to generate predictions at the prediction site (i.e. the ROV location). Utilising this, the experimental data could be comparatively analysed against the algorithm output and the applicability of the method considered. As a further point, a slightly modified version of Algorithm 1 was later implemented within an integrated system simulation, with the key adjustment relating to consideration of the NMPC prediction horizon. From this, the different proposed control methodologies could be analysed in conjunction with the DSWP method; Section 5.5 discusses this in detail.

### 5.3 Wave Prediction Experimental Study

Although there have been studies confirming the validity of DSWP for both unidirectional and multi-directional seas [268, 269, 270], it was desirable to conduct experiments in the FloWave tank to better understand the limitations of the predictable region. As our application is specifically for short-horizon dynamic control, the aim of this study was to deduce if sufficient time-periods could be obtained over extremely short distances; this initial stage will facilitate planned experimental studies with the controller deployed on the vehicle. To this end, a short experimental study was conducted at the FloWave facility.

TABLE 5.1: Longitudinal location of the wave gauges (measurement points) relative to the centre of the tank (0m).

WG1 (m)	WG2 (m)	WG3 (m)	WG4 (m)	WG5 (m)
-7.54	-3.77	0.00	3.77	7.54

TABLE 5.2: Peak spectral period and significant wave height of each wave case tested, with assigned case references.

Case Reference	Peak Spectral Period, $T_p$ (s)	Significant Wave Height, $H_s$ (s)
T1	2.0	0.29
T2	2.5	0.26
T3	3.0	0.19

### 5.3.1 Methodology and Setup

As the underlying theory of DSWP and length of the predictable region relies heavily on the distance between the measurement point and the prediction point, several different measurement points across the tank diameter were specified to deduce how drastically this varied. As a description of the FloWave facilities are provided in Section 4.3, these are not repeated here and only the method behind the experiment itself is discussed.

Although the tank has a diameter of 25m, the maximum obtainable distance where the waves can be considered to be fully developed is  $\approx 15.08\text{m}$ ; this is lower to minimise the level of interference arising from wave generation and similarly reflections at the absorption side of the tank. A 5-piece evenly spaced wave gauge array was placed coincident to the wave propagation direction, which in this case was also coincident to the gantry to provide a sturdy mounting point for the WGs. The WG labels adopted in this study are shown in Fig. 5.6 and the distances relative to the centre of the tank at 0m are given in Table 5.1. Due to time limitations and the interest of the study being JONSWAP spectra with larger peak spectral periods, three different wave formations were tested whose parameters are displayed in Table 5.2. Owing to physical limitations of the tank, the spectral period was maintained  $\leq 3\text{s}$  in order to achieve a reasonable significant wave height; as the period increases, attainable wave height degrades. Each wave was recorded across the WG locations at a frequency of 128Hz for the duration of each test,  $\approx 512\text{s}$ . During the analysis, this was reduced to a 500s temporal segment to ensure the analysed wave was fully developed. It should be noted that the waves analysed during this study are all JONSWAP spectra and no monochromatic waves were tested.

### 5.3.2 Prediction Validation

Utilising the data collected from the experiments, it was possible to validate the functionality and determine the capability of the DSWP algorithm within a numerically

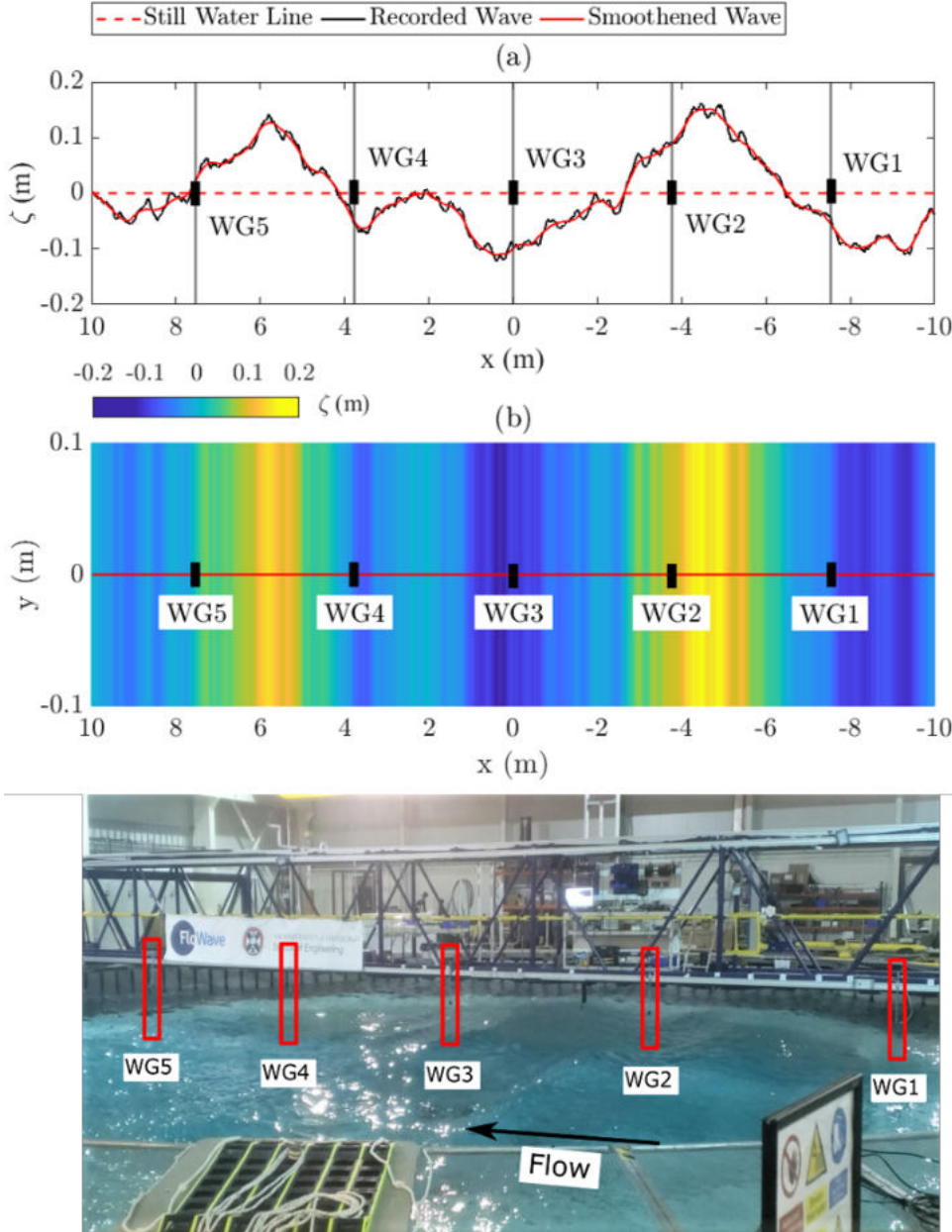


FIGURE 5.6: Experimental procedure for collecting the results, showing (a) A snapshot of the recorded wave train from the side-view, (b) the wave gauge locations and wave height with respect to the tank x-axis from the top view, and (c) the experimental set-up. The constant wave height in subplot (b) owes to the assumption of a uni-directional wave propagating across the tank diameter.

simulated environment. Taking WG1 as a measurement point ( $x_m$  in Fig. 5.3) and WG2-WG5 as prediction points ( $x_p$  in Fig. 5.3), the numerically predicted wave could be compared against the observed wave at the same point in time using the fixed-point method. The main metric for comparison was the error in wave elevation between prediction and measurement through a RMSE value, evaluating each separate prediction instance throughout the whole simulation. For the validation, the first 300s of the fully developed wave was used as the measurement period for accumulating surface elevation measurements (stage 1 in Fig. 5.1 and steps 1-2 in Algorithm

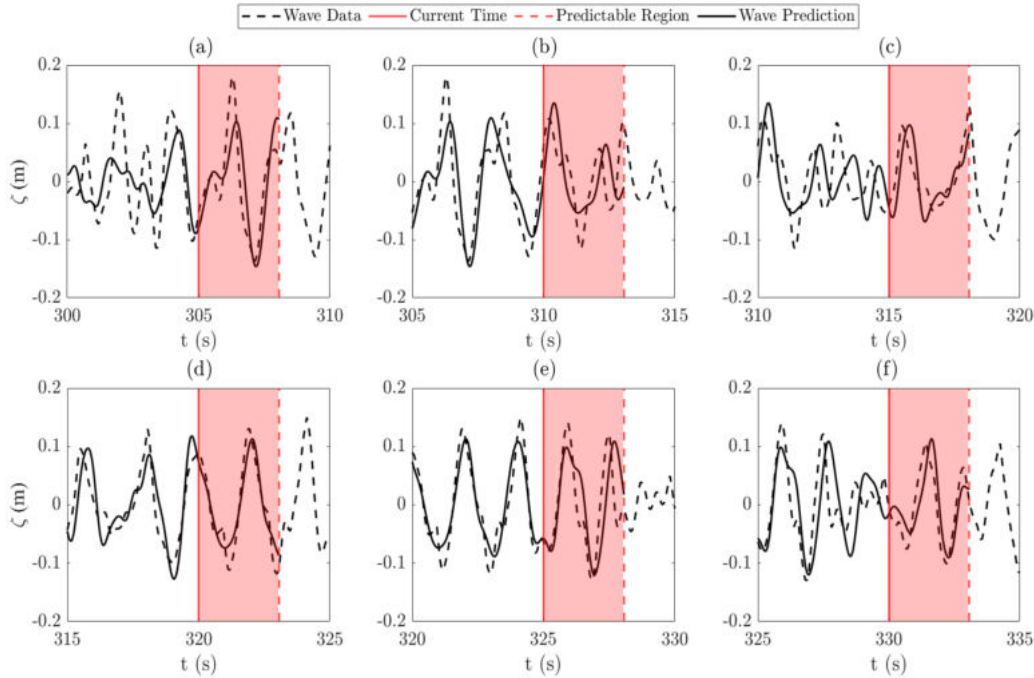


FIGURE 5.7: Comparison of the predicted wave height against the recorded wave gauge data for case T1, showing accurate short-term predictions of the temporal wave-height at various snapshots in time.

[1](#)), after which the DSWP algorithm was deployed for the final 200s. Although the data was collected at a resolution of 128Hz, this was reduced to 16Hz for the sake of practicality with regards to processing speed; therefore, the total number of predictions amounted to 3600 instances. Similarly, the output JONSWAP spectrum was bounded to extend the predictable region using a frequency based threshold and an amplitude based threshold, examined both independently and when combined analogous to that shown in Fig. [5.4](#). All components outwith the specified ranges were neglected and considered to have negligible impact on the predicted waveform. The reasoning behind investigating the different methods was to analyse how the computation speed varied and if there was a significant effect on the prediction length and RMSE achievable, and if so how consequential the effect. Similarly, the prediction point was varied from WG2 - WG5 to determine how drastically the analysed parameters were effected.

### Qualitative Assessment

An initial assessment of the algorithm's ability to predict the waveform was performed by simply testing the different cases and visualising the output waveform, comparing this to the recordings of the wave gauges. Examples are given for all wave cases in Fig. [5.7-5.9](#) where the given subplots show instances at 5s intervals during the simulation. It should be noted that these are only examples and predictions were actually computed at each time-step for analysis purposes. In a practical application

it is unlikely that a wave prediction would be made at every discretized time-step  $\Delta t$  as this would add unnecessary computational burden. Given a prediction in the order of seconds is obtainable, a more suitable approach would be to execute the algorithm at specific time intervals, for example every 0.5s, to update the wave prediction accordingly.

It's quite clear from this initial assessment that the algorithm is capable of predicting the waveform to a high degree of accuracy. This is extremely useful, particularly when considering the only measurements being exploited are of the wave height at a specified distance from the prediction location. From these initial examples, it appears that case T1 is predicted slightly poorer than the other two cases, and reasons for this are discussed in more detail using the quantitative analysis below. Regardless, case T1 is still predicted well in most instances, showing better representation when the waveform is dominated by large amplitude spectral components, as opposed to points where the wave is smaller during short time intervals. This is likely due to the higher amplitude components dominating the shape of the waveform, with a narrower band of components having the largest influence over the resulting surface elevation. At these moments in time, the forces and torques induced on the wave will be largest and it is therefore of more importance to produce an accurate estimation, so this is an encouraging observation. Being able to estimate the largest disturbances with the greatest accuracy suggests that the controller will be able to perform better compensating actions under these waves, provided sufficient thrust can be supplied. Similarly, disparity between estimated and experienced disturbances at lower wave elevations will have less effect on the vehicle state, should the controller produce a poor set of compensating control actions. A possible solution could be to develop a control strategy which only exploits disturbance predictions for large wave elevations, defaulting to a form of optimal feedback controller in the remainder of cases, for example an LQR.

### **Impact of Spectrum Thresholding on Prediction Accuracy**

With regards to the nature of thresholding (see Fig. 5.4 for an example), the recorded values of interest are presented in Table 5.3. All cases relate to a measurement point at WG1 and a prediction point at WG5 for consistency, with these two being furthest apart in the domain and will therefore produce the longest prediction length.

The major advantage of only using a frequency based thresholding technique lies in the constant dependency on the two bounding components. These will remain the same irrespective of the spectrum, and thus the attainable prediction length will not vary. In contrast, adopting an amplitude based technique removes the guarantee associated with obtainable length - although longer prediction lengths are achieved for cases T1 and T3, the opposite is true for case T2. Combining the two approaches clearly is the optimal choice out of the three techniques, as a minimum prediction

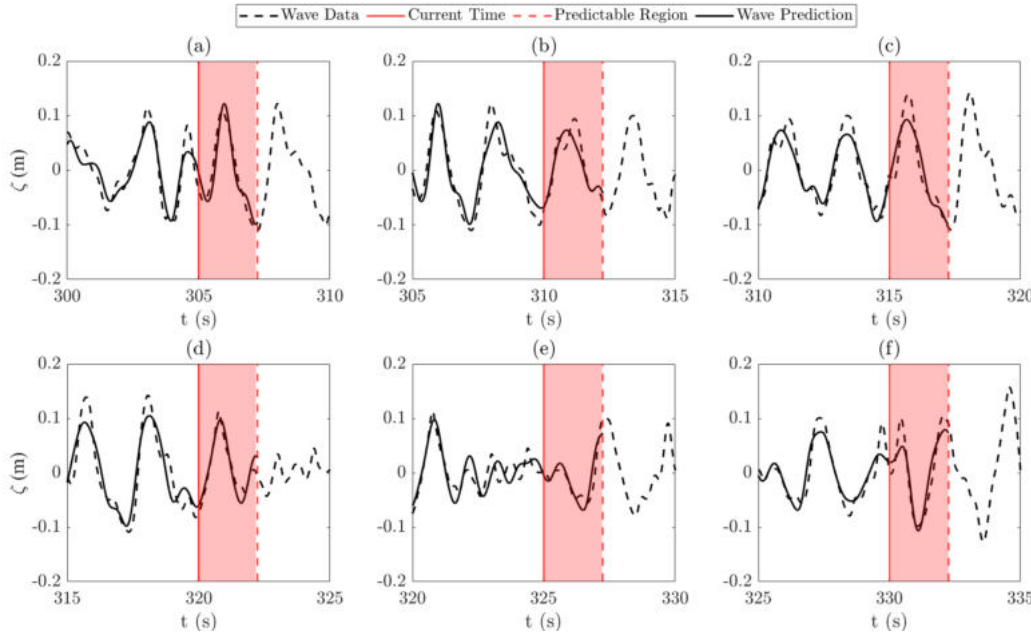


FIGURE 5.8: Comparison of the predicted wave against the recorded wave gauge data for case T2, showing accurate short-term predictions of the temporal wave-height at various snapshots in time.

length is guaranteed whilst components with negligible amplitude are disregarded, reducing processing time with little to no effect on the accuracy of the prediction as shown by the RMSE.

For all cases and techniques, the average RMSE recorded across all instances is  $\leq 0.046\text{m}$  which is the equivalent to 15.52% of the significant wave height for the case in question (T1). For case T3, this value drops to 8.42%, which is likely due to the longer wave length and lower significant height coupled with the operational depth of the FloWave tank. For a prediction technique based upon purely deterministic processes and standard filtering techniques, these values are remarkably low and present a good degree of accuracy relative to computation power requirements. This is supported by the average processing time per prediction across the 3600 instances - it should also be noted this value relates to a simulation in a MATLAB environment, so in practice this value will be even lower when using a lower-level programming language such as C++ or if advanced computing capabilities were exploited like GPU's or parallel processing. Even so, the maximum recorded processing time of 0.052s is fast enough for near real-time applications, which can be extended to real time application when considering a prediction is not required at each time-step. In this analysis, predictions were taken at every single time-step for the sake of error analysis; in reality, there is no requirement for this. The fact that predictions can be obtained which extend over temporal segments of a few seconds supports this, thus processing power requirements can be reduced by only performing predictions at specified time intervals, for example every 0.5s or 1s.

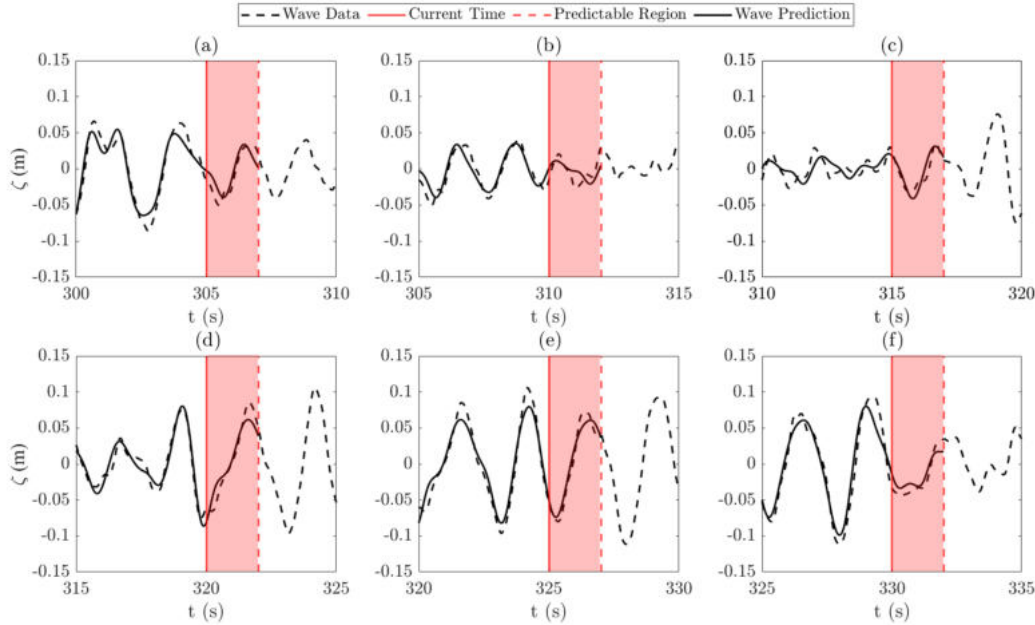


FIGURE 5.9: Comparison of the predicted wave against the recorded wave gauge data for case T3, showing accurate short-term predictions of the temporal wave-height at various snapshots in time.

TABLE 5.3: Effect of different thresholding methods on key parameters for each wave case, considering a measurement location at WG1 and a prediction location at WG5.

Threshold	Case	Pred. Len. (s)	RMSE (m)	Ave. Proc. Time (s)
$0.20 < f < 2.00(\text{Hz})$	T1	1.938	0.045	0.052
	T2	1.938	0.025	0.052
	T3	1.938	0.016	0.052
$A > 0.05A_{max}(\text{m})$	T1	3.063	0.046	0.026
	T2	0.750	0.024	0.027
	T3	2.000	0.016	0.021
$0.20 < f < 2.00(\text{Hz})$ and $A > 0.05A_{max}(\text{m})$	T1	3.063	0.045	0.026
	T2	2.250	0.025	0.027
	T3	2.000	0.016	0.021

### Impact of Point-to-Point Distance on Prediction Accuracy

A fundamental aspect of Fixed-Point DSWP is that two unique points are considered: a measurement point and a prediction point. It is intuitive that the prediction length will degrade with distance between the measurement point and prediction point, but it is of importance to determine how varying this distance affects key parameters, namely the prediction length, the RMSE of the prediction and the average processing time. For future planned experimental studies, these parameters will dictate the breadth of tests possible from a safety perspective. For this analysis, the thresholding technique was maintained as a combination of both frequency and amplitude based

inequalities to maximise the attainable prediction length. Also, the DSWP algorithm was executed at each WG location relating to distances of 3.77m, 7.54m, 11.31m and 15.07m for WG2, WG3, WG4 and WG5 respectively considering a measurement point at WG1. Note that for a prediction point at WG5, the results are given in Table 5.3 and therefore are not repeated here; see the final three rows.

As expected, the observed data given in Table 5.4 returns a linear relationship with respect to the predicted length, dictated by the space-time diagram and the thresholding technique adopted. In terms of absolute values, it is worth stressing that these are heavily reliant on the waveform and the spread of frequency components within the spectrum. Limitations of the FloWave tank restrict this analysis to low peak periods, but real-world conditions would possess a much higher peak period value and thus the measurement to prediction point distance would be required to be extended accordingly. However, for realistic waves (such as those analysed in Section 5.5) prediction lengths in the order of seconds can be obtained for distances of as low as 50m. This distance is much lower than previous works have considered during field trials [268], but still provides a wave prediction long enough to be effectively exploited within a predictive control architecture.

What is promising is that the RMSE increases by only 0.006m between a prediction point at WG2 and WG5, supporting the claim of operation over longer distances in real-world scenarios. As expected the RMSE increases with distance across all cases, which can be attributed to factors such as perturbations in the waveform during propagation or unmodelled dynamics due to the use of a lower-order wave model. Similarly, the processing time remains almost constant at  $\approx 0.025\text{s}$  which reiterates the applicability of the prediction method for obtaining fast estimations for use in a control strategy. It is suspected that incorporation of higher order terms within the wave model would help improve this, but it is also worth noting the increase is marginal given the  $4\times$  increase in distance. Similarly, more accurate modelling techniques can be adopted to re-create the sea state, for example the technique presented in [282], but this results in unwanted increases in computation time and may not produce significant gains in accuracy to be worth the sacrifice of near instantaneous predictions. Again, to fully evaluate this an extensive study is required testing different modelling methodologies for re-creating the sea surface, however this was not the goal of this work. This would offer insight into how accurately the sea state can be reconstructed, which would be beneficial when transitioning into directional spectra cases where complexity increases.

### 5.3.3 Concluding Remarks

This initial validation study of the wave prediction algorithm showed that low prediction error could be achieved for various wave cases, supporting the claim that these explicit predictions can be exploited directly within the vehicle control. Similarly,

TABLE 5.4: Effect of varying distance between measurement and prediction points on key parameters for each wave case.

Meas. → Pred. (m)	Case	Pred. Len. (s)	RMSE (m)	Ave. Proc. Time (s)
3.77 (WG1 → WG2)	T1	0.750	0.026	0.027
	T2	0.563	0.015	0.027
	T3	0.5	0.010	0.021
7.54 (WG1 → WG3)	T1	1.500	0.030	0.027
	T2	1.125	0.014	0.027
	T3	1.000	0.010	0.021
11.31 (WG1 → WG4)	T1	2.313	0.035	0.026
	T2	1.688	0.018	0.027
	T3	1.500	0.011	0.021

prediction lengths were achieved in the region of 2-3s when adopting a combination of frequency and amplitude threshold boundaries, sufficient for deployment in the NMPC control architecture to produce a usable temporal horizon. Along with this, it was also shown that algorithm execution times are fast enough to be applicable for near real-time applications, particularly when considering predictions are only required at specific intervals.

On the other hand, because this study was exclusively undertaken as an initial validation, a select set of different wave cases were tested to determine the validity and length of predictable region obtainable. These initial results provided solid evidence that the wave elevation predictions are sufficiently accurate to be considered explicitly within the control strategy. Quantifying the effect of wave parameters on the validity and accuracy of predictions would require a more extensive systematic study, however this was out of the scope of this work and would be the subject of future work.

## 5.4 Model Predictive Control

MPC is a control strategy which is based around solving an optimisation problem online, with respect to a specified set of constraints and an assigned cost function [23]. The control strategy involves the prediction of future states according to a specified system model, exploiting this information to determine a set of control actions which minimises the specified cost function; a visual representation of this process is shown in Fig. 5.10. A key feature of MPC is the fact that although several control actions are generated for a specific horizon, only the first value in the sequence is applied and the optimisation problem re-calculated at the next time step; this accounts for variations in expected and experienced behaviour due to inaccuracies in the system model. This feature also relates to MPC being known as Receding-Horizon Control, as the prediction horizon is shifted forward at each time step. Along with

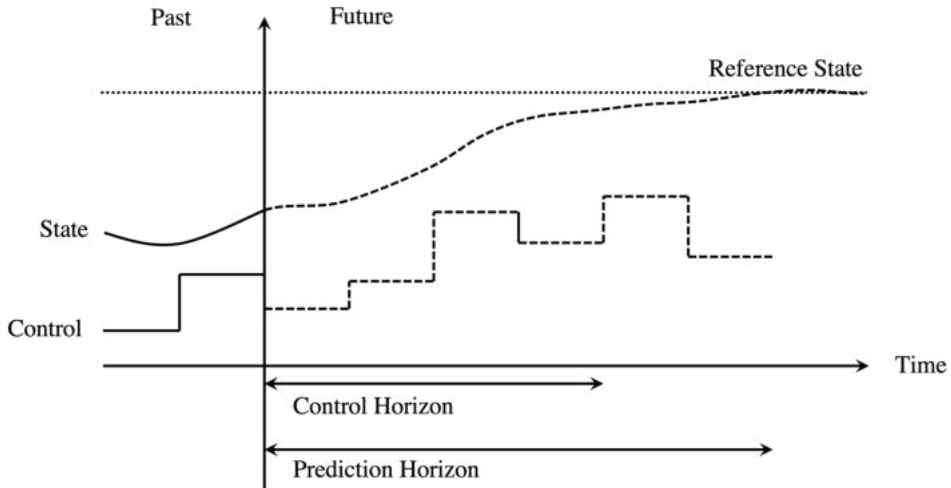


FIGURE 5.10: Model Predictive Control concept, whereby an optimised control trajectory is generated to reach the reference state.

this advantage, the other is the ability to explicitly consider constraints within the optimisation problem - exploiting this, considerations can be made towards elements such as actuator limitations, known obstacles and system dynamics amongst others. This is one of the reasons MPC is much more powerful than typical feedback control methods. [23, 315].

Within the design of the MPC architecture, the main consideration relates to the plant model and the inherent nature of the dynamics, specifically whether these are modelled to be linear or nonlinear. Both can be handled directly and a broad range of different types of MPC have been proposed in the literature to handle variations between these (Explicit, Robust, Constrained to name a few), but the performance of any MPC is largely dictated by the accuracy of the plant model. Hence, accommodations must be made by adopting various different techniques to ensure the system remains stable and a feasible solution can be found, either optimal or suboptimal [316]. In the remainder of this section, the procedure for constructing an MPC architecture using both a linear and nonlinear plant model is presented, followed by comments and considerations towards stability and recursive feasibility. Closing remarks are given in relation to which scheme is adopted in this work and the reasons for this.

#### 5.4.1 Linear Model Predictive Control

If the system is inherently linear or is modelled as a linear system, a form of Linear MPC (LMPC) would be used. Here, the equations of motion can be written in continuous-time linear state-space representation in the form:

$$\dot{\mathbf{x}} = \mathbf{A}\mathbf{x} + \mathbf{B}\boldsymbol{\mu} + \mathbf{E}\mathbf{w} \quad (5.10)$$

$$\mathbf{y} = \mathbf{C}\mathbf{x} + \mathbf{D}\boldsymbol{\mu} \quad (5.11)$$

where  $\mathbf{A}$  is the system matrix,  $\mathbf{B}$  is the input matrix,  $\mathbf{C}$  is the output matrix,  $\mathbf{D}$  is the feed-through matrix and  $\mathbf{E}$  is the noise matrix; commonly  $\mathbf{D} = 0$  unless the system has an instantaneous response. Here,  $\mathbf{x}$ ,  $\boldsymbol{\mu}$  and  $\mathbf{w}$  represent the system state, control input and any noise/disturbances to the system, whilst  $\mathbf{y}$  represents the system output. A corresponding discrete-time model can be derived as:

$$\mathbf{x}_{k+1} = \mathbf{A}_d \mathbf{x}_k + \mathbf{B}_d \boldsymbol{\mu}_k + \mathbf{E}_d \mathbf{w}_k \quad (5.12)$$

$$\mathbf{y}_k = \mathbf{C}_d \mathbf{x}_k \quad (5.13)$$

where the subscript  $d$  relates to the discrete form of each matrix. In Eq. 5.12, each step  $k$  represents a discrete time-step of  $\Delta t$ . Assuming that the state and control trajectory along the prediction horizon  $N_c$  begins at  $k$ , the predicted states  $\mathbf{X}_k$  for a vector of control inputs  $\mathbf{U}_k$  are defined as:

$$\mathbf{X}_k = \begin{bmatrix} \mathbf{x}_k \\ \mathbf{x}_{k+1} \\ \vdots \\ \mathbf{x}_{k+N_c} \end{bmatrix} \quad \mathbf{U}_k = \begin{bmatrix} \boldsymbol{\mu}_k \\ \boldsymbol{\mu}_{k+1} \\ \vdots \\ \boldsymbol{\mu}_{k+N_c-1} \end{bmatrix} \quad (5.14)$$

which is used as the predictive model for the LMPC where  $\mathbf{x}_k \in \mathcal{X}$  and  $\boldsymbol{\mu}_k \in \mathcal{U}$  are the state and input constraints.

From this, the LMPC can be formulated for reference tracking using a quadratic cost structure. Considering a reference state  $\mathbf{X}_r$  and control input  $\mathbf{U}_r$  of the same dimensions as in Eq. 5.14, the optimal control problem is defined as:

$$\begin{aligned} \underset{\mathbf{X}_k, \mathbf{U}_k}{\text{minimize}} \quad & \mathcal{J} = V_f({}^r \mathbf{x}_{k+N_c}) + V_s({}^r \mathbf{X}_k, {}^r \mathbf{U}_k) \\ \text{subject to} \quad & \mathbf{x}_{k+1} = \mathbf{A}_d \mathbf{x}_k + \mathbf{B}_d \boldsymbol{\mu}_k + \mathbf{E}_d \mathbf{w}_k, \\ & \mathbf{x}_k \in \mathcal{X}, \\ & \boldsymbol{\mu}_k \in \mathcal{U}, \\ & \mathbf{x}_{k+N_c} \in \mathcal{X}_f \end{aligned} \quad (5.15)$$

Here,  ${}^r \mathbf{X}_k = \mathbf{X}_k - \mathbf{X}_r$  and  ${}^r \mathbf{U}_k = \mathbf{U}_k - \mathbf{U}_r$  whilst  $V_f$  and  $V_s$  are functions representing the terminal and stage costs respectively, such that:

$$\begin{aligned} V_f({}^r \mathbf{x}_{k+N_c}) &= ({}^r \mathbf{x}_{k+N_c})^T \mathbf{P} ({}^r \mathbf{x}_{k+N_c}) \\ V_s({}^r \mathbf{X}_k, {}^r \mathbf{U}_k) &= \sum_k^{k+N_c} ({}^r \mathbf{x}_k)^T \mathbf{Q} ({}^r \mathbf{x}_k) + \sum_k^{k+N_c-1} ({}^r \boldsymbol{\mu}_k)^T \mathbf{R} ({}^r \boldsymbol{\mu}_k) \end{aligned}$$

where  $\mathbf{P}$ ,  $\mathbf{Q}$  and  $\mathbf{R}$  are weighting matrices on the terminal state, intermediate state and control. Typically, these are designed as block diagonals depending on state

importance and state/control relative importance:

$$\mathbf{P} = \begin{bmatrix} P_1 & 0 & \dots & 0 \\ 0 & P_2 & \dots & 0 \\ \vdots & \vdots & \ddots & \vdots \\ 0 & 0 & \dots & P_n \end{bmatrix} \quad \mathbf{Q} = \begin{bmatrix} Q_1 & 0 & \dots & 0 \\ 0 & Q_2 & \dots & 0 \\ \vdots & \vdots & \ddots & \vdots \\ 0 & 0 & \dots & Q_n \end{bmatrix} \quad \mathbf{R} = \begin{bmatrix} R_1 & 0 & \dots & 0 \\ 0 & R_2 & \dots & 0 \\ \vdots & \vdots & \ddots & \vdots \\ 0 & 0 & \dots & R_m \end{bmatrix}$$

where  $n$  and  $m$  refer to the number of states and control inputs in  $\mathbf{x}_k$  and  $\boldsymbol{\mu}_k$ . The introduction of a terminal cost and constraint on the final stage in the predicted state sequence enforces recursive feasibility and stability within the formulation, which is discussed in more detail in the following section. The advantage of using an LMPC structure is that the optimisation problem is *convex*, thus a well-defined solution exists. This is not the case for NMPC, which is presented and discussed in the next section, however the effect of this trait can largely be mitigated with the adoption of more advanced optimisation techniques and tools.

### 5.4.2 Nonlinear Model Predictive Control

Considering a case where the plant exhibits nonlinear behaviour in the system dynamics, there are two generalised options to deploy a model predictive control scheme; (1) linearise the dynamics around an operating point and deploy LMPC or (2) derive a NMPC and deploy this directly. The latter will more accurately represent the system behaviour when the non-linearities are strong, however there is a possibility that the obtained solution is a local and not global minimum due to the problem now being non-convex. This risk can be reduced by applying methods such as multiple shooting, but cannot be mitigated completely.

The nonlinear dynamics of the system are described by the Ordinary Differential Equation (ODE):

$$\dot{\mathbf{x}} = \mathbf{f}(\mathbf{x}, \boldsymbol{\mu}) \quad (5.16)$$

where  $\mathbf{x}$  and  $\boldsymbol{\mu}$  are used to represent the system state and control input. From this, the ODE is solved in discrete-time form using well established methods such as Euler or more typically Runge-Kutta integration (due to higher accuracy):

$$\mathbf{x}_{k+1} = \mathbf{F}(\mathbf{x}_k, \boldsymbol{\mu}_k) \quad (5.17)$$

Here, each step  $k$  represents a timestep  $\Delta t$ ; the predicted trajectories for the prediction horizon of  $N_c$  steps are then represented as a sequence of states and control inputs such that:

$$\mathbf{X}_k = \begin{bmatrix} \mathbf{F}(\mathbf{x}_k, \boldsymbol{\mu}_k) \\ \mathbf{F}(\mathbf{x}_{k+1}, \boldsymbol{\mu}_{k+1}) \\ \vdots \\ \mathbf{F}(\mathbf{x}_{k+N_c-1}, \boldsymbol{\mu}_{k+N_c-1}) \end{bmatrix} \quad (5.18)$$

**Algorithm 2** Discrete Nonlinear Model Predictive Control Algorithm at  $t_k$ 

- 
- 1: Estimate the system state  $\hat{\mathbf{x}}_k$
  - 2:  $\mathbf{x}_k \leftarrow \hat{\mathbf{x}}_k$
  - 3: Execute Algorithm 1 for  $(x_p, z_p) \leftarrow \mathbf{x}_k$ .
  - 4: Calculate the optimal control sequence  $\mathbf{U}_k$  by solving:

$$\text{Minimise } \mathcal{J} = V_f({}^r\mathbf{x}_{k+N_c}) + V_s({}^r\mathbf{X}_k, {}^r\mathbf{U}_k)$$

$$\text{s.t. } \begin{cases} \mathbf{x}_{k+1} = \mathbf{F}(\mathbf{x}_k, \boldsymbol{\mu}_k) \\ \mathbf{x}_k \in \mathcal{X} \\ \boldsymbol{\mu}_k \in \mathcal{U} \\ \mathbf{x}_{k+N_c} \in \mathcal{X}_f \end{cases}$$

- 5: Pass the first entry in the sequence  $\mathbf{U}_k$  to be allocated (Eq. 3.61).
- 

where  $\mathbf{x} \in \mathcal{X}$  and  $\boldsymbol{\mu} \in \mathcal{U}$  represents the feasible set derived from the defined constraints. The above representation facilitates formulation of the optimal control problem inclusive of a terminal constraint and cost penalty to enforce recursive feasibility and stability:

$$\begin{aligned} & \underset{\mathbf{X}_k, \mathbf{U}_k}{\text{minimize}} && \mathcal{J} = V_f({}^r\mathbf{x}_{k+N_c}) + V_s({}^r\mathbf{X}_k, {}^r\mathbf{U}_k) \\ & \text{subject to} && \mathbf{x}_{k+1} = \mathbf{F}(\mathbf{x}_k, \boldsymbol{\mu}_k), \\ & && \mathbf{X}_k \in \mathcal{X}, \\ & && \mathbf{U}_k \in \mathcal{U}, \\ & && \mathbf{x}_{k+N_c} \in \mathcal{X}_f \end{aligned} \tag{5.19}$$

which is a similar formulation to LMPC with alternative constraints. A key observation is that the constraints now contain a nonlinear equality, thus introducing non-convexity into the optimisation problem. This is the main element which causes NMPC to be more computationally expensive compared to LMPC, but can be tackled using advanced optimisation tools such as those deployed in this thesis. NMPC was the variation investigated within this work, with the implemented algorithm in the simulated environment is given in Algorithm 3.61.

Touching on the stability of MPC in general, this is a well studied topic which is usually discussed in conjunction with what is known as *recursive feasibility*; i.e. ensuring the optimization problem has a feasible solution at all future time steps, given a feasible initial control sequence. The standard approaches applied to achieve this involves placing constraints on the terminal value of the optimisation sequence, along with using a terminal controller and denoting a weight parameter applied specifically to the terminal value of Eq. 5.15 and 5.19, known as the *terminal cost*. By considering this terminal cost, the overall MPC cost is essentially transformed into an infinite horizon, which is the main reason it is one of the more commonly used techniques and is the technique that was adopted in the above formulation; see Eq. 5.19. This method is known to guarantee local stability as the controller can be derived explicitly

for the specified set of states and designed accordingly. As these methods have been proven and noted in countless works throughout the literature [317, 316, 318, 25], they have not been delved into here in detail but it is worth noting the principles of typical techniques.

## 5.5 Integrated System Simulation Study

Considering the results from the validation of the prediction algorithm in Section 5.3, incorporation of these within an overall control architecture was the next stage of development. This was performed within a simulated environment, formulating the NMPC presented in Section 5.4.2 for control of the vehicle and simulating the dynamics numerically according to the theory detailed in Section 3.2. Implementation of the NMPC scheme was performed using the CasADi MATLAB library in conjunction with the IPOPT solver [71], using a direct multiple shooting method discussed in more detail in Section 5.5.1. The block diagram for the overall control architecture of the NMPC is displayed in Fig. 5.11. The DSWP block involves continuous measurement of the wave profile at discrete time steps at the measurement site - when the specified measurement time has elapsed, Algorithm 1 is executed and the estimated load  $\hat{\tau}_E$  is passed to the NMPC to generate an optimal control sequence. Once the optimisation problem has been solved, the relevant control actions are generated and applied to the ROV. Throughout the control mission (i.e. after the elapsed time has passed and the ROV is deployed), the EKF is continuously producing state estimations for Algorithms 1-2 to exploit for evaluating the disturbance estimations and control actions respectively. This forms the sequence of processes which occur throughout execution of the proposed framework.

In conjunction with this, a baseline Cascaded Proportional-Derivative (C-PD) controller was analysed to provide a performance reference and a controller with Feed-forward (FF) disturbance compensation was also implemented, which exploits the disturbance predictions but does not feature an optimisation stage. The focus of the latter comparison is centred around how the inclusion of an optimisation stage affects both computation time and performance. This section details the results from these simulations and the performance of the proposed fully integrated system, inclusive of control and predictions methods.

### 5.5.1 Simulation Configuration

#### Scenario Set-up

Emulating the conditions the ROV may encounter under a typical operating scenario was key to accurately assess the performance of the framework. Given that the proposed controller is for the purpose of mitigating large magnitude wave-induced disturbances, real-world data was sourced and exploited to construct a representative

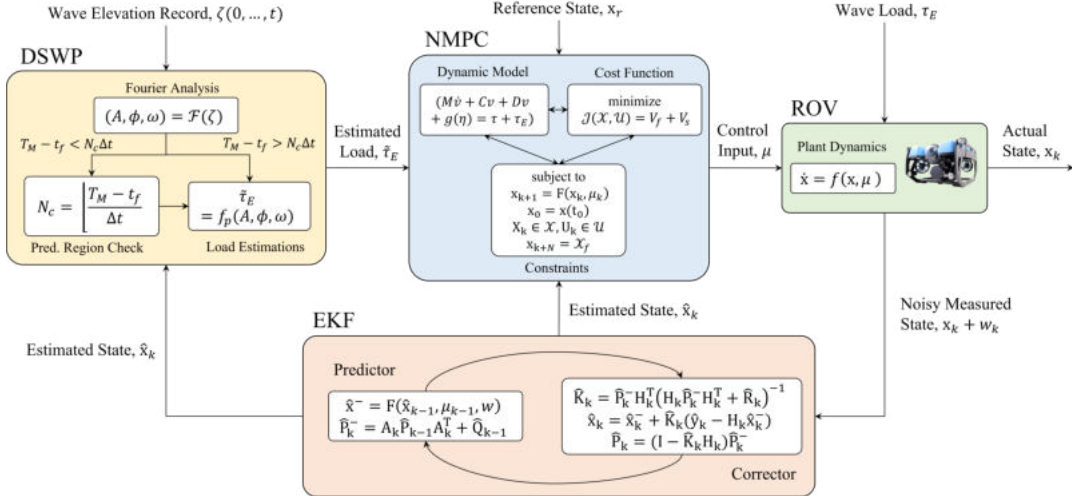


FIGURE 5.11: The proposed framework for predictive disturbance mitigation, showing each element in block diagram format. In the DSWP block,  $f_p$  is a function which transforms the spectral parameters into wave loading; see Eq. 5.9.

TABLE 5.5: Statistical parameters for the 3 wave spectra considered in Chapter 5, varying in peak spectral period and significant wave height.

Case Reference	Peak Period (s)	Significant Wave Height (m)
W1	7.1	2.78
W2	9.5	3.47
W3	11.1	3.24

sea state of a region of the North Sea. The spectral data is the same set used for the analysis in Chapter 4, harvested by a wave buoy located in the Moray Firth and sourced from the online repository of Cefas [246]. As mentioned during the earlier analysis in Section 4.4, the location of the buoy was chosen primarily due to the majority of offshore wind farms being located in areas of similar depth ( $d = 54\text{m}$ ) or below[311, 312] - an offshore wind development is also currently under construction at this location [313].

The vehicle behaviour was simulated under the three different sets of environmental conditions, varying in significant wave height and peak period to demonstrate performance under a variety of wave disturbances. The key parameters of the chosen spectral data are recapped in Table 5.5, previously plotted in Fig. 4.17 to demonstrate how these vary. Large significant wave heights were purposefully chosen to demonstrate the effectiveness of the system in harsh conditions. Each simulation was performed over a 600s temporal segment with a resolution of  $\Delta t = 0.1\text{s}$ . Wave-height measurements were recorded for the initial 300s ( $t_m = 300\text{s}$ ) from a fixed point upstream of the ROV at a distance of  $x_p = 50\text{m}$  from the wave measurement point taken here as  $x_m = 0\text{m}$ . The distance required in these simulated instances are larger than those tested experimentally (Section 4.3) due to the larger peak spectral period tested. The ROV was then simulated to perform a station keeping task for the final

TABLE 5.6: BlueROV2 Heavy dimensions and hydrodynamic parameters utilised in the simulations; data based on [46, 300, 308].

Parameter	Nomenclature	Value	Unit
Weight	$W$	112.8	N
Buoyancy	$B$	114.8	N
Vehicle Length	$l$	457	mm
Vehicle Width	$b$	575	mm
Vehicle Height	$h$	254	mm
Rotational Inertia, $y$	$I_y$	0.253	$\text{kgm}^2$
Added Inertia, $x$	$X_{\dot{u}}$	10.57	kg
Added Inertia, $z$	$Z_{\dot{w}}$	18.68	kg
Added Inertia, $\theta$	$M_{\dot{q}}$	0.65	$\text{kgm}^2$
Added Inertia, $x/\theta$	$X_{\dot{q}}, M_{\dot{u}}$	0.67	$\text{kgm}$
Linear Drag Coefficient, $x$	$X_u$	13.7	$\text{kg/s}$
Linear Drag Coefficient, $z$	$Z_w$	33	$\text{kg/s}$
Linear Drag Coefficient, $\theta$	$M_q$	0.80	$\text{kgm}^2/\text{s}$
Quadratic Drag Coefficient, $x$	$X_{u u }$	141	$\text{Ns}^2/\text{m}^2$
Quadratic Drag Coefficient, $z$	$Z_{w w }$	190	$\text{Ns}^2/\text{m}^2$
Quadratic Drag Coefficient, $\theta$	$M_{q q }$	0.47	$\text{Nms}^2$
Centre of Buoyancy	$\mathbf{r}_B$	[0, 0, 0.028]	m
Maximum Thrust	$T_{max}$	35	N
Thruster Offset	$\alpha$	45	°
Thruster Moment Arm, $\theta$	$l_x$	0.12	m

TABLE 5.7: Parameters for the different ROV control strategies, both MPC and PD related.

Parameter	Nomenclature	Value
Prediction Horizon	$N_c$	$20\Delta t$
State Weight Matrix	$\mathbf{Q}_{\mathbf{x}}$	$\text{diag}(250, 250, 250)$
Terminal State Weight Matrix	$\mathbf{P}_{\mathbf{x}}$	$\text{diag}(250, 250, 250)$
Control Weight Matrix	$\mathbf{R}_{\mu}$	$\text{diag}(1, 1, 1)$
Positional Proportional Gain	$\mathbf{K}_p$	$\text{diag}(1.2, 1.2, 0.5)$
Derivative Gain	$\mathbf{K}_d$	$\text{diag}(3, 3, 1)$
Velocity Proportional Gain	$\mathbf{K}_{p,v}$	$\text{diag}(1.2, 1.2, 0.5)$

300s, attempting to maintain a stationary position beneath the surface by exploiting the disturbance predictions obtained through the DSWP algorithm. Solving for the subsequent state  $\mathbf{x}_{k+1}$  was evaluated through numerical integration over the discrete time interval  $\Delta t$ , using a fourth-order variable step Runge-Kutta method. In all cases, the ROV was tasked with maintaining a stationary position at a fixed depth of  $z = -5\text{m}$ , exposing the vehicle to significant wave-induced disturbances. The vehicle geometric and hydrodynamic parameters are provided in Table 5.6, whilst the control parameters are given in Table 5.7. Remaining hydrodynamic parameters which were

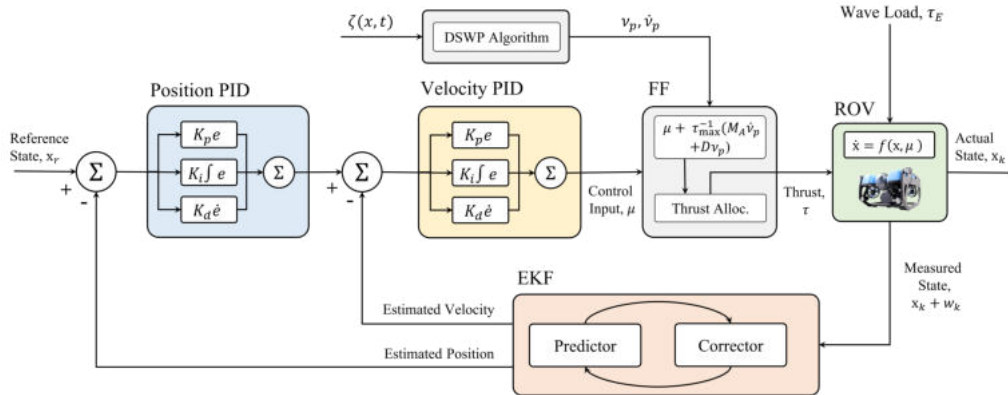


FIGURE 5.12: Block diagram of the feed-forward disturbance mitigation technique, with the grey blocks representing the generation of the additional compensating control actions. Here, the thrust allocation algorithm refers to Eq. 3.61 and the generalized control law in Eq. 5.21.

unavailable were evaluated using WAMIT [309], for example  $X_{\dot{q}}$  and  $M_{\dot{u}}$ .

As a further element to the study, an analogous set of simulations utilising the same configuration as detailed above were performed, however different sources of noise were considered to be affecting the system. Sensor noise was considered in every test and was injected into the wave profile measurements, simulating white noise inherent to (for example) a wave-rider buoy or pressure sensor. Likewise, in separate tests noise was also directly injected into the spectral components obtained by the DSWP algorithm, with the aim of simulating a non-perfect spectral prediction. These are all elements which would affect the real-world deployment of the system, thus it was a critical element of the study to infer robustness under these conditions.

### Baseline Controllers

To comparatively analyse the performance of the proposed framework, the NMPC with DSWP controller was compared against two baseline controllers; a C-PD controller and a C-PD with feed-forward (FF) controller (referred to as FF from henceforth). The former is to provide a basic reference against a standard feedback controller deployed in industry, with the latter incorporating the prediction algorithm to calculate disturbance compensating control actions (but without an optimisation stage on the control trajectory). The block diagram of the FF controller architecture is given in Fig. 5.12 and described in Algorithm 3; for the C-PD controller, the architecture is similar with the DSWP sub-diagram removed as shown in Fig. 5.13. It is postulated that the FF controller will still provide performance improvement but at a fraction of the computation power of an NMPC. In scenarios where wave perturbations are lower, this may be a more appropriate solution. Throughout the analysis, the comparison focuses on these two predictive control schemes as these both incorporated the DSWP algorithm and are therefore closer aligned and of more interest in terms of performance.

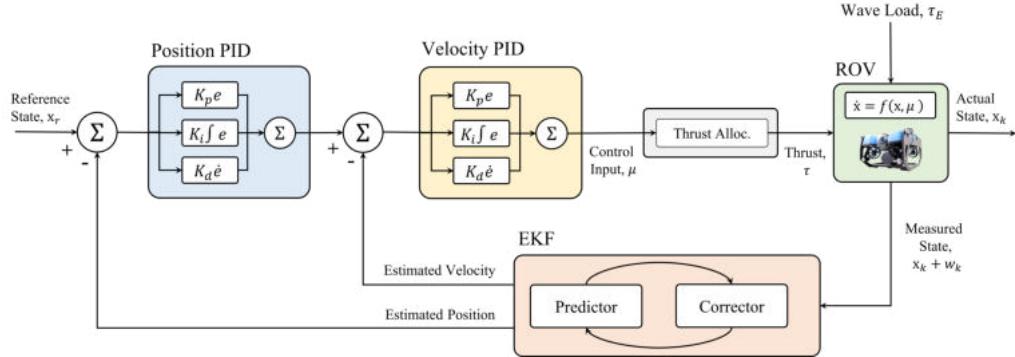


FIGURE 5.13: Block diagram of the feedback Cascaded Position-Velocity PID Controller, with the grey block referring to the thrust allocation algorithm refers to Eq. 3.61 and the generalized control law in Eq. 5.20.

---

**Algorithm 3** Feed-forward Predictive Control Algorithm at  $t_k$ 


---

- 1: Estimate the system state  $\hat{\mathbf{x}}_k$
  - 2:  $\mathbf{x}_k \leftarrow \hat{\mathbf{x}}_k$
  - 3: Execute Algorithm 1 for  $(x_p, z_p) \leftarrow \mathbf{x}_k$ .
  - 4: Calculate the feed-forward compensation control action according to Eq. 5.9.
  - 5: Evaluate the modified control action  $\boldsymbol{\mu}_{FF}$  according to Eq. 5.21 to be allocated (Eq. 3.61).
- 

The generalised control laws for the C-PD controller and FF controller are defined as:

$$\boldsymbol{\mu}_{PD} = \mathbf{K}_{p,v}\{\boldsymbol{\nu} - (\mathbf{K}_p\mathbf{e} + \mathbf{K}_d\dot{\mathbf{e}})\} \quad (5.20)$$

$$\boldsymbol{\mu}_{FF} = \boldsymbol{\mu}_{PD} + \tau_{max}^{-1} \odot (\mathbf{M}\dot{\boldsymbol{\nu}}_p + \mathbf{D}(\boldsymbol{\nu}_p)\boldsymbol{\nu}_p) \quad (5.21)$$

where  $\mathbf{e}$  is the positional error between the reference set-point and current vehicle state. For the FF controller,  $\boldsymbol{\nu}_p$  is the fluid velocity vector at the vehicle location. Each controller exploits the EKF as a state estimator to account for the inherent uncertainty associated with measuring the vehicle state in real-world scenarios. This emulates the presence of sensor noise and implements a method to minimise the effects.

### Nonlinear Solver Method

Specifically for the NMPC, the control problem is inclusive of solving an online nonlinear optimisation problem. Inherently, this can cause issues relating to the non-convex nature of the problem, such as convergence issues and increased computation time. With this in mind, an appropriate solver and solver method were required which can mitigate these issues as best as possible. For this purpose, CasADi was chosen (in particular the OPTI feature) which is an open source tool specifically tailored towards solving nonlinear optimisation problems fast. CasADi has several inbuilt features which are highly useful for this work, such as the ability to set up a Runge-Kutta

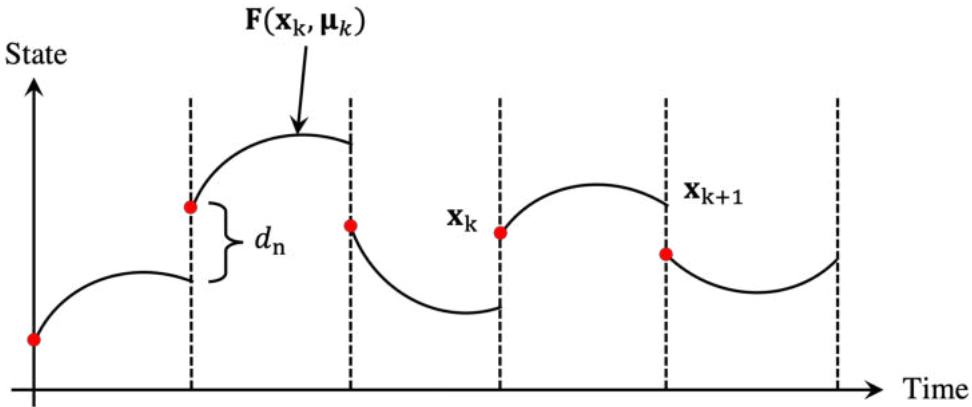


FIGURE 5.14: Multiple shooting method; dynamic feasibility is achieved once the gaps denoted by  $d_n$  are closed and a solution has been found.

integration method and different solver options - in our case, the Operator Splitting Quadratic Program (OSQP) solver [319] was selected.

In conjunction with this, the direct multiple shooting method was adopted which is well-known to generally improve convergence rates [71]. Direct multiple shooting involves taking the time period over which a solution is desired (in this instance this would be the NMPC prediction horizon) and segmenting this into smaller intervals, as shown in Fig. 5.14. The problem is then solved over each of these smaller intervals and the results are matched to form a complete solution over the entire time period. In contrast, a single shooting method considers the whole interval and a solution of discretized control inputs as one. As noted in the CasADi documentation, the multiple shooting method is generally better than the single shooting method due to the problem being handled in higher dimensions, thus improving convergence. Although using multiple shooting increases the size of the nonlinear problem, it becomes much sparser and thus a trade-off is typically achieved to maintain a reasonable computation time. An alternative method that could have been adopted is direct collocation, which approximates the state and control using polynomial splines. The properties of these polynomials simplify the involved integration calculations and thus the computation time is reduced significantly.

Between the three methods considered, multiple shooting was deemed to be the most appropriate. This is due to the control actions being relatively simple to generate (allocation can be calculated using a pseudo-inverse method, Eq. 3.61) and the nonlinear dynamics will be handled better than using a single shooting method. Similarly, a higher degree of accuracy is expected over direct collocation and processing time is not expected to be inordinate; although the dynamics are nonlinear, the problem dimensions are not excessive.

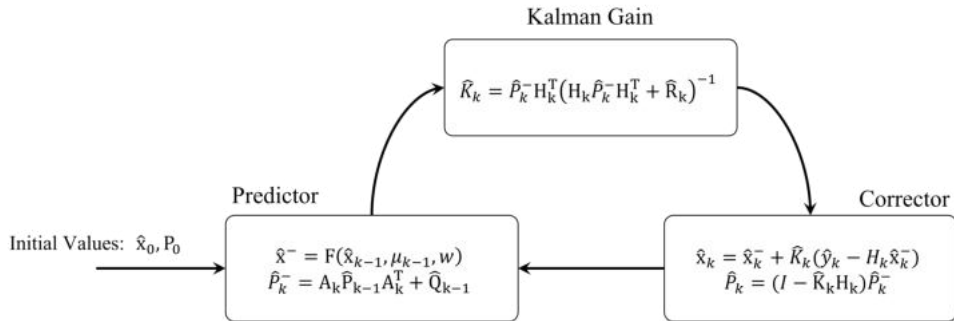


FIGURE 5.15: Block diagram representation of the Extended Kalman Filter (EKF).

### 5.5.2 State Estimation

The control formulations discussed throughout this thesis (inclusive of feedback) assumes that the vehicle state is known in order to compute the control actions. This is a critical factor relating to real-world deployment, which is typically tackled using an array of sensors such as but not limited to IMU's, Global Positioning Systems (GPS) or vision for example. In an underwater scenario, this factor becomes slightly more difficult to address due to the unstructured nature of the environment and the inability to utilise methods such as GPS. In some cases where turbidity is high, this restricts the applicable methods even further as vision can no longer reliably be utilised. However, there are methods to tackle this issue such as the use of Doppler Velocity Logs (DVL's) or sonar amongst others. Therefore, it is assumed that (at minimum) a noisy measurement of either the vehicle position or velocity can be obtained using some form of sensor reading can be extended to form the full vehicle state. This provides the required information for the NMPC to proceed and compute the optimal trajectory, in conjunction with the wave estimations and prescribed vehicle reference pose. It should also be noted that knowledge of the vehicle state is paramount for estimating the disturbances, as the algorithm presented in Section 5.2 requires a position ( $x, z$ ) to be specified to build the predicted fluid trajectories.

Considering these requirements, an EKF [320] was selected as an appropriate method to estimate the vehicle state. This was formulated on the basic assumption the vehicle position or velocity is measurable and extends this to approximate the full state. This can be performed vice-versa and which form of EKF that is deployed would depend on the sensors available on the vehicle. In our case, the position of the vehicle was assumed to be measurable as this would be the process adopted in experimental studies at the FloWave tank, where the same Qualysis system could be exploited as in the experiments in Section 4.3.

**Assumption 5.5.1** *An initial estimate of the state and state error covariance matrix can be obtained, that is*

$$\hat{x}_{k-1} \neq \{\}, \quad \hat{P}_{k-1} \neq \{} \quad (5.22)$$

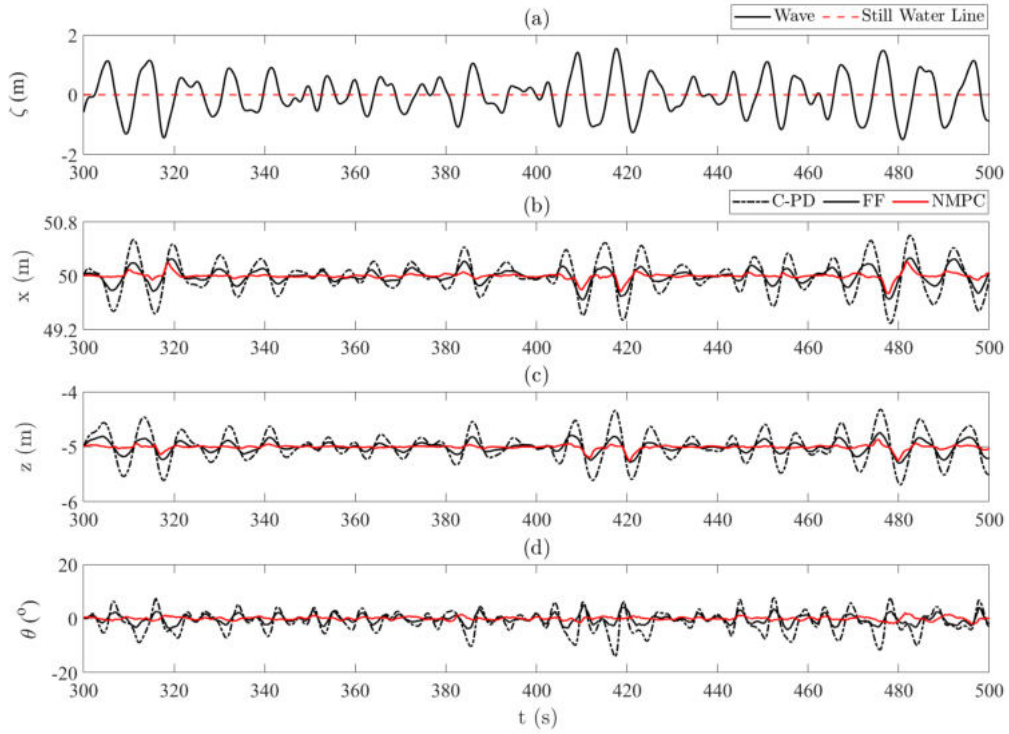


FIGURE 5.16: Temporal segment of the station keeping simulation, showing the positional evolution for case W2. Here, the reference state is defined as  $\mathbf{x}_r = [50, -5, 0]\text{m}$  in the global frame and the model is assumed to be accurate; measurement noise is still considered.

An EKF is the nonlinear counterpart to the linear Kalman Filter (KF) [321, 322] which is considered the optimal estimator for linear models with additive white noise. Essentially, an EKF linearises the nonlinear system dynamics (Eq. 3.31) around an operating point or trajectory through a Taylor series expansion. Alternatively, the modified version in the form of an Unscented Kalman Filter (UKF) was considered as a solution [323, 324], however the EKF was considered sufficient for this case and is a more established and well-known tool used within the field. The EKF algorithm consists of two update phases; the *predictor* phase and the *corrector* phase connected through a gain calculation, as shown in Fig. 5.15. The predictor phase considers the initial estimates of the state,  $\hat{\mathbf{x}}_{k-1}$ , and error covariance,  $\hat{\mathbf{P}}_{k-1}$ , and projects these ahead in time, such that:

$$\hat{\mathbf{P}}_k^- = \mathbf{A}_k \hat{\mathbf{P}}_{k-1} \mathbf{A}_k^T + \hat{\mathbf{Q}}_{k-1} \quad (5.23)$$

$$\hat{\mathbf{x}}_k^- = F(\hat{\mathbf{x}}_{k-1}, \boldsymbol{\mu}_{k-1}, \mathbf{w}) \quad (5.24)$$

where  $\mathbf{A} = \frac{dF}{dx}|_{\mathbf{x}=\hat{\mathbf{x}}}$  is the linearised state transition matrix,  $\hat{\mathbf{Q}}$  is the process error covariance and  $\mathbf{w}$  represents the process noise.

From this, the corrector phase proceeds to compute the Kalman gain:

$$\hat{\mathbf{K}}_k = \hat{\mathbf{P}}_k^- \mathbf{H}_k^T (\mathbf{H}_k \hat{\mathbf{P}}_k^- \mathbf{H}_k^T + \hat{\mathbf{R}}_k)^{-1} \quad (5.25)$$

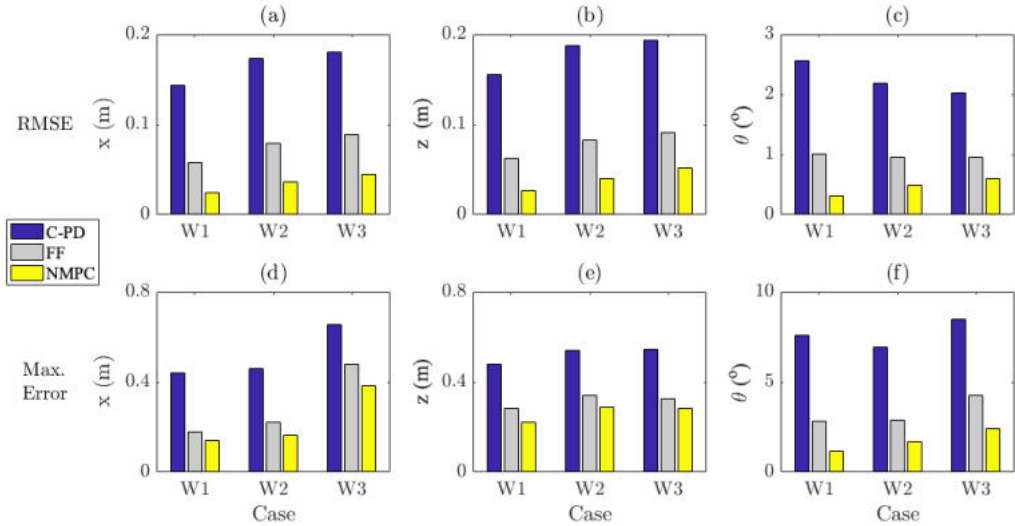


FIGURE 5.17: (a)-(c) RMSE and (d)-(f) maximum error observed for each DoF and sea state considered for the station keeping mission, considering only sensor noise with zero additional spectral noise.

where  $\mathbf{H}$  is a measurement matrix,  $\hat{\mathbf{R}}$  is the measurement error covariance, subsequently updating the estimate with a measurement  $\hat{y}_k$

$$\hat{\mathbf{x}}_k = \hat{\mathbf{x}}_k^- + \hat{\mathbf{K}}_k(\hat{y}_k - \mathbf{H}_k\hat{\mathbf{x}}_k^-) \quad (5.26)$$

Similarly, the error covariance is also corrected in this stage before looping back to Eq. 5.23 and repeating for every time-step  $k$ :

$$\hat{\mathbf{P}}_k = (\mathbf{I} - \hat{\mathbf{K}}_k \mathbf{H}_k) \hat{\mathbf{P}}_k^- \quad (5.27)$$

The EKF is very-well known tool and has been proven to be reliable in various dynamic control applications, both marine-based [165, 98, 325, 326] and outwith [201, 327].

### 5.5.3 Simulation Results

#### Station Keeping Accuracy

Initial analysis focused on the comparative performance against the two baseline controllers with minimal uncertainty in the system - throughout these tests, only noise arising from sensor measurements were considered, inclusive of both wave gauge and state. A Gaussian filter was applied to the wave height measurements, whilst the EKF was utilised to reduce the uncertainty associated with the state measurements and produce the full-state vector. To visualise the temporal evolution of the vehicle behaviour during the station keeping mission, a segment of the simulation for case W2 is displayed Fig. 5.16. For all cases and DoF, the RMSE was analysed along

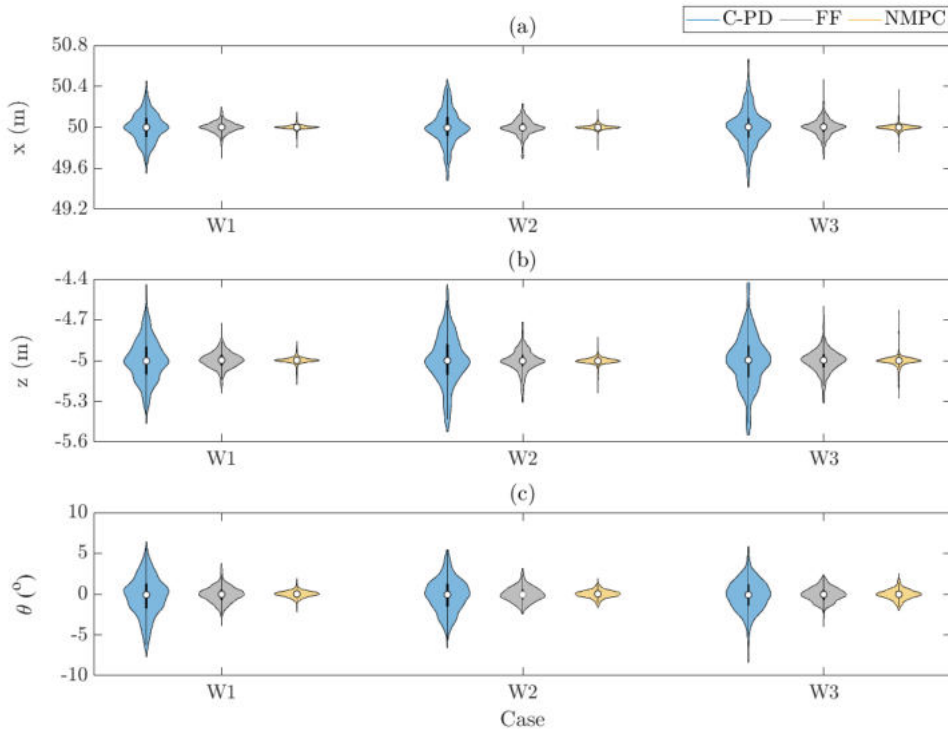


FIGURE 5.18: Violin plot highlighting the density of positional error with respect to each wave case and control strategy. A shorter violin refers to lower variance in error, hence the control is regulating the state with greater effect.

with the maximum error that was recorded throughout the entire temporal segment for reference. The results are displayed in Fig. 5.17.

As anticipated, the NMPC method produces both the lowest RMSE and the lowest maximum error, however it was noted that the disparity in maximum error was much lower with some instances returning only  $\approx 14\%$  improvement over the FF method (heave, case W3). For the surge and heave, a mean improvement in RMSE of  $\approx 52\%$  was witnessed between the NMPC and FF methods, whilst the pitch RMSE was reduced by  $\approx 51.5\%$  showing consistent improvements irrespective of DoF. With respect to maximum error, the mean improvement in RMSE was lower at  $\approx 19.5\%$  and  $\approx 48\%$  for the linear and angular motions respectively, still showing fair improvements particularly for the pitch. Although maximum errors of up to 0.38m and  $2.4^\circ$  were witnessed even for the NMPC method (Case W3), these only occur at short time intervals across the entire mission, supported by the low RMSE observed. The disturbances considered in this work represent an upper bound of those sampled in this geographical region, so the values recorded are very promising - as these methods rely on deterministic processes, it would be possible to specify a safe operational distance relative to the magnitude of wave disturbances, which could also dictate which method is more suitable on a case-by-case basis. A further interesting observation was that the pitch displacement remained low even when using the C-PD method, with a maximum value of  $8.47^\circ$  recorded; the vehicle is naturally restoring

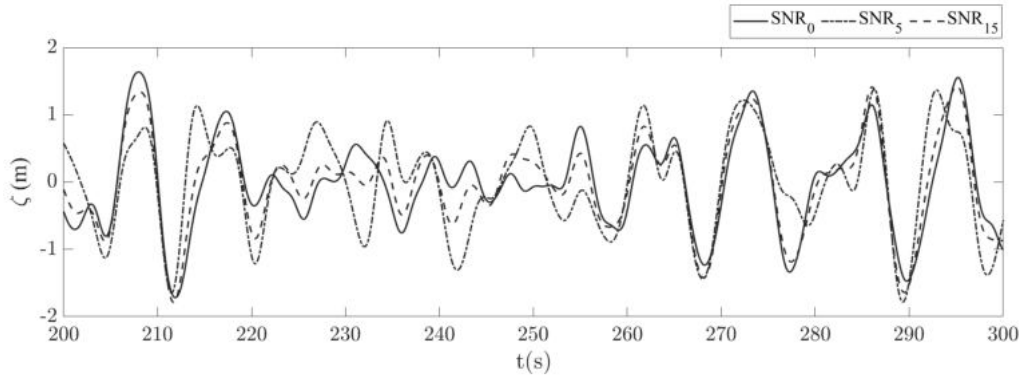


FIGURE 5.19: Effect on the recorded waveform associated with Case W3 when varying levels of spectral noise are added to the output component amplitudes and phases from the DSWP algorithm.

at  $\theta = 0^\circ$ , so the control required to minimise displacement can be less aggressive. The advantage of this is the potential to reduce the computational overhead of the control by only applying a predictive method to the lateral motions, using a typical feedback controller specifically for the pitch plane to reduce the angular displacement sufficiently. This would allow quicker convergence during the optimisation stage and thus assist with applicability to real-time applications.

Finally, Fig. 5.18 displays a violin plot of each test case; a violin plot shows the distribution of the data by using a relative width proportional to the frequency of occurrence. From this, the ability of the NMPC to constrain the vehicle motion to remain largely within a narrow band of positional error is clear, dictated by the shorter and wider plots in all cases and all DoF. Particularly for the surge and heave, the variation in positional error is reduced significantly, in conjunction with the maximum error as previously mentioned. Even when adopting the FF strategy, the frequency of data points recorded in the vicinity of the reference position is clearly apparent, demonstrating that the predicted disturbances are being mitigated effectively.

### System Uncertainty

With the goal of expanding the simulations to feature realistic uncertainties that would be encountered in the field, a large piece of analysis performed in this work focused on the introduction of various sources of noise and disparities in the model. Although sensor noise was considered in all simulations, this can be fairly easily mitigated with standard filtering techniques such as the Gaussian filter and EKF used in this work. As was witnessed in the experimental study presented in Section 5.3, the spectral parameters obtained will not be an exact representation of the real-world sea state; at sea various sources of noise will confound the measurements and this interference will skew the wave spectral parameters. To emulate this, Gaussian noise was directly injected to the output amplitude and phase of the DSWP inferred spectral components, simulating the conditions where predicted and encountered wave

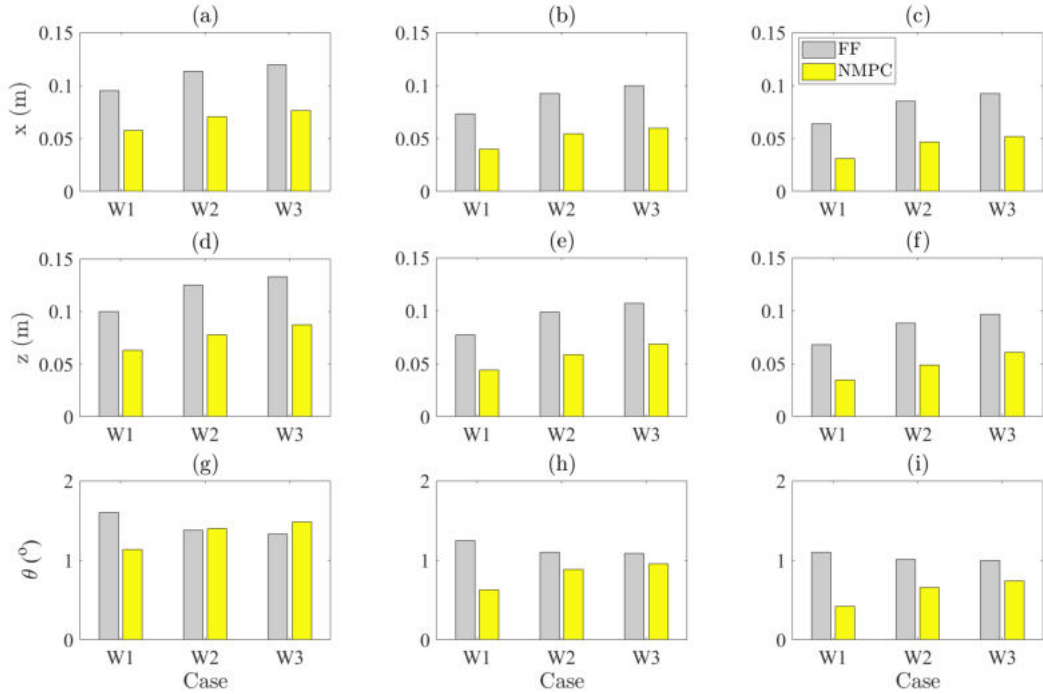


FIGURE 5.20: RMSE error for each DoF and sea state considered when different levels of spectral noise are considered, showing measured white gaussian noise with a (a)(d)(g) SNR = 5, (b)(e)(h) SNR = 10 and (c)(f)(i) SNR = 15 and the comparison between the FF and NMPC schemes.

disturbances differ. The cases covered in this analysis involved Signal-to-Noise Ratios (SNRs) of 5, 10 and 15; Fig. 5.19 demonstrates how these levels of SNR affect the interpreted waveform by the controller against the wave experienced by the vehicle, where  $\text{SNR}_0$  is the ground truth. As with the results presented in Section 5.3, the waves show higher similarity where the profile is well-defined (the period 260 – 275s is a good example of this) and wave height is largest, i.e. points where the spectral noise has least effect.

The performance of the controllers subject to varying degrees of sensor noise are shown in Fig. 5.20. For almost all cases the NMPC outperforms the FF scheme, analogous to the previous cases tested which assumed exact spectral knowledge. The only situation in which the FF performed slightly better was in the pitch plane when considering large amounts of spectral noise (Cases W2 and W3). This is likely due to the fact the vehicle pitch is easily influenced by control actions, thus is more susceptible to unwanted motions if the predictions are not reasonably accurate. This being said, the pitch RMSE never exceeds  $2^\circ$  and so this difference is irrelevant when considering the broader goal. In the surge and heave DoF, a mean reduction across all cases of  $\approx 41\%$  in RMSE between the FF and NMPC schemes was witnessed, showing that even in the presence of significant spectral noise the inclusion of the optimisation step greatly increases station keeping performance.

With reference to the cases presented in Section 5.5.1, the largest increase in RMSE when considering a non-exact wave prediction was  $\approx 19.5\%$  and  $\approx 51\%$  for

TABLE 5.8: Power consumed during the station keeping mission for each wave case and control strategy when the spectral components are perturbed by varying levels of noise. As the C-PD controller does not use the spectral information, the values for the ideal case refer to all cases.

Case	Controller	Power Consumed (W)			
		SNR <sub>0</sub>	SNR <sub>5</sub>	SNR <sub>10</sub>	SNR <sub>15</sub>
W1	C-PD	17.14	—	—	—
	FF	38.51	45.45	40.75	38.23
	NMPC	52.21	87.83	70.66	58.80
W2	C-PD	23.80	—	—	—
	FF	47.08	52.04	46.78	46.13
	NMPC	56.49	99.36	77.80	62.15
W3	C-PD	20.59	—	—	—
	FF	37.83	47.56	40.93	38.94
	NMPC	47.98	88.9	74.73	57.55

the linear and angular motions respectively. It is key to note here that the absolute values of pitch displacement are minimal, thus even though the spectral noise had a significant effect, in absolute terms the station keeping accuracy remains high. These findings demonstrate that the inclusion of even relatively coarse predictions can improve performance substantially, with the inclusion of an optimisation stage over a horizon improving this further.

### Power Efficiency

Although these initial results show promise from the perspective of minimising displacement, this increase in performance naturally coincides with a trade-off in energy expenditure. Model-based predictive control architectures are able to perform better by generating control actions to constantly counteract the wave, however the caveat is that larger control forces will be generated. To this end the power consumed during the station-keeping mission for each simulation was estimated and analysed. It should be noted that this analysis does not consider the hotel load of the vehicle and only concerns the power consumed by any control actions. Regarding this and exploiting data provided by the manufacturer [300] for the T200 thruster (fully-flooded brushless motor, polycarbonate plastic propeller), the power for a typical operating voltage of 16V was approximated as:

$$P_\tau = \sum_{i=1}^8 0.0011\tau_i^3 + 0.0208\tau_i^2 + 0.2970\tau_i \quad (5.28)$$

where  $P_\tau$  is the power consumed by the control actions for all thrusters and  $\tau_i$  is the i-th thruster (the BlueROV2 possessing 8 in total). The cumulative power over

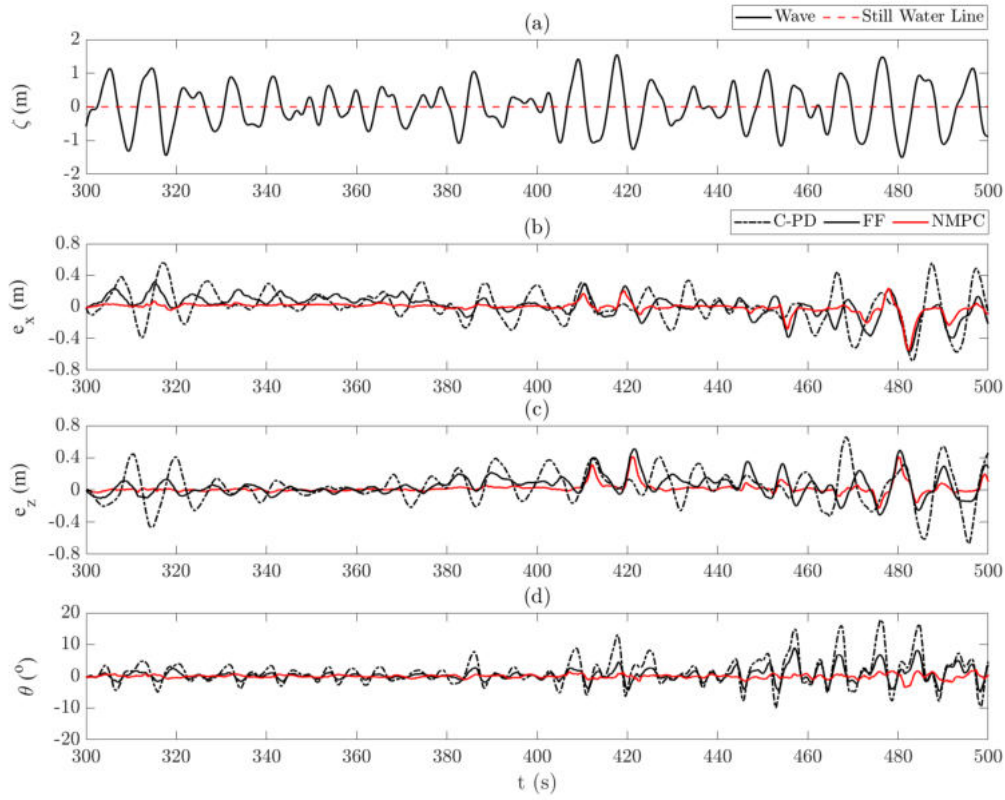


FIGURE 5.21: Temporal segment of the trajectory tracking mission for the (a) wave in case W2, displaying the positional error relative to the trajectory in the (b) surge, (c) heave and (d) pitch.

the entire mission was evaluated as a time-averaged summation.

Power expenditure are evaluated both in the cases with non-noisy spectral data and in the case with noisy spectral data (Table 5.8), similar to those shown in Fig. 5.19. Firstly considering the non-noisy spectral data case where the variation between predicted and encountered sea state is purely a product of sensor noise on the state and wave gauge, the relative increase in performance surpassed the relative increase in power consumption for all cases. A mean increase of  $\approx 27.5\%$  in consumed power coincided with a mean reduction of linear station keeping error of  $\approx 52\%$ , whilst also reducing the pitch error by  $\approx 51.5\%$  indicating that the additional energy required is utilised to good effect. The consumed power is found to increase with increasing spectral noise, however the increase is much sharper for the NMPC method which is most likely attributed to the controller attempting to minimise the cost function, as opposed to the one-step estimated control action produced by the FF scheme. For high spectral noise, the power consumed when using the NMPC method was almost double that of the FF method for case W2, showing a much higher dependence on accurate disturbance predictions to minimise consumed power. Between the instances when considering an SNR of 5 and 15 of spectral noise the power consumed increased by  $\approx 54.5\%$  for the NMPC, whilst only an increase of  $\approx 18\%$  was witnessed for the FF cases, again supporting the previous hypothesis relating to the optimisation stage.

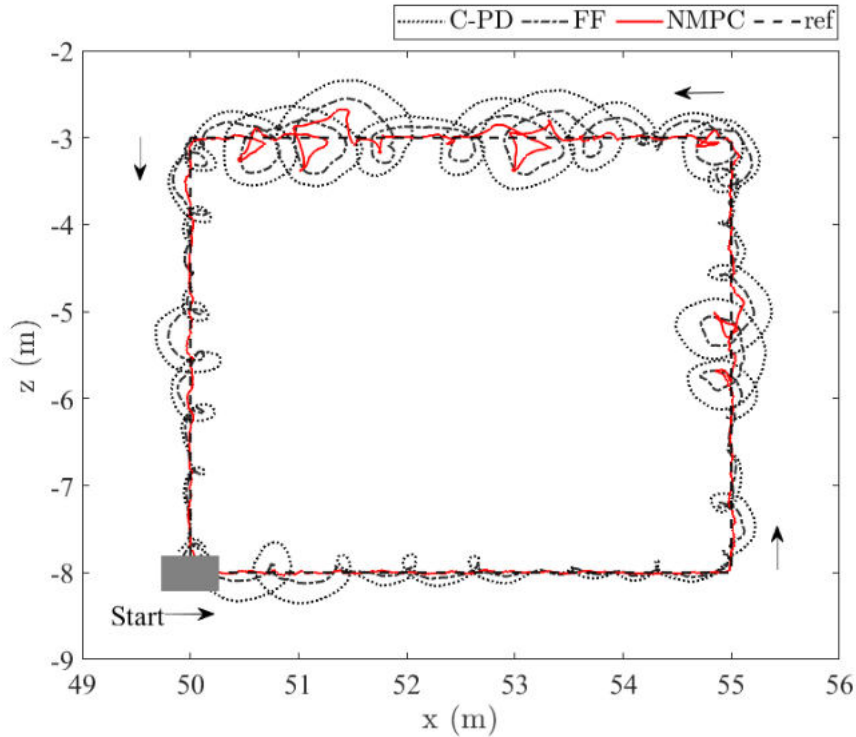


FIGURE 5.22: Trajectory tracking spatial comparison for case W2.

The underlying finding from this analysis is that when power consumption is not a critical factor (such as tethered operations) or when station-keeping accuracy is crucial, the NMPC method offers much higher performance. However, the FF scheme is still capable of offering improved station keeping performance over the C-PD method, but at a fraction of the power cost relative to the NMPC method. For operations where high accuracy isn't required and operation longevity is more critical, a FF-based method could be a viable solution for reducing perturbations arising from wave-induced disturbances.

### Trajectory Tracking

As an additional point of analysis, the proposed framework was also tested for an alternative mission of following a square trajectory under disturbances from a wave field; this could relate to a typical inspection task over a specified area. To do so, the disturbance prediction must be amended to consider the time-varying position of the vehicle along the trajectory. With the prediction method being purely deterministic, this can be conveniently accomplished by varying the prediction point through the output of the EKF and ensuring the predictable region is still sufficient in length for the NMPC. The uncertainty within the system here is majorly based on these two parameters; if a fairly accurate positioning system is deployed such as (for example) a DVL, this can be minimised and reasonable predictions obtained according to the results in Chapter 4.

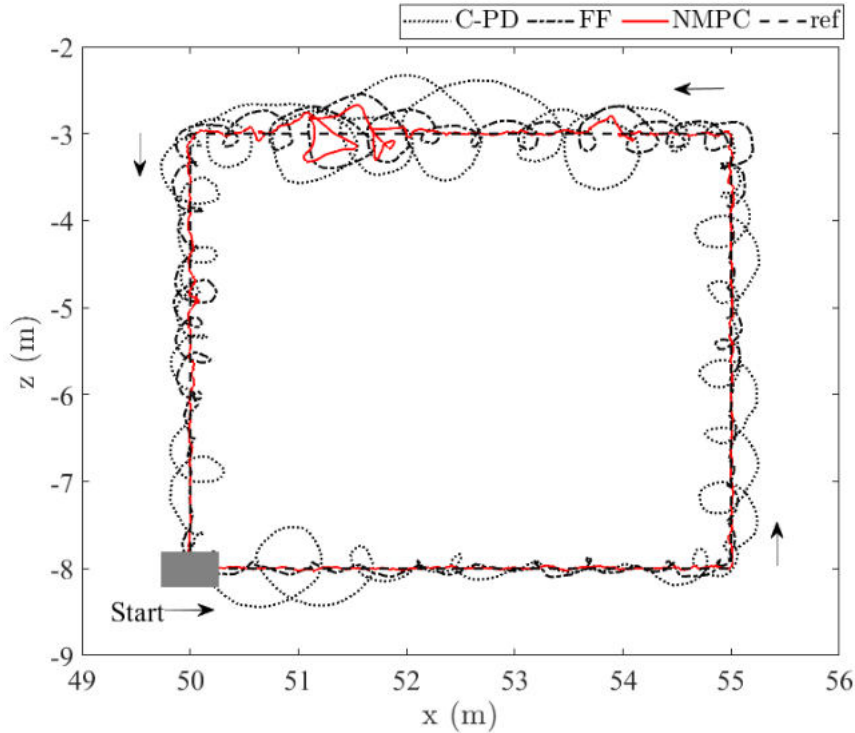


FIGURE 5.23: Trajectory tracking spatial comparison for case W1.

With regards to this, the start and end point of the tracking mission was specified at  $(50, -8)$ m with respect to the prediction point at  $(0, 0)$ m (the sea-surface). The mission was then specified to translate forward 5m longitudinally, ascend 5m, translate backward 5m longitudinally and finally descend 5m back to the original position all whilst minimising pitch displacement. This is shown in Fig. 5.21-5.24, firstly showing a temporal segment of the vehicle behaviour for case W2 (Fig. 5.21) before depicting the spatial directions of motion and the performance of the three different control strategies in tracking the reference (Fig. 5.23-5.24). Visually, the circular trajectories are an interesting trait as these relate to the wave-induced particle motions; these are naturally elliptical and decay exponentially with depth [298], hence the displacements are much more apparent at 3m depth. This can also be observed by the fact that in Fig. 5.24 the C-PD controller undergoes larger circular motions at 8m, demonstrating the disturbances propagating deeper beneath the free surface. Qualitatively it is apparent from this that the NMPC is the most accurate, with the vehicle very rarely diverging from the reference apart from one instance - unsurprisingly this relates to a point when the wave height is largest and the operational depth is lowest, thus disturbances are largest.

Quantitative measures of performance are also presented, with the RMSE across the entire mission shown in Fig. 5.25 for instances where spectral noise is both considered and neglected. Even in the instances where the spectral components are considered inaccurate, the NMPC strategy outperforms the FF strategy owing to the optimisation stage of the control, allowing projection of the disturbances relative to

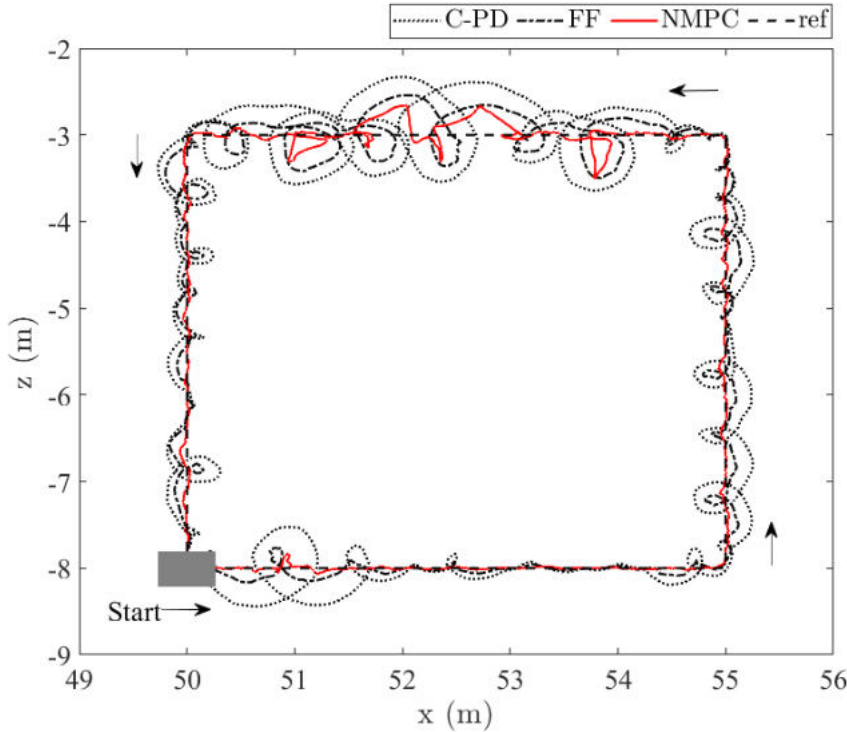


FIGURE 5.24: Trajectory tracking spatial comparison for case W3.

the vehicle trajectory. At minimum across all cases there was a reduction of  $\approx 42\%$  in the surge,  $\approx 41\%$  in the heave and  $\approx 5\%$  in the pitch when comparing the NMPC with noise case to the ideal FF case. The reduction in the pitch is not as significant as expected, mainly due to the operational depth and the fact that the natural restoring forces of the vehicle assist in maintaining an equilibrium even without active control.

In terms of the effect of spectral noise on performance, the degradation appears marginal which supports the claim that disturbance estimations can feature some inaccuracy and still be exploited to good effect. In the lateral motions, an average relative increase of  $\approx 5\%$  was witnessed for the FF scheme, whilst  $\approx 30\%$  was witnessed for the NMPC scheme suggesting that the latter is more susceptible to noise. However, in absolute terms the error is still maintained  $< 0.1\text{m}$  and the increase is minimal, showing greater tracking performance in general. In terms of the pitch, the increase was more significant with case W2 showing a 90% relative increase, but again the error was maintained at  $\approx 1^\circ$  across all cases - well below an acceptable threshold of high performance.

As with all cases considered in this work, the power consumed naturally increases when deploying the predictive control methods, however what is interesting is that minimal difference was observed in power consumed for the FF method when neglecting and considering spectral noise. Interestingly, the consumed power actually decreased for the FF strategy by  $\approx 2 - 3\text{W}$  across all cases. This is likely attributed to poor disturbance predictions leading to less aggressive corrective action, supported

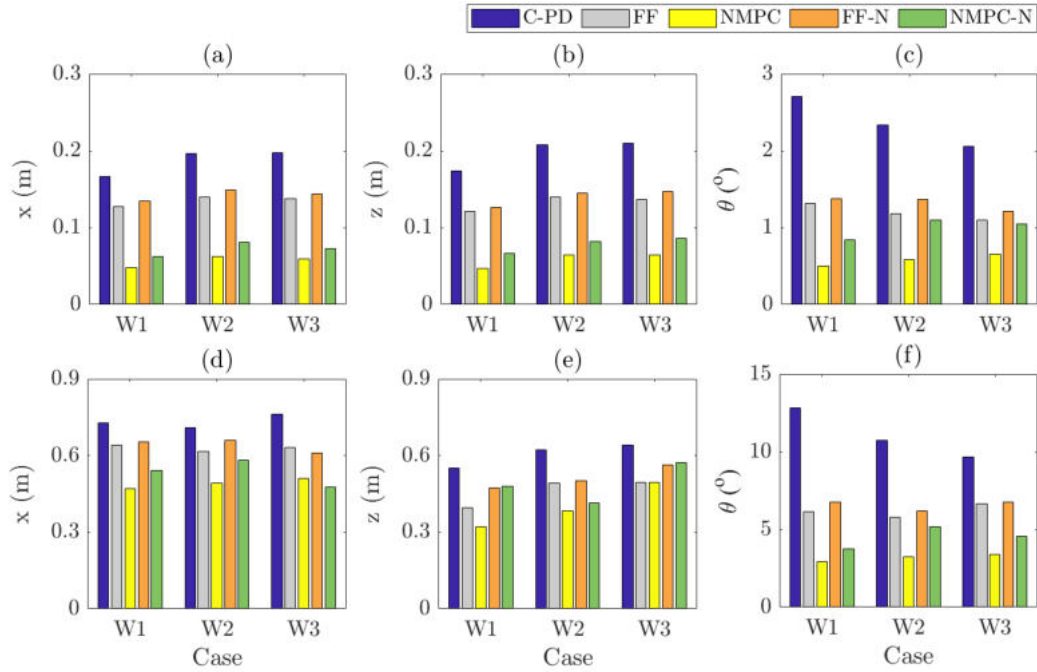


FIGURE 5.25: (a)-(c) RMSE and (d)-(f) maximum error for each DoF and sea state considered for the trajectory tracking mission, where FF-N and NMPC-N refer to cases where measured white gaussian noise with a SNR = 10 is injected directly to the spectral components output by the DSWP algorithm.

by the increase in positional error shown in Fig. 5.25. A comparison of power consumption scaled relatively to RMSE is displayed in Fig. 5.26(b), which provides a metric to rigorously compare the improved control performance against added power expenditure. Here, the reciprocal of the power is scaled by  $1/\text{RMSE}$  to provide an intuitive measure of efficiency which scales approximately proportionally. This relative ratio shows similar behaviour across all wave cases, fluctuating between  $0.4 - 0.5 \text{W/m}$  for case W1 and  $\approx 0.2 \text{W/m}$  for the other two cases. This supports the statement that the additional power consumed by the predictive strategies is utilised effectively, with longer wavelengths exhibiting comparable behaviour. This is interesting, as it could indicate a potential inflection point of spectral period where the performance increase to consumed power relationship plateaus. For calmer conditions, the FF method may be more applicable to sufficiently track the trajectory well with less computational overhead. Relative to standard feedback control, the FF scheme still offers a reasonable improvement in performance, which could be useful for missions where power conservation is critical as touched on earlier. This is the major advantage over only including a one-stage predictive control action, however the trade-off lies in the performance.

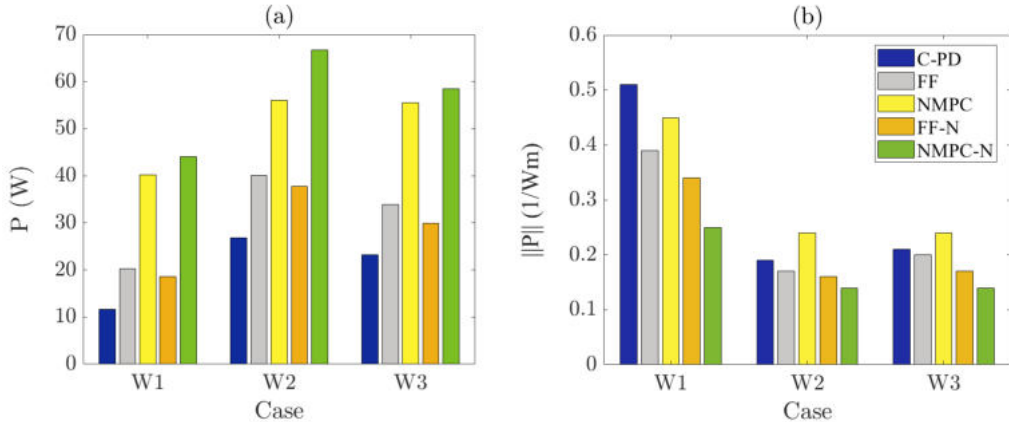


FIGURE 5.26: The (a) power consumed during the trajectory tracking mission and (b) the power consumption relative to RMSE error, where the scaling is  $1/\text{RMSE}$ .

### 5.5.4 Concluding Remarks

In this section, a method for the predictive disturbance mitigation of ocean waves was investigated for underwater vehicles, utilising preview information of future disturbances derived through the inclusion of a wave prediction method. With regards to the wave predictor, an experimental study focusing on short-term short-distance predictions returned a maximum RMSE of 0.045m over a 2s wave prediction, validating applicability for use within a predictive control architecture; this can also be extended to larger distances and prediction intervals.

Upon embedding of the wave predictor within two different predictive control methods (FF and NMPC), both were shown to effectively reduce the positional error of the vehicle for both station keeping and trajectory tracking. With regards to station keeping, the NMPC returned a mean improvement of 52% in comparison to the FF scheme due to the inclusion of an optimisation stage; for trajectory tracking, the NMPC reduced the RMSE by at least 42%. The strategy was tested under three different scenarios, demonstrating effective performance independent of wave conditions. Significant wave heights were of magnitude several times larger than the vehicle length (at minimum  $6\times$ ) in all cases, proving the controller's ability to mitigate large wave loads. A power analysis was also performed, showing marginal difference in scaled power expenditure relative to displacement. Finally, performance improvements were demonstrated in the presence of various sources of noise, highlighting the robustness of the system to variations between the predicted disturbances and those encountered by the vehicle.

## 5.6 Conclusions

Throughout this chapter, a control method for wave-induced disturbance rejection has been investigated for dynamic control of underwater vehicles. A complete end-to-end framework was proposed, incorporating a DSWP algorithm to provide preview

information of the wave-induced disturbances to a NMPC. Similarly, a FF control scheme was proposed which exploits analogous preview information, but omits the optimisation stage and only produces a single compensating control action; in contrast, the NMPC generates an optimal control sequence relative to a specified cost function. An experimental study was undertaken to initially validate the accuracy of the DSWP algorithm, followed by an extensive simulation study to analyse the performance of the different control schemes. Analysis was undertaken when considering both an accurate prediction and in the presence of sensor and spectral noise. Both schemes were shown to outperform a standard C-PD controller for station keeping and trajectory tracking missions, with the NMPC performing best with regards to state error.

The results presented in this chapter provide evidence that predictive control, once supported by a robust disturbance predictor, can indeed represent a solution to the current limitations associated with the employment of autonomous vehicles in hazardous ocean climates. The presented solution points to a viable, realistic solution to the problem of robust operation in hazardous wave climates, which can greatly assist in facilitating underwater vehicle uptake and deployment in a broader range of offshore operations.



## Chapter 6

# Predictive Disturbance Rejection for Soft Underwater Manipulators

### 6.1 Introduction

In Chapter 4, a control-based approach for disturbance mitigation of an underwater vehicle was proposed, formulating a prediction of the wave-induced loads and explicitly considering this as an additional input for a NMPC scheme. This method exploits the system dynamics in conjunction with the wave disturbance prediction to generate control inputs for both station keeping and trajectory tracking. The approach in general provides a method for obtaining wave predictions (through deterministic processes) in conjunction with a partnering control scheme. Given the promising findings from the experimental and simulation study, applications featuring highly nonlinear dynamics were also considered to test the ability of the framework further. This led to an investigation deploying the same methodology for control of a soft robotic manipulator subject to wave disturbances.

Soft robotic manipulators have several traits which are desirable in an underwater scenario, particularly in a shallow water environment; the presence of increased magnitude disturbances can restrict the use of traditional rigid-link manipulators, mainly due to risk of damage to both the plant and the manipulator itself. The natural compliance associated with the soft structure reduces this risk substantially, whilst retaining the ability to include design features such as tunable stiffness (as alluded to in Section 2.1.4) and reduced weight. This makes them ideal for manipulation tasks or operating in harsh environments, however this also introduces a large degree of non-linearity and susceptibility to state perturbations within the dynamical model in contrast to classical manipulators. This trait poses the question whether the solution proposed in Chapter 5 could be deployed to mitigate wave-induced effects in the case of soft manipulator operation, examining the behaviour of a predictive control architecture for a system where multiple manipulator configurations can provide a valid solution to the same control problem (as is inherent in multi-segment soft robots).

This chapter details the application of a similar control scheme to that developed in Chapter 5, discussing the end-effector tracking performance in the presence of wave-induced disturbances. An extensive simulation study is undertaken, also covering cases where the manipulator is only partially actuated. Concluding remarks are then given to discuss the findings of this additional branch of research, the current limitations of the solution and future developments required to continue progression.

## 6.2 Control Methodologies

Given that the purpose of this study is focused on mitigating modelled dynamic disturbances to the manipulator state, it is intuitive that a model-based control approach would be adopted. Additionally, to perform the study comparatively against a typical controller for soft manipulators, two control methodologies were considered with the aim of demonstrating the necessity of active disturbance rejection, using one as a baseline. For this purpose, a model-based kinematic controller was deployed as a baseline controller that considers the robot posture as a point in the task space  $\mathbf{x}_s \in \mathbb{R}^2$  and evaluates a configuration vector of suitable joint angles,  $\mathbf{q}$ . Alternatively a NMPC (that forms the contribution of this section) was also tested to explicitly consider the disturbances and minimise end-effector postural error. Both strategies were formulated to return a set of joint angles, with the NMPC utilising preview of the disturbances to optimise this set. Subsequently, a low-level PD with FF compensation controller was deployed to transform this set of joint angles into applicable control torques. It should be noted that throughout this chapter the specific method of actuation was not considered; several different methods can be adopted for this (e.g. cable drives, pneumatics or hydraulics) in practice, but this was purposefully left unspecified to provide a generalised control formulation agnostic to the type of actuation. In reality an additional transformation would be considered between the actuation method and the torque produced. This section therefore focuses on the formulation of the controllers, rather than the physical actuation method.

### 6.2.1 Model-Based Kinematic Control

Stemming from the foundational theory presented in Section 3.3, control of the posture and end-effector position of a soft robot can be largely achieved using feed-forward terms, assuming prior knowledge of the robot's properties and dynamics such as stiffness and damping coefficients (largely material dependent and easily obtainable). To achieve a specific posture, the key terms alluded to above are mainly the stiffness of the robot (which is directly related to the configuration) and the effects of gravity (inclusive of buoyancy when operating in a fluid). Additional dissipation occurs due to other damping effects (such as internal friction) and these can also be compensated, however their magnitude is often negligible in comparison to stiffness

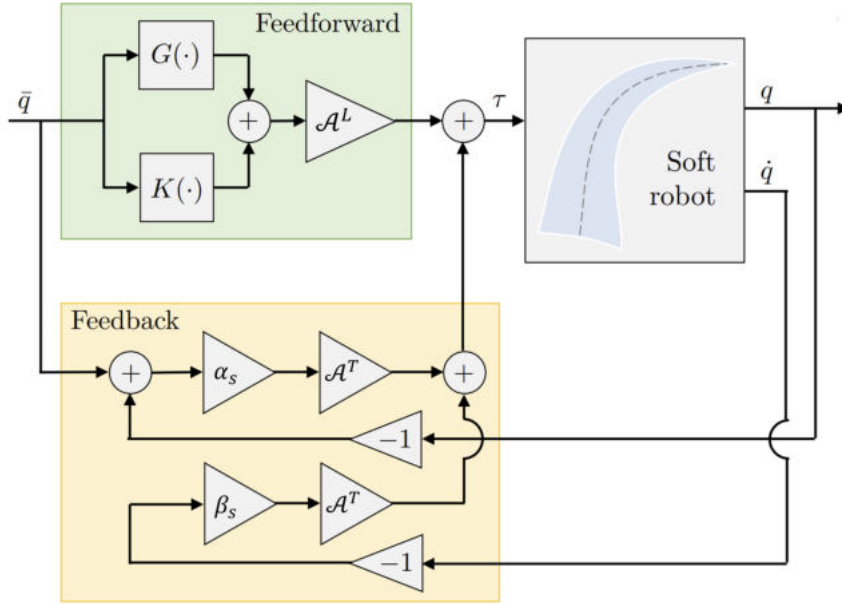


FIGURE 6.1: Block diagram for the soft robot feed forward with PD control strategy, described by Eq. 6.1. Here,  $\mathcal{A}$  is an actuation mapping matrix (see Eq. 3.77, where  $\mathcal{A}^L$  and  $\mathcal{A}^T$  are the left inverse and transpose of  $\mathcal{A}$  respectively [197], with the dependency on  $\mathbf{q}$  has been dropped for conciseness.

and gravitational effects. The inclusion of a typical feedback controller in conjunction with these feed-forward elements is a common solution to improve regulation/tracking performance further, inherently accounting for the above mentioned forcing terms. Fig. 6.1 shows the block diagram form of this strategy.

Assuming that each segment is independently actuated and considering the soft robot dynamics in Eq. 3.66, the feed forward with PD control law (FF-PD) can be defined according to:

$$\boldsymbol{\tau}(\bar{\mathbf{q}}, \mathbf{q}, \dot{\mathbf{q}}) = \mathbf{K}(\bar{\mathbf{q}}) + \mathbf{G}(\bar{\mathbf{q}}) + \boldsymbol{\alpha}_s(\bar{\mathbf{q}} - \mathbf{q}) - \boldsymbol{\beta}_s\dot{\mathbf{q}} \quad (6.1)$$

where  $\bar{\mathbf{q}} \in \mathbb{R}^n$  defines the desired joint angle configuration and the matrices  $\boldsymbol{\alpha}_s \in \mathbb{R}^{n \times n}$  and  $\boldsymbol{\beta}_s \in \mathbb{R}^{n \times n}$  are two gain matrices for the proportional and derivative control actions.

Given that it is desirable to operate in the task-space defined by Cartesian coordinates rather than the joint-space defined by the configuration variable  $\mathbf{q}$ , it is useful to define a planning strategy which can solve for a set of joint angles given an end-effector position. If the desired end-effector position is defined as  $\mathbf{x}_r \in \mathbb{R}^2$ , it is possible to solve for a desired configuration  $\bar{\mathbf{q}}$  which satisfies this position according to:

$$\dot{\mathbf{q}} = J^\dagger(\bar{\mathbf{q}})(K_e(\mathbf{x}_r - h(\bar{\mathbf{q}}))) \quad (6.2)$$

where  $J^\dagger$  is the Moore-Penrose psuedo-inverse and  $K_e$  is an error gain. This strategy has similar traits to the thrust allocation method adopted in Chapter 5, however varies

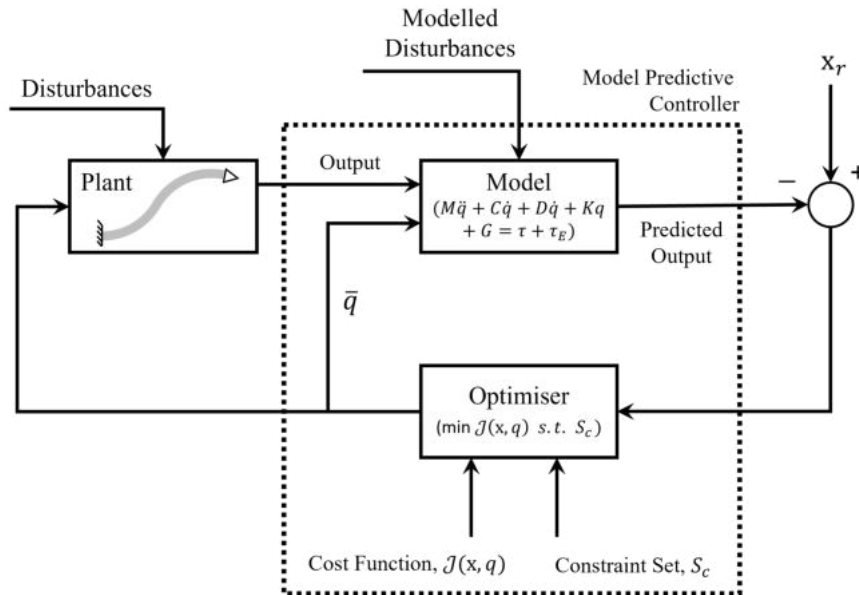


FIGURE 6.2: Block diagram overview of the control architecture deployed for end-effector disturbance rejection; it should be noted dependencies have been dropped here in the model for the sake of space.

in that a transformation between two reference spaces is considered. In practice, Eq. 6.2 is integrated numerically and serves as an input for the low level controller in Eq. 6.1. When adopting this strategy, the obvious assumption is that the desired position  $\bar{x}_s$  is attainable and that a valid solution of the configuration variables  $\mathbf{q}$  exists.

### 6.2.2 Nonlinear Model Predictive Control

As in the case of vehicle dynamic control, the use of a predictive control strategy that contained an optimisation stage was of interest to investigate how the dynamics of the robot could be exploited to produce higher accuracy control. The asset of MPC lies in the ability to handle constraints as well as to account for the system future dynamic response over a short time-horizon. In the case presented here, this latter quality is exploited to incorporate impending hydrodynamic disturbances within the future sequence of control actions (Fig. 6.2), aiming to adapt the optimal control output to minimise environmental disturbances. As the general theory of MPC is presented in detail in Section 5.4, a concise description of the NMPC formulation for the soft robot is given here that aligns with the related notation.

The assumption is made that the initial end-effector state of the robot  $\mathbf{x}_{init} \in \mathbb{R}^2$  is known and a reference state is defined at each timestep  $k$  such that  $\mathbf{x}_{r,k} = [x_{r,k}, z_{r,k}]^T \in \mathbb{R}^2$ . Formulating the problem as an optimisation over the state and control trajectory, the goal of the NMPC is to evaluate a set of control inputs, formulated as a set of joint angles  $\bar{\mathbf{q}}$  in this instance, which minimise a specified cost function. These control inputs are then passed to the lower level kinematic controller given in Eq. 6.1 to generate an applied actuation torque vector.

Firstly, following an analogous approach to the case with an ROV, the soft robot dynamics in Eq. 3.66 can be defined as a function such that:

$$\dot{\mathbf{x}} = \mathbf{f}_m(\mathbf{x}, \bar{\mathbf{q}}) \quad (6.3)$$

where  $\mathbf{x}$  and  $\bar{\mathbf{q}}$  are used to represent the system state and the commanded joint configuration. Subsequently, the dynamics are solved in discrete time through a Runge-Kutta integration:

$$\mathbf{x}_{k+1} = \mathbf{F}_m(\mathbf{x}_k, \bar{\mathbf{q}}) \quad (6.4)$$

at each timestep  $k$ . According to Eq. 6.4, the predicted soft robot configurations  $\mathbf{X}_k$  for a given sequence of command joint configurations  $\mathbf{Q}_k$  along the horizon  $N_c$  is given by:

$$\mathbf{X}_k = \begin{bmatrix} \mathbf{F}_m(\mathbf{x}_k, \bar{\mathbf{q}}_k) \\ \mathbf{F}_m(\mathbf{x}_{k+1}, \bar{\mathbf{q}}_{k+1}) \\ \vdots \\ \mathbf{F}_m(\mathbf{x}_{k+N_c-1}, \bar{\mathbf{q}}_{k+N_c-1}) \end{bmatrix} \quad \mathbf{Q}_k = \begin{bmatrix} \bar{\mathbf{q}}_k \\ \bar{\mathbf{q}}_{k+1} \\ \vdots \\ \bar{\mathbf{q}}_{k+N_c-1} \end{bmatrix} \quad (6.5)$$

where  $\mathbf{x} \in \mathcal{X}$  and  $\bar{\mathbf{q}} \in \mathcal{Q}$  represents the feasible sets limited by the defined constraints, mainly the actuation capabilities along with the geometrical and physical properties of the soft robot. From the above, we solve the following optimal control problem:

$$\begin{aligned} & \underset{\mathbf{X}_k, \mathbf{Q}_k}{\text{minimize}} && \mathcal{J} = V_{f,m}(^r\mathbf{x}_{k+N_c}) + V_{s,m}(^r\mathbf{X}_k, \mathbf{Q}_k) \\ & \text{subject to} && \mathbf{x}_{k+1} = \mathbf{F}_m(\mathbf{x}_k, \bar{\mathbf{q}}_k), \\ & && \mathbf{X}_k \in \mathcal{X}, \\ & && \mathbf{Q}_k \in \mathcal{Q}, \\ & && \mathbf{x}_{k+N_c} \in \mathcal{X}_f \end{aligned} \quad (6.6)$$

where  $V_{s,m}$  and  $V_{f,m}$  represent the stage and terminal costs given by:

$$V_{f,m}(^r\mathbf{x}_{k+N_c}) = (^r\mathbf{x}_{k+N_c})^T \mathbf{P}_m (^r\mathbf{x}_{k+N_c}) \quad (6.7)$$

$$V_{s,m}(^r\mathbf{X}_k, \mathbf{Q}_k) = \sum_k^{k+N_c} (^r\mathbf{x}_k)^T \mathbf{P}_m (^r\mathbf{x}_k) + \sum_k^{k+N_c-1} (\Delta \bar{\mathbf{q}}_k)^T \mathbf{R}_m (\Delta \bar{\mathbf{q}}_k) \quad (6.8)$$

Here,  $\mathbf{P}_m \in \mathbb{R}^{n \times n}$  and  $\mathbf{R}_m \in \mathbb{R}_m^{n \times n}$  are positive definite weighting matrices on the state and control respectively;  $^r\mathbf{x}_k = \mathbf{x}_{r,k} - \mathbf{x}_k$  is the state error relative to the reference state at each instance along the control horizon. As the control input takes the form of a commanded joint angle configuration,  $\Delta \bar{\mathbf{q}}$  represents the intermediate angular step; these terms are incorporated within Eq. 6.6 to prevent large step changes and minimise the required control effort where possible. As we consider a generalised actuation, we only place constraints on the desired joint angle rather than directly on the produced actuation torque; the NMPC constraints can be easily adapted for

this to include consideration of effects such as saturation. The optimised joint-angle sequence is the direct input to Eq. 6.1 to actively adapt the robot configuration to the disturbance. Although the control inputs are applied in the joint-space, the optimisation is performed with reference to the task-space in order to operate around a Cartesian position rather than a joint angle configuration.

### 6.3 Soft Robot Wave Disturbance Model

As the operational environment of the proposed manipulator is underwater, the interaction with the fluid must be considered within the dynamic model, namely the effects of hydrodynamic drag and added mass. Generally, there isn't a widely accepted method for modelling these effects, but across the little literature dealing with this problem [232, 233, 328] there are some analogies. Similar to what is accepted in the offshore industry, a modelling process can be adopted by considering concepts stemming from Morison theory [303] and following a similar framework described throughout Section 3.3.2, whereby element-wise forces are evaluated as a summation along the segment length and transformed into the joint-space (Fig. 6.3).

Intuitively and as in Eq. 3.66, it follows that the environmental disturbances can be grouped into a generalized vector  $\boldsymbol{\tau}_E \in \mathbb{R}^n$  defined as:

$$\boldsymbol{\tau}_E = \sum_{i=1}^n \int_0^1 \mathbf{J}_i^T(s, \mathbf{q}) \mathcal{F}_i(\mathbf{v}, \dot{\mathbf{v}}) ds \quad (6.9)$$

where

$$\mathcal{F}(\mathbf{v}, \dot{\mathbf{v}}) = \mathcal{F}_A(\dot{\mathbf{v}}) + \mathcal{F}_D(\mathbf{v}) \quad (6.10)$$

is the total normal force acting on the  $i$ -th element relative to the Cartesian velocity vector  $\mathbf{v}$  in the local frame, consisting of the added mass contributions,  $\mathcal{F}_A$ , and drag contributions,  $\mathcal{F}_D$ . These can be defined according to their hydrodynamic definitions as:

$$\mathcal{F}_A(\dot{\mathbf{v}}) = \mathcal{M}_A \dot{\mathbf{v}}, \quad \mathcal{F}_D(\mathbf{v}) = \mathcal{D} \mathbf{v}_r \quad (6.11)$$

where  $\mathbf{v}_r \in \mathbb{R}^3$  is a vector of Cartesian relative velocity components with null rotational magnitude in the local frame. Also,  $\mathcal{D} \in \mathbb{R}^{3 \times 3}$  is a matrix of hydrodynamic drag coefficients evaluated according to the manipulator properties.

Similarly and in accordance with the same assumptions given in Section 3.3.3, the added mass and drag forces can also be defined in relation to the Cartesian velocities evaluated at each point  $s$  along the robot abscissa. If the velocity vector in Eq. 6.9 is defined relative to the soft robot posture, it follows that:

$$\mathbf{v}(s, q) = \mathbf{R}_q(s, q) \dot{\mathbf{x}}_s(s, q) \quad (6.12)$$

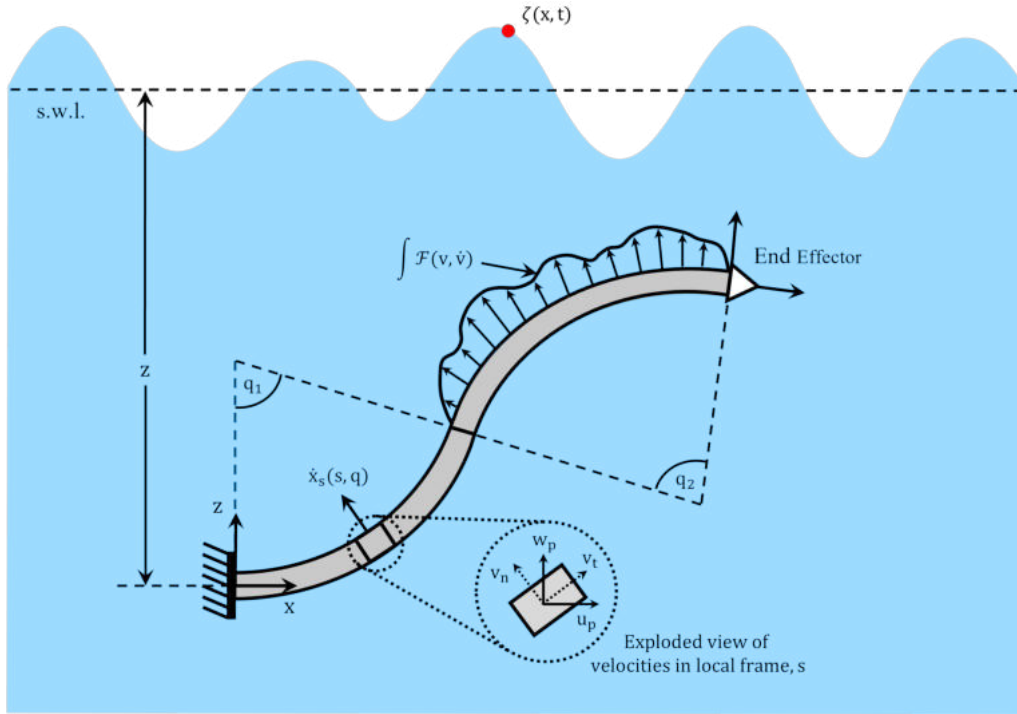


FIGURE 6.3: Visual representation of the fluid force integration across the segment body, where the relative motion of the fluid is considered to account for non-steady flows and evaluation is performed at each local point,  $s$ , along the manipulator length.

where the rotation matrix  $\mathbf{R}_q(s, q)$  is defined relative to the base frame as

$$\mathbf{R}_q(s, q) = \begin{bmatrix} \cos sq & \sin sq \\ -\sin sq & \cos sq \end{bmatrix} \quad (6.13)$$

An analogous approach is also applied to determine the relative velocity of each point  $s$  with respect to the fluid flow

$$\mathbf{v}_r(s, q) = \mathbf{R}_q(s, q) [\dot{\mathbf{x}}_s(s, q) - \mathbf{v}_f(s, q)] \quad (6.14)$$

where  $\mathbf{v}_f = [u_p \quad w_p]^T$  can be obtained using numerical methods such as those given in Eq. 3.11-3.12. From this, the forces acting on each section  $s$  can be evaluated in the local frame:

$$\mathcal{F}_A = -\mathcal{M}_A \dot{\mathbf{v}} = \begin{bmatrix} X_{\dot{u}} & 0 \\ 0 & Z_{\dot{w}} \end{bmatrix} \begin{bmatrix} v_x \\ v_z \end{bmatrix} \quad (6.15)$$

$$\mathcal{F}_D = -\mathcal{D} \mathbf{v}_r = \begin{bmatrix} \mathcal{D}_x & 0 \\ 0 & \mathcal{D}_z \end{bmatrix} \begin{bmatrix} v_{r,x} \\ v_{r,z} \end{bmatrix} \quad (6.16)$$

where  $v_x$  and  $v_z$  are defined in the local frame. The hydrodynamic properties in the matrix of added mass coefficients  $\mathcal{M}_A$  and drag coefficients  $\mathcal{D}$  can be determined using several means, as discussed in the following section. Finally, Eq. 6.15-6.16 are directly substituted into Eq. 6.9 to be integrated along the robot body and evaluate

the effect of the fluid disturbances on the robot dynamics.

### 6.3.1 Hydrodynamic Parameter Specification

Considering this model, several hydrodynamic parameters are required to calculate the wave-induced loads enforced on the soft manipulator according to Eq. 6.11. Generally these can be evaluated either experimentally or analytically; for the sake of generality in the modelling process, the latter approach was adopted in this work. For the added mass coefficients, these are evaluated as [329]:

$$\mathcal{M}_A = \begin{bmatrix} X_{\dot{u}} & 0 \\ 0 & Z_{\dot{w}} \end{bmatrix} = \frac{\pi D_s^2}{4} \mathcal{L} \rho_f \begin{bmatrix} C_{m,x} & 0 \\ 0 & C_{m,z} \end{bmatrix} \quad (6.17)$$

where  $D_s$  is the diameter of the segment cross-section,  $\mathcal{L}$  is the segment length and  $C_{m,x}, C_{m,z}$  are inertia coefficients relating to the body added mass where  $C_m = 1 + C_a$  dictates the relationship with the added mass coefficient. The drag coefficients can be obtained in similar fashion through:

$$\mathcal{D} = \begin{bmatrix} \mathcal{D}_x & 0 \\ 0 & \mathcal{D}_z \end{bmatrix} = \frac{1}{2} \rho_f A_f \begin{bmatrix} C_d |v_n| & 0 \\ 0 & C_f |v_t| \end{bmatrix} \quad (6.18)$$

and  $A_f, C_d, C_f$  are the projected area to the flow, the drag coefficient of the segment and the frictional coefficient of the segment. It is worth noting that if Assumption 3.3.3 had not been adopted, the off-diagonal elements of these matrices can and most likely would be non-zero. The hydrodynamic properties of the robot will vary according to the morphology of each segment, both due to the nature of the cross-section and the associated segment length. For longer segments with larger cross-sections, an increased area will be subjected to hydrodynamic loading. However, the generalised approach remains consistent and these values can be determined accordingly through analogous experimentation or empirical calculations.

## 6.4 Simulation Study

To initially investigate the validity of applying the predictive control approach to a system with a higher degree of non-linearity, a simulation study was undertaken in which the multi-segment soft manipulator was fully submerged and situated at low depth. Thus, disturbances arising from the presence of ocean waves are of higher magnitude and will have greater influence over the robot dynamic behaviour, offering better insight into the capabilities of the proposed control scheme. The manipulator was assumed to be mounted on a fixed structure, approximating a floating base which is performing station keeping accurately. This is analogous to the scenario depicted in Fig. 6.3 which visualises the wave-induced loading on the manipulator body.

TABLE 6.1: Soft manipulator geometric and hydrodynamic parameters for each identical segment; values do not relate to any particular manipulator, but were chosen as generic values to demonstrate the proposed control methodology.

Parameter	Nomenclature	Value	Unit
Mass	$m_s$	0.5	kg
Length	$\mathcal{L}$	300	mm
Diameter	$D_s$	50	mm
Local Stiffness	$\kappa(s)$	0.5	Nm
Local Damping	$d_s(s)$	0.5	Nms
Drag Coefficient	$C_d$	0.5	-
Frictional Coefficient	$C_f$	0.5	-
Added Mass Coefficient	$C_a$	0.6	-
Fluid Density	$\rho_f$	1025	kg/m <sup>3</sup>
Body Density	$\rho_s$	2330	kg/m <sup>3</sup>

TABLE 6.2: Control parameters for the soft robot.

Parameter	Nomenclature	Value
Prediction Horizon	$N_c$	15
State Weight Matrix	$\mathbf{P}_m$	diag(1,1,1)
Control Weight Matrix	$\mathbf{R}_m$	diag(0.01,0.01,0.01)
Error Gain	$K_e$	3.0
Proportional Gain	$\alpha_s$	2.0
Derivative Gain	$\beta_s$	1.0

The manipulator is modelled with three independently actuated segments which are all assumed to be identical with regards to their physical properties and hydrodynamic characteristics, provided in Table 6.1. Similarly, the control parameter specifications are listed in Table 6.2. The justification for selecting three segments is that this offers a complete operational workspace over only using two. Each segment typically has control over 2DoF (PCC approach assumes zero torsion, only bending), therefore three segments provides full 6DoF motion capability at the end-effector upon extension to a spatial case from the planar motion assumed here. Essentially, possessing  $> 3$  segments is only advantageous with respect to forming more complex postures, but this analogously increases the complexity of the dynamics and control.

The remainder of this section covers the configuration of the simulation environment, followed by the assumptions employed and an in-depth discussion of the results obtained. Concluding remarks are then given based on these findings.

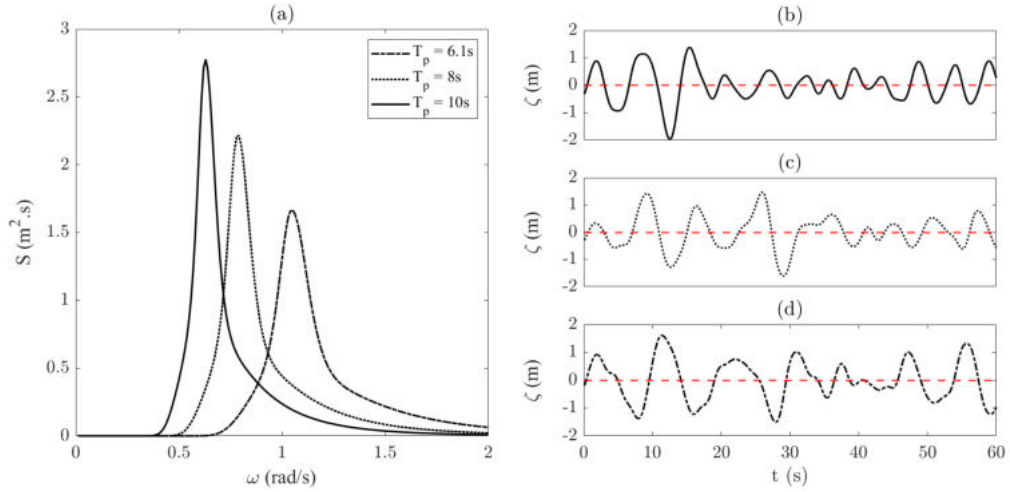


FIGURE 6.4: Tested wave spectra for the soft robot control analysis, showing (a) the frequency spectrum of the 3 different waves and (b)-(d) a temporal snapshot for wave evolution for each wave.

TABLE 6.3: Statistical parameters for the 3 wave spectra considered throughout Chapter 6, varying in peak spectral period and scaled in significant wave height.

Case Reference	Peak Period (s)	Significant Wave Height Range (m)
S1	6.1	0.5-3 (0.5 increments)
S2	8.0	0.5-3 (0.5 increments)
S3	10.0	0.5-3 (0.5 increments)

#### 6.4.1 Simulation Configuration

Following the approach adopted in Section 5.5, the simulated scenario was configured to replicate the conditions the vehicle-manipulator system may encounter. This is motivated by the desire to eventually deploy the control method on a real soft robotic manipulator fitted to a subsea vehicle, which although sits outside the scope of this thesis is currently planned for future work upon fabrication of a physical manipulator. In consideration of this and consistently with the previous studies in Chapters 4-5, real-world data was obtained to emulate a realistic shallow-water environment and form a comparative study. This data was collected from the same location and source as in Section 5.5, however alternative spectra was utilised in this instance. This stems from the desire to test spectra at specific values and even intervals of peak spectral period, with a particular interest on any potential relationship with the soft robot dynamics. Similarly, as the wave height is to be scaled in the analysis, the chosen spectral periods represent viable values where the range of scaled wave heights are plausible. As previously mentioned, the offshore renewable energy industry is also active in this geographical area, confirming that the conditions tested align with the tasks the proposed system is intended for. Similarly, this fact presents grounds for deploying the DSWP approach utilised previously by exploiting the local

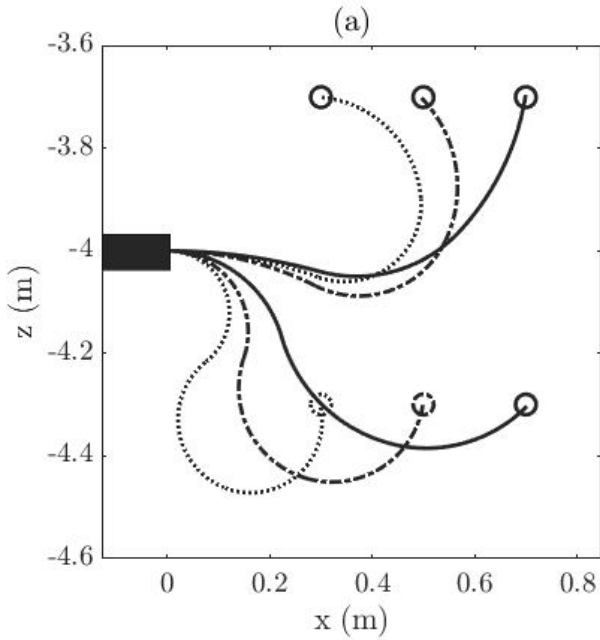


FIGURE 6.5: Set-point regulation of six separate points, at two different depths and three different longitudinal positions.

infrastructure - this would also entail further work, but would be achievable using similar methodologies.

In total three different wave spectra were selected, purposefully choosing varying spectral peak periods to analyse any direct effect on the controller performance. These are displayed in Fig. 6.4 with assigned case references in Table 6.3. A key reason for varying this parameter in particular is to analyse how the variation of flow across the slender body of the manipulator affects the induced oscillations; for lower periods, this variation should be sharper thus may require more aggressive corrective control. Likewise, the induced particle motions vary in shape and magnitude directly in line with the wave period, so situating the manipulator at low depth implies wave disturbances will possess significant magnitude and therefore have larger influence over the dynamic behaviour of the robot. To this end, for each test performed a 60s temporal segment was analysed with the manipulator situated at an operating depth of  $z = -4\text{m}$ .

Within the simulation, solving for the subsequent state  $\mathbf{x}_{k+1}$  is performed through numerical integration over the discrete time interval  $\Delta t = 0.1\text{s}$ , adopting a fifth-order variable step Runge-Kutta method. For this analysis, the prediction horizon for the NMPC was defined as  $t_p = 15\Delta t$ .

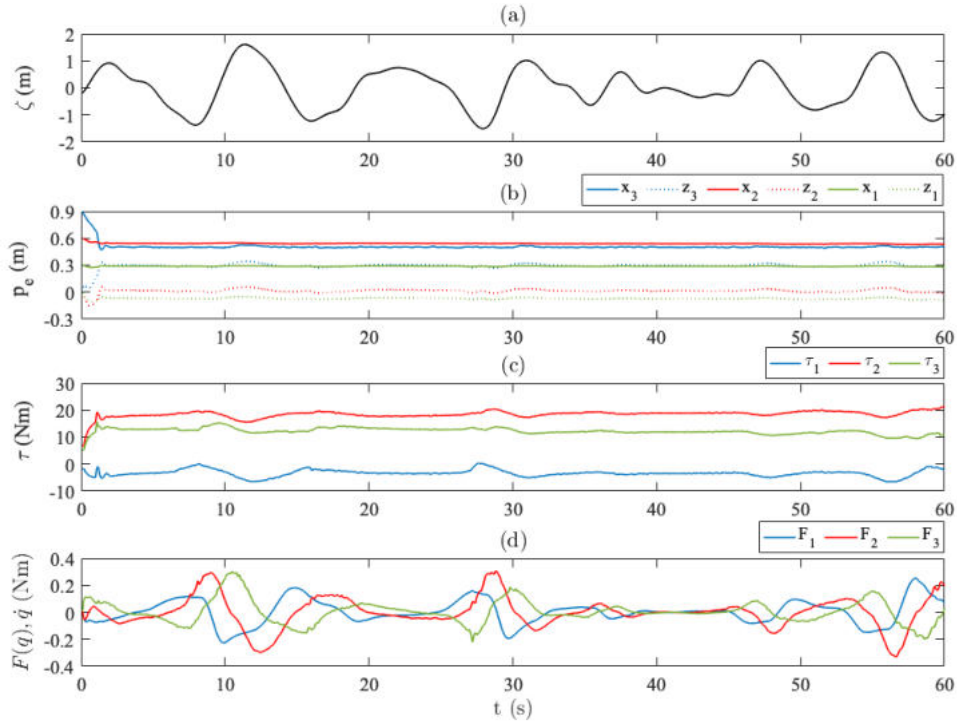


FIGURE 6.6: When subjected to the (a) wave train, the evolution of the (b) segment tip positions with respect to the base at (0m,0m) shows good regulation, with the (c) actuation torques and (d) wave loading torques also analysed. Shown are the evolution's for case S3 with  $H_s = 3\text{m}$ .

### 6.4.2 Simulation Results

#### Set-point Regulation

Initial validation of the controller behaviour encapsulated testing the ability to achieve different configurations within the manipulator task-space. For these simulations, disturbances were first neglected to qualitatively validate the capability of achieving a suitable set of segment curvatures. As can be seen in Fig. 6.5, this was successful for 6 different desired set-points, where the tested set-points were purposefully chosen to validate different depths and degrees of curvature, ranging from highly deformed to highly extended. It should be noted that these figures display a snapshot from the simulations and a selected set of attempted poses for demonstrative purposes. To further illustrate the behaviour of the control when considering disturbances across the temporal interval, Fig. 6.6 shows the evolution of the position, control torques and wave loading for each of the three segments under the wave train depicted in Fig. 6.6(a). Indexes 1, 2 and 3 respectively refer to the base, middle and end-effector segments. With reference to the hydrodynamic torques, Fig. 6.6(d) shows the independent fluid loading across each segment. As can be seen, the actuation torque applied by the controller varies at each wave loading point of inflection, showing an active effort to compensate for the disturbance and maintain the end-effector position steady by exploiting the preview knowledge provided to the controller.

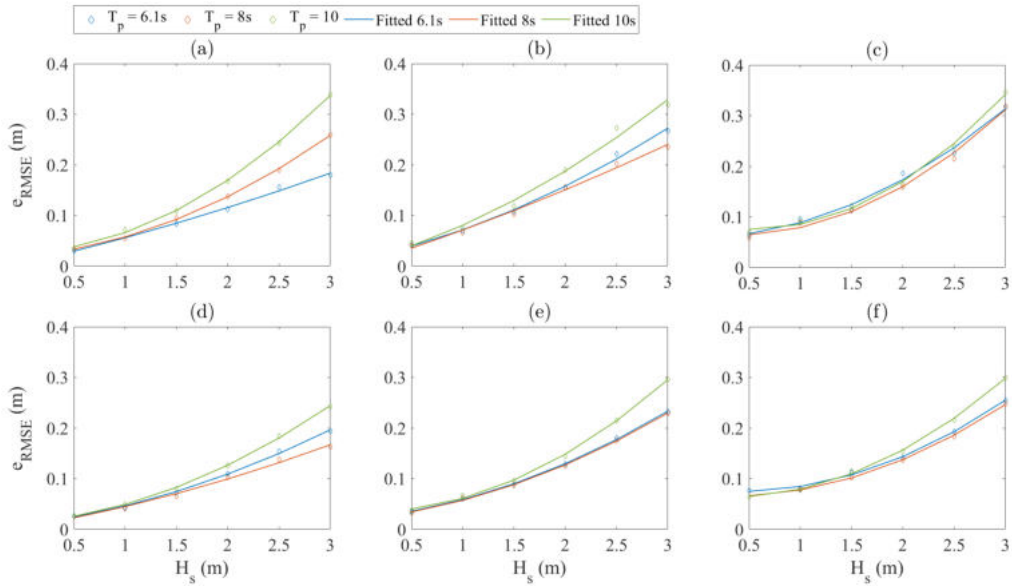


FIGURE 6.7: RMSE error of the end-effector position controlled with MPC under a range of significant wave heights and spectra peak periods, where the desired set-points in  $(x, z)$  for each subplot are (a)  $(0.3\text{m}, -3.7\text{m})$ , (b)  $(0.5\text{m}, -3.7\text{m})$ , (c)  $(0.7\text{m}, -3.7\text{m})$ , (d)  $(0.3\text{m}, -4.3\text{m})$ , (e)  $(0.5\text{m}, -4.3\text{m})$ , (f)  $(0.7\text{m}, -4.3\text{m})$  with reference to an earth-fixed frame.

The overall controller capability to compensate for wave disturbances was assessed by undertaking set-point regulation tasks over a broad range of cases, as listed in Table 6.3. For consistency, each case was tested across six end effector set-points:  $(x, z) = (0.3\text{m}, -3.7\text{m}); (0.5\text{m}, -3.7\text{m}); (0.7\text{m}, -3.7\text{m}); (0.3\text{m}, -4.3\text{m}); (0.5\text{m}, -4.3\text{m}); (0.7\text{m}, -4.3\text{m})$ , as shown in Fig. 6.5. The RMSE calculated across 60s temporal intervals is reported in Fig. 6.7. This provided an impression of the deviation of the end-effector with respect to the specified desired set-point, which for all simulations can be seen to be relatively low, substantially lower for larger waves and intuitively larger disturbance torques in particular. Another observation taken from the results in Fig. 6.7 is the peak period of the wave appears to have a notable effect on the RMSE recorded, particularly when the manipulator is attempting to maintain an end-effector position close to the base, i.e. when all segments undergo high curvatures. This observation is also apparent by the fact that in Fig. 6.7(c) and 6.7(f) there is less of an obvious deviation between the different wave formations. Unsurprisingly, in all cases the highest error is witnessed when the manipulator is subjected to the wave with the largest peak period. This likely owes to the fact that experienced wave torques are larger due to the fluid particle motions becoming elongated with respect to lower periods [297], thus the influence on the end-effector position is more apparent.

To quantify the performance against the baseline controller specified in Section 6.2.1, identical tasks were undertaken and the RMSE of both strategies compared. These extensive results are displayed in Fig. 6.8 by means of a non-dimensional error

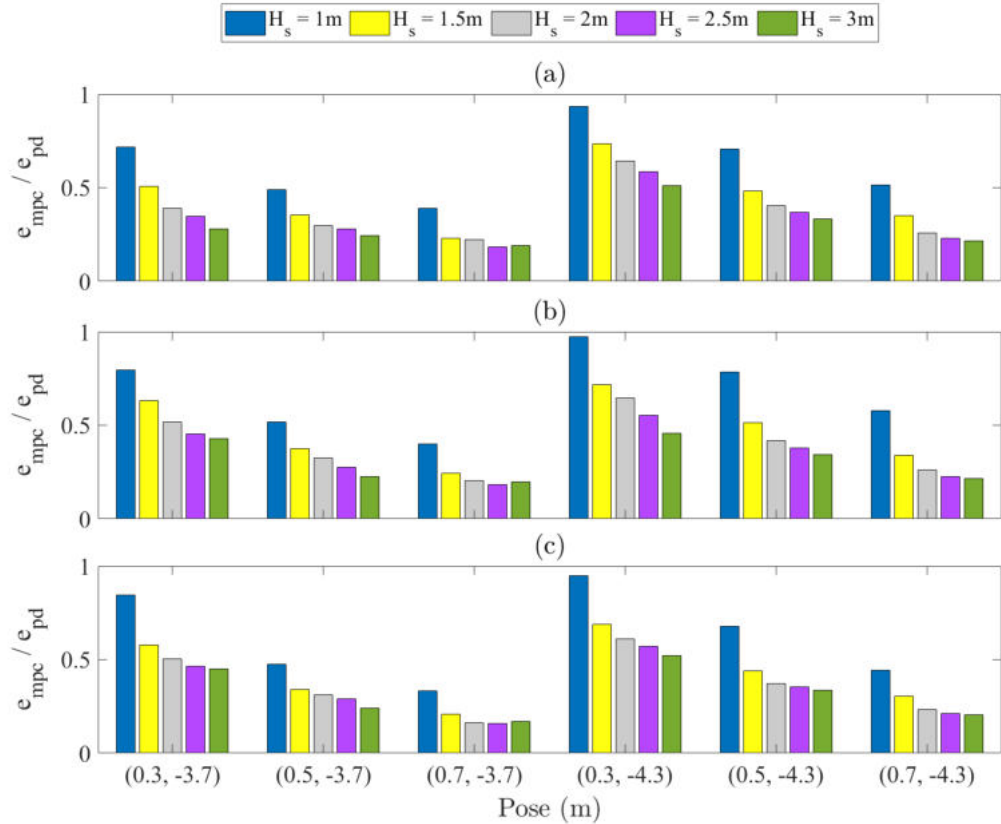


FIGURE 6.8: Variation in error between the MPC strategy and the baseline feedforward + PD strategy, represented as a normalised RMSE ratio. Shown are the results for case (a) S1 with  $T_p = 6.1\text{s}$ , (b) S2 with  $T_p = 8.0\text{s}$  and (c) S3 with  $T_p = 10.0\text{s}$ .

ratio normalized by the positional error obtained with the feed-forward kinematic control. These results highlight the superior performances of the MPC against the baseline controller across all cases, showing substantial improvement in end-effector control under disturbances. An intuitive observation is that the reduction in error becomes more significant as the magnitude of disturbances grow. This is expected as the baseline control performance will deteriorate at a faster rate, largely due to the ability of the MPC to consider disturbances within the control architecture. The largest reductions in error for each period across all poses and wave heights were 81.67%, 81.60% and 83.78% for cases S1, S2 and S3 respectively, whilst the lowest reductions were 6.48%, 2.82% and 5.12%. Interestingly, these all referred to the same pose; the larger reductions related to a set-point of  $(0.7\text{m}, -3.7\text{m})$  and the lowest to  $(0.3\text{m}, -4.3\text{m})$ . The inference here is that when the soft robot experiences higher curvatures, the improvement in set-point regulation is less drastic due to the fact that the body is experiencing a lower variation in flow and therefore a lower disturbance torque. A similar cause is that higher depth will also imply lower disturbance torques, so the variation in performance is expected to be lower. Ocean wave effects decay exponentially with depth and in shallow conditions this decay is amplified [297], so it is unsurprising that a clear difference can be seen between all set-points at  $z = -3.7\text{m}$ .

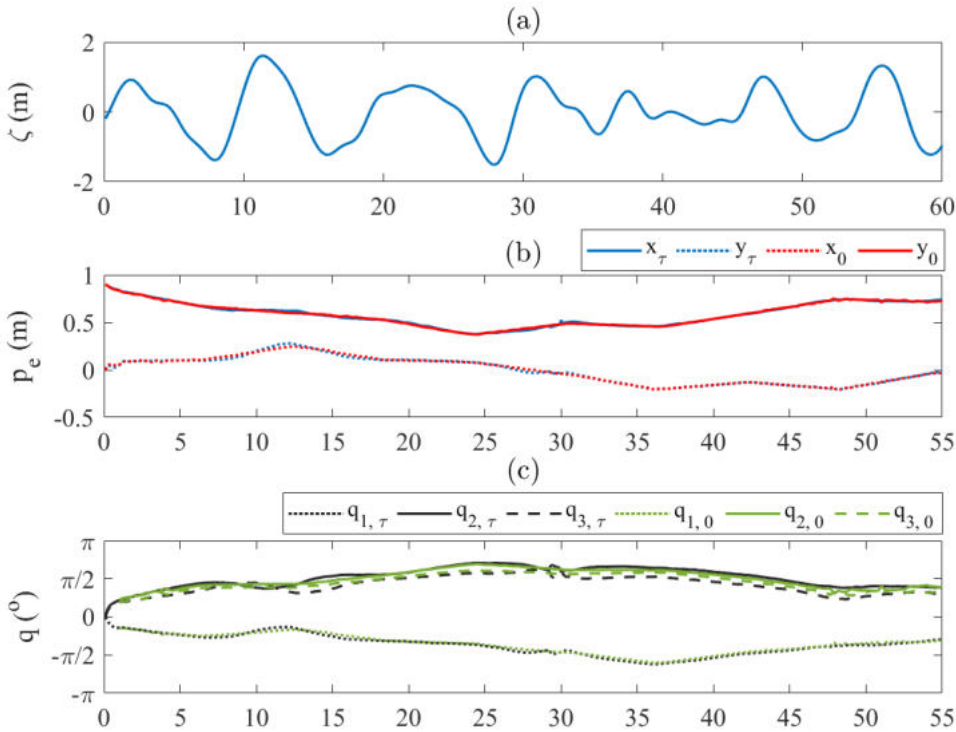


FIGURE 6.9: End-effector trajectory tracking task for a star path, initial condition fully extended. Shown are the (a) wave elevation for case S3 with  $H_s = 3\text{m}$ , (b) end-effector position with respect to the base at  $(0\text{m}, 0\text{m})$  and (c) joint angle trajectories. Subscripts  $\tau$  and 0 refer to cases under disturbances and neglecting disturbances respectively.

compared to  $z = -4.3\text{m}$ .

### Trajectory Tracking

All tests in the previous section involve defining a constant target position which the controller attempts to regulate under disturbances. This is useful when performing intervention tasks or maintenance tasks, where the focus of the prescribed goal is fixated on a specific point. In contrast, tasks such as inspection typically occur over a specified area, in which case the end effector is required to actively move. This is an intuitive further extension to the analysis covered thus far, with the modification to the control task being to define a trajectory which the end-effector must follow as opposed to regulating a state. As previously, the goal here is to follow the reference trajectory with minimal fluctuations while subject to wave loading.

With respect to this and to add some complexity to the task, a star trajectory was prescribed (in the same task space reference as the control) for the controller to attempt to track with the end-effector. All three wave spectra were considered for this demonstration (Fig. 6.4) with significant wave height  $H_s = 3\text{m}$ , to analyse if the peak spectral period affected the controller performance in any form. A visual representation of the task for case S3 can be seen in Fig. 6.9-6.10, which shows evidence of minimal discrepancy even under a considerable magnitude of wave disturbance. Inspecting Fig. 6.9(c) closer, active varying of the joint angles can be seen to keep

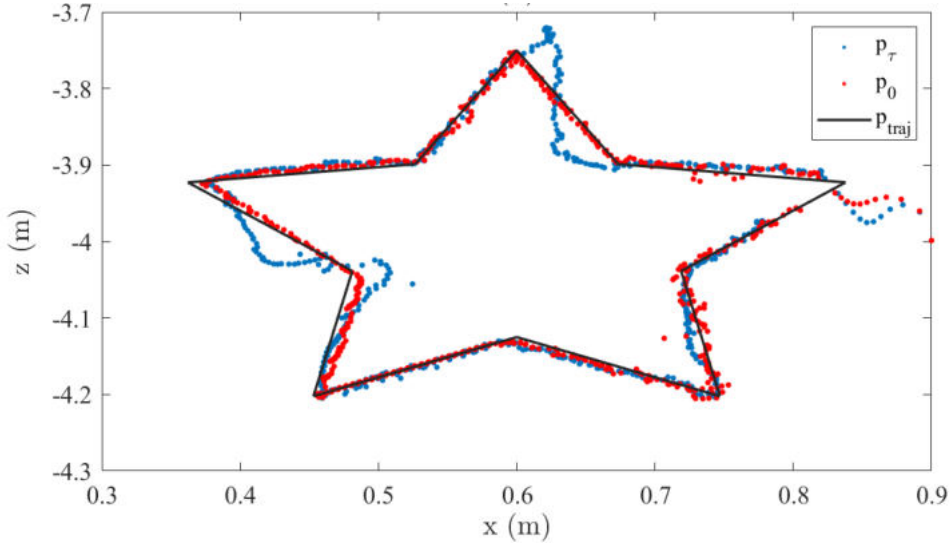


FIGURE 6.10: Spatial representation of the end-effector trajectory tracking task for a star path, initial condition fully extended. Subscripts  $\tau$  and 0 refer to cases under disturbances and neglecting disturbances respectively.

the positional error to a minimum, particularly in the case of joint angle  $q_3$ . As anticipated, there are some minor instances where the end-effector varies from the reference trajectory, however this appears to be limited to  $\approx 0.05\text{m}$  at most. During tasks such as non-destructive testing, the compliance of a soft manipulator has a higher chance of adapting to these wave-induced variations than in the case of a rigid-link manipulator, without the need for high-precision impedance control at the tip.

Evaluation of controller performance across the three spectra over a 60s time interval yields RMSE of 0.2491m, 0.2944m and 0.2821m for case S1, S2 and S3 respectively. This shows relatively consistent performance irrespective of wave period when tracking a trajectory, a markedly distinct behaviour from other underwater floating-base systems such as ROVs as demonstrated in the work undertaken in Chapter 5. This is justifiable by considering that, at such wave lengths, drag-based forcing will be predominant and acting on the manipulator over timescales which are much larger than the control timescale.

### Robustness to Actuation Failure

An interesting aspect of deploying MPC for in these instances is the increased robustness that comes with utilising advanced control over typical feedback methods. As a plant model is exploited in the optimisation of the control inputs, adaptations to adverse scenarios become simpler and more accessible. The example we consider in this instance is one of the actuated segments "failing", i.e. it can no longer be actively actuated and becomes passive. In this situation, the controller must compensate for lack of control by manipulating the actuation of the other segments so that the desired

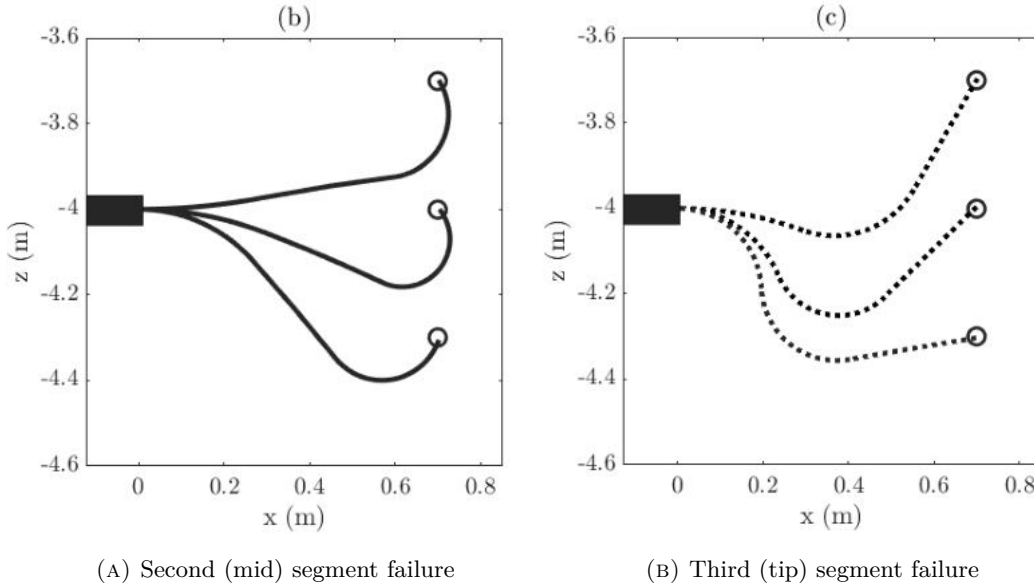


FIGURE 6.11: Set-point regulation validation of the control with varying actuation capability, showing poses at different depths and degrees of curvature when the (a) mid segment is unactuated and (b) the tip segment is unactuated.

goal state is still achieved. Considering this, simulations were performed emulating instances where a segment could not be actuated or controlled directly and the end-effector position was purely controlled by the configuration of the other segments. This was initially tested for three target positions across the same set of spectra:  $(x, z) = (0.7\text{m}, -3.7\text{m})$ ;  $(0.7\text{m}, 0.0\text{m})$ ;  $(0.7\text{m}, 4.3\text{m})$ , in the absence of wave disturbances to validate functionality. Subsequently, a quantitative comparison between the fully actuated robot and a robot with a mid-segment actuation failure was performed, analysing the RMSE of the end-effector position for the same targets. Inspecting the data displayed in Fig. 6.7, a key inflection point can be seen at  $H_s \approx 1.5\text{m}$  where the value of  $T_p$  appears to become influential. Therefore, a reduced set of significant wave heights in the range  $H_s = 1.5 - 3\text{m}$  were analysed.

As displayed in Fig. 6.11, the controller was able to reconfigure the soft robot to successfully reach the desired end-effector position, both when the second and third segment were un-actuated and could not be controlled (independent of each other). This is highly advantageous when considering the proposed application and operational environment of these systems; it is likely the manipulator could sustain some damage during operation, so if the instance arose where the actuation failed, using advanced control like the MPC proposed here mitigates the risk of mission failure. The limitation in this instance is that the workspace is reduced significantly, however the ability to still partially operate is desirable when operating in extreme environments. Generally, it is beneficial to maintain some functionality and attempt to continue operating rather than abandoning the mission completely, particularly from a costs incurred perspective.

With regards to quantitative performance, the results presented in Fig. 6.12

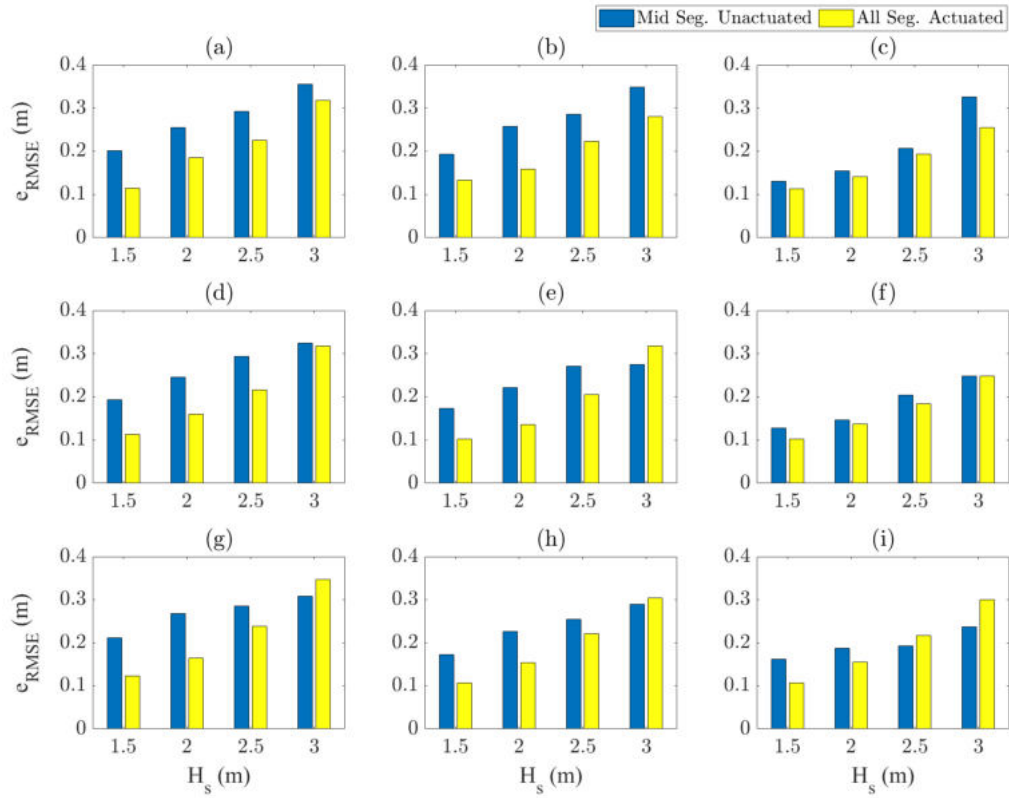


FIGURE 6.12: RMSE of the soft robot end-effector in the presence of a mid-section actuation failure, in comparison to a fully actuated soft robot. Shown are the results for cases (a)-(c) S1, (d)-(f) S2 and (g)-(i) S3 when attempting to regulate the end-effector at the position  $(x, z) =$  (a)(d)(g) (0.7m, -3.7m), (b)(e)(h) (0.7m, 0.0m) and (c)(f)(i) (0.7m, -4.3m).

provide further evidence of the ability of the controller to still regulate the end-effector position with minimal increase in RMSE. Across all positions and spectra tested, only a 19.2% increase in RMSE was witnessed with respect to the fully actuated case, which given that the robot has lost 1/3 of its manoeuvring ability is quite remarkable. Still comparing the partially actuated case to the fully actuated case, the wave with the largest peak period (case S3) showed the lowest disparity, recording a 14.3% increase in disparity. Although the largest wave is expected to induce the highest torques, this result could point to the higher frequency waves causing a passive excitation of the middle segment, thus driving the error higher than when the segment is controlled. Interestingly, there were some instances where the fully actuated robot actually recorded larger RMSE than the partially actuated robot. However, a key observation is that these cases exclusively relate to waves with the largest significant wave height tested. The inference here is that when the wave becomes substantially larger than the robot body length ( $\approx 3$ x larger), the control has difficulty regulating the end-effector position regardless of actuation capability. It could also be argued that the unactuated segment adds significant uncertainty to the controller dynamic model, reducing the reliability and consistency of performance. It should be noted

however that the values recorded are still a significant improvement in comparison to standard control techniques which do not consider a time-history of the wave disturbances within the control, as demonstrated in Fig. 6.8.

## 6.5 Conclusions

This chapter has proposed, implemented and successfully demonstrated a predictive control strategy in simulation on a multi-segment soft robot for rejection of active time-varying disturbances. The proposed strategy was shown to offer improved performance in contrast to an alternative and widely used model-based feed-forward plus PD controller, limiting the positional error of the end-effector in both set-point regulation scenarios and end-effector trajectory tracking missions. The controller was tested under numerous realistic scenarios which underwater manipulators commonly encounter, varying the wave-profile in spectral period to indicate performance independent of loading behaviour. Additionally, the control strategy demonstrated robustness in the form of fault compensation, where one of the soft robot actuated segments was simulated as failing. The MPC still successfully attained the desired end-effector position even in these instances, with a minimal increase in RMSE of 19.2% on average.

It was clear throughout the analysis that incorporation of the modelled disturbances within the control through the MPC strategy showed significant performance improvements, with up to 84% reduction in error witnessed during set-point regulation tasks. Successful trajectory tracking tests under wave disturbances were also observed, showing constrained positional error throughout the tracking task irrespective of wave conditions. With reference to points raised regarding difficulties of operating in a marine environment, MPC shows potential for improving the control of underwater manipulators by accounting for disturbances explicitly within the control sequence optimisation, while accounting for system dynamics to minimize such disturbances. The overall performances of the MPC are found to scale positively with wave heights, further supporting the use of MPC as the definitive control solution for real-world operation of soft manipulators.

These findings present evidence of the high potential related to using predictive strategies for soft manipulator control, but also present a potential research direction of combining this with the solution proposed in Chapter 5. The possibility of full body ROV-soft manipulator control possess a multitude of advantages; these are discussed in greater depth in Section 7.2.



## Chapter 7

# Conclusions

### 7.1 Summary

Targeting the development of effective control solutions to mitigate wave-induced disturbances for underwater robots, predictive approaches with embedded disturbance preview information were investigated throughout this thesis. Broadly, the work was undertaken in three parts:

- Development and experimental validation of a low-order wave-induced disturbance model, generalised for vehicle geometric and hydrodynamic parametrizations (Chapter 4).
- Inclusion of an experimentally validated wave prediction algorithm within an NMPC control strategy, providing a complete end-to-end solution for state regulation and trajectory tracking (Chapter 5).
- Analogous demonstration of an NMPC strategy for end-effector position regulation and trajectory tracking of a highly dynamic, soft robotic manipulator (Chapter 6).

With reference to the research objectives set in Section 1.2 prior to this work, the above points tackle these through the following aspects:

- Optimality - the NMPC framework performs an online optimisation to produce a control action with greater suitability than typical feedback approaches. As shown in Table 7.3, the lowest error with respect to the prescribed control goal refers to the NMPC with disturbance preview information strategy.
- Robustness - the presence of noise within the simulated system was handled effectively by the control; also, the case of partial actuation failure in the soft robot was mitigated.
- Flexibility - the formulation of disturbance models was moulded to be applicable to robots with varying geometric and hydrodynamic parameters, aiming for generalisation in all aspects.

TABLE 7.1: Summary of load estimation accuracy recorded during the analysis undertaken in Chapter 4, where Cor-Coeff and Norm-Error refer to the correlation coefficient and normalised error respectively for each wave case (see Table 4.1). Also,  $F_x$ ,  $F_z$  and  $M_\theta$  are the surge, heave and pitch wave load respectively.

Variable	Measurement	Wave Case					
		R01	R02	R03	JS01	JS02	JS03
$F_x$	Cor-Coeff	0.9250	0.9811	0.7207	0.9349	0.9661	0.9459
	Norm-Error	0.1651	0.1024	0.053	0.1093	0.0633	0.0462
$F_z$	Cor-Coeff	0.9205	0.9882	0.6567	0.9688	0.9707	0.9317
	Norm-Error	0.2729	0.1304	0.0144	0.1674	0.0779	0.0454
$M_\theta$	Cor-Coeff	0.8728	0.8796	0.4570	0.6571	0.7637	0.6402
	Norm-Error	0.2905	0.3063	0.2406	0.3383	0.1478	0.1318

TABLE 7.2: Summary of achievable DSWP accuracy during the analysis undertaken in Chapter 5, displaying the length of wave prediction, RMSE and average prediction processing time achievable for each wave case tested (see Table 5.2).

Wave Case	Pred. Len. (s)	RMSE (m)	Ave. Proc. Time (s)
T1	3.063	0.045	0.026
T2	2.250	0.025	0.027
T3	2.000	0.016	0.021

Considering the aspect of optimality, the research was structured and undertaken with the requirement of real-time deployment considered throughout. Estimation of wave-induced disturbances was formulated by applying low-order and computationally light techniques which maintained a sufficient degree of accuracy. Deterministic predictions were proven to predict the wave temporal profile accurately in Chapter 5, providing the relevant spectral information to apply the model developed and validated in Chapter 4. A generalised modelling approach was key when deriving simplified scaling models for the ROV station keeping in waves, analysing the accuracy of established models and low-order modelling techniques for fast yet accurate parameter estimations. Likewise, by maintaining a theme of generalised modelling in different aspects of the proposed solution, the overall framework inherently possesses a sense of flexibility and remains agnostic to the specificity of the control, the underlying hardware or actuation type. Effects of noise were handled effectively by the control, particularly in scenarios where the anticipated wave and experienced wave varied substantially in Chapter 5, highlighting a sense of robustness.

Quantitatively the findings from these research have been conveniently summarised in Tables 7.1-7.4. Initially, the low-order wave loading model presented in Chapter 4 was demonstrated experimentally to produce high correlation and low normalised point-by-point errors for the vast majority of cases investigated, detailed in Table 7.1. This supported the initial hypothesis that knowledge of key spectral parameters and hydrodynamic properties of the robot were sufficient to deduce the forces and torques

TABLE 7.3: Summary of RMSE errors recorded during the analysis undertaken in Chapter 5 for each irregular wave case with  $\gamma = 3.3$  (see Table 5.5). The cases reported considering noise (FF-N and NMPC-N) relate to a SNR = 10.

Task	Wave Case	DoF	RMSE (m)				
			C-PD	FF	NMPC	FF-N	NMPC-N
Station Keeping	W1 $T_p = 7.1\text{s}$ $H_s = 2.78\text{m}$	x (m)	0.1436	0.0573	0.0241	0.0731	0.0396
		z (m)	0.1557	0.0620	0.0271	0.0771	0.0438
		$\theta (\text{°})$	2.5583	1.0068	0.3167	1.2433	0.6278
	W2 $T_p = 9.5\text{s}$ $H_s = 3.47\text{m}$	x (m)	0.1731	0.0793	0.0365	0.0925	0.0543
		z (m)	0.1870	0.0825	0.0401	0.0986	0.0584
		$\theta (\text{°})$	2.1831	0.9641	0.4853	1.1018	0.8829
	W3 $T_p = 11.1\text{s}$ $H_s = 3.24\text{m}$	x (m)	0.1807	0.0887	0.0451	0.0996	0.0597
		z (m)	0.1936	0.0915	0.0515	0.1071	0.0687
		$\theta (\text{°})$	2.0190	0.9466	0.6023	1.0841	0.9561
Trajectory Tracking	W1 $T_p = 7.1\text{s}$ $H_s = 2.78\text{m}$	x (m)	0.1667	0.1270	0.0482	0.1342	0.0621
		z (m)	0.1740	0.1210	0.0473	0.1260	0.0662
		$\theta (\text{°})$	2.7067	1.3093	0.4952	1.3800	0.8409
	W2 $T_p = 9.5\text{s}$ $H_s = 3.47\text{m}$	x (m)	0.1964	0.1399	0.0624	0.1486	0.0813
		z (m)	0.2074	0.1393	0.0641	0.1450	0.0822
		$\theta (\text{°})$	2.3330	1.1773	0.5788	1.3679	1.0976
	W3 $T_p = 11.1\text{s}$ $H_s = 3.24\text{m}$	x (m)	0.1971	0.1376	0.0595	0.1443	0.0724
		z (m)	0.2093	0.1368	0.0641	0.1469	0.0857
		$\theta (\text{°})$	2.0605	1.0967	0.6508	1.2116	1.0455

acting on the vehicle, fuelling the investigation in Chapter 5. Here, obtaining the aforementioned parameters was experimentally tested, with the results in Table 7.2 relating to the instance when a threshold is placed on both amplitude and frequency and considering a measurement to prediction site distance of 15.07m. These clearly show that acceptable prediction lengths, RMSE and processing times were achievable to advance and embed the load estimation process within an NMPC structure. Subsequently, the integrated system was tested within a simulated environment for both station keeping and trajectory tracking of a ROV; Table 7.3 demonstrates that even in the presence of significant noise valuable reductions in RMSE were recorded, highlighting the potential of the proposed methodology. In conjunction, analysis regarding power expenditure in Chapter 5 supported the use of the NMPC, showing that the relative power consumed to normalised RMSE was in a similar range as a typical feedback controller. Finally, a similar methodology was analysed when applied for control of a highly dynamic system susceptible to system disturbances, namely a generic soft robot manipulator. The results from this investigation are given in Table 7.4, again highlighting the effectiveness of predictive control at mitigating state perturbations

TABLE 7.4: Summary of RMSE errors recorded during the end-effector regulation analysis undertaken in Chapter 6 for each wave case (see Table 6.3), given as an average RMSE across all analysed end-effector set-points per control. Here, NMPC-F refers to the scenarios where the robot is only partially actuated.

Task	Wave Case	RMSE (m)		
		FF+PD	NMPC	NMPC-F
End-Effector Regulation	S1	0.4166	0.1297	0.2504
	S2	0.3920	0.1274	0.2271
	S3	0.5011	0.1531	0.2328

and regulating a desired end-effector position, even when the controlled system loses part of its actuation capabilities as displayed in the final column (NMPC-F).

Overall, the research detailed within this thesis presents valuable insights and key findings, strongly supporting the plausibility and effectiveness of directly applying modelled short-horizon time history evolution's of impending wave disturbances within a predictive control structure. However, additional research is required to fully form the proposed system and prove applicability thoroughly, as discussed in further detail below.

## 7.2 Future Research Directions

Given the findings in this thesis, it is clear that a significant potential exists in the proposed solution for disturbance mitigation of underwater robotic systems. However, as with every project which focuses on an initial validation, several further developments are required to prove applicability in a real-world scenario. As this thesis concerned two unique applications for the proposed framework, these will be discussed separately for clarity before suggesting other interesting avenues which may produce interesting branches for research projects stemming from the work conducted in this thesis.

### 7.2.1 Nonlinear Model Predictive Dynamic Positioning Exploiting Wave Disturbance Preview

For the application of a predictive strategy to improve the wave-induced disturbance rejection capability of an underwater vehicle, the following areas have been identified as being critical to advance this research further.

#### Extension into the Spatial Domain

The extension into three dimensions is intuitive but is a key element required to completely validate the applicability of the proposed solution; this is a relatively simple adaptation to the simulations from a theoretical perspective but introduces

additional complexities with regards to dynamic coupling. Within this thesis, this was neglected to present an initial validation of a planar case, partly owing to early work utilising DSWP which focused on predicting predominantly planar shallow water waves.

This relates to both the modelling of the plant and the prediction algorithm; for the latter, this can be achieved by leveraging the work in [268]. An array of sensors measuring the wave profile can be exploited to deduce the directionality of the spectral wave components, providing the required information to spatially reconstruct the predicted wave field.

### **Integrated Experimental Studies**

Although experimental studies were undertaken to validate the prediction and disturbance estimation aspects of the work, the opportunity to test the full control framework in experiments was unfortunately not possible in the allotted time-frame. Given this, an obvious next step would be to synthesise the NMPC and perform some initial validation and testing to confirm functionality when considering the wave to be known at the plant location - the natural extension is incorporation of the DSWP algorithm and inspection of control performance when exploiting the wave-induced disturbance predictions in real-time. This would constitute a lengthy experimental study which would test the framework in a controlled environment. If successful, this constitutes a solid basis to advance into sea trials to rigorously test the solution outwith a controlled experimental setting.

Outwith the control and prediction aspects but in relation to the above aims, work would be required to explore communication protocols for achieving a link between the wave measurement device and the ROV on-board computer. This would largely depend on the vehicle platform adopted; if the current vehicle is maintained (the BlueROV2), this would simplify this aspect owing to the use of the tether. Wireless subsea communication would no longer become critical by using a computer above the surface to receive the wave measurements, transmitting these to the ROV via the tether directly. Of course this may introduce time-delays, but it is anticipated these would be minimal. Typical approaches can be leveraged to establish full wireless connectivity directly with the ROV (which would effectively allow the vehicle to operate autonomously without pilot control), but this could constitute an entire project in itself to determine suitable solutions.

### **Wave Prediction Algorithm Optimisation**

Considering the prediction element of the framework, an interesting area of expansion would be to investigate alternative algorithms, examining the accuracy to computational burden relationship. As this is a key factor which will affect the performance of the control, it is critical to find a trade-off between these two parameters. It would

also be interesting to test the suitability of the fixed-point method or using mixed space-time data, with the aim of exploring various solutions to real-world deployment.

Similarly, assuming that the DSWP algorithm is maintained in future work, applying some of the suggested tools in [265] will be key to extend the attainable predictable region and improve prediction accuracy. This would entail a further experimental study with both planar and multi-directional waves, examining which of the techniques prove useful to extend predictions into longer time periods.

### 7.2.2 Predictive Disturbance Rejection for Soft Underwater Manipulators

For the application of a predictive strategy to improve wave-induced disturbance rejection in the context of a soft underwater manipulator, the following areas have been identified as being critical to advance this research further.

#### Extension into the Spatial Domain

As with the case for vehicle control, the current system must be expanded into a spatial case to include bending and wave disturbances which are not only planar. Adapting the dynamic model of the soft manipulator to display this behaviour is easily achievable using a constant curvature model, but it is uncertain how the wave-disturbances will affect the highly coupled system in three dimensions. This could lead to some erratic behaviour as the body is excited in different planes, so particular attention will be required when applying the control. A similar approach can still be followed for modelling of the wave profile, but requires inclusion of a directional parameter to determine the propagation direction of each spectral component. For non-spherical bodies, this becomes a key point of consideration as the wave-induced load can no longer always be assumed as acting normal to the surface. As a first port of call the normal force component can be extracted and analysed, but it is unclear how the tangential force component may affect different geometries (for example a square cylindrical body).

Similarly, the model employed throughout this section of work was the PCC representation; this has proved useful in a large body of cases described in literature [237, 196], but can lack detail in some instances when the body has a high level of compliance or is capable of twisting excessively. It would be interesting to investigate alternative models and their applicability, for example Cosserat approaches have been shown to offer greater flexibility when bending cannot be assumed constant; these also account for shear and torsion which is assumed null in the PCC approach [330]. This could offer greater control over the soft manipulator configuration, but may require careful consideration upon integration with the MPC scheme. It is likely this will intensify the optimisation procedure - this leads nicely into the final element of this additional research direction.

The application of an efficient optimisation solving method similar to that implemented for the ROV NMPC is key if this proposed approach is to be advanced further. In Chapter 6 this was not adopted stemming from the additional complexities within the robot dynamics (namely struggles when considering the configuration dependent optimisation procedure), but to realise the system on a real world platform this is a critical factor. Although processing time was not excessive in the cases presented in this thesis, to be applied in real time improvements would be required which could include applying model-reduction techniques in conjunction with an efficient nonlinear solver, amongst others.

These points link closely with the next research direction given below, which involves experimentally validating the wave-induced disturbances acting on the soft manipulator.

### Wave-Induced Disturbance Model Validation

Assuming that the model expansion into three dimensions was achieved successfully, an intuitive next step is to begin experimental validation of the proposed solution.

Firstly, the current model for wave-induced disturbances acting on a slender, soft manipulator has been formulated and adapted from principles relating to Morison strip theory [303], supported by previous works taking similar approaches [232]. There is some disparity between these works and the cases considered in this thesis however, namely the presence of an active fluid which is perturbed by a time-varying propagating wave. A key element of proving this framework therefore lies in experimentally validating the wave-induced disturbance model presented in Section 6.3. This would initially concern a spherical cylindrical body but can easily be expanded to consider non-spherical bodies and also non-symmetrical, although the latter may prove difficult to characterise from a hydrodynamic coefficient perspective. Nevertheless, this forms a critical next step as the predictive controller is highly dependent on disturbance preview information featuring a reasonable degree of accuracy to perform well, as was seen in the case for the ROV (Section 5.5.3). This point can also include the integration of a wave prediction algorithm, such as Algorithm 1. This forms a minor advancement owing to the successful validation undertaken in Section 5.3 for DSWP, but similar to the case for an ROV could form a work package in itself investigating different prediction tools for system optimisation.

Analogously, an interesting aspect of these experiments would be the variation of results obtained when considering bodies manufactured with materials that can and cannot deform under loading. For example, a plastic or metallic tendon driven robot may display contrasting behaviour to a pneumatically driven silicone-based soft robot, even though both can be modelled under the same principles of PCC.

### 7.2.3 Combined Vehicle-Soft Manipulator Control

The discussions above consider each system independently, but high potential lies in combining the two systems for the purpose of performing safe and robust inspection or intervention at close-vicinity.

MPC was shown to greatly improve regulation and tracking performance independently in Chapters 5-6, so the extension to full body control of an ROV equipped with a soft manipulator is expected to share the same potential. In particular, the possibility of the controller being able to optimise for both a vehicle and soft manipulator pose in tandem is a proposal which is yet to be tackled. This would add a great deal of robustness to the system, notably due to the compliance of the soft manipulator increasing the ability to withstand unexpected torques and collisions. This application has been proposed for delicate grasping of organisms [226], but these were completely piloted and focused on the design element over the control. It should also be noted that much higher transmitted forces and torques are required if a soft manipulator is to be functional for operating elements of underwater energy-related plants; this aspect falls under the design remit of this extension but also concerns the control. A related factor which could help tackle this problem is the inclusion of variable stiffness mechanisms to actively alter the load bearing capacity of the manipulator [220, 216]. This would facilitate greater capabilities at the end-effector whilst retaining the advantageous compliance inherent to soft robots, taking a hybrid soft-rigid approach. This can be achieved through concepts related to bead-based designs and tendon driven actuation for example, amongst others.

Inherently a soft manipulator can achieve configurations a standard manipulator cannot, improving the operational capabilities of current systems substantially. Combined ROV manipulator control has been the topic of some research in recent times [331, 332], so this extension can potentially replace current systems within industry if proven to be successful. If implementation of these recommended advancements in an integrated system can be achieved, this paves the way for autonomous vehicles with augmented manipulation and inspection capabilities to become a reality. Not only that, but operation in environments normally precluded to robots and humans becomes possible, taking a significant step towards safer, reliable and efficient exploitation of marine renewable energy technologies.

## 7.3 Implementation in the Field

Translating research from a lab-based setting into the field can present a multitude of challenges, thus considerations must be made and possible areas of concern addressed throughout the research process. The concerns relating to this work will be addressed

here in two parts: those relating to obtaining the wave prediction, and those relating to exploiting the wave prediction within the control.

Obtaining the wave prediction through DSWP relies heavily on being able to measure the wave profile in some manner. Measuring the wave profile directly can be facilitated through some apparatus such as a wave-rider buoy, a wave gauge attached to a nearby structure or using more recent technological developments such as LIDAR (which has been adopted in recent works 2.11). In a lab setting this is easily acquired through wave gauge apparatus, however translation into the field is not so achievable given our intended application is for operating nearby structures. This provides a localised point to take measurements from, particularly in the case of an offshore wind farm where there is an array of structures. This has the advantage over wave-rider apparatus of being a fixed structure, although deployed wave buoys possess accurate GPS location capability and so drift can be accounted for by leveraging this. Alternatively, pressure or fluid velocity measurements also present potential for acquiring measurements, given they possess the same frequency components. The drawback here is that an additional transformation may be required to obtain parameters such as wave elevation, but it is certainly a viable solution to obtain the information required to evaluate the disturbance model.

Addressing how the disturbance estimations can then be exploited requires a discussion on communication methods. For a tethered operation this forms less of a problem, as communication from the measurement apparatus can be performed above the surface to a "ground station" and subsequently transferred to the ROV via the tether. Latency would have to be considered, but given that predictions of 2s were obtainable during this work, a minor time delay in data transfer should not cause problems. Un-tethered operations would be more challenging, but by no means impossible by leveraging standard methods such as acoustic communications used for AUVs. The other consideration on the exploitation side is estimating the vehicle state. Typically this is performed through sensor fusion, using multiple measurements from sensors such as (but not limited to) a DVL, sonar, etc. - as is done in this work, these are then fused using some form of state estimator to provide state feedback. It should be noted that in an experimental setting this does not form an issue as highly accurate tracking apparatus is readily available, specifically the Qualisys system as used in Chapter 4. Both state and wave measurement information can be fed into a local computer and transferred to the ROV through the tether, therefore implementation does form a major concern.

In general, the major concerns noted above can be addressed using typical methods and by taking sufficient steps to account for communication latency and state uncertainty. Overall, translation in the field is certainly viable and a future target upon further experimental validation of the proposed method.



## Appendix A

# Publications

### A.1 Published

Listed below are all publications which have been accepted for inclusion within the proceedings of conferences or a journal issue, inclusive of those which have been accepted but are still in press and being processed.

- K. L. Walker, A. A. Stokes, A. Kiprakis and F. Giorgio-Serchi, "Investigating PID control for station keeping ROVs", *Proc. UKRAS20: "Robots into the Real World", Lincoln, U.K., pp. 51-53, 17 April 2020.*
- R. Gabl, T. Davey, Y. Cao, Q. Li, K. L. Walker, F. Giorgio-Serchi, S. Aracri, A. Kiprakis, A. A. Stokes and D. M. Ingram, "Experimental force data of a restrained ROV under waves and current", *Data*, vol. 5, no. 3, 30 June 2020.
- K. L. Walker, A. A. Stokes, A. Kiprakis and F. Giorgio-Serchi, "Impact of Thruster Dynamics on the Feasibility of ROV Station Keeping in Waves", *Proc. of Global Oceans 2020: Singapore-U.S. Gulf Coast*, pp. 1-7, 05 Oct. 2020.
- K. L. Walker, R. Gabl, S. Aracri, Y. Cao, A. A. Stokes, A. Kiprakis, F. Giorgio-Serchi, "Experimental Validation of Wave Induced Disturbances for Predictive Station Keeping of a Remotely Operated Vehicle", *IEEE Robotics and Automation Letters*, vol. 6, no. 3, pp. 5421-5428, 27 April 2021.
- K. L. Walker, R. Gabl, S. Aracri, Y. Cao, A. A. Stokes, A. Kiprakis, F. Giorgio-Serchi, "Experimental Validation of Unsteady Wave Induced Loads on a Stationary Remotely Operated Vehicle", *Proc. of IEEE International Conference on Robotics and Automation (ICRA)*, Xi'an, China, pp. 2242-2248, 30 May 2021.
- R. Gabl, T. Davey, Y. Cao, Q. Li, K. L. Walker, F. Giorgio-Serchi, S. Aracri, A. Kiprakis, A. A. Stokes and D. M. Ingram, "Hydrodynamic loads on a restrained ROV under waves and current", *Ocean Engineering*, vol. 234, 15 Aug. 2021.
- M. Chellapurath, K. L. Walker, E. Donato, G. Picardi, S. Stefanni, C. Laschi, F. Giorgio-Serchi and M. Calisti, "Analysis of Station Keeping Performance of

an Underwater Legged Robot", *IEEE/ASME Transactions on Mechatronics*, vol. 27, no. 5, pp. 3730-3741, 22 Dec. 2021.

- **K. L. Walker**, A. A. Stokes, A. Kiprakis and F. Giorgio-Serchi, "Feed-forward Disturbance Compensation for Station Keeping in Wave-dominated Environments", *Proc. of Oceans 2023*, Limerick, Ireland, 2023. **In Press**.
- **K. L. Walker** and F. Giorgio-Serchi, "Disturbance Preview for Nonlinear Model Predictive Trajectory Tracking of Underwater Vehicles in Wave Dominated Environments", *Proc. of IEEE International Conference on Intelligent Robots and Systems (IROS)*, Detroit, Michigan, U.S.A, 2023. **In Press**.

## A.2 Under Review

Listed below are all publications which have been submitted for inclusion within the proceedings of conferences or a journal issue, but at the time of submission of this thesis have not received a final decision. It is anticipated that these will be published after review and form further contributions to the field.

- **K. L. Walker**, C. D. Santina and F. Giorgio-Serchi, "Model Predictive Disturbance Rejection for Underwater Soft Robotic Manipulators", *IEEE RoboSoft*, 2024.
- **K. L. Walker**, L. B. Jordan and F. Giorgio-Serchi, "Nonlinear Model Predictive Dynamic Positioning of Underwater Robots with Wave Disturbance Preview", *International Journal of Robotics Research*, 2023.

## Appendix B

# Reference MATLAB Scripts

### B.1 WAMIT Symmetrising Script

Sourced and provided by [310].

```
%This script properly formats and averages out the added
mass matrix data from WAMIT.

rho_w = 1025;

%Setting up the added mass matrix for no-wave zone.
Added_mass = dlmread('brov2.1');
M_a = zeros(6,6);
row = Added_mass(:, 2);
col = Added_mass(:, 3);
val = Added_mass(:, 4);
T_gdf = diag([1, -1, -1, 1, -1, -1]);
for i = 1:length(val)
    M_a(row(i), col(i)) = rho_w*val(i);
end
M_a = T_gdf*M_a*T_gdf;
M_a_assym = M_a;
for i = 1:6
    for j = 1:6
        M_avg = (M_a(i,j) + M_a(j,i))/2;
        M_a(i,j) = M_avg;
        M_a(j,i) = M_avg;
    end
end
format shortG;
dlmwrite('Added Mass.txt', M_a, '\t');
```



# Bibliography

- [1] R. M. Oosthuizen, “The Fourth Industrial Revolution – Smart Technology, Artificial Intelligence, Robotics and Algorithms: Industrial Psychologists in Future Workplaces,” *Frontiers in Artificial Intelligence*, vol. 5, pp. 90–95, July 2022.
- [2] M. Xu, J. M. David, and K. S. H., “The Fourth Industrial Revolution: Opportunities and Challenges,” *International Journal of Financial Research*, vol. 9, pp. 90–95, March 2018.
- [3] D. C. Bellicoso, M. Bjelonic, L. Wellhausen, K. Holtman, Günther, M. Tranzatto, P. Fankhauser, and M. Hutter, “Advances in real-world applications for legged robots,” *Journal of Field Robotics*, vol. 35, pp. 1311–1326, Nov 2018.
- [4] M. H. Frederiksen and M. P. Knudsen, “Drones for offshore and maritime missions: Opportunities and barriers,” *Innovation Fund Denmark*, April 2018.
- [5] E. Zereik, M. Bibuli, Mišković, P. Ridao, and A. Pascoal, “Challenges and future trends in marine robotics,” *Annual Reviews in Control*, vol. 46, pp. 350–368, Oct. 2018.
- [6] G. Ferri, A. Munafó, A. Tesei, P. Braca, F. Meyer, K. Pelekanakis, R. Petroccia, J. Alves, C. Strode, and K. LePage, “Cooperative robotic networks for underwater surveillance: an overview,” *IET Radar, Sonar & Navigation*, vol. 11, pp. 1740–1761, Dec. 2017.
- [7] G. Smart and Offshore Renewable Energy Catapult, “The Economic Opportunity for Robotics in Offshore Wind and Key Energy Markets,” Offshore Renewable Energy Catapult, Tech. Rep. September, 2021.
- [8] A. Koltsidopoulos, D. Wavell, and A. Gray, “Quantifying the impact of Robotics in Offshore Wind,” Offshore Wind Innovation Hub, Tech. Rep. July, 2021.
- [9] S. Aracri, F. Giorgio-Serchi, G. Suaria, M. E. Sayed, M. P. Nemitz, S. Mahon, and A. A. Stokes, “Soft Robots for Ocean Exploration and Offshore Operations: A Perspective,” *Soft Robotics*, vol. 8, no. 6, pp. 625–639, dec 2021.
- [10] A. Shukla and H. Karki, “Application of robotics in offshore oil and gas industry— A review Part II,” *Robotics and Autonomous Systems*, vol. 75, pp. 508–524, jan 2016.

- [11] H. A. Kermorgant and D. Scourzic, "Interrelated functional topics concerning autonomy related issues in the context of autonomous inspection of underwater structures," *Oceans 2005 - Europe*, vol. 2, pp. 1370–1375, 2005.
- [12] Ö. Netland, I. B. Sperstad, M. Hofmann, and A. Skavhaug, "Cost-benefit Evaluation of Remote Inspection of Offshore Wind Farms by Simulating the Operation and Maintenance Phase," *Energy Procedia*, vol. 53, no. C, pp. 239–247, jan 2014.
- [13] O. Khalid, G. Hao, C. Desmond, H. Macdonald, F. D. McAuliffe, G. Dooly, and W. Hu, "Applications of robotics in floating offshore wind farm operations and maintenance: Literature review and trends," *Wind Energy*, vol. 25, no. 11, pp. 1880–1899, nov 2022.
- [14] Y. R. Petillot, G. Antonelli, G. Casalino, and F. Ferreira, "Underwater Robots: From Remotely Operated Vehicles to Intervention-Autonomous Underwater Vehicles," *IEEE Robotics & Automation Magazine*, vol. 26, pp. 94–101, June 2019.
- [15] S. C. Martin, L. L. Whitcomb, D. Yoerger, and H. Singh, "A Mission Controller for High Level Control of Autonomous and Semi-Autonomous Underwater Vehicles," in *OCEANS 2006*. Boston, MA, U.S.A: IEEE, 18-21 Sept. 2006.
- [16] I. Schjølberg and I. B. Utne, "Towards autonomy in ROV operations," *IFAC-PapersOnLine*, vol. 48, pp. 183–188, 2015.
- [17] B. Johansson, J. Siesjö, and M. Furuholmen, "Seaeye Sabertooth: A hybrid AUV/ROV offshore system," in *MTS/IEEE Seattle, OCEANS 2010*, Seattle, WA, USA, 2010.
- [18] H. Malekpoor, A. Ramudhin, and N. M. September, "Autonomous Vehicles for O & M : Parts Delivery and Other Applications," Offshore Renewable Energy Catapult, Tech. Rep. September, 2018.
- [19] S. Sivčev, J. Coleman, E. Omerdić, G. Dooly, and D. Toal, "Underwater Manipulators: A Review," *Ocean Engineering*, vol. 163, pp. 431–450, Sept. 2018.
- [20] T. G. Thuruthel, Y. Ansari, E. Falotico, and C. Laschi, "Control Strategies for Soft Robotic Manipulators: A Survey," *Soft Robotics*, vol. 5, no. 2, pp. 149–163, 2018.
- [21] D. C. Fernandez and G. A. Hollinger, "Model Predictive Control for Underwater Robots in Ocean Waves," *IEEE Robotics and Automation Letters*, vol. 2, no. 1, pp. 88–95, 2017.
- [22] C. E. S. Koch, "Model Predictive Control for Six Degrees-of-Freedom Station-Keeping of an Underwater Vehicle-Manipulator System," Ph.D. dissertation, KTH Royal Institute of Technology, 2017.

- [23] W. Liuping, *Model Predictive Control System Design and Implementation Using MATLAB*. Springer, 2009.
- [24] F. Renda and C. Laschi, “A general mechanical model for tendon-driven continuum manipulators,” in *IEEE International Conference on Robotics and Automation*. Saint Paul, Minnesota, USA: Institute of Electrical and Electronics Engineers Inc., 2012, pp. 3813–3818.
- [25] X. Fang and W.-H. Chen, “Model Predictive Control With Preview: Recursive Feasibility and Stability,” *IEEE Control Systems Letters*, vol. 6, pp. 2647–2652, May 2022.
- [26] O. Landstad, H. S. Halvorsen, H. Øveraas, V. Smies, and T. A. Johansen, “Dynamic positioning of ROV in the wave zone during launch and recovery from a small surface vessel,” *Ocean Engineering*, vol. 235, p. 109382, sep 2021.
- [27] R. Gabl, T. Davey, Y. Cao, Q. Li, B. Li, K. L. Walker, F. Giorgio-serchi, S. Aracri, A. Kiprakis, A. A. Stokes, and D. M. Ingram, “Experimental Force Data of a Restrained ROV under Wave and Current,” *Data*, pp. 1–16, 2020.
- [28] R. Gabl, T. Davey, Y. Cao, Q. Li, B. Li, K. L. Walker, F. Giorgio-Serchi, S. Aracri, A. Kiprakis, A. A. Stokes, and D. M. Ingram, “Hydrodynamic loads on a restrained ROV under waves and current,” *Ocean Engineering*, vol. 234, p. 109279, aug 2021.
- [29] K. L. Walker, R. Gabl, S. Aracri, Y. Cao, A. A. Stokes, A. Kiprakis, and F. Giorgio-Serchi, “Experimental Validation of Unsteady Wave Induced Loads on a Stationary Remotely Operated Vehicle,” in *IEEE International Conference on Robotics and Automation*. Xi'an, China: Institute of Electrical and Electronics Engineers Inc., 2021, pp. 2242–2248.
- [30] ———, “Experimental Validation of Wave Induced Disturbances for Predictive Station Keeping of a Remotely Operated Vehicle,” *IEEE Robotics and Automation Letters*, vol. 6, no. 3, pp. 5421–5428, jul 2021.
- [31] K. L. Walker, A. A. Stokes, A. Kiprakis, and F. Giorgio-Serchi, “Feed-forward Disturbance Compensation for Station Keeping in Wave-dominated Environments,” in *Oceans 2023 MTS/IEEE Limerick*. Limerick, Ireland: arXiv preprint, June 2023.
- [32] K. Ogata, *Modern Control Engineering*, 4th ed. Prentice Hall, 2002.
- [33] P. J. Gawthrop, “Self-Tuning PID Controllers: Algorithms and Implementation,” *IEEE Transactions on Automatic Control*, vol. 31, no. 3, pp. 201–209, 1986.

- [34] K. K. Tan, S. Huang, and R. Ferdous, “Robust self-tuning PID controller for nonlinear systems,” *Journal of Process Control*, vol. 12, no. 7, pp. 753–761, oct 2002.
- [35] R. Rout and B. Subudhi, “Inverse optimal self-tuning PID control design for an autonomous underwater vehicle,” *International Journal of Systems Science*, vol. 48, no. 2, pp. 367–375, jan 2016.
- [36] O. Yildiz, R. B. Gökalp, and A. E. Yilmaz, “A review on motion control of the Underwater Vehicles,” in *International Conference on Electrical and Electronics Engineering - ELECO 2009*. Bursa, Turkey: IEEE, 05-08 Nov. 2009.
- [37] M. Kim, H. Joe, J. Pyo, J. Kim, H. Kim, and S.-C. Yu, “Variable-structure PID controller with anti-windup for autonomous underwater vehicle,” in *2013 OCEANS - San Diego*. San Diego, CA. U.S.A.: IEEE, 23-27 Sept. 2013.
- [38] F. Kong, Y. Guo, and W. Lyu, “Dynamics Modeling and Motion Control of an New Unmanned Underwater Vehicle,” *IEEE Access*, vol. 8, pp. 30 119 – 30 126, Feb. 2020.
- [39] I. Carlucho, B. Menna, M. De Paula, and G. G. Acosta, “Comparison of a PID controller versus a LQG controller for an autonomous underwater vehicle,” in *3rd IEEE/OES South American International Symposium on Oceanic Engineering (SAISOE)*. Buenos Aires, Argentina: IEEE, 15-17 June 2013.
- [40] K. L. Walker, A. A. Stokes, A. Kiprakis, and F. Giorgio-Serchi, “Investigating PID Control for Station Keeping ROVs,” in *UKRAS20 Conference: “Robots into the real world” Proceedings*. Lincoln, UK: EPSRC UK-RAS Network, may 2020, pp. 51–53.
- [41] R. Hernández-Alvarado, L. G. García-Valdovinos, T. Salgado-Jiménez, A. Gómez-Espinosa, and F. Fonseca-Navarro, “Neural Network-Based Self-Tuning PID Control for Underwater Vehicles,” *Sensors*, vol. 16, no. 9, p. 1429, sep 2016.
- [42] M. Abdellatif, O. Rashed, M. Transport, S. Shaaban, M. Transport, and A. M. Abdulaziz, “Online Ocean Current Estimation and Mapping for Autonomous Underwater Vehicle,” in *Mechatronics 2018*, no. September, 2018.
- [43] A. J. Healey and D. Lienard, “Multivariable Sliding Mode Control for Autonomous Diving and Steering of Unmanned Underwater Vehicles,” *IEEE Journal of Oceanic Engineering*, vol. 18, pp. 108–120, July 1993.
- [44] L. G. García-Valdovinos, T. Salgado-Jiménez, M. Bandala-Sánchez, L. Navarrete-Balanzar, R. Hernández-Alvarado, and J. A. Cruz-Ledesma, “Modelling, Design

- and Robust Control of a Remotely Operated Underwater Vehicle," *International Journal of Advanced Robotic Systems*, vol. 11, no. 1, pp. 1–16, jan 2014.
- [45] T. Elmokadem, M. Zribi, and K. Youcef-Toumi, "Terminal sliding mode control for the trajectory tracking of underactuated Autonomous Underwater Vehicles," *Ocean Engineering*, vol. 129, pp. 613–625, jan 2017.
- [46] M. Von Benzon, F. Sorensen, J. Liniger, S. Pedersen, S. Klemmensen, and K. Schmidt, "Integral Sliding Mode Control for a Marine Growth Removing ROV with Water Jet Disturbance," *2021 European Control Conference, ECC 2021*, pp. 2265–2270, 2021.
- [47] L. Hsu, R. R. Costa, F. Lizarralde, and J. P. Da Cunha, "Dynamic positioning of remotely operated underwater vehicles," *IEEE Robotics and Automation Magazine*, vol. 7, no. 3, pp. 21–31, sep 2000.
- [48] E. A. Tannuri, A. C. Agostinho, H. M. Morishita, and L. Moratelli, "Dynamic positioning systems: An experimental analysis of sliding mode control," *Control Engineering Practice*, vol. 18, no. 10, pp. 1121–1132, oct 2010.
- [49] J. Javadi-Moghaddam and A. Bagheri, "An adaptive neuro-fuzzy sliding mode based genetic algorithm control system for under water remotely operated vehicle," *Expert Systems with Applications*, vol. 37, no. 1, pp. 647–660, jan 2010.
- [50] W. M. Bessa, M. S. Dutra, and E. Kreuzer, "Depth control of remotely operated underwater vehicles using an adaptive fuzzy sliding mode controller," *Robotics and Autonomous Systems*, vol. 56, no. 8, pp. 670–677, aug 2008.
- [51] L. Qiao and W. Zhang, "Adaptive non-singular integral terminal sliding mode tracking control for autonomous underwater vehicles," *IET Control Theory & Applications*, vol. 11, no. 8, pp. 1293–1306, may 2017.
- [52] G. Bartolini, A. Ferrara, and E. Usai, "Chattering avoidance by second-order sliding mode control," *IEEE Transactions on Automatic Control*, vol. 43, no. 2, pp. 241–246, 1998.
- [53] H. Lee and V. I. Utkin, "Chattering suppression methods in sliding mode control systems," *Annual Reviews in Control*, vol. 31, no. 2, pp. 179–188, jan 2007.
- [54] J. S. Wang and C. S. Lee, "Self-adaptive recurrent neuro-fuzzy control of an autonomous underwater vehicle," *IEEE Transactions on Robotics and Automation*, vol. 19, no. 2, pp. 283–295, apr 2003.
- [55] K. D. Do, J. Pan, and Z. P. Jiang, "Robust and adaptive path following for underactuated autonomous underwater vehicles," *Ocean Engineering*, vol. 31, no. 16, pp. 1967–1997, nov 2004.

- [56] C. Barbalata, V. De Carolis, M. W. Dunnigan, Y. Pétillot, and D. Lane, "An adaptive controller for autonomous underwater vehicles," in *IEEE International Conference on Intelligent Robots and Systems*. Institute of Electrical and Electronics Engineers Inc., dec 2015, pp. 1658–1663.
- [57] D. Maalouf, A. Chemori, and V. Creuze, "L1 Adaptive depth and pitch control of an underwater vehicle with real-time experiments," *Ocean Engineering*, vol. 98, pp. 66–77, apr 2015.
- [58] R. Cui, X. Zhang, and D. Cui, "Adaptive sliding-mode attitude control for autonomous underwater vehicles with input nonlinearities," *Ocean Engineering*, vol. 123, pp. 45–54, sep 2016.
- [59] Z. Yan, M. Wang, and J. Xu, "Robust adaptive sliding mode control of underactuated autonomous underwater vehicles with uncertain dynamics," *Ocean Engineering*, vol. 173, pp. 802–809, feb 2019.
- [60] Z. Peng, J. Wang, and J. Wang, "Constrained Control of Autonomous Underwater Vehicles Based on Command Optimization and Disturbance Estimation," *IEEE Transactions on Industrial Electronics*, vol. 66, no. 5, pp. 3627–3635, may 2019.
- [61] H. Trentelman, "Linear Quadratic Optimal Control," *Encyclopedia of Systems and Control*, pp. 1–8, 2013.
- [62] R. D. S. Tchilian, E. Rafikova, S. A. Gafurov, and M. Rafikov, "Optimal Control of an Underwater Glider Vehicle," *Procedia Engineering*, vol. 176, pp. 732–740, jan 2017.
- [63] M. G. Joo and Z. Qu, "An autonomous underwater vehicle as an underwater glider and its depth control," *International Journal of Control, Automation and Systems*, vol. 13, no. 5, pp. 1212–1220, oct 2015.
- [64] A. A. R. Al Makdah, N. Daher, D. Asmar, and E. Shammas, "Three-dimensional trajectory tracking of a hybrid autonomous underwater vehicle in the presence of underwater current," *Ocean Engineering*, vol. 185, pp. 115–132, aug 2019.
- [65] H. S. Halvorsen, H. Øveraas, O. Landstad, V. Smnes, T. I. Fossen, and T. A. Johansen, "Wave motion compensation in dynamic positioning of small autonomous vessels," *Journal of Marine Science and Technology*, 2020.
- [66] Y. Cao, B. Li, Q. Li, A. A. Stokes, D. M. Ingram, and A. Kiprakis, "A nonlinear model predictive controller for remotely operated underwater vehicles with disturbance rejection," *IEEE Access*, vol. 8, pp. 158 622–158 634, 2020.

- [67] R. A. Fernandez, D. Grande, A. Martins, L. Bascetta, S. Dominguez, and C. Rossi, "Modeling and Control of Underwater Mine Explorer Robot UX-1," *IEEE Access*, vol. 7, pp. 39 432–39 447, 2019.
- [68] J. Cao, J. Cao, Z. Zeng, and L. Lian, "Nonlinear multiple-input-multiple-output adaptive backstepping control of underwater glider systems," *International Journal of Advanced Robotic Systems*, vol. 13, no. 6, pp. 1–14, dec 2016.
- [69] C. Mai, S. Pedersen, L. Hansen, K. Jepsen, and Z. Yang, "Modeling and Control of Industrial ROV's for Semi-Autonomous Subsea Maintenance Services," *IFAC-PapersOnLine*, vol. 50, no. 1, pp. 13 686–13 691, jul 2017.
- [70] B. Houska, H. J. Ferreau, and M. Diehl, "ACADO toolkit—An open-source framework for automatic control and dynamic optimization," *Optimal Control Applications and Methods*, vol. 32, no. 3, pp. 298–312, may 2011.
- [71] J. A. Andersson, J. Gillis, G. Horn, J. B. Rawlings, and M. Diehl, "CasADI: a software framework for nonlinear optimization and optimal control," *Mathematical Programming Computation*, vol. 11, no. 1, pp. 1–36, mar 2019.
- [72] P. Falcone, F. Borrelli, J. Asgari, H. E. Tseng, and D. Hrovat, "Predictive active steering control for autonomous vehicle systems," *IEEE Transactions on Control Systems Technology*, vol. 15, no. 3, pp. 566–580, may 2007.
- [73] E. Kayacan, H. Ramon, and W. Saeys, "Robust trajectory tracking error model-based predictive control for unmanned ground vehicles," *IEEE/ASME Transactions on Mechatronics*, vol. 21, no. 2, pp. 806–814, apr 2016.
- [74] B. Li, W. Zhou, J. Sun, C.-Y. Wen, and C.-K. Chen, "Development of Model Predictive Controller for a Tail-Sitter VTOL UAV in Hover Flight," *Sensors*, vol. 18, pp. 1–21, 2018.
- [75] T. Wang, H. Gao, and J. Qiu, "A Combined Adaptive Neural Network and Nonlinear Model Predictive Control for Multirate Networked Industrial Process Control," *IEEE Transactions on Neural Networks and Learning Systems*, vol. 27, no. 2, pp. 416–425, feb 2016.
- [76] W. Naeem, "Model Predictive Control of an Autonomous Underwater Vehicle," in *UKACC 2002 Postgraduate Symposium*, 2002.
- [77] R. Smierzchalski, M. Kwiesielewicz, M. Szymanski, and R. Sutton, "Predictive Control and Dynamic Planning of an Autonomous Underwater Vehicle," *IFAC Proceedings Volumes*, vol. 34, no. 7, pp. 161–166, jul 2001.
- [78] G. Marafioti, R. R. Bitmead, and M. Hovd, "Model Predictive Control with State Dependent Input Weight: an Application to Underwater Vehicles," *IFAC Proceedings Volumes*, vol. 41, no. 2, pp. 15 979–15 984, 2008.

- [79] C. V. Caldwell, D. D. Dunlap, and E. G. Collins, "Motion planning for an autonomous underwater vehicle via sampling based model predictive control," in *MTS/IEEE Seattle, OCEANS 2010*, 2010.
- [80] L. V. Steenson, A. B. Phillips, E. Rogers, M. E. Furlong, and S. R. Turnock, "Experimental verification of a depth controller using model predictive control with constraints onboard a thruster actuated AUV," in *Second International Symposium on Marine Propulsors*, vol. 3, Hamburg, Germany, 2012, pp. 275–280.
- [81] L. V. Steenson, "Experimentally Verified Model Predictive Control of a Hover-Capable AUV," Ph.D. dissertation, University of Southampton, 2013.
- [82] L. V. Steenson, S. R. Turnock, A. B. Phillips, C. Harris, M. E. Furlong, E. Rogers, L. Wang, K. Bodles, and D. W. Evans, "Model predictive control of a hybrid autonomous underwater vehicle with experimental verification," *Proceedings of the Institution of Mechanical Engineers Part M: Journal of Engineering for the Maritime Environment*, vol. 228, no. 2, pp. 166–179, 2014.
- [83] E. M. Einarsson and A. Lipenitis, "Model Predictive Control for the BlueROV2: Theory and Implementation," Ph.D. dissertation, Aalborg University, 2020.
- [84] J. Wallen, N. Ulm, and Z. Song, "Underwater docking system for a wave energy converter based mobile station," in *OCEANS 2019 MTS/IEEE Seattle*. Seattle, WA, USA: Institute of Electrical and Electronics Engineers Inc., oct 2019.
- [85] L. Medagoda and S. B. Williams, "Model predictive control of an autonomous underwater vehicle in an in situ estimated water current profile," *OCEANS 2012 MTS/IEEE Yeosu, South Korea*, 2012.
- [86] V. T. Huynh, M. Dunbabin, and R. N. Smith, "Predictive motion planning for AUVs subject to strong time-varying currents and forecasting uncertainties," *Proceedings - IEEE International Conference on Robotics and Automation*, vol. 2015-June, no. June, pp. 1144–1151, 2015.
- [87] S.-Y. Zhan and G. Li, "Linear optimal noncausal control of wave energy converters," *IEEE Transactions on Control Systems Technology*, vol. 27, p. 1526–1536, July 2019.
- [88] S.-B. Xu and H. Peng, "Design, analysis, and experiments of preview path tracking control for autonomous vehicles," *IEEE Transactions on Intelligent Transport Systems*, vol. 21, p. 48–58, Jan. 2020.
- [89] P. R. B. Monasterios and P. A. Trodden, "Model Predictive Control of Linear Systems With Preview Information: Feasibility, Stability, and Inherent Robustness," *IEEE Transactions on Intelligent Transport Systems*, vol. 64, pp. 3831–3838, Jan. 2019.

- [90] A. M. Moore, H. G. Arango, G. Broquet, B. S. Powell, A. T. Weaver, and J. Zavala-Garay, “The Regional Ocean Modeling System (ROMS) 4-dimensional variational data assimilation systems. Part I - System overview and formulation.” *Progress in Oceanography*, vol. 91, no. 1, pp. 34–49, oct 2011.
- [91] B. A. Ling and B. A. Batten, “Real time estimation and prediction of wave excitation forces on a heaving body,” in *Proceedings of the International Conference on Offshore Mechanics and Arctic Engineering - OMAE*, vol. 9. St John’s, Newfoundland, Canada: American Society of Mechanical Engineers (ASME), 2015.
- [92] K. P. Carroll, S. R. McClaran, E. L. Nelson, D. M. Barnett, D. K. Friesen, and G. N. Williams, “AUV path planning: An A-star approach to path planning with consideration of variable vehicle speeds and multiple, overlapping, time-dependent exclusion zones,” in *Proceedings of the 1992 Symposium on Autonomous Underwater Vehicle Technology, AUV 1992*. Institute of Electrical and Electronics Engineers Inc., 1992, pp. 79–84.
- [93] B. Garau, A. Alvarez, and G. Oliver, “Path planning of autonomous underwater vehicles in current fields with complex spatial variability: An A\* approach,” in *Proceedings - IEEE International Conference on Robotics and Automation*, vol. 2005, 2005, pp. 194–198.
- [94] T. B. Koay and M. Chitre, “Energy-efficient path planning for fully propelled AUVs in congested coastal waters,” in *OCEANS 2013 MTS/IEEE Bergen: The Challenges of the Northern Dimension*, 2013.
- [95] J. S. Riedel and A. J. Healey, “Shallow water station keeping of AUVs using multi-sensor fusion for wave disturbance prediction and compensation,” in *Oceans 1998 MTS/IEEE*, vol. 2. Nice, France: IEEE, 1998, pp. 1064–1068.
- [96] J. M. Selvakumar and T. Asokan, “A Novel Approach to Measure under Water Vehicle Disturbance Force for Station Keeping Control,” in *9th International Conference on Informatics, Control, Automation and Robotics*, Rome, Italy, 2012, pp. 460–463.
- [97] ——, “Station keeping control of underwater robots using disturbance force measurements,” *Journal of Marine Science and Technology (Japan)*, vol. 21, no. 1, pp. 70–85, 2016.
- [98] C. Long, X. Qin, Y. Bian, and M. Hu, “Trajectory tracking control of ROVs considering external disturbances and measurement noises using ESKF-based MPC,” *Ocean Engineering*, vol. 241, dec 2021.

- [99] Z. Yan, P. Gong, W. Zhang, and W. Wu, "Model predictive control of autonomous underwater vehicles for trajectory tracking with external disturbances," *Ocean Engineering*, vol. 217, dec 2020.
- [100] Y. Zhang, X. Liu, M. Luo, and C. Yang, "MPC-based 3-D trajectory tracking for an autonomous underwater vehicle with constraints in complex ocean environments," *Ocean Engineering*, vol. 189, oct 2019.
- [101] G. Li and M. R. Belmont, "Model predictive control of sea wave energy converters - Part I: A convex approach for the case of a single device," *Renewable Energy*, vol. 69, pp. 453–463, 2014.
- [102] ——, "Model predictive control of sea wave energy converters - Part II: The case of an array of devices," *Renewable Energy*, vol. 68, pp. 540–549, 2014.
- [103] C. Shen, Y. Shi, and B. Buckham, "Integrated path planning and tracking control of an AUV: A unified receding horizon optimization approach," *IEEE/ASME Transactions on Mechatronics*, vol. 22, no. 3, pp. 1163–1173, jun 2017.
- [104] ——, "Path-Following Control of an AUV: A Multiobjective Model Predictive Control Approach," *IEEE Transactions on Control Systems Technology*, vol. 27, no. 3, pp. 1334–1342, 2019.
- [105] J. Zhang, T. Sun, and Z. Liu, "Robust model predictive control for path-following of underactuated surface vessels with roll constraints," *Ocean Engineering*, vol. 143, pp. 125–132, oct 2017.
- [106] S. Heshmati-Alamdar, G. C. Karras, P. Marantos, and K. J. Kyriakopoulos, "A Robust Predictive Control Approach for Underwater Robotic Vehicles," *IEEE Transactions on Control Systems Technology*, vol. 28, no. 6, pp. 2352–2363, nov 2020.
- [107] S. Heshmati-Alamdar, A. Nikou, and D. V. Dimarogonas, "Robust Trajectory Tracking Control for Underactuated Autonomous Underwater Vehicles in Uncertain Environments," *IEEE Transactions on Automation Science and Engineering*, vol. 18, no. 3, pp. 1288–1301, jul 2021.
- [108] M. B. Saltik, L. Özkan, J. H. Ludlage, S. Weiland, and P. M. Van den Hof, "An outlook on robust model predictive control algorithms: Reflections on performance and computational aspects," *Journal of Process Control*, vol. 61, p. 77–102, Jan 2018.
- [109] C. Shen, Y. Shi, and B. Buckham, "Trajectory Tracking Control of an Autonomous Underwater Vehicle Using Lyapunov-Based Model Predictive Control," *IEEE Transactions on Industrial Electronics*, vol. 65, no. 7, pp. 5796–5805, jul 2018.

- [110] H. Wei, C. Shen, and Y. Shi, “Distributed Lyapunov-Based Model Predictive Formation Tracking Control for Autonomous Underwater Vehicles Subject to Disturbances,” *IEEE Transactions on Systems, Man, and Cybernetics: Systems*, vol. 51, no. 8, pp. 5198–5208, aug 2021.
- [111] C. Shen, Y. Shi, and B. Buckham, “Model predictive control for an AUV with dynamic path planning,” in *2015 54th Annual Conference of the Society of Instrument and Control Engineers of Japan, SICE 2015*. Hangzhou, China: Institute of Electrical and Electronics Engineers Inc., sep 2015, pp. 475–480.
- [112] W. Gan, D. Zhu, Z. Hu, X. Shi, L. Yang, and Y. Chen, “Model predictive adaptive constraint tracking control for underwater vehicles,” *IEEE Transactions on Industrial Electronics*, vol. 67, no. 9, pp. 7829–7840, sep 2020.
- [113] A. Bemporad, “Explicit Model Predictive Control,” *Encyclopedia of Systems and Control*, pp. 1–9, 2013.
- [114] R. Rout and B. Subudhi, “Design of Line-of-Sight Guidance Law and a Constrained Optimal Controller for an Autonomous Underwater Vehicle,” *IEEE Transactions on Circuits and Systems II: Express Briefs*, vol. 68, no. 1, pp. 416–420, jan 2021.
- [115] M. Leomanni, E. Rogers, and S. B. Gabriel, “Explicit Model Predictive Control Approach for Low-Thrust Spacecraft Proximity Operations,” *Journal of Guidance, Control and Dynamics*, vol. 37, no. 6, pp. 1780–1790, oct 2014.
- [116] S. Heshmati-Alamdari, A. Eqtami, G. C. Karras, D. V. Dimarogonas, and K. J. Kyriakopoulos, “A self-triggered visual servoing model predictive control scheme for under-actuated underwater robotic vehicles,” in *Proceedings - IEEE International Conference on Robotics and Automation*. Institute of Electrical and Electronics Engineers Inc., sep 2014, pp. 3826–3831.
- [117] J. Gao, G. Zhang, P. Wu, X. Zhao, T. Wang, and W. Yan, “Model Predictive Visual Servoing of Fully-Actuated Underwater Vehicles with a Sliding Mode Disturbance Observer,” *IEEE Access*, vol. 7, pp. 25 516–25 526, 2019.
- [118] M. A. Müller and F. Allgwer, “Improving performance in model predictive control: Switching cost functionals under average dwell-time,” *Automatica*, vol. 48, no. 2, pp. 402–409, feb 2012.
- [119] A. Nag, S. S. Patel, K. Kishore, and S. A. Akbar, “A robust H-infinity based depth control of an autonomous underwater vehicle,” in *Proceedings of the 2013 International Conference on Advanced Electronic Systems, ICAES 2013*, 2013, pp. 68–73.

- [120] L. Qiao, S. Ruan, G. Zhang, and W. Zhang, "Robust H<sub>2</sub> optimal depth control of an autonomous underwater vehicle with output disturbances and time delay," *Ocean Engineering*, vol. 165, pp. 399–409, oct 2018.
- [121] H. Yang and F. Zhang, "Robust control of formation dynamics for autonomous underwater vehicles in horizontal plane," *Journal of Dynamic Systems, Measurement and Control*, vol. 134, no. 3, may 2012.
- [122] C. L. Logan, "Comparison between H-infinity/Mu-synthesis control and sliding-mode control for robust control of a small autonomous underwater vehicle," in *IEEE Symposium on Autonomous Underwater Vehicle Technology*. IEEE, 1994, pp. 399–416.
- [123] J. Petrich and D. J. Stilwell, "Robust control for an autonomous underwater vehicle that suppresses pitch and yaw coupling," *Ocean Engineering*, vol. 38, no. 1, pp. 197–204, jan 2011.
- [124] L. xin Pan, H. zhang Jin, and L. lin Wang, "Robust control based on feedback linearization for roll stabilizing of autonomous underwater vehicle under wave disturbances," *China Ocean Engineering*, vol. 25, no. 2, pp. 251–263, jun 2011.
- [125] P. Millan, L. Orihuela, I. Jurado, and F. R. Rubio, "Formation control of autonomous underwater vehicles subject to communication delays," *IEEE Transactions on Control Systems Technology*, vol. 22, no. 2, pp. 770–777, mar 2014.
- [126] M. R. Katebi and M. J. Grimble, "Integrated control, guidance and diagnosis for reconfigurable autonomous underwater vehicle control," *International Journal of Systems Science*, vol. 30, no. 9, pp. 1021–1032, 2010.
- [127] B. E. Sedhom, M. M. El-Saadawi, A. Y. Hatata, and E. H. E. Abd-Raboh, "H-Infinity versus model predictive control methods for seamless transition between islanded- And grid-connected modes of microgrids," *IET Renewable Power Generation*, vol. 14, no. 5, pp. 856–870, apr 2020.
- [128] P. W. Van De Ven, C. Flanagan, and D. Toal, "Neural network control of underwater vehicles," *Engineering Applications of Artificial Intelligence*, vol. 18, no. 5, pp. 533–547, aug 2005.
- [129] C. Gaskett, D. Wettergreen, and A. Zelinsky, "Reinforcement Learning applied to the control of an Autonomous Underwater Vehicle," in *Proceedings of the Australian conference on robotics and automation (AuCRA99)*., 1999, pp. 125–131.
- [130] A. El-Fakdi, M. Carreras, N. Palomeras, and P. Ridao, "Autonomous underwater vehicle control using reinforcement learning policy search methods," *Oceans 2005 - Europe*, vol. 2, pp. 793–798, 2005.

- [131] R. Yu, Z. Shi, C. Huang, T. Li, and Q. Ma, “Deep reinforcement learning based optimal trajectory tracking control of autonomous underwater vehicle,” in *Chinese Control Conference, CCC*. Dalian, China: IEEE Computer Society, sep 2017, pp. 4958–4965.
- [132] E. Anderlini, G. G. Parker, and G. Thomas, “Docking Control of an Autonomous Underwater Vehicle Using Reinforcement Learning,” *Applied Sciences*, vol. 9, no. 17, p. 3456, aug 2019.
- [133] M. Carreras, J. Yuh, J. Batlle, and P. Ridao, “A behavior-based scheme using reinforcement learning for autonomous underwater vehicles,” *IEEE Journal of Oceanic Engineering*, vol. 30, no. 2, pp. 416–427, apr 2005.
- [134] Y. Wang, C. Tang, S. Wang, L. Cheng, R. Wang, M. Tan, and Z. Hou, “Target Tracking Control of a Biomimetic Underwater Vehicle Through Deep Reinforcement Learning,” *IEEE Transactions on Neural Networks and Learning Systems*, vol. 33, no. 8, pp. 3741–3752, aug 2022.
- [135] Z. Chu, F. Wang, T. Lei, and C. Luo, “Path Planning Based on Deep Reinforcement Learning for Autonomous Underwater Vehicles Under Ocean Current Disturbance,” *IEEE Transactions on Intelligent Vehicles*, vol. 8, pp. 108–120, Jan 2023.
- [136] C. Williamson and R. Govardhan, “Vortex induced vibrations,” *Annual Review of Fluid Mechanics*, vol. 36, no. 1, p. 413–455, 2004.
- [137] L. Mathelin and E. de Langre, “Vortex-induced vibrations and waves under shear flow with a wake oscillator model,” *European Journal of Mechanics - B/Fluids*, vol. 24, no. 4, p. 478–490, 2005.
- [138] M. Facchinetti, E. de Langre, and F. Biolley, “Coupling of structure and wake oscillators in vortex-induced vibrations,” *Journal of Fluids and Structures*, vol. 19, no. 2, p. 123–140, 2004.
- [139] P. Bhopale, F. Kazi, and N. Singh, “Reinforcement Learning Based Obstacle Avoidance for Autonomous Underwater Vehicle,” *Journal of Marine Science and Application*, vol. 18, no. 2, pp. 228–238, jun 2019.
- [140] I. Carlucho, D. W. Stephens, and C. Barbalata, “An adaptive data-driven controller for underwater manipulators with variable payload,” *Applied Ocean Research*, vol. 113, p. 102726, aug 2021.
- [141] Y. Shi, W. Qian, W. Yan, and J. Li, “Adaptive Depth Control for Autonomous Underwater Vehicles Based on Feedforward Neural Networks,” *Intelligent Control and Automation*, pp. 207–218, oct 2006.

- [142] O. Elhaki and K. Shojaei, "A robust neural network approximation-based prescribed performance output-feedback controller for autonomous underwater vehicles with actuators saturation," *Engineering Applications of Artificial Intelligence*, vol. 88, p. 103382, feb 2020.
- [143] K. Duan, S. Fong, and C. L. Chen, "Multilayer neural networks-based control of underwater vehicles with uncertain dynamics and disturbances," *Nonlinear Dynamics*, vol. 100, no. 4, pp. 3555–3573, jun 2020.
- [144] R. Cui, C. Yang, Y. Li, and S. Sharma, "Adaptive Neural Network Control of AUVs with Control Input Nonlinearities Using Reinforcement Learning," *IEEE Transactions on Systems, Man, and Cybernetics: Systems*, vol. 47, no. 6, pp. 1019–1029, jun 2017.
- [145] M. J. Zhang and Z. Z. Chu, "Adaptive sliding mode control based on local recurrent neural networks for underwater robot," *Ocean Engineering*, vol. 45, pp. 56–62, may 2012.
- [146] I. Carlucho, M. De Paula, S. Wang, Y. Petillot, and G. G. Acosta, "Adaptive low-level control of autonomous underwater vehicles using deep reinforcement learning," *Robotics and Autonomous Systems*, vol. 107, pp. 71–86, sep 2018.
- [147] S. Negahdaripour, A. Shokrollahi, J. Fox, and S. Arora, "Improved methods for undersea optical stationkeeping," in *International Conference on Robotics and Automation*. Institute of Electrical and Electronics Engineers (IEEE), dec 1991, pp. 2752–2758.
- [148] L. Jin, X. Xu, S. Negahdaripour, C. Tsukamoto, and J. Yuh, "Real-time vision-based stationkeeping system for underwater robotics applications," in *Oceans Conference Record (IEEE)*, vol. 3. IEEE, 1996, pp. 1076–1081.
- [149] S. Negahdaripour, X. Xu, A. Khamene, and Z. Awan, "3-D motion and depth estimation from sea-floor images for mosaic-based station-keeping and navigation of ROVs/AUVs and high-resolution sea-floor mapping," in *Proceedings of the IEEE Symposium on Autonomous Underwater Vehicle Technology*. IEEE, 1998, pp. 191–200.
- [150] X. Xu and S. Negahdaripour, "Automatic optical station keeping and navigation of an ROV; sea trial experiments," in *Oceans Conference Record (IEEE)*, vol. 1. IEEE, 1999, pp. 71–76.
- [151] K. N. Leabourne, S. M. Rock, S. D. Fleischer, and R. Burton, "Station keeping of an ROV using vision technology," in *Oceans Conference Record (IEEE)*, vol. 1. IEEE, 1997, pp. 634–640.

- [152] J. Santos-Victor, N. Gracias, and S. Van Der Zwaan, "Using vision for underwater robotics: video mosaics and station keeping," in *1st International Workshop on Underwater robotics for Sea Exploitation and Environmental Monitoring, Rio de Janeiro.*, 2001.
- [153] S. Van Der Zwaan and J. Santos-Victor, "Real-time vision-based station keeping for underwater robots," *Oceans Conference Record (IEEE)*, vol. 2, pp. 1058–1065, 2001.
- [154] S. Van der Zwaan, A. Bernardino, and J. Santos-Victor, "Visual station keeping for floating robots in unstructured environments," *Robotics and Autonomous Systems*, vol. 39, no. 3-4, pp. 145–155, 2002.
- [155] R. Marks, H. Wang, M. Lee, and S. Rock, "Automatic visual station keeping of an underwater robot," in *Proceedings of OCEANS'94*, Brest, France, 2002, pp. II/137-II/142.
- [156] X. Cufí, R. Garcia, and P. Ridao, "An approach to vision-based station keeping for an unmanned underwater vehicle," in *IEEE International Conference on Intelligent Robots and Systems*, vol. 1, 2002, pp. 799–804.
- [157] J. F. Lots, D. M. Lane, and E. Trucco, "Application of 2 1/2 D visual servoing to underwater vehicle station-keeping," in *Oceans Conference Record (IEEE)*, vol. 2. IEEE, 2000, pp. 1257–1262.
- [158] J. F. Lots, D. M. Lane, E. Trucco, and F. Chaumette, "A 2-D visual servoing for underwater vehicle station keeping," *Proceedings - IEEE International Conference on Robotics and Automation*, vol. 3, pp. 2767–2772, 2001.
- [159] C. Silpa-Anan, T. Brinsmead, S. Abdallah, and A. Zelinsky, "Preliminary experiments in visual servo control for autonomous underwater vehicle," *IEEE International Conference on Intelligent Robots and Systems*, vol. 4, pp. 1824–1829, 2001.
- [160] S. Reed, J. Evans, B. Privat, and J. Wood, "Automated visual servoing for close inspection using low-cost, man-portable vehicles," *OCEANS 2013 MTS/IEEE - San Diego: An Ocean in Common*, pp. 1–6, 2013.
- [161] M. Caccia, "Vision-based ROV horizontal motion control: Near-seafloor experimental results," *Control Engineering Practice*, vol. 15, no. 6, pp. 703–714, jun 2007.
- [162] M. Hildebrandt and L. Christensen, "Visual Station Keeping and Target Tracking with a Hovering Underwater Vehicle," DFKI RIC Bremen, Tech. Rep., 2014.
- [163] K. Sun, W. Cui, and C. Chen, "Review of Underwater Sensing Technologies and Applications," *Sensors*, vol. 21, pp. 1–28, November 2021.

- [164] D. Akkaynak and T. Treibitz, "Sea-thru: A Method For Removing Water From Underwater Images," in *IEEE/CVF Conference on Computer Vision and Pattern Recognition (CVPR)*, Long Beach, CA, USA, 2019, pp. 1682–1691.
- [165] A. Manzanilla, S. Reyes, M. Garcia, D. Mercado, and R. Lozano, "Autonomous navigation for unmanned underwater vehicles: Real-time experiments using computer vision," *IEEE Robotics and Automation Letters*, vol. 4, no. 2, pp. 1351–1356, apr 2019.
- [166] R. Capocci, G. Dooly, E. Omerdić, J. Coleman, T. Newe, and D. Toal, "Inspection-Class Remotely Operated Vehicles - A Review," *Journal of Marine Science and Engineering*, vol. 5, pp. 1–32, March 2017.
- [167] O. Yildiz, A. E. Yilmaz, and B. Gokalp, "State-of-the-Art System Solutions for Unmanned Underwater Vehicles," *Radioengineering*, vol. 18, pp. 1–28, 2009.
- [168] J. Snyder, "Doppler Velocity Log (DVL) navigation for observation-class ROVs," in *OCEANS 2010 MTS/IEEE Seattle*, Seattle, WA, USA, 20-23 Sept. 2010.
- [169] J. Keranen, G. Schultz, C. Bassani, C. Segal, and B. Kinnaman, "Remotely-Operated Vehicle applications in port and harbor site characterization: Payloads, platforms, sensors, and operations," in *OCEANS 2012 MTS/IEEE Hampton Roads*, Hampton Roads, VA, USA, 14-19 Oct. 2012.
- [170] R. Henthorn, D. Caress, H. Thomas, R. McEwan, W. Kirkwood, C. Paull, and R. Keaten, "High-Resolution Multibeam and Subbottom Surveys of Submarine Canyons, Deep-Sea Fan Channels, and Gas Seeps Using the MBARI Mapping AUV," in *OCEANS 2006 MTS/IEEE Hampton Roads*, Boston, MA, USA, 19-21 Sept. 2006.
- [171] G. Troni and L. L. Whitcomb, "Experimental evaluation of a MEMS inertial measurements unit for Doppler navigation of underwater vehicles," in *OCEANS 2012 MTS/IEEE Hampton Roads*, Hampton Roads, VA, USA, 14-19 Oct. 2012.
- [172] M. De Agostino, A. M. Manzino, and M. Piras, "Performances comparison of different MEMS-based IMUs," in *IEEE/ION Position, Location and Navigation Symposium*, Indian Wells, CA, USA, 04-06 May 2010.
- [173] F. Ferreira, D. Machado, G. Ferri, S. Dugelay, and J. Potter, "Underwater optical and acoustic imaging: A time for fusion? a brief overview of the state-of-the art," in *OCEANS 2016 MTS/IEEE Monterey*. Monterey, CA, USA: IEEE/MTS, 19-23 Sept. 2016.
- [174] F. Dukan, M. Ludvigsen, and A. J. Sorensen, "Dynamic positioning system for a small size ROV with experimental results," in *OCEANS 2011 MTS/IEEE Santander*, Santander, Spain, 06-09 June 2011.

- [175] A. Zieliński and L. Zhou, “Precision acoustic navigation for remotely operated vehicles (ROV),” *Hydroacoustics*, vol. 8, pp. 255–264, 2005.
- [176] Y. Watanabe, “An Experimental Consideration On Accuracy Of Inverse Super Short Baseline Underwater Positioning Using Acoustic Data Transmission,” in *ASME 2016 35th International Conference on Ocean, Offshore and Arctic Engineering*, Busan, Korea, 19-23 Sept. 2016.
- [177] S. Majumder, S. Scheding, and H. F. Durrant-Whyte, “Multisensor data fusion for underwater navigation,” *Robotics and Autonomous Systems*, vol. 35, pp. 97–108, 2001.
- [178] J. Potter, A. Pack, J. Reidenberg, M. Hoffman-Kuhnt, P. Seekings, M. Chitre, T. B. Koay, and L. Herman, ““Humpback whale song source location in the head, source levels and directionality from in-situ rebreather diver recordings,”,” in *17th Biennal conference on the biology of marine mammals*, Cape Town, South Africa, 2007.
- [179] D. Moroni, M. A. Pascali, M. Reggiannini, and O. Salvetti, “Underwater scene understanding by optical and acoustic data integration,” *Proceedings of Meetings on Acoustics*, vol. 17, Jul 2013.
- [180] B. Kalyan and A. Balasuriya, “Multisensor data fusion approach for terrain aided navigation of autonomous underwater vehicles,” *Oceans '04 MTS/IEEE Techno-Ocean '04*, Nov 2004.
- [181] D. Krout, G. Okpal, and E. Hanusa, “Video data and sonar data: Real world data fusion example,” in *14th International Conference on Information Fusion*, Chicago, IL, USA, 05-08 July 2011.
- [182] F. S. Hover, R. M. Eustice, A. Kim, B. Englot, H. Johannsson, M. Kaess, and J. J. Leonard, “Advanced perception , navigation and planning for autonomous in-water ship hull inspection,” *International Journal of Robotics Research*, vol. 31, pp. 1445–1464, 2012.
- [183] J. Preisig, “Acoustic propagation considerations for underwater acoustic communications network development,” *Proceedings of the 1st ACM international workshop on Underwater networks (WUWNet) '06*, Sep 2006.
- [184] D. Rus and M. T. Tolley, “Design, fabrication and control of soft robots,” *Nature*, vol. 521, pp. 467–475, may 2015.
- [185] C. D. Santina, R. K. Katzschmann, A. Bicchi, and D. Rus, “Dynamic Control of Soft Robots Interacting with the Environment,” in *IEEE International Conference on Soft Robotics (RoboSoft)*, Livorno, Italy, 2018, pp. 46–53.

- [186] C. D. Santina, A. Bicchi, and D. Rus, "Dynamic Control of Soft Robots with Internal Constraints in the Presence of Obstacles," in *IEEE/RSJ International Conference on Intelligent Robots and Systems (IROS)*, 2019, pp. 6622–6629.
- [187] P. R. Ouyang, J. Acob, and V. Pano, "PD with sliding mode control for trajectory tracking of robotic system," *Robotics and Computer-Integrated Manufacturing*, vol. 30, no. 2, pp. 189–200, apr 2014.
- [188] A. D. Kapadia, I. D. Walker, D. M. Dawson, and E. Tatlicioglu, "A Model-Based Sliding Mode Controller for Extensible Continuum Robots," in *Proceedings of the 9th WSEAS International Conference on Signal Processing, Robotics and Automation (ISPRA'10)*, Cambridge, UK, 2010, pp. 113–120.
- [189] A. D. Kapadia, K. E. Fry, and I. D. Walker, "Empirical investigation of closed-loop control of extensible continuum manipulators," in *IEEE International Conference on Intelligent Robots and Systems*. Chicago, IL, USA: Institute of Electrical and Electronics Engineers Inc., oct 2014, pp. 329–335.
- [190] A. H. Khan and S. Li, "Sliding Mode Control with PID Sliding Surface for Active Vibration Damping of Pneumatically Actuated Soft Robots," *IEEE Access*, vol. 8, pp. 88 793–88 800, 2020.
- [191] G. Tonietti and A. Bicchi, "Adaptive simultaneous position and stiffness control for a soft robot arm," in *IEEE International Conference on Intelligent Robots and Systems*, Lausanne, Switzerland, 2002, pp. 1992–1997.
- [192] A. Kazemipour, O. Fischer, Y. Toshimitsu, K. W. Wong, and R. K. Katzschmann, "Adaptive Dynamic Sliding Mode Control of Soft Continuum Manipulators," in *IEEE International Conference on Robotics and Automation*. Philadelphia, PA, USA: Institute of Electrical and Electronics Engineers Inc., sep 2021, pp. 3259–3265.
- [193] H. Wang, B. Yang, Y. Liu, W. Chen, X. Liang, and R. Pfeifer, "Visual Servoing of Soft Robot Manipulator in Constrained Environments With an Adaptive Controller," *IEEE/ASME Transactions on Mechatronics*, vol. 22, no. 1, pp. 41–50, feb 2017.
- [194] E. H. Skorina, M. Luo, W. Tao, F. Chen, J. Fu, and C. D. Onal, "Adapting to Flexibility: Model Reference Adaptive Control of Soft Bending Actuators," *IEEE Robotics and Automation Letters*, vol. 2, no. 2, pp. 964–970, apr 2017.
- [195] C. Della Santina, M. Bianchi, G. Grioli, F. Angelini, M. Catalano, M. Garabini, and A. Bicchi, "Controlling Soft Robots: Balancing Feedback and Feedforward Elements," *IEEE Robotics and Automation Magazine*, vol. 24, no. 3, pp. 75–83, sep 2017.

- [196] C. D. Santina, R. K. Katzschmann, A. Bicchi, and D. Rus, “Model-based dynamic feedback control of a planar soft robot : trajectory tracking and interaction with the environment,” *International Journal of Robotics Research*, vol. 39, no. 4, pp. 490–513, 2018.
- [197] C. D. Santina, C. Duriez, and D. Rus, *Model Based Control of Soft Robots : A Survey of the State of the Art and Open Challenges*. arXiv, 2021.
- [198] V. Falkenhahn, A. Hildebrandt, R. Neumann, and O. Sawodny, “Model-based feedforward position control of constant curvature continuum robots using feedback linearization,” in *IEEE International Conference on Robotics and Automation*. Seattle, Washington, USA: Institute of Electrical and Electronics Engineers Inc., jun 2015, pp. 762–767.
- [199] A. D. Marchese, R. Tedrake, and D. Rus, “Dynamics and Trajectory Optimization for a Soft Spatial Fluidic Elastomer Manipulator,” in *IEEE International Conference on Robotics and Automation*, 2015, pp. 2528–2535.
- [200] E. Franco, A. Garriga Casanoves, F. Rodriguez y Baena, and A. Astolfi, “Model based adaptive control for a soft robotic manipulator,” in *IEEE 58th Conference on Decision and Control (CDC)*. Nice, France: IEEE, 11-13 Dec. 2019.
- [201] J. Y. Loo, C. P. Tan, and S. G. Nurzaman, “H-infinity based extended kalman filter for state estimation in highly non-linear soft robotic system,” in *Proceedings of the American Control Conference*. Philadelphia, PA, USA: Institute of Electrical and Electronics Engineers Inc., jul 2019, pp. 5154–5160.
- [202] N. Lin, P. Wu, M. Wang, J. Wei, F. Yang, S. Xu, Z. Ye, and X. Chen, “IMU-Based Active Safe Control of a Variable Stiffness Soft Actuator,” *IEEE Robotics and Automation Letters*, vol. 4, no. 2, pp. 1247–1254, apr 2019.
- [203] J. Hughes, F. Stella, C. D. Santina, and D. Rus, “Sensing Soft Robot Shape Using IMUs: An Experimental Investigation,” in *Proceedings of International Symposium on Experimental Robotics*. Springer Science and Business Media B.V., 2021, pp. 543–552.
- [204] G. Cao, B. Huo, L. Yang, F. Zhang, Y. Liu, and G. Bian, “Model-Based Robust Tracking Control without Observers for Soft Bending Actuators,” *IEEE Robotics and Automation Letters*, vol. 6, no. 3, pp. 5175–5182, jul 2021.
- [205] T. G. Thuruthel, B. Shih, C. Laschi, and M. T. Tolley, “Soft robot perception using embedded soft sensors and recurrent neural networks,” *Science Robotics*, vol. 4, no. 26, p. 1488, jan 2019.
- [206] C. M. Best, M. T. Gillespie, P. Hyatt, L. Rupert, V. Sherrod, and M. D. Killpack, “A New Soft Robot Control Method: Using Model Predictive Control for

- a Pneumatically Actuated Humanoid,” *IEEE Robotics and Automation Magazine*, vol. 23, no. 3, pp. 75–84, sep 2016.
- [207] F. A. Spinelli and R. K. Katzschmann, “A Unified and Modular Model Predictive Control Framework for Soft Continuum Manipulators under Internal and External Constraints,” in *IEEE/RSJ International Conference on Intelligent Robots and Systems (IROS)*. Kyoto, Japan: IEEE, apr 2022, pp. 9393–9400.
- [208] D. Bruder, B. Gillespie, C. David Remy, and R. Vasudevan, “Modeling and Control of Soft Robots Using the Koopman Operator and Model Predictive Control,” in *Robotics: Science and Systems*, Freiburg im Breisgau, Germany, 2019.
- [209] J. Chen, Y. Dang, and J. Han, “Offset-free model predictive control of a soft manipulator using the Koopman operator,” *Mechatronics*, vol. 86, p. 102871, oct 2022.
- [210] P. Hyatt and M. D. Killpack, “Real-Time Nonlinear Model Predictive Control of Robots Using a Graphics Processing Unit,” *IEEE Robotics and Automation Letters*, vol. 5, no. 2, pp. 1468–1475, apr 2020.
- [211] M. Khadem, J. O’Neill, Z. Mitros, L. da Cruz, and C. Bergeles, “Autonomous steering of concentric tube robots via nonlinear model predictive control,” *IEEE Transactions on Robotics*, vol. 36, no. 5, pp. 1595–1602, oct 2020.
- [212] C. M. Best, L. Rupert, and M. D. Killpack, “Comparing model-based control methods for simultaneous stiffness and position control of inflatable soft robots,” *International Journal of Robotics Research*, vol. 40, no. 1, pp. 470–493, jan 2021.
- [213] B. Ouyang, H. Mo, H. Chen, Y. Liu, and D. Sun, “Robust Model-Predictive Deformation Control of a Soft Object by Using a Flexible Continuum Robot,” in *IEEE International Conference on Intelligent Robots and Systems*. Madrid, Spain: Institute of Electrical and Electronics Engineers Inc., dec 2018, pp. 613–618.
- [214] D. Braganza, D. M. Dawson, I. D. Walker, and N. Nath, “A neural network controller for continuum robots,” *IEEE Transactions on Robotics*, vol. 23, no. 6, pp. 1270–1277, dec 2007.
- [215] S. Satheeshbabu, N. K. Uppalapati, G. Chowdhary, and G. Krishnan, “Open loop position control of soft continuum arm using deep reinforcement learning,” in *IEEE International Conference on Robotics and Automation*, vol. 2019-May. Institute of Electrical and Electronics Engineers Inc., may 2019, pp. 5133–5139.

- [216] K. Tadakuma, T. Fujimoto, M. Watanabe, T. Shimizu, E. Takane, M. Konyo, and S. Tadokoro, “Fire-Resistant Deformable Soft Gripper Based on Wire Jamming Mechanism,” in *3rd IEEE International Conference on Soft Robotics (RoBoSoft)*. Institute of Electrical and Electronics Engineers Inc., may 2020, pp. 740–747.
- [217] I. Onda, K. Tadakuma, M. Watanabe, K. Abe, T. Watanabe, M. Konyo, and S. Tadokoro, “Highly Articulated Tube Mechanism with Variable Stiffness and Shape Restoration Using a Pneumatic Actuator,” *IEEE Robotics and Automation Letters*, vol. 7, no. 2, pp. 3664–3671, apr 2022.
- [218] C.-P. Chou and B. Hannaford, “Measurement and modeling of McKibben pneumatic artificial muscles,” *IEEE Transactions on Robotics and Automation*, vol. 12, no. 1, pp. 90–102, 1996.
- [219] Y. Jiang, D. Chen, C. Liu, and J. Li, “Chain-Like Granular Jamming: A Novel Stiffness-Programmable Mechanism for Soft Robotics,” *Soft Robotics*, vol. 6, no. 1, pp. 118–132, 2019.
- [220] R. Mukaide, M. Watanabe, K. Tadakuma, Y. Ozawa, T. Takahashi, M. Konyo, and S. Tadokoro, “Radial-Layer Jamming Mechanism for String Configuration,” *IEEE Robotics and Automation Letters*, vol. 5, no. 4, pp. 5221–5228, oct 2020.
- [221] J. Choi, D.-Y. Lee, J.-H. Eo, Y.-J. Park, and K.-J. Cho, “Tendon-Driven Jamming Mechanism for Configurable Variable Stiffness,” *Soft Robotics*, vol. 8, no. 1, pp. 109–118, 2021.
- [222] V. Wall, R. Deimel, and O. Brock, “Selective Stiffening of Soft Actuators Based on Jamming,” in *IEEE International Conference on Robotics and Automation (ICRA)*, 2015, pp. 252–257.
- [223] N. R. Sinatra, C. B. Teeple, K. K. Vogt, Daniel M. Parker, D. F. Gruber, and R. J. Wood, “Ultragentle manipulation of delicate structures using a soft robotic gripper,” *Science Robotics*, vol. 4, pp. 1–11, August 2019.
- [224] S. Kurumaya, B. T. Phillips, K. P. Becker, M. H. Rosen, D. F. Gruber, K. C. Galloway, K. Suzumori, and R. J. Wood, “A Modular Soft Robotic Wrist for Underwater Manipulation,” *Soft Robotics*, vol. 5, no. 4, pp. 399–409, 2018.
- [225] B. T. Phillips, K. P. Becker, S. Kurumaya, K. C. Galloway, G. Whittredge, D. M. Vogt, C. B. Teeple, M. H. Rosen, V. A. Pieribone, D. F. Gruber, and R. J. Wood, “A Dexterous, Glove-Based Teleoperable Low-Power Soft Robotic Arm for Delicate Deep-Sea Biological Exploration,” *Scientific Reports*, vol. 8, no. 1, pp. 1–9, 2018.

- [226] K. C. Galloway, K. P. Becker, B. Phillips, J. Kirby, S. Licht, D. Tchernov, R. J. Wood, and D. F. Gruber, "Soft Robotic Grippers for Biological Sampling on Deep Reefs," *Soft Robotics*, vol. 3, no. 1, pp. 23–33, mar 2016.
- [227] Z. Gong, X. Fang, X. Chen, J. Cheng, Z. Xie, J. Liu, B. Chen, H. Yang, S. Kong, Y. Hao, T. Wang, J. Yu, and L. Wen, "A soft manipulator for efficient delicate grasping in shallow water: Modeling, control, and real-world experiments," *International Journal of Robotics Research*, vol. 40, pp. 449–469, Jan. 2021.
- [228] C. D. Santina, R. L. Truby, and D. Rus, "Data-Driven Disturbance Observers for Estimating External Forces on Soft Robots," *IEEE Robotics and Automation Letters*, vol. 5, no. 4, pp. 5717–5724, oct 2020.
- [229] F. Campisano, A. A. Remirez, S. Calo, J. H. Chandler, K. L. Obstein, R. J. Webster, and P. Valdastri, "Online Disturbance Estimation for Improving Kinematic Accuracy in Continuum Manipulators," *IEEE Robotics and Automation Letters*, vol. 5, no. 2, pp. 2642–2649, apr 2020.
- [230] F. Renda, M. Giorelli, M. Calisti, M. Cianchetti, and C. Laschi, "Dynamic model of a multibending soft robot arm driven by cables," *IEEE Transactions on Robotics*, vol. 30, no. 5, pp. 1109–1122, oct 2014.
- [231] F. Renda, F. Giorgio-Serchi, F. Boyer, C. Laschi, J. Dias, and L. Seneviratne, "A unified multi-soft-body dynamic model for underwater soft robots," *The International Journal of Robotics Research*, vol. 37, no. 6, pp. 648–666, may 2018.
- [232] C. Armanini, M. Farman, M. Calisti, F. Giorgio-Serchi, C. Stefanini, and F. Renda, "Flagellate Underwater Robotics at Macroscale: Design, Modeling, and Characterization," *IEEE Transactions on Robotics*, vol. 38, no. 2, pp. 731–747, apr 2022.
- [233] C. Armanini, A. A. Alshehhi, A. T. Mathew, I. B. Hmida, C. Stefanini, and F. Renda, "Model-Based Design Optimization of Underwater Flagellate Propellers," *IEEE Robotics and Automation Letters*, vol. 7, no. 4, pp. 10 089–10 096, oct 2022.
- [234] Rongjie Kang, A. Kazakidi, E. Guglielmino, D. T. Branson, D. P. Tsakiris, J. A. Ekaterinidis, and D. G. Caldwell, "Dynamic model of a hyper-redundant, octopus-like manipulator for underwater applications," in *IEEE/RSJ International Conference on Intelligent Robots and Systems (IROS)*. San Francisco, CA, USA: Institute of Electrical and Electronics Engineers (IEEE), sep 2011, pp. 4054–4059.

- [235] D. B. Camarillo, C. F. Milne, C. R. Carlson, M. R. Zinn, and J. K. Salisbury, “Mechanics modeling of tendon-driven continuum manipulators,” *IEEE Transactions on Robotics*, vol. 24, no. 6, pp. 1262–1273, 2008.
- [236] B. Zhang, F. Renda, M. Cianchetti, M. Giorelli, A. Arienti, and C. Laschi, “A 3D steady-state model of a tendon-driven continuum soft manipulator inspired by the octopus arm,” *Bioinspiration & Biomimetics*, vol. 7, pp. 1–12, 2012.
- [237] R. J. Webster and B. A. Jones, “Design and Kinematic Modeling of Constant Curvature Continuum Robots: A Review,” *The International Journal of Robotics Research*, vol. 29, no. 13, pp. 1661–1683, jun 2010.
- [238] J. Tang, Y. Zhang, F. Huang, J. Li, Z. Chen, W. Song, S. Zhu, and J. Gu, “Design and Kinematic Control of the Cable-Driven Hyper-Redundant Manipulator for Potential Underwater Applications,” *Applied Sciences*, vol. 9, no. 6, p. 1142, mar 2019.
- [239] W. McMahan, V. Chitrakaran, M. Csencsits, D. Dawson, I. D. Walker, B. A. Jones, M. Prittis, D. Dienno, M. Grissom, and C. D. Rahn, “Field trials and testing of the OctArm continuum manipulator,” in *IEEE International Conference on Robotics and Automation*, Orlando, Florida, USA, 2006, pp. 2336–2341.
- [240] F. Aikman, “Coastal ocean forecast system for the U.S. East Coast,” in *Oceans Conference Record (IEEE)*, vol. 1. IEEE, 1996, pp. 231–235.
- [241] N. Pinardi, I. Allen, E. Demirov, P. De Mey, G. Korres, A. Lascaratos, P. Y. Le Traon, C. Maillard, G. Manzella, and C. Tziavos, “The Mediterranean ocean forecasting system: first phase of implementation (1998–2001),” *Annales Geophysicae*, vol. 21, no. 1, pp. 3–20, jan 2003.
- [242] M. Tonani, N. Pinardi, C. Fratianni, J. Pistoia, S. Dobricic, S. Pensieri, M. De Alfonso, and K. Nittis, “Mediterranean Forecasting System: forecast and analysis assessment through skill scores,” *Ocean Science*, vol. 5, pp. 649–660, 2009.
- [243] E. B. Clark, A. Branch, S. Chien, F. Mirza, J. D. Farrara, Y. Chao, D. Fratantonio, D. Aragon, O. Schofield, M. M. Flexas, and A. Thompson, “Station-Keeping Underwater Gliders Using a Predictive Ocean Circulation Model and Applications to SWOT Calibration and Validation,” *IEEE Journal of Oceanic Engineering*, vol. 45, no. 2, pp. 371–384, 2020.
- [244] S. Albarakati, R. M. Lima, L. Giraldi, I. Hoteit, and O. Knio, “Optimal 3D trajectory planning for AUVs using ocean general circulation models,” *Ocean Engineering*, vol. 188, no. 106266, 2019.
- [245] D. Kularatne, S. Bhattacharya, and M. A. Hsieh, “Optimal path planning in time-varying flows using adaptive discretization,” *IEEE Robotics and Automation Letters*, vol. 3, no. 1, pp. 458–465, 2018.

- [246] M. F. W. Site, “Wave Spectra Datasets.” [Online]. Available: <https://www.cefas.co.uk>
- [247] F. Fusco and J. V. Ringwood, “Linear models for short term wave forecasting,” *Proc. World Renewable Energy Conference X*, no. 2, p. 6, 2008.
- [248] ——, “A Study on Short-Term Sea Profile Prediction for Wave Energy Applications,” in *Proceedings of the 8th European Wave and Tidal Energy Conference*, Uppsala, Sweden, 2009, pp. 756–765.
- [249] ——, “Short-term wave forecasting for real-time control of wave energy converters,” *IEEE Transactions on Sustainable Energy*, vol. 1, no. 2, pp. 99–106, 2010.
- [250] F. Fusco, J. C. Gilloteaux, and J. Ringwood, “A study on prediction requirements in time-domain control of wave energy converters,” *IFAC Proceedings Volumes (IFAC-PapersOnline)*, vol. 43, no. 20, pp. 372–377, 2010.
- [251] F. Fusco and J. Ringwood, “A Study of the Prediction Requirements in Real-Time Control of Wave Energy Converters,” *IEEE Transactions on Sustainable Energy*, vol. 3, no. 1, pp. 176 – 184, 2012.
- [252] M. Ge and E. C. Kerrigan, “Short-term Ocean Wave Forecasting Using an Autoregressive Moving Average Model,” in *UKACC 11th International Conference on Control (CONTROL)*. Belfast, U.K.: IEEE, 31st Aug. - 01 Sept. 2016.
- [253] I. Malekmohamadi, M. R. Bazargan-Lari, R. Kerachian, M. R. Nikoo, and M. Fallahnia, “Evaluating the efficacy of SVMs, BNs, ANNs and ANFIS in wave height prediction,” *Ocean Engineering*, vol. 38, pp. 487–497, feb 2011.
- [254] M. Pirhooshyaran and L. V. Snyder, “Forecasting, hindcasting and feature selection of ocean waves via recurrent and sequence-to-sequence networks,” *Ocean Engineering*, vol. 207, jul 2020.
- [255] K. Günaydin, “The estimation of monthly mean significant wave heights by using artificial neural network and regression methods,” *Ocean Engineering*, vol. 35, no. 14-15, pp. 1406–1415, oct 2008.
- [256] D. Gopinath and G. Dwarakish, “Wave Prediction Using Neural Networks at New Mangalore Port along West Coast of India,” *Aquatic Procedia*, vol. 4, pp. 143–150, jan 2015.
- [257] S. C. James, Y. Zhang, and F. O'Donncha, “A machine learning framework to forecast wave conditions,” *Coastal Engineering*, vol. 137, pp. 1–10, jul 2018.

- [258] D. Adytia, D. Saepudin, S. R. Pudjaprasetya, S. Husrin, and A. Sopaheluwakan, “A Deep Learning Approach for Wave Forecasting Based on a Spatially Correlated Wind Feature, with a Case Study in the Java Sea, Indonesia,” *Fluids*, vol. 7, no. 1, 2022.
- [259] S. Gaur and M. C. Deo, “Real-time wave forecasting using genetic programming,” *Ocean Engineering*, vol. 35, no. 11-12, pp. 1166–1172, aug 2008.
- [260] P. Jain and M. C. Deo, “Artificial Intelligence Tools to Forecast Ocean Waves in Real Time,” *The Open Ocean Engineering Journal*, vol. 1, no. 1, pp. 13–20, sep 2008.
- [261] P. Jain, M. C. Deo, G. Latha, and V. Rajendran, “Real time wave forecasting using wind time history and numerical model,” *Ocean Modelling*, vol. 36, no. 1-2, pp. 26–39, jan 2011.
- [262] H. Kagemoto, “Forecasting a water-surface wave train with artificial intelligence- A case study,” *Ocean Engineering*, vol. 207, p. 107380, jul 2020.
- [263] M. R. Belmont, J. M. Horwood, R. W. Thurley, and J. Baker, “Filters for linear sea-wave prediction,” *Ocean Engineering*, vol. 33, no. 17-18, pp. 2332–2351, 2006.
- [264] M. R. Belmont, J. M. K. Horwood, R. W. F. Thurley, and J. Baker, “Shallow Angle Wave Profiling Lidar,” *Journal of Atmospheric and Oceanic Technology*, vol. 24, pp. 1150–1156, 2006.
- [265] L. F. Abusdra, “Signal Processing Issues Related to Deterministic Sea Wave Prediction,” Ph.D. dissertation, University of Exeter, 2009.
- [266] L. F. Abusdra and M. Belmont, “Prediction diagrams for deterministic sea wave prediction and the introduction of the data extension prediction method,” *International Shipbuilding Progress*, vol. 58, pp. 59–81, 2011.
- [267] A. Simanesew, “Deterministic Prediction Of Sea Waves-Long Crested Sea,” Ph.D. dissertation, University of Oslo, 2013.
- [268] M. R. Belmont, J. Christmas, J. Dannenberg, T. Hilmer, J. Duncan, J. M. Duncan, and B. Ferrier, “An examination of the feasibility of linear deterministic sea wave prediction in multidirectional seas using wave profiling radar: Theory, simulation, and sea trials,” *Journal of Atmospheric and Oceanic Technology*, vol. 31, no. 7, pp. 1601–1614, 2014.
- [269] M. Al-Ani, J. Christmas, M. R. Belmont, J. M. Duncan, J. Duncan, and B. Ferrier, “Deterministic Sea Waves Prediction Using Mixed Space–Time Wave Radar Data,” *Journal of Atmospheric and Oceanic Technology*, vol. 36, no. 5, pp. 833–842, may 2019.

- [270] M. Al-Ani, M. Belmont, and J. Christmas, “Sea trial on deterministic sea waves prediction using wave-profiling radar,” *Ocean Engineering*, vol. 207, jul 2020.
- [271] M. Previsic, A. Karthikeyan, and D. Lyzenga, “In-Ocean Validation of a Deterministic Sea Wave Prediction (DSWP) System leveraging X-Band Radar to Enable Optimal Control in Wave Energy Conversion Systems,” *Applied Ocean Research*, vol. 114, p. 102784, sep 2021.
- [272] M. Huchet, A. Babarit, G. Ducrozet, J. C. Gilloteaux, and P. Ferrant, “Non-linear deterministic sea wave prediction using instantaneous velocity profiles,” *Ocean Engineering*, vol. 220, p. 108492, jan 2021.
- [273] Y. Z. Law, H. Santo, K. Y. Lim, and E. S. Chan, “Deterministic wave prediction for unidirectional sea-states in real-time using Artificial Neural Network,” *Ocean Engineering*, vol. 195, jan 2020.
- [274] N. Köllisch, J. Behrendt, M. Klein, and N. Hoffmann, “Nonlinear real time prediction of ocean surface waves,” *Ocean Engineering*, vol. 157, pp. 387–400, jun 2018.
- [275] N. Desmars, Y. Perignon, G. Ducrozet, C. A. Guerin, S. T. Grilli, and P. Ferrant, “Phase-Resolved Reconstruction Algorithm and Deterministic Prediction of Nonlinear Ocean Waves From Spatio-Temporal Optical Measurements,” *Proceedings of the International Conference on Offshore Mechanics and Arctic Engineering - OMAE*, vol. 7B, sep 2018.
- [276] M. Klein, M. Dudek, G. F. Clauss, S. Ehlers, J. Behrendt, N. Hoffmann, and M. Onorato, “On the deterministic prediction of water waves,” *Fluids*, vol. 5, no. 1, pp. 1–19, 2020.
- [277] J. Tedd and P. Frigaard, “Short term wave forecasting, using digital filters, for improved control of Wave Energy Converters,” in *Seventeenth (2007) International Offshore and Polar Engineering Conference*, Lisbon, Portugal, 2007, pp. 388–394.
- [278] J. C. Nieto Borge and K. Hessner, “Inversion of Marine Radar Images for Surface Wave Analysis,” *Journal of Atmospheric and Oceanic Technology*, vol. 21, no. 8, pp. 1291–1300, 2004.
- [279] P. Naaijen and R. Huijsmans, “Real time wave forecasting for real time ship motion predictions,” *Proceedings of the International Conference on Offshore Mechanics and Arctic Engineering - OMAE*, vol. 4, no. January, pp. 607–614, 2008.
- [280] Z. Chang, F. Han, Z. Sun, Z. Gao, and L. Wang, “Three-dimensional dynamic sea surface modeling based on ocean wave spectrum,” *Acta Oceanologica Sinica*, vol. 40, no. 10, pp. 38–48, 2021.

- [281] L. Cavalieri, S. Abdalla, A. Benetazzo, L. Bertotti, J. R. Bidlot, Breivik, S. Carniel, R. E. Jensen, J. Portilla-Yandun, W. E. Rogers, A. Roland, A. Sanchez-Arcilla, J. M. Smith, J. Staneva, Y. Toledo, G. P. van Vledder, and A. J. van der Westhuysen, “Wave modelling in coastal and inner seas,” *Progress in Oceanography*, vol. 167, pp. 164–233, oct 2018.
- [282] T. Kanehira, H. Mutsuda, S. Draycott, N. Taniguchi, T. Nakashima, Y. Doi, and D. Ingram, “Numerical re-creation of multi-directional waves in a circular basin using a particle based method,” *Ocean Engineering*, vol. 209, p. 107446, aug 2020.
- [283] B. Vujkov, B. Dumnić, T. Grbić, B. Popadić, N. Vukajlović, and S. Medić, “Spectral analysis of ocean waves for determination of fundamental energy parameters,” in *EUROCON 2019 - 18th International Conference on Smart Technologies*. Institute of Electrical and Electronics Engineers Inc., jul 2019.
- [284] G. Li, G. Weiss, M. Mueller, S. Townley, and M. R. Belmont, “Wave energy converter control by wave prediction and dynamic programming,” *Renewable Energy*, vol. 48, pp. 392–403, 2012.
- [285] J. Woolfrey, D. Liu, and M. Carmichael, “Kinematic control of an Autonomous Underwater Vehicle-Manipulator System (AUVMS) using autoregressive prediction of vehicle motion and Model Predictive Control,” *Proceedings - IEEE International Conference on Robotics and Automation*, vol. 2016-June, pp. 4591–4596, jun 2016.
- [286] N. Faedo, S. Olaya, and J. V. Ringwood, “Optimal control, mpc and mpc-like algorithms for wave energy systems: An overview,” *IFAC Journal of Systems and Control*, vol. 1, p. 37–56, Sep 2017.
- [287] S. Draycott, D. R. Noble, T. Davey, T. Bruce, D. M. Ingram, L. Johanning, H. C. Smith, A. Day, and P. Kaklis, “Re-creation of site-specific multi-directional waves with non-collinear current,” *Ocean Engineering*, vol. 152, pp. 391–403, mar 2018.
- [288] S. Draycott, B. Sellar, T. Davey, D. R. Noble, V. Venugopal, and D. M. Ingram, “Capture and simulation of the ocean environment for offshore renewable energy,” *Renewable and Sustainable Energy Reviews*, vol. 104, pp. 15–29, apr 2019.
- [289] S. Draycott, P. Stansby, M. McAllister, T. Davey, L. Jordan, T. Tosdevin, and M. Hann, “The numerical re-creation of experimentally generated nonlinear irregular wave fields using a time-reversal approach,” *Applied Ocean Research*, vol. 129, p. 103397, dec 2022.

- [290] L. E. Borgman, "Ocean Wave Simulation for Engineering Design," *Journal of the Waterways and Harbors Division*, vol. 95, no. 4, pp. 557–583, nov 1969.
- [291] E. Baekkedal, "Alternative methods of realizing the sea spectrum for time-domain simulations of marine structures in irregular seas," Ph.D. dissertation, Norwegian University of Science and Technology, 2014.
- [292] T. I. Fossen, *Guidance and Control of Ocean Vehicles*. Wiley, 1994.
- [293] C. L. Bretschneider, "Wave Variability and Wave Spectra for Wind Generated Gravity Waves," Beach Erosion Board, Corps. of Engineers., Tech. Rep., 1959.
- [294] W. J. Pierson and L. Moskowitz, "A proposed spectral form for fully developed wind seas based on the similarity theory of S. A. Kitaigorodskii," *Journal of Geophysical Research*, vol. 69, no. 24, pp. 5181–5190, dec 1964.
- [295] O. M. Phillips, "The equilibrium range in the spectrum of wind-generated waves," *Journal of Fluid Mechanics*, vol. 4, pp. 426–434, Feb. 1958.
- [296] K. Hasselmann, T. Barnett, E. Bouws, H. Carlson, D. Cartwright, K. Enke, J. Ewing, H. Gienapp, D. Hasselmann, P. Kruseman, A. Meerburg, P. Müller, D. Olbers, K. Richter, W. Sell, and H. Walden, "Measurements of wind-wave growth and swell decay during the Joint North Sea Wave Project (JONSWAP)," *Deutschen Hydrographischen Zeitschrift*, vol. 8, no. 12, 1973.
- [297] D. Reeve, A. Chadwick, and C. Fleming, *Coastal engineering: Processes, theory and design practice, second edition*. Abingdon: Spon Press, 2012.
- [298] M. McCormick, *Ocean Engineering Mechanics with Applications*. Cambridge: Cambridge University Press, 2009.
- [299] T. I. Fossen, *Handbook of Marine Craft Hydrodynamics and Motion Control*. Wiley, 2011.
- [300] B. Robotics, "Blue Robotics BlueROV2," 2020.
- [301] O. M. Faltinsen, *Sea loads on ships and offshore structures*. Cambridge University Press, 1990.
- [302] S. Echeandia and P. M. Wensing, "Numerical Methods to Compute the Coriolis Matrix and Christoffel Symbols for Rigid-Body Systems," *Journal of Computational and Nonlinear Dynamics*, vol. 16, no. 9, 2021.
- [303] J. R. Morison, M. P. O'brien, J. W. Johnson, and S. A. Schaaf, "The Force Exerted by Surface Waves on Piles," *Journal of Petroleum Technology*, vol. 2, no. 05, pp. 149–154, may 1950.

- [304] D. Ingram, R. Wallace, A. Robinson, and I. Bryden, “The design and commissioning of the first, circular, combined current and wave test basin,” in *OCEANS 2014 - TAIPEI*. Taipei, Taiwan: Institute of Electrical and Electronics Engineers Inc., nov 2014, pp. 15–29.
- [305] “APPLIED MEASUREMENTS Ltd., 2020. Submersible Load Cell – DDEN,” 2020. [Online]. Available: <https://appmeas.co.uk/products/load-cells-force-sensors/in-line-submersible-load-cell-dden/>
- [306] A. Savitzky and M. J. E. Golay, “Smoothing and Differentiation of Data by Simplified Least Squares Procedures,” *Analytical Chemistry*, vol. 36, p. 1627–1639, July 1964.
- [307] S. Lack, E. Rentzow, and T. Jeinsch, “Experimental Parameter Identification for an open-frame ROV: Comparison of towing tank tests and open water self-propelled tests,” in *IFAC-PapersOnLine*, vol. 52, no. 21. Elsevier B.V., jan 2019, pp. 271–276.
- [308] C.-j. Wu, “6-DoF Modelling and Control of a Remotely Operated Vehicle,” Ph.D. dissertation, Flinders University, 2018.
- [309] “WAMIT User Manual Version 7.4,” WAMIT Inc., Chestnall Hill, MA, USA, Tech. Rep., 2020.
- [310] V. Berg, “Development and Commissioning of a DP system for ROV SF 30k,” Ph.D. dissertation, Norwegian University of Science and Technology, 2012.
- [311] H. Bailey, K. L. Brookes, and P. M. Thompson, “Assessing environmental impacts of offshore wind farms: Lessons learned and recommendations for the future,” *Aquatic Biosystems*, vol. 10, no. 1, pp. 1–13, sep 2014.
- [312] K. Y. Oh, W. Nam, M. S. Ryu, J. Y. Kim, and B. I. Epureanu, “A review of foundations of offshore wind energy convertors: Current status and future perspectives,” *Renewable and Sustainable Energy Reviews*, vol. 88, pp. 16–36, may 2018.
- [313] “Moray East Offshore Wind Farm.” [Online]. Available: <https://www.morayeast.com/current-works/offshore-works>
- [314] G. H. Keulegan and L. H. Carpenter, “Forces on Cylinders and Plates in an Oscillating Fluid,” *Journal of Research of the National Bureau of Standards*, vol. 60, pp. 423–440, May 1958.
- [315] A. Botelho, B. Parreira, P. N. Rosa, and J. M. Lemos, *Predictive Control for Spacecraft Rendezvous*, ser. SpringerBriefs in Applied Sciences and Technology. Cham: Springer International Publishing, 2021.

- [316] D. Q. Mayne, J. B. Rawlings, C. V. Rao, and P. O. Scokaert, “Constrained model predictive control: Stability and optimality,” *Automatica*, vol. 36, no. 6, pp. 789–814, 2000.
- [317] P. Scokaert, D. Mayne, and J. Rawlings, “Model Predictive Control (Feasibility Implies Stability),” *IEEE Transactions on Automation and Control*, vol. 44, p. 648–654, Dec. 1999.
- [318] D. Mayne, “An Apologia for Stabilising Terminal Conditions in Model Predictive Control,” *International Journal of Control*, vol. 86, pp. 2090–2095, Nov. 2013.
- [319] B. Stellato, G. Banjac, P. Goulart, A. Bemporad, and S. Boyd, “OSQP: an operator splitting solver for quadratic programs,” *Mathematical Programming Computation*, vol. 12, no. 4, pp. 637–672, dec 2020.
- [320] A. Gelb, J. F. Kasper Jr., R. A. Nash Jr., C. F. Price, and A. A. Sutherland Jr., *Applied Optimal Estimation*. Reading, Massachusetts: The Analytic Sciences Corporation, 1974.
- [321] R. E. Kalman, “A New Approach to Linear Filtering and Prediction Problems,” *Journal of Basic Engineering*, vol. 82, no. 1, pp. 35–45, mar 1960.
- [322] R. E. Kalman and R. S. Bucy, “New Results in Linear Filtering and Prediction Theory,” *Journal of Basic Engineering*, vol. 83, no. 1, pp. 95–108, mar 1961.
- [323] S. J. Julier and J. K. Uhlmann, “A New Extension of the Kalman Filter to Nonlinear Systems,” *Signal processing, sensor fusion, and target recognition VI*, vol. 3068, pp. 182–193, 1997.
- [324] E. A. Wan and R. Van Der Merwe, “The unscented Kalman filter for nonlinear estimation,” in *IEEE 2000 Adaptive Systems for Signal Processing, Communications, and Control Symposium*. Lake Louise, AB, Canada: Institute of Electrical and Electronics Engineers Inc., 2000, pp. 153–158.
- [325] S. Soylu, A. A. Proctor, R. P. Podhorodeski, C. Bradley, and B. J. Buckham, “Precise trajectory control for an inspection class ROV,” *Ocean Engineering*, vol. 111, pp. 508–523, jan 2016.
- [326] A. Munafó and G. Ferri, “An Acoustic Network Navigation System,” *Journal of Field Robotics*, vol. 34, pp. 1332–1351, March 2017.
- [327] L. Jetto, S. Longhi, and G. Venturini, “Development and experimental validation of an adaptive extended Kalman filter for the localization of mobile robots,” *IEEE Transactions on Robotics and Automation*, vol. 15, no. 2, pp. 219–229, 1999.

- [328] F. Stella, N. Obayashi, C. D. Santina, and J. Hughes, “An Experimental Validation of the Polynomial Curvature Model: Identification and Optimal Control of a Soft Underwater Tentacle,” *IEEE Robotics and Automation Letters*, vol. 7, no. 4, pp. 11 410–11 417, oct 2022.
- [329] J. . M. J. Journée and W. W. Massie, *Offshore Hydromechanics*, 1st ed. Delft: Delft University of Technology, 2001.
- [330] F. Renda, F. Boyer, J. Dias, and L. Seneviratne, “Discrete Cosserat Approach for Multisection Soft Manipulator Dynamics,” *IEEE Transactions on Robotics*, vol. 34, pp. 1518–1533, Dec. 2018.
- [331] C. Barbalata, “Modelling and Control of Lightweight Underwater Vehicle-Manipulator Systems,” Ph.D. dissertation, Heriot Watt University, 2017.
- [332] D. Youakim, P. Ridao, N. Palomeras, F. Spadafora, D. Ribas, and M. Muzzuappa, “MoveIt!: Autonomous Underwater Free-Floating Manipulation,” *IEEE Robotics & Automation Magazine*, vol. 24, pp. 41–51, Sept. 2017.